Gravity observations for hydrocarbon reservoir monitoring

Gravity observations for hydrocarbon reservoir monitoring

Proefschrift

ter verkrijging van de graad van doctor
aan de Technische Universiteit Delft,
op gezag van de Rector Magnificus prof. K.C.A.M. Luyben,
voorzitter van het College voor Promoties,
in het openbaar te verdedigen op dinsdag 5 maart 2013 om 10:00 uur

door
Marcin Albert Glegola,
Master of Science in Applied Mathematics,
geboren te Krosno Odrzanskie, Polen.

Dit proefschrift is goedgekeurd door de promotoren:
Prof. dr.-ing. habil. R. Klees
Prof. dr. ir. R.J. Arts

Samenstelling promotiecommissie:

Rector Magnificus,	voorzitter
Prof. dr.-ing. habil. R. Klees,	Technische Universiteit Delft, promotor
Prof. dr. ir. R.J. Arts,	Technische Universiteit Delft, promotor
Prof. dr. ir. A. W. Heemink,	Technische Universiteit Delft
Prof. dr. ir. J.D. Jansen,	Technische Universiteit Delft
Prof. dr. W.R. Rossen,	Technische Universiteit Delft
Dr. ir. F. C. Vossepoel,	Shell International Exploration & Production
Dr. E. K. Biegert, P.G.	Shell International Exploration & Production

This research was carried out within the context of the ISAPP Knowledge Centre. ISAPP (Integrated Systems Approach to Petroleum Production) is a joint project of the Netherlands Organization for Applied Scientific Research TNO, Shell International Exploration and Production, and Delft University of Technology.

Printed in The Netherlands by Optima Grafische Communicatie, Rotterdam

Contents

Chapter 1

Introduction

1.1 Hydrocarbon recovery

Fossil fuels are bonds of carbon and hydrogen called hydrocarbons that can be found in three major forms: solid (coal), liquid (oil) and gaseous (natural gas). Hydrocarbons have been formed from organic material such as plants, trees and living organisms, which were buried deep in the subsurface for millions of years and exposed to high pressure and temperature.

A mixture of hydrocarbons, called petroleum, can be trapped in hydrocarbon reservoirs, i.e, porous rock formations surrounded by some sort of a geological flow barrier preventing hydrocarbons from escaping to the surface. Hydrocarbon reservoir rock, as rocks in general, are composed from a solid material (rock matrix) and a void space. A ratio of the volume of void space to the total volume of a reservoir rock is called porosity. The higher the porosity the more petroleum the reservoir rock can contain. Permeability is a measure characterizing the ability of a rock to transmit fluids. It is related to the connectivity of rock pore spaces which depends on rock grain sorting and rock grain geometry. The higher the reservoir permeability the easier the reservoir fluid flow through the formation. Therefore, porosity and permeability are important parameters characterizing hydrocarbon reservoirs.

The increasing energy demand and decreasing fossil fuels reserves stimulate more efficient production of hydrocarbon reservoirs. It is predicted (IEO 2011) that the World's energy consumption within the coming $20-30$ years may increase by 50% or more. In this context, efficient production of hydrocarbon reservoirs becomes more relevant than ever. Depending on the type and life-time of the reservoir various recovery techniques are used. In general, production of oil fields can be divided into three phases: primary recovery, secondary recovery and tertiary recovery (Fig. 1.1). The primary reservoir recovery starts at the beginning of the reservoir life and is driven by initially high reservoir pressure and expansion of reservoir fluids. Typically, only about 10% of the oil originally in place can be recovered in this way. The main purpose of a secondary recovery is to maintain the reservoir pressure and displace hydrocarbons towards producing wells. Additional drive-energy is supplied into the reservoir mostly by injecting water and/or gas (e.g., CO_2). Both, the primary and the secondary recovery can on average produce only a third of the oil in place and the recovery can also be as low as 5% and as high as 80%, depending on the reservoir characteristics (Speight 2009). Tertiary recovery, also called enhanced oil recovery (EOR), aims to increase the production further by improving mobility of reservoir fluids so they can flow easily into the wellbore. Various techniques are being applied, such as gas or chemicals injection and thermal methods based on e.g., steam flooding. The application of EOR techniques can increase oil recovery up to 30-60% or more (Speight 2009).

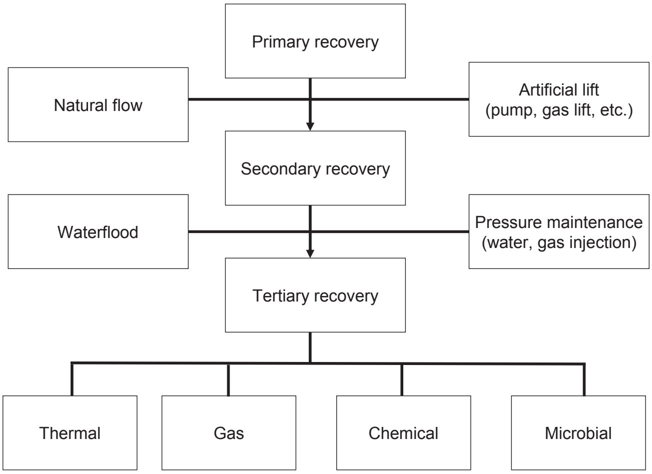

Figure 1.1: Methods for oil recovery, after Speight (2009).

For gas fields the recovery factors are usually higher than those of oil fields and can reach 50-90% (Ahmed 2006). This is because gas is significantly less dense than oil and can flow easier through the reservoir formation. Therefore, production of gas fields is mostly based on a natural-drive mechanism, i.e., pressure depletion or water-drive. In case of pressure depletion, the flow of gas towards the wellbore is driven by volumetric gas expansion and in the case of water-drive, it is additionally enhanced by pressure support provided by an aquifer, i.e., a water reservoir.

Regardless of the reservoir type and the recovery mechanism applied, reservoir production management can be very challenging. Decisions need to be made about e.g., the number and placement of wells or fluid injection and production rates. These decisions are usually associated with significant uncertainties related to the reservoir characteristics and its future performance. Therefore, to facilitate reservoir management and to better understand the reservoir characteristics and dynamics, numerical reservoir models are constructed. They are based on all available information including geological knowledge, hard data such as core samples, and geophysical data. The model uses physical flow equations (for reservoir flow modeling see, e.g., Peaceman 1977) discretized in space and time to simulate hydrocarbon flow in the reservoir. It may contain many uncertain parameters such as structure delineation, petrophysical properties such as porosity, permeability, and others. The number of unknowns may easily reach several thousands or millions. The uncertain parameters are usually adjusted by measuring the output from the real reservoir, e.g., production rates and well pressures, and by comparing the real observations with the synthetic data predicted from the numerical model. If the real observations do not match the model predictions, the uncertain parameters are adjusted accordingly. This process is called history matching. It is believed that the model fitting the observed data should have better prediction capabilities of the field performance. Consequently, the field management strategy can be optimized to fit given criteria. This concept, called closed-loop reservoir management, is described in more detail in the next subsection.

1.2 Closed-loop reservoir management

Closed-loop reservoir management (called also ”real-time reservoir management”, ”smart reservoir management” or ”closed-loop optimization”) uses a combination of model-based optimization and data assimilation (computer-assisted history matching). Its objective is continuous or real-time reservoir management to optimize field operations and to improve its long-term production (Jansen et al. 2008, Jansen et al. 2009). The key elements of the closed-loop concept are shown in Fig. 1.2.

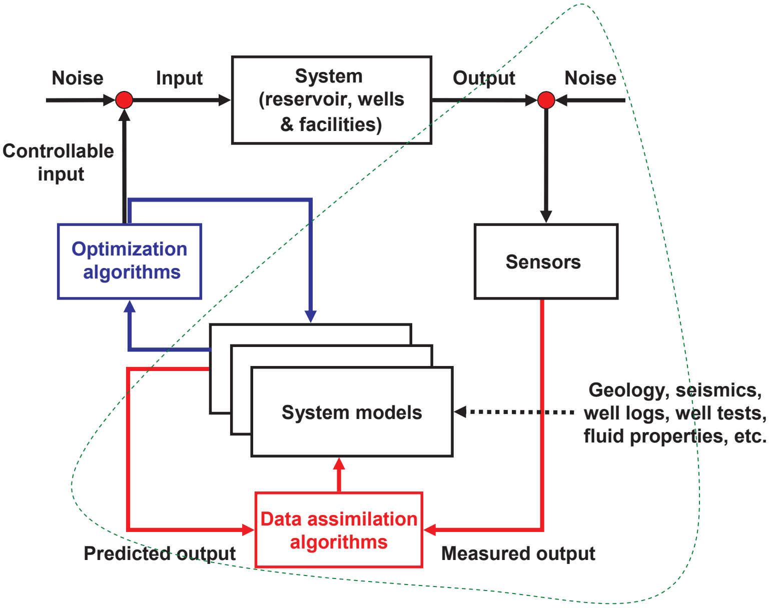

Figure 1.2: Key elements of the closed-loop reservoir management, after Jansen et al. (2009). The research content included in this thesis is within the green dashed line.

In the top of the diagram the real physical system is shown. It includes a hydrocarbon reservoir, wells and other field facilities. Typically, as we already mentioned, the system is represented with synthetic models, shown at the center. They are based on the available field data such as well logs, well tests, fluid properties, geological knowledge and assumptions. The system models may include static (geological) or dynamic (reservoir flow) numerical models with many uncertain parameters. Many model realizations can be used to express the uncertainty of the unknown parameters. The response of the physical system, i.e., the hydrocarbon reservoir, is measured with sensors, shown at the right. The sensors provide various data including reservoir production data and other surveillance data. Typically, the system performance cannot be measured perfectly and the measured output contains some sort of the noise. The noisy output is used to update the models (red loop). The system model parameters are adjusted so that the predicted data match the observations within some specified bounds, typically related to the uncertainty of the measurements. For that purpose various data assimilation methods are applied. The updated models are subsequently used in the optimization loop, which provides a control input to the physical system. Using numerical optimization algorithms and updated system models, an optimal field production strategy can be searched. Various optimality criteria can be defined, and usually the net present value (NPV) is maximized. The control parameters can be injection rates, well-valve settings and general field management decisions such as the placement of new wells. The inputs to the system are also uncertain because of device measurement errors, e.g., of water/gas injection rates or because of poorly known reservoir boundary conditions such as aquifer support characteristics.

The research results presented in this thesis fit into the data assimilation loop (embedded by the dashed green line in Fig. 1.2) and the major focus is on the added value of gravimetric observations for system models updates. We also consider various sources of gravimetric noise and available gravity measurements systems applicable for hydrocarbon reservoir monitoring.

1.3 Data Assimilation

Data assimilation (computer-assisted history matching) is a methodology used to estimate the unknown variables and/or parameters of a physical system by merging available observations into a dynamic model of that system. The model of a system contains a mathematical description of physical processes with a set of uncertain parameters. In the context of hydrocarbon reservoirs, the system model includes a numerical model of reservoir flow with parameters such as, e.g., reservoir saturation, pressure, porosity, permeability, structure, initial conditions (e.g., fluid contacts). Because the unknown parameters need to be estimated for every grid cell of the reservoir model, which can be very complex, the number of unknowns can be very large and can easily reach 10^6-10^8. For such large-scale data assimilation problems two classes of methods, namely variational methods and ensemble Kalman filtering, have been demonstrated to be suitable and powerful (Heemink et al. 2010).

Within variational data assimilation methods uncertain parameters of a model are estimated by the minimization of a cost function. The cost function includes the data misfit term, i.e., the difference between observed and predicted observations and often also an additional regularization term to stabilize the solution. For large-scale problems the optimization is usually performed using iterative gradient-based methods and quasi-Newton schemes are often applied (Oliver et al. 2008, Heemink et al. 2010). Kalman filtering methods provide a sequential updating of the system state based on the predictor-corrector structure (see, e.g., Heemink et al. 2010). For a particular time step when measurements become available, a prediction of the state of the system is made based on all previous information. The mismatch between observed and predicted data is used to update (correct) the modeled system state and to produce a forecasted state for the next assimilation time. Furthermore, the error statistics of estimation/prediction errors can be determined and propagated forward. The Kalman filter is the optimal sequential assimilation method for linear system dynamics and Gaussian assumptions about the system and measurement noise (Evensen 2007). The optimality refers to the minimization of errors in the updated state estimate. For nonlinear dynamics, various modifications of the filter such as the ensemble Kalman filter (EnKF) were developed resulting in approximate solutions. The EnKF is a sequential Monte Carlo method, which approximates the state covariance matrix using a finite set of randomly generated system states. The EnKF method has been widely applied for reservoir engineering applications (Aanonsen et al. 2009, Oliver & Chen 2011). This method will further be used in the thesis and introduced in more detail in Chapter 4.

1.4 Reservoir monitoring

The closed-loop reservoir management process and reservoir management in general, would not be possible without reservoir monitoring. Reservoir monitoring provides information about changes taking place in the reservoir which are triggered by reservoir management decisions and actions and/or are induced by natural processes such as, e.g., a water influx from the aquifer. For reservoir monitoring, various observations are acquired and they typically include production data and time-lapse (4D) seismic measurements. The time-lapse data are obtained by computing the difference between measurements gathered over two surveys: a monitoring survey performed while the reservoir is produced and a baseline survey, ideally acquired before the reservoir production starts. In this research we consider the use of time-lapse gravimetry for reservoir monitoring.

1.4.1 Production data

Production data are collected at well locations and typically include measurements of pressure, oil, gas and water rates. Production measurements can be acquired very frequently, e.g., pressures daily, phase rates monthly, and therefore provide large amount of data for the field (Oliver et al. 2008). However, due to a limited number of wells, the well data cannot provide sufficient information about the state of the whole reservoir. Therefore, areal observations are needed, which are usually provided by time-lapse seismics.

1.4.2 Time-lapse seismic monitoring

Seismic data are measurements of elastic waves, i.e., waves of energy, that have traveled through the Earth's subsurface. In reservoir engineering the waves are usually generated with explosions and vibrators or with air guns in case of offshore measurement campaigns. They are recorded with receivers, such as geophones (or hydrophones offshore), which convert mechanical motion into an electrical signal. Once the waves are generated they propagate through the subsurface and reflect at boundaries where a change in elastic properties occurs. Some reflected waves travel back to the surface and are recorded by receivers. The wave travel time depends, among others, on the depth of the reflector and on the wave velocity, the later one being related to the elastic properties of the medium through which the wave is traveling. Therefore, the analysis of seismic waves may provide, for instance, information about rock types as well as about the geometry of interfaces separating different layers, thus resulting in a structural image of the subsurface. Seismic data are sensitive not only to the static rock properties such as rock matrix density, but also to dynamic variables such as pressure or fluid saturation, which change with time when the reservoir is produced. Therefore, time-lapse seismics may provide useful information about the areal time-evolution of reservoir fluids and pore pressure. Nevertheless, acquiring seismic data for reservoir monitoring is usually expensive, may be difficult and sometimes prohibitive, e.g., in urban or industrial areas with high levels of environmental noise (AhmadZamri et al. 2009). Time-lapse (4D) gravimetry, which is a direct measure of the subsurface mass redistribution, has the potential to provide independent and valuable information for hydrocarbon reservoir monitoring.

1.4.3 Time-lapse gravimetric monitoring

The objective of time-lapse (4D) gravimetry is to determine spatio-temporal changes of the Earth's gravity field by performing repeated measurements of gravity and spatial gravity gradients. On a local scale, variations in the gravity field can be caused by subsurface mass redistribution resulting from a hydrocarbon reservoir production (see Fig. 1.3 for an illustration). Therefore, 4D gravimetric observations have the potential to provide useful information about fluid flow in the reservoir.

However, gravimetric reservoir monitoring requires very high (at the μGal level[1]) measurement precision, which was difficult to achieve until recently. Therefore, despite the fact that the gravity exploration method has been known for centuries (LaFehr 1980, Torge 1989, Nabighian et al. 2005), time-lapse gravimetry has been used for geophysical applications only for about five decades (see e.g., Biegert et al. 2008). Nowadays, thanks to developments in gravimetric instrumentation and data acquisition procedures, high precision time-lapse gravity measurements have become a mature monitoring technique both for land and offshore applications. We present a brief overview of applications of 4D gravity in geophysics, and in particular in reservoir engineering, in Chapter 2.

The observed temporal gravity variation is an integrated effect of all mass redistri-

---

[1] $1\mu\text{Gal}=10^{-8}\text{m/s}^2$

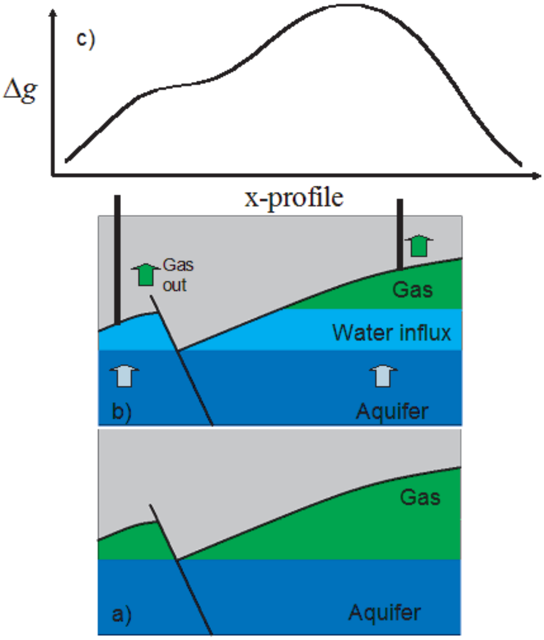

Figure 1.3: Schematic illustration of 4D gravimetric reservoir monitoring. Gas takeout causes the reservoir pressure drop and, consequently, water influx from the aquifer (b). Denser water replaces gas and creates positive subsurface mass variation with respect to the initial conditions (a). The subsurface mass change is a source of temporal gravity variation (Δg) that can be observed at the surface (c) and from which the aquifer water influx can be inferred.

bution around the observation point. Therefore, it contains not only the signal of interest, in our case originating from a hydrocarbon reservoir, but also additional signals induced by various environmental processes. The most common examples are solid Earth tides and ocean tides, polar motion, and air pressure changes. They can add tens and hundreds of μGal to the measured signal. Correcting for their influences can be done with the application of various models and/or the acquisition of additional observations. Another source of noise are local hydrological variations such as temporal changes of the water table (Harnisch & Harnisch 2006, Amalvict et al. 2004). Their direct gravitational effect can reach 10-20 μGal and more (Creutzfeldt et al. 2008, Torge 1989) and may significantly affect the feasibility of gravimetric reservoir monitoring (see Fig. 1.4 for illustration). For that reason, the hydrological influences on gravity need to be estimated and properly corrected for. In practice, due to the lack of measurements, a detailed hydrological model is rarely available. Consequently, hydrological gravity corrections can be based on only a few local observations of the water table and soil moisture variations. This may not be sufficient to appropriately remove all the disturbances leaving an unknown hydrological noise in gravity observations. Therefore, influence of hydrological noise in particular, and of other noise sources, on gravimetric reservoir monitoring needs to be investigated.

Despite the increasing number of applications of time-lapse gravimetry for the monitoring of hydrocarbon reservoirs, there is little published material on the added value of gravimetric observations within a broader context of modern reservoir engineering, such as in closed-loop reservoir management. The potential contribution of gravity data for an improved reservoir characterization, production forecast accuracy and hydrocarbon reserves estimation, is still to be addressed in more detail.

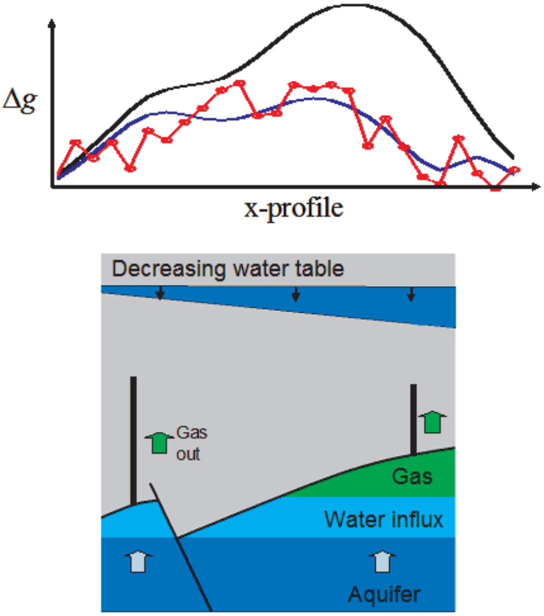

Figure 1.4: Schematic illustration of 4D gravimetric reservoir monitoring affected by hydrological and instrumental noise. Gas takeout causes the reservoir pressure drop and, consequently, water influx from the aquifer (b). Denser water replaces gas and creates positive subsurface mass variation with respect to the initial conditions shown in Fig. 1.3a) and positive temporal gravity (Δg) variation (in black). Decrease in water table is a source of negative gravity change. The sum of two signals, i.e., originating from the reservoir and from the water table, is shown in blue. The observed data (in red) are additionally contaminated with a random measurement (e.g., instrumental) noise.

1.5 Research Objectives

The main objective of this research is to

> *investigate the added value of gravity observations for hydrocarbon reservoir monitoring and characterization.*

For this purpose we:

- Investigate which reservoir processes and reservoir types are the most suitable for gravimetric monitoring, develop a forward modeling approach and couple it with the forward reservoir simulation.
- Analyze and model various noise sources and noise properties in temporal gravity observations. In particular, investigate the influence of spatio-temporal hydrological variations.
- Perform data assimilation experiments to investigate the contribution of gravity data for reservoir monitoring. In particular, investigate the added value of gravity for the estimation of spatio-temporal mass variations in the reservoir and of the total amount of water influx from the aquifer.
- Perform data assimilation experiments to investigate the contribution of gravity data for improved reservoir characterization, considering the estimation of static reservoir parameters, such as, porosity, permeability, reservoir structure and aquifer characteristics.
- Perform data assimilation experiments to investigate the added value of a joint assimilation of gravity and reservoir production data for reservoir monitoring and characterization.

1.6 Thesis Outline

The thesis is organized as follows:

- In Chapter 2, the applicability of time-lapse gravimetry for hydrocarbon reservoir monitoring is discussed. Measurement systems available for reservoir monitoring are briefly introduced and a literature overview of field case gravity applications is presented. The forward gravity modeling approach used in the thesis is described and it is explained how the gravimetric signal relates to the reservoir mass redistribution.
- In Chapter 3 we discuss major noise sources affecting monitoring of hydrocarbon reservoirs with time-lapse gravimetry. Special attention is devoted to the analysis of hydrological influences on gravimetric observations, in particular originating from groundwater variations. A potential contribution of groundwater to the uncertainty budget is evaluated with forward simulations of hypothetical variations of water table changes. The chapter is concluded with a summary of the total uncertainty budget in gravity measurements. The content of this chapter is partly based on (Glegola et al. 2009).

- In Chapter 4 we introduce the inversion/estimation methods used throughout the thesis: the focusing inversion and two ensemble-based data assimilation techniques, namely the ensemble Kalman filter and the ensemble smoother. A common framework between the focusing inversion and data assimilation is briefly discussed and some illustrative application examples are presented.

- Chapter 5 summarizes the findings of the feasibility study on gravimetric monitoring of the Thermally-Assisted Gas-Oil Gravity Drainage (TA-GOGD) process at the carbonate field in the North of Oman. The study includes a quantification of the expected temporal gravity changes resulting from the reservoir mass redistribution induced by the TA-GOGD process. Furthermore, the estimates of noise in gravity data related to the specific hydrological conditions in the field are considered and it is investigated under which conditions the hydrological influences can be minimized. Finally, we perform the focusing inversion of gravimetric observations and analyze the achievable accuracy of heat-front position estimates under the specific hydrological conditions. Major findings included in this chapter have been submitted for a publication (Glegola et al. n.d.).

- In Chapter 6 we investigate the added value of gravimetric observations for monitoring water-influx into a gas field. For this purpose we use data assimilation with the ensemble Kalman filter (EnKF). We begin with a sensitivity study by making various assumptions about the level of gravity measurement noise and the distance from the gravity observation network to the reservoir formation. Next we investigate the effect of a combined assimilation of gravity and production data. The content of this chapter is to a large extent based on the results published in (Glegola et al. 2012a).

- Chapter 7 extends the work included in Chapter 6 from a 2D to a more realistic 3D reservoir model. As in Chapter 6 we investigate the added value of gravimetric observations for gas field monitoring. However, this time not only the permeability field is considered uncertain but also the aquifer support characteristics and other parameters, such as porosity and reservoir structure. We assimilate both gravity and production data using the ensemble smoother (ES) and investigate their added value for the field monitoring and characterization. The content of this chapter is to a large extent based on (Glegola et al. 2012b).

- In Chapter 8 an example of application of the bias-aware data assimilation methodology is presented. Synthetic experiments based on the the 2D gas reservoir model, used in the data assimilation in Chapter 6, are included. Similarly as in Chapter 6, we assimilate gravity data to estimate the reservoir permeability and the reservoir mass redistribution. This time, however, we consider not only random noise in the observations but also systematic errors (biases) in both the observations and the forward model.

- Chapter 9 contains conclusions and recommendations for future research.

Chapter 2

Time-lapse gravimetry for hydrocarbon reservoir monitoring

In this chapter the applicability of time-lapse gravimetry for hydrocarbon reservoir monitoring is discussed. Furthermore, a literature overview on the topic is included and some basics of gravimetry are introduced. Subsequently, the state-of-the-art measurement systems applicable for reservoir monitoring are briefly discussed. We also present the forward gravity modeling approach used in the thesis and explain how the gravimetric signal relates to the reservoir mass redistribution. Finally, we include a simplified sensitivity analysis to analyze the applicability of various gravimetric measurement concepts in reservoir monitoring.

2.1 Introduction

The task of time-lapse (4D) gravimetry is to measure spatio-temporal changes of the Earth's gravity field by performing repeated measurements of gravity and its gradients. Local changes in the gravity field can result from subsurface mass redistribution induced by hydrocarbon reservoir production. Therefore, 4D gravimetric observations have a potential to provide useful information about mass transport in the reservoir. However, variations in the gravity field caused by reservoir production are incredibly small compared to the total Earth's gravity field (Fig. 2.1). For that reason, the monitoring of hydrocarbon reservoirs requires a very high, μGal-level ($1\mu\text{Gal}=10^{-8}\text{m/s}^2$), measurement sensitivity and precision, which was difficult to achieve until recently. Therefore, despite the fact that the gravity exploration method has been known for centuries, (for a comprehensive historical overview see, LaFehr 1980, Torge 1989, Nabighian et al. 2005) with roots originating in Galilei's time (1564-1642)[1] and foundations provided by Newton (1642-1727), the time-lapse gravimetry has been used for geophysical applications only for about five decades (for an overview see, Biegert et al. 2008).

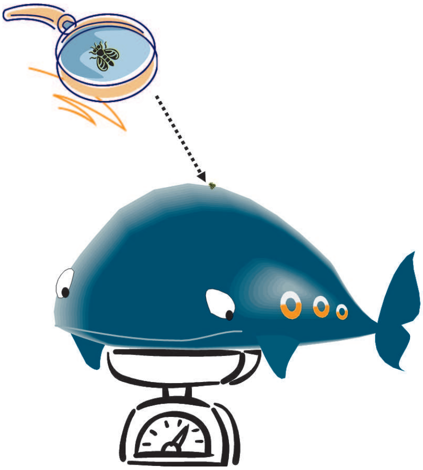

Figure 2.1: Schematic illustration of measurement challenges related to gravimetric monitoring of hydrocarbon reservoir. Gravity field variations caused by reservoir mass redistribution are typically on a μGal-level which is about 10^{-9} of the average acceleration due to gravity at the Earth's surface. Thus, measuring subtle gravity changes in reservoir monitoring is like determining the weight of a fly sitting on a whale. Picture after Larry Beyer, 1984, USGS

In one of the early applications dating back to 1961 time-lapse gravimetric observations were used to monitor subsurface water/steam mass redistribution at Wairakei geothermal field on the North Island of New Zeeland (Allis & Hunt 1986). Examples of other applications include monitoring of volcanic activities where the temporal gravity signal was related to the subsurface mass redistribution and/or surface deformation (Yokoyama 1989, Rymer 1994, Battaglia et al. 2008).

---

[1] the memory of Galileo is honored with the primary unit of acceleration, $1\text{Gal}=\text{cm/s}^2$

Nowadays, high precision time-lapse gravimetry has become a mature reservoir monitoring technique both for land and for offshore applications. With advancements in data acquisition and data processing procedures a μGal-level measurement precision can be achieved. Recent synthetic and field studies have shown that 4D gravity can be used for monitoring of reservoir mass redistribution induced by a water-gas displacement. For instance, Hare et al. (1999) investigated the feasibility of gravimetric monitoring of Gas-Water Contact (GWC) at Prudhoe Bay reservoir in Alaska. For a 2500 m deep reservoir they predicted a maximum gravity variation of about 250 μGal and demonstrated that the water front propagation could effectively be mapped with surface gravity observations. Biegert & Witte (2001) investigated the feasibility of gravimetric monitoring of a GWC rise in the Mars reservoir, Gulf of Mexico. For a 1700 m deep gas reservoir and several tens of meters of GWC rise they predicted temporal gravity variation of about 100 μGal, which is far above the typical measurement uncertainty. Stenvold et al. (2008) provided a comprehensive insight into typical subsurface density changes for water-drive gas fields and associated time-lapse surface gravity variations. They concluded that with the current technology the repeated surface gravity measurements can be used for water influx monitoring even for moderate-size gas reservoirs ($\sim$ 23 Gm^3 gas in place) at fairly large depths ($\sim$ 2000 m). Encouraging results of many synthetic studies stimulated field applications of time-lapse gravimetry. For instance, van Gelderen et al. (1999) showed the results of gravimetric monitoring of the large Groningen gas field in the Netherlands. The initial purpose of monitoring there was possible replacement of costly leveling surveys for land subsidence caused by compaction of the gas reservoir. Thanks to long-term gravimetric observations, spanning a period of 18 years (1974-1996), the gravity effect of mass extraction of produced gas could also be detected. The observed trends of gravity decline were in accordance with the reservoir production data. Van Popta et al. (1990) presented results of a successful application of borehole gravimetry to monitor gas saturation in Gas-Oil Gravity Drainage (GOGD) process in the Natih field in Oman. Alixant & Mann (1995) reported a successful use of repeated borehole gravity surveys to estimate in-situ residual oil saturation in Gabon's Rabi field. In more recent publications Ferguson et al. (2007) and Ferguson et al. (2008) described the 4D gravity methodology used for monitoring the GWC movement in the arctic environment at the Prudhoe Bay reservoir in Alaska. It is the first applications where absolute gravimetry was used for field-wide (approximately 300 stations) reservoir monitoring. Despite challenging environmental conditions (weather, snow mass spatio-temporal redistribution) they achieved precision better than 10 μGal in 4D gravity signal. In parallel papers Hare et al. (2008) and Brady et al. (2008) discussed the 4D gravity monitoring results at Prudhoe Bay and showed that the redistribution of the injected water mass could effectively be monitored with gravimetry. AhmadZamri et al. (2009) described an application of 4D gravimetry for monitoring of waste gas injected into an aquifer. They showed that despite operating in an active construction area, which excluded the use of seismic monitoring, gravity provided useful information on the propagation of the gas front. Zumberge et al. (2008) described the high-precision seabed time-lapse gravity methodology developed for offshore applications. Thanks to improvements in data acquisition and data processing procedures (including simultaneous measuring with multiple sensors, repeated instrument calibrations and minimization of vibrational and thermal perturbations to the sensors), 3 μGal precision in time-lapse gravity observations can be achieved, which, as will be shown later, is an order of magnitude smaller than the typical signals of interest. Seabed gravimetry has been recently applied to survey a number of offshore fields. For instance, Nooner et al. (2007), Alnes et al. (2008) and Alnes et al. (2011) showed results of seafloor gravimetric monitoring of gas production and CO_2 storage at the Sleipner field in the North Sea. The 4D gravimetric observations were used there to constrain the in-situ CO_2 density and to estimate the mass change distribution caused by gas production and water influx into the reservoir. Eiken et al. (2008) discussed results of the gravimetric monitoring of water influx into the giant Troll gas field in the North Sea. Siddique (2011) described the application of time-lapse gravimetry for monitoring Midgard gas field, offshore Norway. There, the positive time-lapse gravity variations indicated the water influx, which was not inferred from other data. Thanks to information provided by gravity the gas in place volumes were updated and the water breakthrough in one of the wells was predicted properly.

There are also examples of oil fields monitoring with gravimetry. In a recent publication, Alawiyah et al. (2011) presented results of the gravimetric monitoring of a very shallow ($\sim$ 700 m deep) oil field in Sumatra, Indonesia. Gravimetric observations were used to monitor field-wide density changes caused by oil production and by water injection. Thanks to the information provided by gravimetric observations, a recommendation for the placement of new production and injection wells could be made.

Not only gravity but also spatial gravity gradients can be measured. Droujinine et al. (2007) examined the feasibility of hydrocarbon reservoir monitoring using time-lapse gravity gradiometry. They considered simplified-geometry synthetic models but also more realistic examples inspired by some real fields, e.g., the Teal South oil reservoir in Gulf of Mexico or Athabasca tar sands in Canada. They concluded that time-lapse gravity gradiometry can contribute to the monitoring of Gas-Oil Contact (GOC) and temperature front expansion during steam injection in heavy oil reservoirs at shallow ($\sim$ 200 m) to moderate ($\sim$ 1000 m) depths. However, monitoring reservoirs at moderate to large depths can be very challenging. This is because of the very rapid (approximately proportional to cubic distance) gravity gradient signal attenuation with distance from an observation point to the target. We will demonstrate this effect in Section 2.5.3.

2.2 Time-lapse gravimetry

The Earth's gravity field is a vector field generated by the Earth's gravitation and centrifugal force resulting from the Earth's rotation, i.e., (Torge 1989)

$$\mathbf{g} = \mathbf{b} + \mathbf{z}, \tag{2.1}$$

where $\mathbf{g}$ denotes the gravity acceleration, $\mathbf{b}$ is the gravitational acceleration and $\mathbf{z}$ is the centrifugal acceleration. The gravity field can be expressed as the gradient of the gravity potential W, which is a scalar quantity

$$\mathbf{g} = \nabla W = (W_x, W_y, W_z)^T, \tag{2.2}$$

where

$$W = U + Z, \tag{2.3}$$

U denotes the gravitational potential, Z is the centrifugal potential and subscripts x, y, z stand for the spatial derivatives in the respective directions. Because the centrifugal potential of the Earth can be determined to a high accuracy, changes in the gravitational potential U, are of interest in practical applications of time-lapse gravimetry.

Typically, the magnitude of the gravity acceleration vector, often denoted with g, is measured. On the Earth's surface g equals to about 9.8 m/s^2 .

Taking the gradient of $\mathbf{g}$ yields the gravity gradient tensor (called also the Eötvös tensor)

$$\nabla \mathbf{g} = \nabla(\nabla W) = \begin{pmatrix} W_{xx} & W_{xy} & W_{xz} \\ W_{yx} & W_{yy} & W_{yz} \\ W_{zx} & W_{zy} & W_{zz} \end{pmatrix}, \tag{2.4}$$

with Eötvös units abbreviated by E, where $1\text{E} = 10^{-9}/\text{s}^2 = 0.1\mu\text{Gal/m}$. Measuring and analyzing the gravity gradient tensor components is the task of gravity gradiometry.

Time-lapse gravity or gravity gradiometry surveys measure the variations in gravity or its spatial gradients by taking the difference in measurements acquired at different time epochs.

2.3 Measurement systems and instrumentation

2.3.1 Gravity measurements

Measurements of gravity can be performed in an absolute and a relative sense. Absolute gravimeters measure the actual value of g at a given location. In the past, the pendulum method was used, which was based on observation of the oscillation time of the pendulum of a known length (Torge 1989). The application of the pendulum method has been abandoned after 1960s, when much more accurate free-fall method was developed. Nowadays, the value of g is estimated from the repeated falling mass experiment where the free-fall acceleration of a proof mass, dropped in a vacuum chamber, is measured. Many drops are preformed, typically hundreds to thousands, and the value of g is determined by averaging. With this method an accuracy of about 1μGal can be achieved but it requires extremely accurate measurements of time (nanoseconds) and length (nanometers) obtained with atomic clock and laser interference, respectively. An example of state-of-the-art absolute gravimeter is the FG-5 (Fig. 2.2a). Also well-known is the field-portable instrument, A-10 (Fig. 2.2b) used e.g., to monitor water mass injection at Prudhoe Bay in Alaska (Ferguson et al. 2008).

Relative gravimeters can be used to sense the difference in gravity between two measurement points or between two epochs for a given measurement point. Though, in

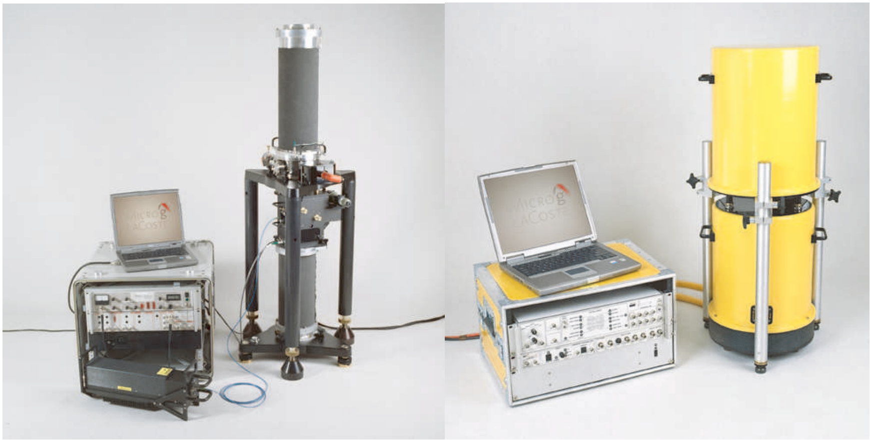

(a) FG-5 **(b)** A-10

Figure 2.2: Two examples of absolute gravimeters, source http://www.microglacoste.com

many geophysical applications the relative gravity differences are sufficient, the absolute gravity value can also be established by referencing the relative measurements to a point with a known absolute gravity. The most common relative gravimeter design is based on a mass-spring system, which senses variations of gravity field. For instance, an increase in gravity at a given point, causes the spring to elongate. A force feedback system restores the mass to its reference position, and the restoring force, which is proportional to the force of gravity, is measured (Fig. 2.3).
Since the first introduction of this type of instruments in the 1930s many of them have been developed (for a comprehensive gravimeters overview see, e.g., Chapin 1998). The most known are the LaCoste-Romberg gravimeters equipped with a metal spring (Fig. 2.3). Nowadays, also Scintrex's instruments (CG-5), based on the quartz spring (Fig.2.3), are frequently used. With CG-5 instrument accuracy better than 1 μGal and precision better than $2-3$ μGal (see, e.g., Christiansen et al. 2011) can be achieved. The state-of-the-art seabed gravity measurement system is based on the simultaneous (to statistically improve the measurement precision by averaging) use of three CG-5 sensors operated in temperature-, pressure- and vibration-protected housing (Zumberge et al. 2008).

Relative gravimeters suffer from instrument drift caused by a stretching of the spring with time. Therefore dedicated data acquisition and data processing procedures to ensure good quality measurements are required. Despite this, relative gravimetry offers the fastest, most portable, and therefore most widely used gravity measurement method in land surveys.
Not only surface but also borehole gravimeters were developed (Fig. 2.4). The only field-deployed system for reservoir monitoring (see e.g., Van Popta et al. 1990, Alixant & Mann 1995) is the Micro-g LaCoste borehole relative gravimeter (BHGM), based on the LaCoste & Romberg design (Fig. 2.4a). Recently, another borehole gravimeter, called Gravilog (Fig. 2.4b), has been developed. It is based on the quartz spring

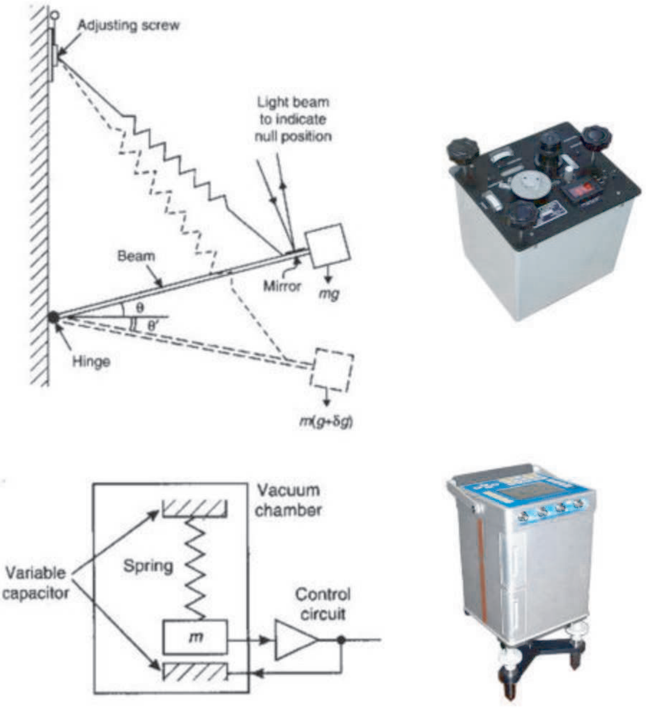

Figure 2.3: Examples of the relative gravimeter design concepts. In the top row the LaCoste-Romberg design and the instrument are shown and in the bottom row the Scintrex CG-5 concept and the instrument are shown.

system as used in the CG-5 relative gravimeter. Thanks to its small dimensions and the fact that it can operate in deviated wells, Gravilog may soon become more widely used in the petroleum industry.

The borehole gravimeter measures gravity at discrete points along the borehole. Measuring gravity in a borehole implies not only an instrument miniaturization challenge but also harsh operating environment. The sensor is exposed to high pressure and temperature variations. For that reason, borehole gravity observations are typically more noisy than surface ones. The nominal precision of the BHGM meter is about 7 μGal[1] and examples of field-reported uncertainty estimates are 8 μGal (MacQueen & Mann 2007) and 17 μGal (Alixant & Mann 1995). Because the gravity field is not shielded by any type of material, borehole gravimetry is not affected by the borehole rugosity and damage, cementation and casing, which may influence measurements carried out with other logging techniques. For that reason, borehole gravimetry is a very attractive density logging tool.

---

[1] Microg-LaCoste, http://www.microglacoste.com/

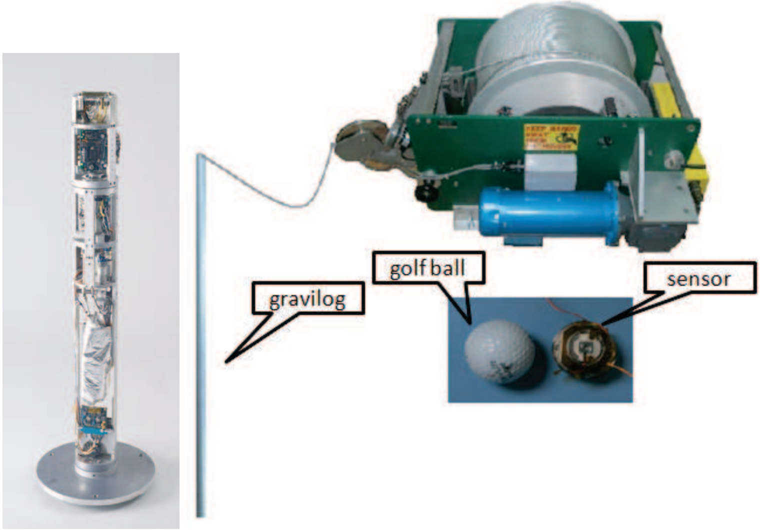

(a) LaCoste&Romberg gravimeter

(b) Gravilog gravimeter

Figure 2.4: Borehole relative gravimeters: (a) based on LaCoste&Romberg concept (www.microglacoste.com); (b) based on the quartz spring concept (www.scintrexltd.com).

2.3.2 Gravity gradient measurements

Gravity gradiometers have been used for geophysical exploration since the 19th century, starting from the first torsion balance instrument developed by Baron Roland von Eötvös. As a matter of fact, the gravity gradiometry measurements with the Eötvös torsion balance were the first geophysical data leading to oil and gas discovery (Nabighian et al. 2005).

Nowadays, various gradiometer systems are available (for an overview see, DiFrancesco 2007). A land-based gravity gradiometer system intended for time-lapse reservoir monitoring has been developed by Lockheed Martin (DiFrancesco 2007). It uses 8 accelerometers mounted on a disc rotating around a vertical axis. This system is capable of measuring W_{xy} and $W_{xx} - W_{yy}$ gradient tensor components (personal communication, D.J. DiFrancesco, Lockheed Martin) with demonstrated repeatability of about 0.2 E (DiFrancesco 2002).

Another gradiometer system potentially applicable in reservoir monitoring is being developed by Gravitec Instruments Ltd. It uses a novel concept based on a single sensing element (a ribbon) responding to gravity gradient forcing. This system is capable of measuring W_{xy}, W_{xz} and W_{yz} and can be used in airborne, ground, or borehole measurements. The Gravitec sensor is in the final stage of its development (personal communication, F. Neill, Gravitec).

2.3.3 Summary

Recent feasibility studies and field cases have shown that modern gravimeters are capable of measuring subtle gravity variations caused by hydrocarbon reservoir production. They can achieve accuracy better than 1μGal and precision better than $2-3$ μGal. Various measurement systems are available for measuring gravity both in the absolute and in the relative sense. Relative gravimetry is the most commonly used field measurement technique because it is faster and more portable than absolute gravimetry. Relative gravimeters have also been adapted for offshore applications, including surveys performed at the seabed, and for borehole gravity data acquisition.
Land gravity gradiometers have been developed with potential application in reservoir monitoring. They are capable of measuring gravity gradients with 0.2 E precision. Gradiometers applicable also in a borehole environment are being developed and they may become available soon.

2.4 Forward gravity modeling

To compute the gravity field variations generated by 3D reservoir mass redistribution we approximate the reservoir body with a number of rectangular prisms. The advantage of this approach relies on the availability of exact analytical solutions for the gravitational potential and its derivatives for the prism. Furthermore, this approach offers a great geometrical flexibility allowing complex-shape mass redistributions to be approximated. The analytical solutions for the gravitational potential of a prism presented in this section can be found in Nagy et al. (2000).
First, let us assume that the prism is defined by the coordinates $x_1, x_2, y_1, y_2, z_1, z_2$ in a right-handed coordinate system. To simplify the notation, the observation point P is defined as the origin of the coordinate system, i.e., $P = (x_P, y_P, z_P) = (0, 0, 0)$. Practically, this is equivalent to a simple 3D shift applied to the coordinates defining the prism

$$\begin{aligned} x_1^* &= x_1 - x_P \\ x_2^* &= x_2 - x_P \\ y_1^* &= y_1 - y_P \\ y_2^* &= y_2 - y_P \\ z_1^* &= z_1 - z_P \\ z_2^* &= z_2 - z_P \end{aligned} \tag{2.5}$$

where x_P, y_P, z_P are the coordinates of the observation point P.
Further, it is assumed that the density ρ of the prism is constant. Then, the gravitational potential at point P obtained by triple integration over the prism can be written as

$$U(P) = G\rho u(P), \tag{2.6}$$

where

$$u(P) = \int_{x_1}^{x_2} \int_{y_1}^{y_2} \int_{z_1}^{z_2} \frac{dxdydz}{r}, \tag{2.7}$$

and $G = 6.673 \times 10^{-11}$ $\mathrm{m^3kg^{-1}s^{-2}}$ is the gravitational constant. Equation (2.7) has the analytical solution given by (Nagy et al. 2000)

$$\begin{aligned} u(P) = \quad & f(x_2, y_2, z_2) - f(x_2, y_2, z_1) \\ & + f(x_1, y_2, z_1) - f(x_1, y_2, z_2) \\ & + f(x_2, y_1, z_1) - f(x_2, y_1, z_2) \\ & + f(x_1, y_1, z_2) - f(x_1, y_1, z_1), \end{aligned} \tag{2.8}$$

where

$$\begin{aligned} f(x, y, z) \quad = \quad & xy \ln(z + r) + yz \ln(x + r) + zx \ln(y + r) \\ & -\frac{x^2}{2} \tan^{-1} \frac{yz}{xr} - \frac{y^2}{2} \tan^{-1} \frac{xz}{yr} - \frac{z^2}{2} \tan^{-1} \frac{xy}{zr} \end{aligned} \tag{2.9}$$

and $r = \sqrt{x^2 + y^2 + z^2}$.

From (2.9) it follows that the analytical solution of (2.7) is undefined at every point of $\mathbb{R}^3$, e.g., it is undefined at the points where the denominator in expression (2.9) becomes zero. Nagy et al. (2000) showed that at those points where any of the terms of Eq. (2.9) is not defined, the specific term has to be set equal to zero in practical computations. In this way the applicability of Eq. (2.9) can be extended to the whole 3D space. The same applies to the first order derivatives of u, e.g.

$$\begin{aligned} u_z(P) = \quad & f_z(x_2, y_2, z_2) - f_z(x_2, y_2, z_1) \\ & + f_z(x_1, y_2, z_1) - f_z(x_1, y_2, z_2) \\ & + f_z(x_2, y_1, z_1) - f_z(x_2, y_1, z_2) \\ & + f_z(x_1, y_1, z_2) - f_z(x_1, y_1, z_1), \end{aligned} \tag{2.10}$$

where

$$f_z(x, y, z) = x \ln(y + r) + y \ln(x + r) - z \tan^{-1} \frac{xy}{zr}. \tag{2.11}$$

The second derivatives of the gravitational potential of the prism do not exist at the points of density discontinuity, i.e., at the corners and boundary surfaces of the prism. However they do exist at every point of the interior and the exterior of the prism. For those points the following expressions can be used which can be written in the same form as (2.10), where

$$f_{xz}(P) = \ln(y + r), \tag{2.12}$$

$$f_{yz}(P) = \ln(x + r), \tag{2.13}$$

$$f_{xy}(P) = \ln(z + r), \tag{2.14}$$

$$f_{xx}(P) = -\tan^{-1}\frac{yz}{xr}, \tag{2.15}$$

$$f_{yy}(P) = -\tan^{-1}\frac{xz}{yr}, \tag{2.16}$$

$$f_{zz}(P) = -\tan^{-1}\frac{xy}{zr}. \tag{2.17}$$

Because the function u and its partial derivatives higher than order one are continuous where they exist, the order of differentiation can be interchanged. This means that e.g.: $u_{xy} = u_{yx}$.

Using the above we can write the gravitational attraction of prism i

$$g^i(P) = U_z(P) = G\rho^i u_z^i(P), \tag{2.18}$$

where ρ denotes the prism density, and $u_z(P)$ is determined from (2.10). The total gravitational attraction of the reservoir body is the superposition of the gravitational attractions of individual prisms

$$g(P) = \sum_{i=1}^{M} g^i(P), \tag{2.19}$$

where M denotes the number of prisms. In an analogous way $U_{xz}, \ldots, U_{zz}$ can be determined.

2.5 Gravity signal sensitivity to reservoir mass redistribution

To better understand how the reservoir mass redistribution affects the gravity field, let us observe first (see Eq. 2.18) that the gravitational attraction of a grid cell (here prism) scales proportionally with the grid cell density. The bulk density of a grid cell i can be expressed as

$$\rho_b^i = \phi^i \rho_f^i + (1 - \phi^i)\rho_m^i, \tag{2.20}$$

where ϕ denotes the porosity, ρ_f is the fluid density and ρ_m denotes the rock matrix density. For a three-phase system, the fluid density is determined from

$$\rho_f^i = \rho_o^i S_o^i + \rho_g^i S_g^i + \rho_w^i S_w^i, \tag{2.21}$$

where S denotes saturation and subscripts o, g, and w stand for oil, gas and water, respectively. The time-lapse gravity variation is determined from

$$\Delta g_k^i(P) = g_k^i(P) - g_0^i(P), \tag{2.22}$$

where k is the time index. Assuming a fixed reservoir geometry and a fixed position of the observation point, (2.22) can be expressed as

$$\Delta g_k^i(P) = G\Delta\rho_{b,k}^i u_z^i(P), \tag{2.23}$$

where $\Delta\rho_{b,k}^i = \rho_{b,k}^i - \rho_{b,0}^i$ is the bulk density change.
From (2.23) it follows that the time-lapse gravity variations scale proportionally with bulk density changes. Therefore, the larger the porosity, the difference in phase densities and change in the saturation, the larger the gravity variation. For that reason, reservoir processes involving fluids with high density contrast (e.g., gas versus water) are especially promising for gravimetric monitoring.
Certainly many combinations of phase densities, porosity and change in the saturation can result in the same bulk density change. To simplify the study further, we consider three intervals for density change, namely those which are likely to occur in case of oil/water replacement (Oil-Water-Contact, OWC): $10-80$ kg/m^3 , gas/water replacement (Gas-Water-Contact, GWC): $80-150$ kg/m^3 and oil/steam replacement (Steam-Oil-Contact, SOC): $150-200$ kg/m^3.

2.5.1 Surface gravity measurements

We perform a simplified study to investigate the sensitivity of surface gravity observations to reservoir mass redistribution. Let us consider the gravitational attraction at a point on the symmetry axis of a vertical cylinder (see, e.g., Telford et al. 1990)

$$\Delta g = 2\pi G\Delta\rho\left(h + \sqrt{(z^2+r^2)} - \sqrt{(z+h)^2+r^2}\right), \tag{2.24}$$

where z is the cylinder depth, r is the cylinder radius and h is the cylinder height (Fig. 2.5).

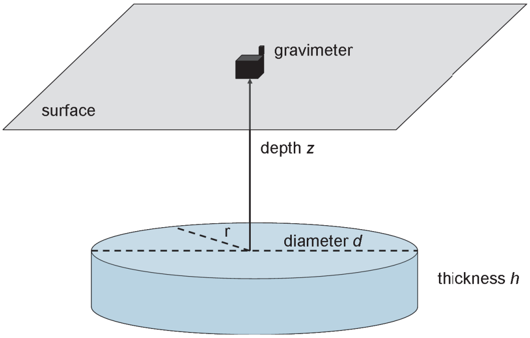

(a)

Figure 2.5: Schematic illustration of a vertical cylinder model used in the sensitivity analysis of gravimetric observations.

The expression (2.24) can be approximated using a formula for the gravitational attraction of a thin horizontal slice (i.e., a circle) through the cylinder, multiplied by the cylinder height (Stenvold et al. 2008)

$$\Delta g = 2\pi G \Delta\rho \left(1 - \frac{1}{\sqrt{1 + \dfrac{r^2}{z^2}}} \right) h. \tag{2.25}$$

The relative error introduced by using (2.25) instead of the exact formula (2.24) is less than 1% if $h/z < 0.2$ and if $r/z > 0.2$.

The approximation (2.25) is very useful because the ratio of the cylinder radius r to the cylinder depth z can be used while computing gravity attraction rather the separate values of these parameters. In this case with the single parameter value for the ratio one can cover a whole range of possible scenarios for the values of r and z. Rearranging terms in (2.25) the cylinder height h can be expressed as

$$h = \frac{\Delta g}{2\pi G \Delta\rho \left(1 - \frac{1}{\sqrt{1 + \frac{r^2}{z^2}}} \right)}. \tag{2.26}$$

Then for a given ratio of r and z and a given density contrast $\Delta\rho$ formula (2.26) can be applied to determine the cylinder height h that produces a given gravity variation Δg. This is very useful to evaluate the sensitivity of gravimetric measurements to reservoir mass redistribution. We demonstrate this with the following example.

Fig. 2.6a shows the cylinder heights h (in meters) corresponding to the temporal gravity variation of 3 μGal and Fig. 2.6b to the variation of 10 μGal for a range of dimensionless ratios of the cylinder diameter to the cylinder depth and a range of temporal density variations. To interpret these results we assume that the gravity signal is detectable if it is larger than 2σ, where σ denotes the uncertainty (noise standard deviation) of time-lapse gravity measurement. Under Gaussian assumptions for the measurement noise $\pm 2\sigma$ defines about 95% confidence interval. Further, we consider two cases for the measurement uncertainty: first with $\sigma = 5$ μGal and the other with $\sigma = 1.5$ μGal. Note, that in practice σ is related not only to the instrument precision but also to other noise sources. They will be analyzed in more detail in Chapter 3 of the thesis. At this stage we can say that the first scenario with $\sigma = 5$ μGal refers to the often achievable measurement uncertainty in gravity field campaigns. The other, is highly optimistic and used here to demonstrate the potential sensitivity of gravimetric technique.

For $\Delta g = 10$ μGal, which under the above assumptions is equivalent to $\sigma = 5$ μGal, and for the diameter/depth ratio of 1, which corresponds to a small-size or very deep reservoirs, gravimetric monitoring of most reservoir processes can be very challenging. For instance, only a very large OWC rise, in the order of $30 - 220$ m and more, could be detected. Similarly, several tens of meters of GWC rise are required to produce a detectable signal. Only for a very high density contrast, in the order of $150 - 200$ kg/m^3, the delectability threshold is improved to about $10 - 15$ m. Under more favorable conditions, say, e.g., for the diameter/depth ratio of 3, the delectability is about $3 - 7$ m for GWC and about $2 - 3$ m for OSC. Still practical monitoring of OWC may be challenging in this case. If σ is reduced to 1.5 μGal the sensitivity of gravimetric observations increases proportionally (see formula 2.26). In this case, a fluid contact movement in the order of $1-2$ m for moderate size/depth reservoirs (diameter/depth ratio of 3) and for density contrast larger than 100 kg/m^3 (GWC or OSC) is detectable. For low density contrasts resulting from oil/water substitution ($20-80$ kg/m^3 range) several meters of contact rise are needed to give detectable gravity variation. A brief summary of these results is given in Tab. 2.1 and Tab. 2.2.

Table 2.1: The cylinder heights that produce 10 μGal signal for a range of cylinder diameter/depth ratios and a range of density contrasts.

	diam./depth = 1	diam./depth = 3
$\Delta\rho = 10-80$ kg/m^3 (oil/water)	$30-220$ m	$7-50$ m
$\Delta\rho = 80-150$ kg/m^3 (gas/water)	$15-30$ m	$3-7$ m
$\Delta\rho = 150-200$ kg/m^3 (oil/steam)	$10-15$ m	$2-3$ m

Table 2.2: Same as Tab. 2.1 but for 3 μGal.

	diam./depth= 1	diam./depth = 3
$\Delta\rho = 10-80$ kg/m^3 (oil/water)	$8-65$ m	$2-16$ m
$\Delta\rho = 80-150$ kg/m^3 (gas/water)	$4-8$ m	$1-2$ m
$\Delta\rho = 150-200$ kg/m^3 (oil/steam)	$3-4$ m	~ 1 m

2.5.2 Borehole gravity measurements

A similar analysis can be performed for borehole gravity measurements. For instance, the sensitivity of the signal recorded in the borehole to the approaching injection front can be investigated (Fig. 2.7).

In this case however, expressions (2.24-2.25) for the gravitational attraction of the vertical cylinder cannot be used directly because they are valid only for an observation point aligned with the cylinder axis. For an arbitrary observation point, solutions are also available (see, e.g., Kwok 1991) but at this time we prefer to use our forward modeling approach based on the prisms. We approximate a cylinder body with a number of fine, rectangular prism (Fig. 2.8) and apply the analytical solutions, shown in Section 2.4. With this approach we demonstrate also great flexibility of the forward modeling method that will be applied in the thesis.

Fig. 2.9 shows the maximum value of the borehole gravity signal as a function of distance from the injection front to the gravimeter and temporal density variations. Four cases (a-d) are considered for the height h of the front, namely $10,\ 20,\ 30,\ 40$ m. To interpret the results we assume that uncertainty of borehole gravity measurements (σ) is 7 μGal. Following the reasoning used in the previous analysis, the signal is considered detectable if it is larger (in the absolute sense) than 2σ, i.e., 14 μGal. For a thin injection front, $h = 10$ m, the borehole gravity signal is detectable only for very high density contrasts of about $130-200$ kg/m^3 and at very close distances (several meters) between the front and the gravimeter (Fig. 2.9). For $h = 20 - 30$ m the front becomes detectable at larger distances, up to 100 m and more. However, this holds

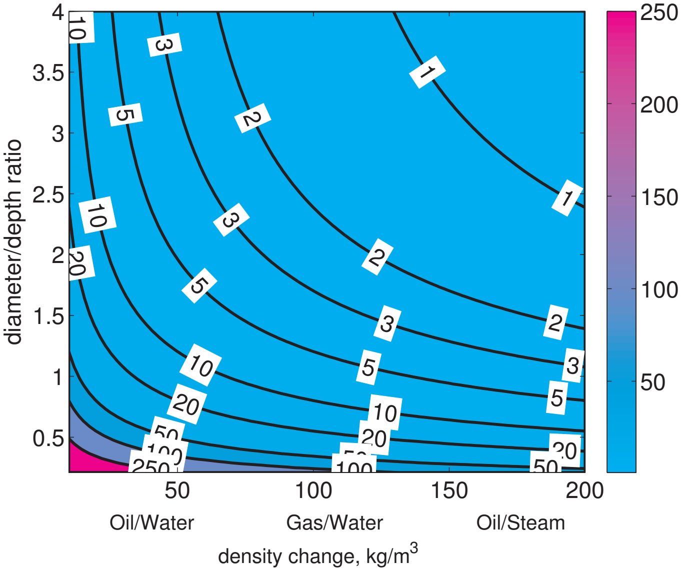

(a) $\Delta g = 3$ μGal

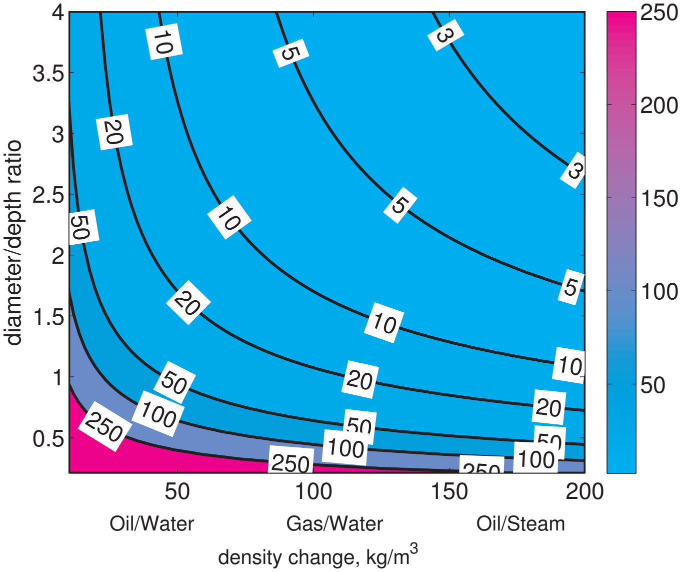

(b) $\Delta g = 10$ μGal

Figure 2.6: The cylinder heights h (in meters) resulting in temporal gravity variation of 3 μGal (Fig. 2.6a) and 10 μGal (Fig. 2.6b) for a range of combinations of dimensionless ratio of the cylinder diameter to the cylinder depth and a range of temporal density variations.

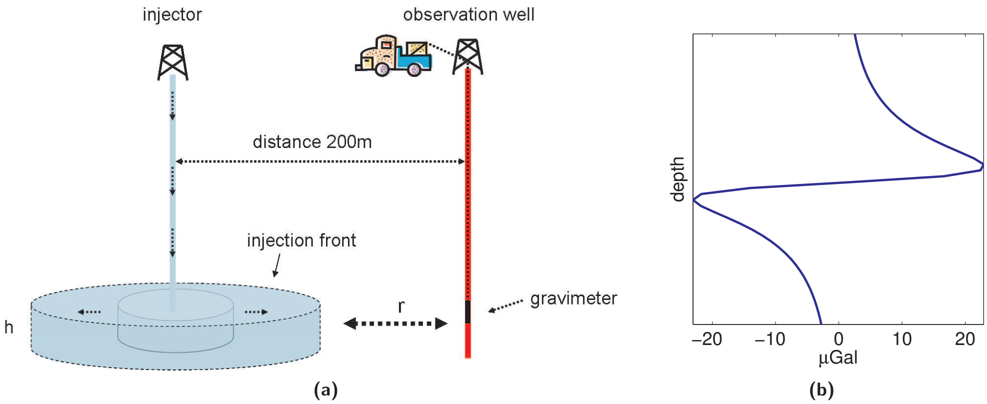

Figure 2.7: Schematic illustration of the setup for the sensitivity analysis of borehole gravity measurements. The figure on the right shows that shape of a typical borehole gravity profile corresponding to the positive mass variation in the borehole vicinity. Because a symmetric mass redistribution was assumed (represented by the vertical cylinder) the gravity signal is axially symmetric.

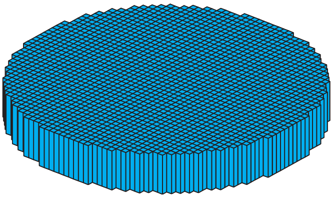

Figure 2.8: Schematic illustration of a vertical cylinder approximated with a number of fine rectangular prisms.

only for sharp density contracts of about $40 - 200$ kg/m^3. For minor density changes, e.g., oil/water replacement, the front is detectable only within $10 - 60$ m from the borehole. For $\sigma = 2$ μGal, which is equivalent to a delectability threshold of 4 μGal, the injection front could be detected from several tens of meters for most of the cases and also for the low density-contrast processes when the front thickness is $10 - 20$ m and more. The summary of these results is shown in Tab. 2.3 and Tab. 2.4.

Table 2.3: Maximum distances, from the injection front to the gravimeter placed in the borehole, for which the maximum of borehole gravity signal is equal to 14 μGal.

	$h = 10$ m	$h = 20$ m	$h = 30$ m	$h = 40$ m
$\Delta\rho = 10 - 80$ kg/m^3	-	< 30 m	< 50 m	< 65 m
$\Delta\rho = 80 - 150$ kg/m^3	< 20 m	$30 - 60$ m	$50 - 85$ m	$65 - 100$ m
$\Delta\rho = 150 - 200$ kg/m^3	$20 - 30$ m	$60 - 75$ m	$85 - 100$ m	$100 - 110$ m

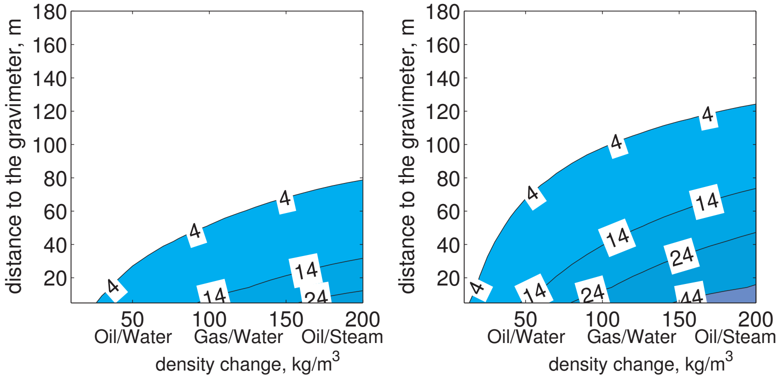

(a) front height 10 m **(b)** front height 20 m

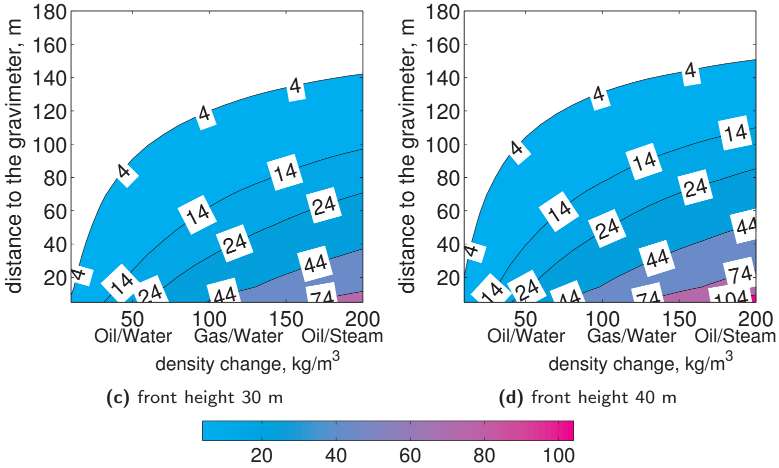

(c) front height 30 m **(d)** front height 40 m

Figure 2.9: The maximum of the borehole temporal gravity variation (μGal) as a function of a distance from the gravimeter to the approaching injection front (r in Fig. 2.7) and density change induced by the front. A cylinder-shape of the injection front is assumed (Fig. 2.7) and the cylinder radius is $200 - r$ (inter-well distance minus distance from the front to the gravimeter).

Table 2.4: Same as Tab. 2.3 but for 4 μGal.

	$h = 10$ m	$h = 20$ m	$h = 30$ m	$h = 40$ m
$\Delta\rho = 10 - 80$ kg/m^3	< 45 m	$20 - 90$ m	$40 - 110$ m	$60 - 125$ m
$\Delta\rho = 80 - 150$ kg/m^3	$45 - 70$ m	$90 - 115$ m	$110 - 135$ m	$125 - 145$ m
$\Delta\rho = 150 - 200$ kg/m^3	$70 - 80$ m	$115 - 125$ m	$135 - 145$ m	$145 - 155$ m

2.5.3 Gravity gradient measurements

Since gravity gradients reflect the spatial rate of change of gravity they can provide detailed spatial information about distribution of the parameter of interest (density anomaly, mass change, etc.). We will illustrate this with simple examples where we will simulate the $\frac{\partial g}{\partial z}$ signal. Let us introduce (see, e.g., Zhdanov 2009) the formula for the vertical component of the gravitational attraction of a point mass (Fig. 2.10)

$$g(P) = \frac{Gmz}{r^3}, \tag{2.27}$$

and its $z-$ derivative

$$\frac{\partial g}{\partial z}(P) = \frac{Gm}{r^3}\left(3\frac{z^2}{r^2} - 1\right), \tag{2.28}$$

where $P = (0,0,0)$, $r = \sqrt{x^2+y^2+z^2}$, G is the gravitational constant, and m denotes the mass. By applying a 3D shift (2.5) to the point mass coordinates, Eqs. (2.27)-(2.28) can be used for an arbitrary observation point $P = (x_P, y_P, z_P)$.

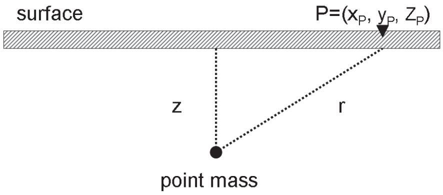

Figure 2.10: Schematic illustration of the point mass; $z-$denotes the point mass depth, $r-$ is the distance between the point mass and gravity observation location.

Fig. 2.11 shows the normalized gravitational attraction (g) and its z-derivative ($\frac{\partial g}{\partial z}$) for different separation distances s between the two point masses. The separation distance s is varied from $s = 0.5z$ to $s = 2z$, where z denotes the point mass depth. For the smallest separation distance $s = 0.5z$, it is not possible to distinguish the location of the two point masses neither from the total g nor from the total $\frac{\partial g}{\partial z}$ signal. For $s \geq z$ the total $\frac{\partial g}{\partial z}$ signal shows two maxima, and hence indicates that there is more than one signal source whereas the total g signal shows two maxima for $s \geq 1.5z$. From Fig. 2.11 it is clear that measurements of the gravity gradient can provide more detailed spatial information as compared to measurements of the vertical component of gravity. It does not say however, that the spatial resolution of gravimetry is as good/or as bad as the distance to the target. Similar conclusions cannot be drawn for gravity gradiometry either. The spatial resolution is not a function of the signal only but it also depends on the measurement noise and the inversion procedure applied to estimate the distribution of the unknown parameter. We will demonstrate in Chapter 4 of the thesis that by performing regularized inversion of gravity observations the spatial resolution can, in some instances be, enhanced.

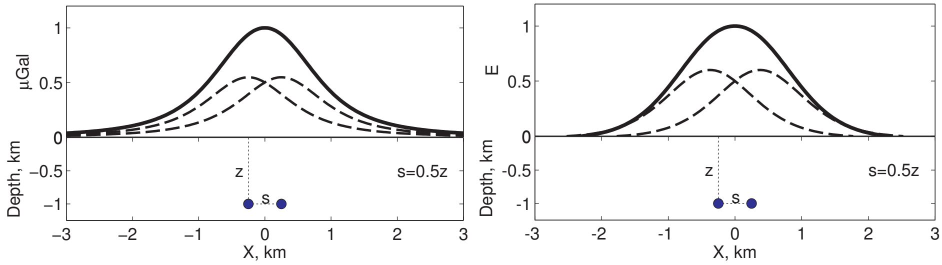

(a) $g,\ s = 0.5z$

(b) $\frac{\partial g}{\partial z},\ s = 0.5z$

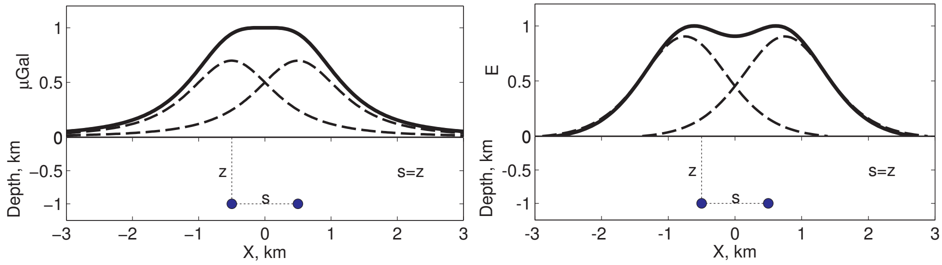

(c) $g,\ s = z$

(d) $\frac{\partial g}{\partial z},\ s = z$

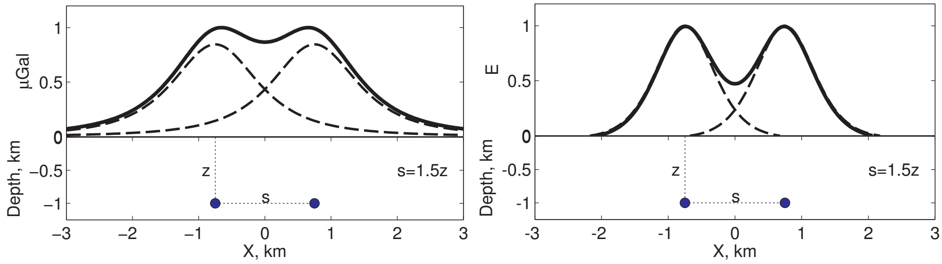

(e) $g,\ s = 1.5z$

(f) $\frac{\partial g}{\partial z},\ s = 1.5z$

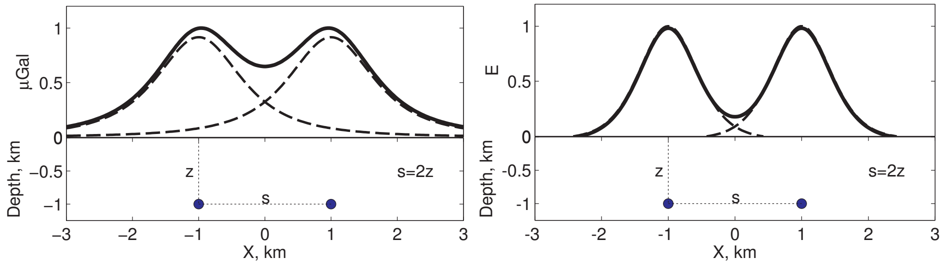

(g) $g,\ s = 2z$

(h) $\frac{\partial g}{\partial z},\ s = 2z$

Figure 2.11: Normalized point mass gravity (g, μGal) and gravity gradient ($\frac{\partial g}{\partial z}$, Eötvös unit, 1E=$10^{-9}/s^2$) signal for different separation distances between two point masses. The signal of individual point masses is shown with the dashed line and the total signal with the solid line.

Another important difference between measurements of gravity and gravity gradients is the signal dependence on distance to the signal source. For instance, for the point masses, the peak of the signal is attainted when the observation point is aligned with the position of the point mass, i.e., when $r = z$ (Fig. 2.10). From Eqs. (2.27)-(2.28) it follows that the signals' maxima are

$$\frac{Gm}{z^2}, \tag{2.29}$$

for g and

$$\frac{2Gm}{z^3}, \tag{2.30}$$

for its $z-$derivative $\frac{\partial g}{\partial z}$. Thus, we can see that the g signal decays at a rate proportional to the inverse of the distance squared whereas $\frac{\partial g}{\partial z}$ signal decays proportionally to the inverse of a cubic distance. The difference in rate of the signal decay is illustrated in Fig. 2.12. The percentage of the maximum of reference g and $\frac{\partial g}{\partial z}$ signal is shown for range of point mass depths. The maximum of the reference signal is computed for the distance to the point mass equal to 1000 m. Increasing the point mass depth from 1000 m to 1500 m reduces the g signal to about 45% of the reference value and the $\frac{\partial g}{\partial z}$ signal to about 30%. Further, increasing the depth to 2000 m reduces the signal to about 25% and 12% of the reference value, for g and $\frac{\partial g}{\partial z}$, respectively.

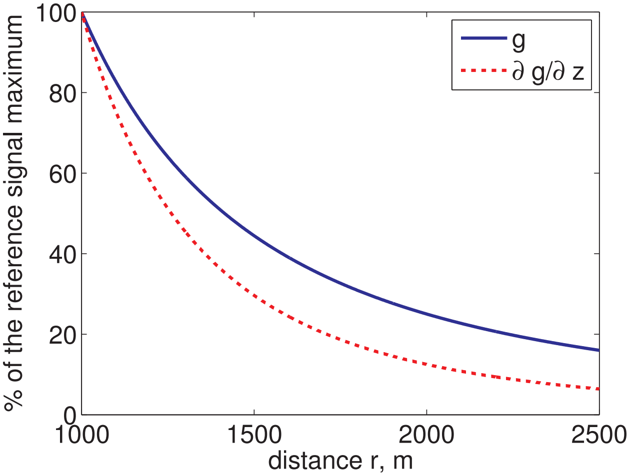

Figure 2.12: The difference in rate of the signal decay for the point mass. The maximum of the reference signal is computed for the distance to the point mass equal to 1000 m.

We perform a forward modeling exercise to show some of the above differences in the context of hydrocarbon reservoir monitoring. A simplified gas reservoir model is considered which is affected by water influx entering the reservoir via the western reservoir boundary. The amount of water influx is predicted by running forward reservoir simulator for 3500 days. More details of the gas reservoir characteristic are provided in Chapter 6 of the thesis, where they are more relevant. Fig. 2.13 shows the temporal gravity (g) and gravity gradient ($\frac{\partial g}{\partial z}$) variations caused by the water influx. Since denser water replaces gas, positive signal variations are predicted. For shallow depths the $\frac{\partial g}{\partial z}$ variation provides more details, compared to g variation, about the water-front geometry. However, if we assume $\sigma = 5$ μGal for the standard deviation of the gravity noise and 0.2 E for the gradiometry noise and, as before, consider the signal detectable if it is larger than 2σ, we can see that the gravity gradient signal is detectable only for very shallow targets, 500 m in our case. Contrary to that, the g variation is detectable down to 2500 m, which is comparable to the lateral reservoir extent (3000 m × 3000 m). This illustrates clearly, that gradiometry can provide enhanced spatial information about reservoir mass redistribution, but only for very shallow targets, whereas gravimetry can be useful also for deeper reservoirs.

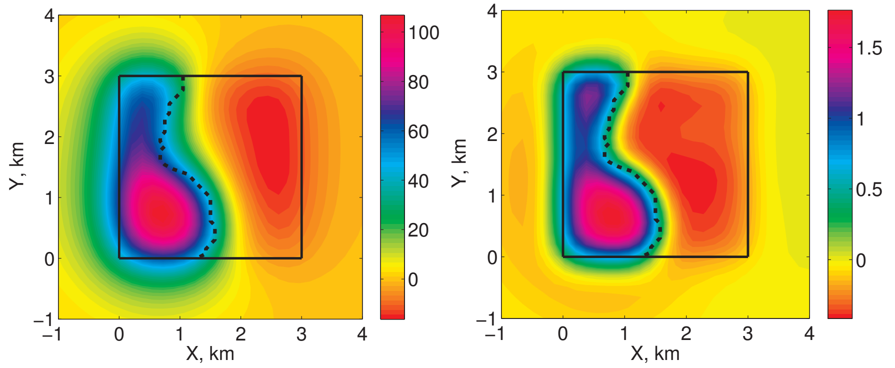

(a) g, z=500 m **(b)** $\frac{\partial g}{\partial z}$, z=500 m

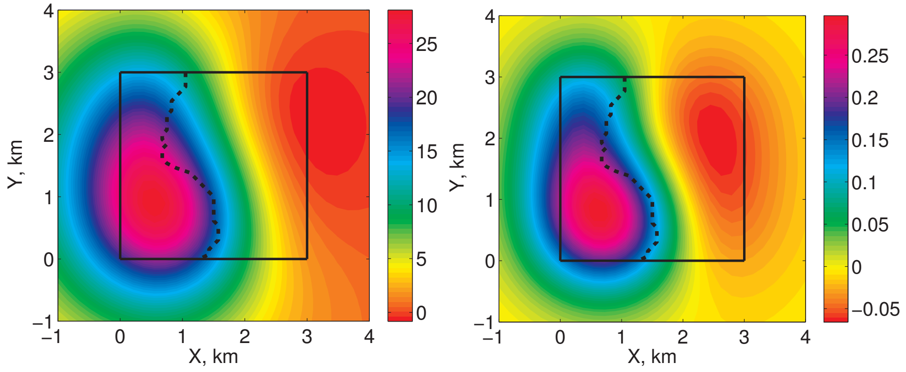

(c) g, z=1500 m **(d)** $\frac{\partial g}{\partial z}$, z=1500 m

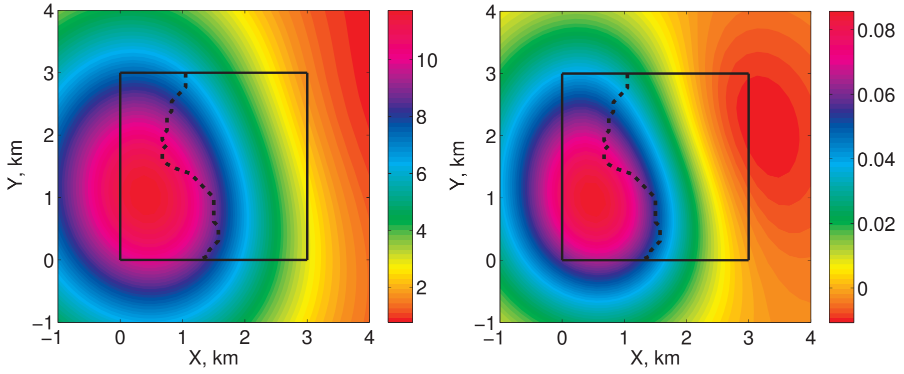

(e) g, z=2500 m **(f)** $\frac{\partial g}{\partial z}$, z=2500 m

Figure 2.13: Temporal gravity (g, μGal) and gravity gradient ($\frac{\partial g}{\partial z}$, E) variation resulting from water influx into a gas reservoir for different reservoir depths z. The black rectangle shows the boundaries of the reservoir. The black dashed curve shows the position of the water front.

2.5.4 Summary

Temporal gravity variations scale proportionally with density changes. Therefore, monitoring with time-lapse gravimetry reservoir processes involving fluids with large density contrast, such as, e.g., gas and water, is especially promising. Monitoring small and/or deep reservoirs, i.e., with a size/depth ratio of 1, is very challenging. With the currently achievable measurement uncertainty of about 5 μGal only tens and hundreds of meters of OWC rise have a chance to be reliably detected. For larger density contrasts, 100 kg/m^3 and more (gas/water, oil/steam), $10-30$ m of a contact rise can result in a detectable signal. For more favorable reservoir geometries configurations, e.g., for size/depth ratio of 3, $2-7$ m of contacts rise can be seen from gravimetric observations. If the measurement uncertainty was reduced to 1.5 μGal then potentially even several meters $(2-16$ m) of OWC rise could be deduced from gravity. A sensitivity of $1-2$ m and better for large density contrasts could be achieved in this case.

Borehole gravity measurements can provide reservoir monitoring information, about, e.g., a propagating injection front, but only on a local scale. With currently achievable 7 μGal uncertainty, thin injection fronts ($<$ 10 m) can only be detected in very close borehole vicinity ($< 20-30$ m) and only for large fluid-density contrasts ($>$ 100 kg/m^3). Thicker injection fronts $(30-40$ m) can already be detected from about 100 m distance from the borehole. If 2 μGal measurement uncertainty was possible then also thinner fronts could be monitored at distances larger than several tens of meters.

With the current technology the time-lapse gravity gradiometry can give spatial information about reservoir mass redistribution, but only for very shallow ($<$ 1km depth) targets. It is because the gravity gradient signal vanishes very rapidly with distance. Measurement precision better than $0.05-0.1$ E is required to monitor deeper reservoirs ($>$ 1km).

2.6 Summary

In this chapter applicability of time-lapse (4D) gravimetry for hydrocarbon reservoir monitoring was discussed. State-of-the-art gravimeters and gravity gradiometers are available which are capable of measuring subtle variations in the Earth's gravity field caused by reservoir mass redistribution. Recent feasibility studies and field cases show that time-lapse gravimetry is already a mature monitoring technique. It can especially add the value when used to monitor reservoirs containing fluids with high density contrast, such as gas and water or steam and oil. Also reservoir geometric configuration (size/depth) is relevant. Small and deep reservoirs are difficult to monitor compared to shallow and large fields. This is due to the gravity signal attenuation with distance to the target which not only affects the signal amplitude but also deteriorates the spatial resolution. Borehole gravity measurements can provide monitoring information on a local scale. For instance they can indicate the approaching injection front from several tens of meters from the borehole, depending on the front thickness and the fluid density contrasts. Time-lapse gravity gradiometry has a potential to be useful for the monitoring of very shallow targets ($<$ 1 km).

Chapter 3

Time-lapse gravimetry noise sources

In this chapter we discuss major noise sources affecting the monitoring of hydrocarbon reservoirs with time-lapse gravimetry. Special attention is devoted to the analysis of hydrological influences on gravimetric observations, in particular originating from groundwater table variations. A potential contribution of groundwater to the uncertainty budget is evaluated with forward simulations of hypothetical variations of water table changes. The hydrological simulations are coupled with the forward gravity modeling of gravity signal. We show that the influence of groundwater variations on observed gravity can be very large and can easily reach several tens of μGals. Therefore, there is a need to acquire groundwater observations to correct observed gravity. Further, we analyze various scenarios for the density of a hypothetical measurements grid of the groundwater table and for the groundwater correlation scales. We demonstrate that using even a single groundwater measurement, the hydrological noise can be reduced 2-3 times, depending on the correlations scales of groundwater.
At the end of the chapter we provide estimates for the total uncertainty budget in gravity measurements.

3.1 Introduction

Measurement noise can be defined as that part of the signal that is not of interest but is recorded along with the signal. Therefore, the definition of noise sources depends on the target of monitoring: what is considered as signal in one application is treated as noise in another one, and vice versa. Because gravity field variations reflect the overall mass changes, many noise/signal sources can be defined. In this section we limit ourselves to noise sources relevant for hydrocarbon reservoir monitoring. Most of these sources however, are also common for other applications of time-lapse gravimetry. A good example here is the gravimeter itself. For instance, in relative gravimetry a major source of instrumental noise originates from instrument drift, caused by stretching of the gravimeter spring with time. Gravimeter drift can reach several hundreds of μGal/day and a proper survey design (e.g., repeated visits to the same stations) and data processing (fitting a drift model) are needed to estimate the drift and remove it from observations (see, e.g., Ferguson et al. 2007, Zumberge et al. 2008, Christiansen et al. 2011, Kang et al. 2011).

Dynamic processes in the Earth's system induce temporal gravity field variations. The most common examples are solid Earth tides and ocean tides, polar motion, seismic waves and air pressure changes. They can add a few to hundreds of μGal and correcting for their influences requires the application of various models and/or the acquisition of additional observations. Background local mass changes caused by hydrological processes such as soil moisture and groundwater temporal variations, are potentially one of the strongest noise sources of this type. It is because hydrological variations can result in direct gravitational effect in the order of 10-20 μGal or more (Torge 1989, Creutzfeldt et al. 2008), whereas field-wide (tens or hundreds of km^2) in-situ observations/models to correct for these influences are seldom available. This stresses the importance of investigating the potential contribution of hydrological gravity noise to the overall gravity error budget.

A schematic illustration of various sources that can affect gravimetric reservoir monitoring is shown in Fig. 3.1.

We start the chapter with a literature review of some of the major noise sources affecting time-lapse gravimetry. Next, based on a numerical study we investigate the potential influence of hydrological processes. We estimate the magnitude of gravity errors resulting from water table and soil moisture temporal variations, taking into account hydrological observations and imperfect hydrological gravity corrections. For that purpose a stochastic forward modeling approach is applied. Via simulations of spatially correlated random fields representative for water table and soil moisture temporal variations, a wide range of hydrological scenarios is considered. The sensitivity of the results on a density of hydrological measurements network is analyzed.

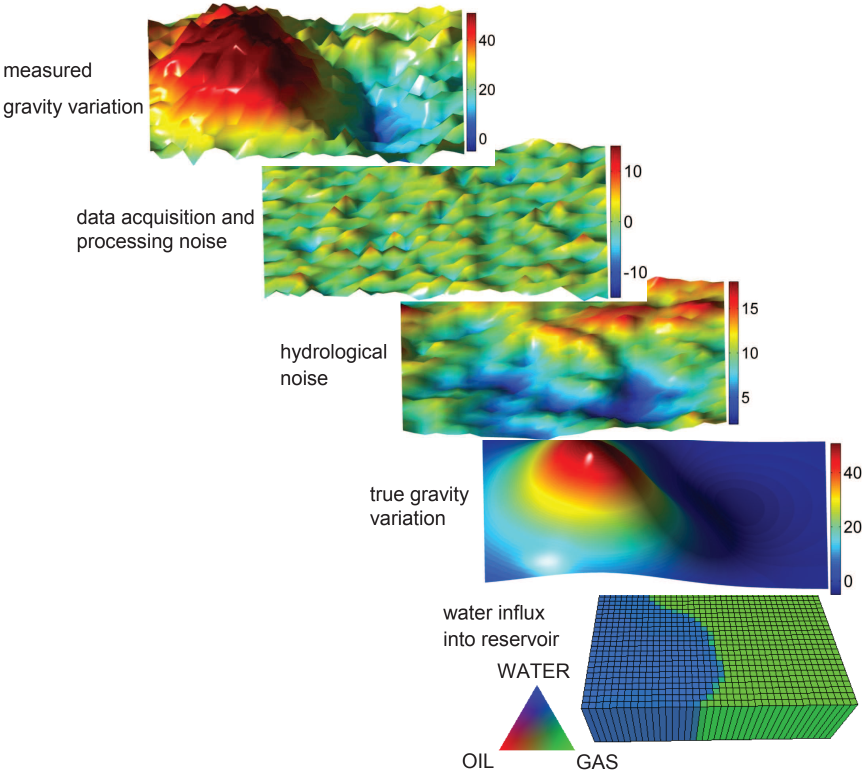

Figure 3.1: Schematic illustration of gravimetric monitoring of gas reservoir in the presence of gravity noise. Water influx causes positive mass redistribution in the subsurface (water replaces gas in the pore space) and, consequently, positive gravity variations at the surface. The observed gravity variations are contaminated by various noise sources. The hydrological noise originates from spatio-temporal variation of groundwater. The data acquisition and the data processing noise includes, e.g., instrument noise, residual signal uncertainty after gravimetric corrections for tidal effects, atmospheric effects, height corrections etc. All values are in μGal.

3.2 Time-lapse gravimetry noise sources

3.2.1 Earth and ocean tides

The gravitational attraction of the Moon and the Sun (generally referred to as tidal effects) causes periodic variations of the Earth's gravity field (for more details see, e.g., Torge 1989, Kantha & Clayson 2000). For the rigid Earth the direct gravitational effect of tides can reach up to 240 μGal. However, since the Earth is not a rigid body it experiences elastic deformations, known as Earth body tides (solid Earth tides). They result in Earth's surface sub-meter movements and mass displacements, and hence, cause additional gravity field variations. Gravitational forcing of the Moon and the Sun causes not only the solid Earth tides but also the ocean tides which are periodic variations of seawater level. The ocean tides affect the gravity field of the Earth through a direct gravitational attraction caused by water mass redistribution and also through the water mass loading effect acting on the Earth surface. The signal can reach $10 - 20$ μGal and is the strongest near coastal regions (Torge 1989). In continental areas it usually accounts only for a few tens of μGal.

Various Earth and ocean tide models are available which have been improved and validated over the last decades with help of, e.g., high-accuracy gravimetry and satellite altimetry data (Baker & Bos 2003, Lyard et al. 2006, Bosch et al. 2009). The simplest approach to model Earth tides accounts only for the direct gravitational attraction of the Moon and the Sun. Since the masses and also the positions of the Moon and the Sun are known, the rigid Earth tides can be modeled accurately with residual uncertaities smaller than 0.1 μGal (Torge 1989). More advanced Earth tide modeling apart from the gravitational attraction takes into account the elastic deformation response of the solid Earth. At another, higher level, both the solid Earth tides and ocean tides are modeled. Literature-reported (Niebauer et al. 1995, Van Camp 2003, Bos & Baker 2005) residual uncertainty estimates are $0.2 - 0.5$ μGal for the solid Earth tide signal corrections and about 0.2 μGal for the ocean tide corrections. However, larger uncertainties in ocean tide modeling can be expected onshore in coastal areas and offshore. This is because of a close distance of measurement location to the tidal signal-generating source and because of a limited ability of large-scale ocean tide models (often $0.5° \times 0.5°$ grid resolution) to account accurately for local effects. Sasagawa et al. (2008) used a time series of 446 days of seabed gravimetric and water pressure measurements (in the North Sea) to verify the accuracy of both Earth and ocean tidal models. They found a standard deviation of the difference between observed (and filtered) tidal gravity and the model prediction to be in the order of 1.3 μGal during a period of quiet sea conditions. Certainly, a part of this difference could be explained by a centimeter-level discrepancies between seawater heights predicted by the tidal model and the water heights derived from the in-situ pressure measurements. Therefore, in offshore gravimetry simultaneous recording of the actual ocean tide data in the vicinity of the measurement location is recommended (Zumberge et al. 2008).

3.2.2 Corrections for height changes

Because gravity varies with the distance to the Earth's center of mass, gravimetric measurements are sensitive to height changes. The time-lapse height variations can have many causes such as, e.g., tectonic activity, surface subsidence caused by reservoir compaction (Zumberge et al. 2008), surface uplift resulting from, e.g., volcano pressurization (Battaglia et al. 2008) or snow/ice accumulations (Ferguson et al. 2008). The free air gravity gradient is equal to about 3.086 μGal/cm (Torge 1989) and the underwater gravity gradient is about $3.086 - 4\pi\gamma\rho_w = 3.086 - 0.862 = 2.224\mu$Gal/cm, where $4\pi\gamma\rho_w$ is 2 times (one for below position of the observation point, one for above position of the observation point, see Fig. 3.2) the Bouguer plate gravitational attraction of 1 cm thick seawater column with 1028 kg/m^3 density and γ is the gravitational constant. A sub-centimeter change in height at a gravity station may introduce gravity noise in the same order of magnitude as the instrument sensitivity. Therefore, a stable station position and/or accurate position monitoring are crucial for time-lapse gravimetric surveys.

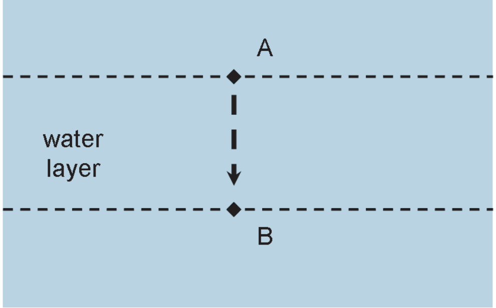

Figure 3.2: Schematic illustration of underwater gravity gradient computation. The observation point is moved 1 cm from point A to point B. The underwater gradient to correct for the height change is computed as: 3.086 (the free air gravity gradient) - 2 × 0.431 (2× the Bouguer plate gravitational attraction of 1 cm thick seawater column with 1028 kg/m^3 density) = 2.224 μGal/cm.

To maintain a station stability some sort of solid platforms can be used, e.g., concrete benchmarks (Zumberge et al. 2008). Repeated height-changes monitoring can be performed with, e.g., GPS measurements in land surveys and with pressure measurements offshore. Ferguson et al. (2008) reported centimeter precision with a GPS application in case of gravimetric monitoring of gas/water contact movement in the arctic environment at Prudhoe Bay. The corresponding uncertainty in height corrections was about $3-4$ μGal. Zumberge et al. (2008) reported 3-5 mm precision of monitoring of benchmark depth changes caused by seabed subsidence in some offshore (North Sea) 4D gravity applications. Because seabed subsidence does not involve water mass changes below the instrument (Fig. 3.3), $3.086 - 2\pi\gamma\rho_w = 3.086 - 0.431 = 2.655\mu$Gal/cm underwater gradient was applicable. This resulted in uncertainty in gravity height corrections of about $0.8 - 1.3$ μGal.

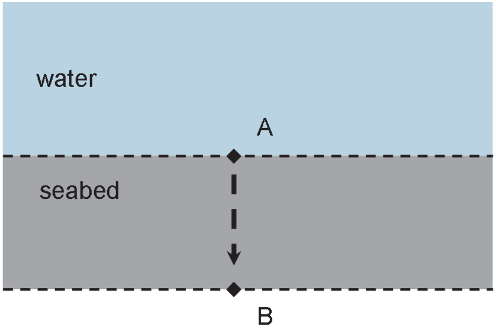

Figure 3.3: Schematic illustration of gravity correction for seabed subsidence. The observation point is moved 1 cm from point A to point B. The underwater gradient to correct for the height change is computed as: 3.086 (the free air gravity gradient) - 0.431 (the Bouguer plate gravitational attraction of 1 cm thick seawater column with 1028 kg/m^3 density) = 2.655 μGal/cm.

3.2.3 Atmospheric effects

The influence of atmospheric pressure variations on gravimetric measurements is twofold. First, air pressure changes result in mass changes above the gravimeter and, through Newtonian attraction, directly affect gravity measurements: the air pressure increase will decrease the measured gravity value. The direct gravitational effect of air pressure changes is usually < 1 μGal in short-term (few hours), can reach 3 μGal over a season and up to $15 - 20$ μGal over several days at extreme weather conditions (Torge 1989, Crossley et al. 2002). Secondly, atmospheric load (which acts in the opposite direction as compared to the mass attraction effect) deforms the Earth's surface. The peak-to-peak vertical surface displacements can reach 20-30 mm for large regional air pressure changes ($\geq$50 hPa) occurring over extended area ($\geq$100 km in radius, Sun et al. (1995)).

There are two main approaches to model the effect of atmospheric pressure variation on gravity. The first is based on a physical model, whereas the second one uses an admittance (transfer) function between gravity and local pressure changes (El-Gelil et al. 2008).

The model-based approach requires, except pressure, measurements of other atmospheric parameters (e.g., temperature, humidity) at the Earth's surface with good spatial resolution (often better than 1°×1° grid covering hundreds or thousands of km's). Green's functions are used to estimate the direct Newtonian effect and the indirect (loading) effect of the 2D pressure field on gravity (Boy et al. 2002, Kroner & Jentzsch 1999, Boy et al. 1998, Mukai et al. 1995). If atmospheric data are available at different altitudes, then more complete 3D models can be used (Neumeyer et al. 2004). The physical model requires data covering large areas. Therefore, in practice due to limited data availability, this approach is not frequently applied.

The other, more common approach, uses an admittance function between pressure and gravity changes. The combined mass attraction and loading effect is usually corrected using a factor of 0.3 μGal/hPa factor (IAG[2] Resolution No. 9, 1983). The gravity correction based on this relation generally removes 90% of the atmospheric effect (Crossley et al. 2002) and reduces the residual errors to $< 1-2$ μGal (Torge 1989). The simplicity of this correction method has lead to its wide use.

3.2.4 Polar motion

Polar motion is a movement of the Earth's rotation axis with respect to the mean pole CIO[3] (Torge 1989). The polar motion induced gravity fluctuations on the Earth's surface are mostly below a few μGal. However, in mid-latitude regions, the peak-to-peak gravity variations can reach 10-13μGals (Xu et al. 2004).
Because the changes are slow, corrections for polar motion are not necessary for short-term surveys (shorter than 1 month). For long-term time-lapse surveys, as for hydrocarbon reservoir monitoring, the corrections must be applied. They can be performed to a high accuracy with a residual uncertainty of the order of $0.01 - 0.05$ μGal (Niebauer et al. 1995, Ferguson et al. 2008).

3.2.5 Local mass displacements due to reservoir compaction

Hydrocarbon fluid extraction usually leads to pressure decline in the reservoir formation. Consequently, reservoir rock may compact under the overburden load. Then reservoir volume decreases (mostly the reservoir height) and associated surface subsidence may occur (Fig. 3.4).

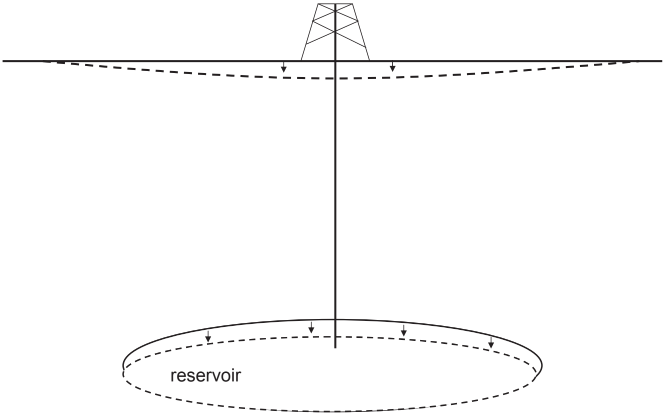

Figure 3.4: Schematic illustration of reservoir compaction and surface subsidence, after Fjar et al., 2008.

---

[2] International Association of Geodesy

[3] Conventional International Origin - based on average pole position over time interval 1900-1906

Most oil and gas reservoirs experience little compaction and negligible subsidence. For a significant subsidence to occur several conditions are needed (Fjar et al. 2008):

- reservoir pressure drop must be significant; pressure maintenance through, e.g., water injection and/or aquifer support may counteract the compaction;
- reservoir rock must be compressible; the compaction is likely to be relevant for soft rocks;
- reservoir must be thick (several tens up to hundreds of meters);
- elastic/geological properties of reservoir overburden must allow propagation of reservoir compaction to the surface; how reservoir compaction affects the surface subsidence depends on reservoir depth, reservoir geometry and contrast of reservoir rock properties with the properties of overburden rock.

Therefore, production of large and thick gas reservoirs where a significant pressure drop is expected (often down to 30% of the initial reservoir pressure) can induce surface subsidence. Examples of real gas fields where surface/seabed subsidence was observed include the Groningen gas field in the Netherlands (van Gelderen et al. 1999) and the Troll field, offshore Norway (Eiken et al. 2008, Eiken & Stenvold 2005).

Reservoir compaction and surface subsidence may result in temporal gravity variations and, therefore, can be considered as one of the potential noise sources in the context of gravimetric reservoir monitoring. A part of the noise is caused by position (mostly height) changes of gravity observation points, discussed in the previous section, and can be accounted for by applying corrections based on gravity gradient and subsidence data, if available. The other part of gravity noise originates from temporal mass shifts caused by local changes in the subsurface density distribution. Little material is published on this topic in the context of reservoir engineering and most of the literature is related to time-lapse volcano gravimetry (Battaglia et al. 2008). There, both a surface uplift and subsidence can be observed, which are caused by magma intrusion/depletion and/or subsurface pressure variations related to volcano dynamics. Analytical and numerical approaches have been used to estimate temporal gravity changes related not only to mass changes (magma in- and outflow) but also taking into account (sub-) surface deformation (see Battaglia et al. 2008 and references therein). Here we assume a fixed mass of the system, fixed gravity observation points at some reference level and, hence, investigate only temporal gravity changes associated with medium deformation.

Walsh & Rice (1979) showed that for a fixed gravity observation point and a spherical homogenous deformation source embedded in an elastic homogenous half-space (Fig. 3.5), the combination of gravity changes induced by the source inflation/shrinkage (at fixed source mass) and surrounding medium deformation is zero. However, nonzero gravity changes can be generated when medium heterogeneities and source-shape asymmetry are taken into account. For instance, results included in Bonafede & Mazzanti (1998) show that for a spherical source model embedded in a density-stratified half space gravity changes induced by medium deformation, though small, are not zero: the signal estimate was in the range of $0.1 - 0.2\mu$Gal/cm for some of the gravity stations in Campi Flegrei (Italy) volcanic region. Therefore, in reality a few μGal of gravity variation can be expected when significant (tens of cm) surface deformation occurs. For gravimetric reservoir monitoring this signal adds to the observation noise. Certainly, it could, at least partly, be estimated and removed by coupling geomechanical and gravimetric modeling. This however, is beyond the scope of this research.

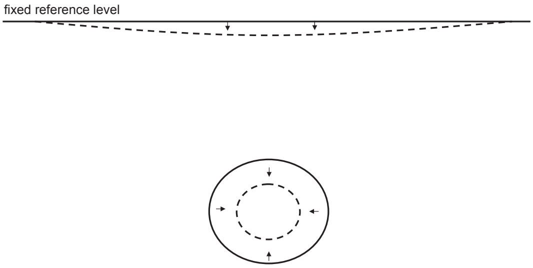

Figure 3.5: Schematic illustration of a compacting spherical source.

3.2.6 Hydrological effects

Gravity observations can be affected by hydrological processes (Amalvict et al. 2004, Harnisch & Harnisch 2006, Naujoks et al. 2010), in particular, local variations of water table and soil moisture (Fig. 3.6) and regional/global water storage changes (Fig. 3.7). The natural or man-made groundwater variations can reach several meters (Fig. 3.8b) and their direct gravitational effect can reach 10-20 μGal and more (Torge 1989, Creutzfeldt et al. 2008). Therefore, the hydrological influences on gravity need to be estimated and properly corrected for. In practice, due to the lack of measurements, a detailed hydrological model is rarely available. Consequently,

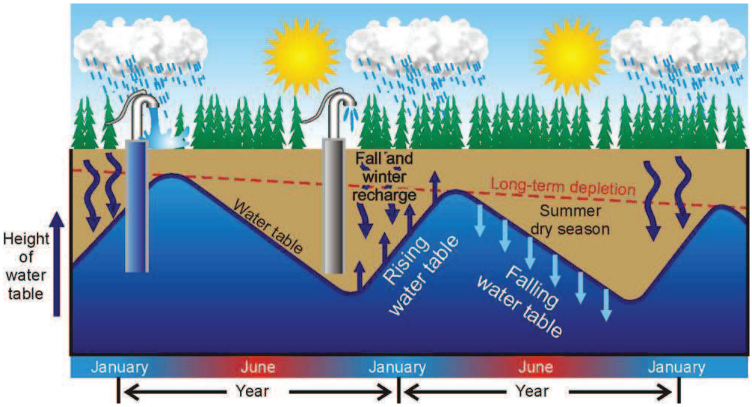

Figure 3.6: Water table ups and downs through the seasons. Source: http://geoscape.nrcan.gc.ca.

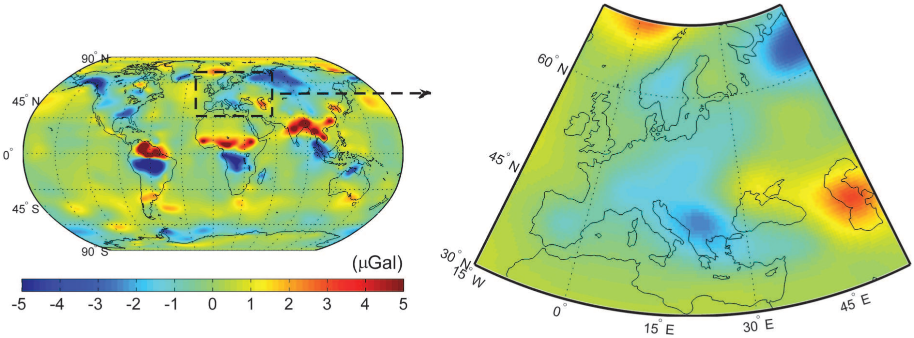

(a) global gravity field variation **(b)** global gravity field variation, zoomed

Figure 3.7: Global gravity field variations derived from satellite GRACE mission. A deviation in August 2004 with respect to the yearly mean is shown. Source: DMT-1 model, Delft University of Technology, The Netherlands; courtesy of P. Ditmar and H. Hashemifarahani

hydrological gravity corrections can be based on only a few (often a single) local observations of water table and soil moisture variations. This may not be sufficient to appropriately remove all hydrological disturbances leaving an unknown error in gravity observations.

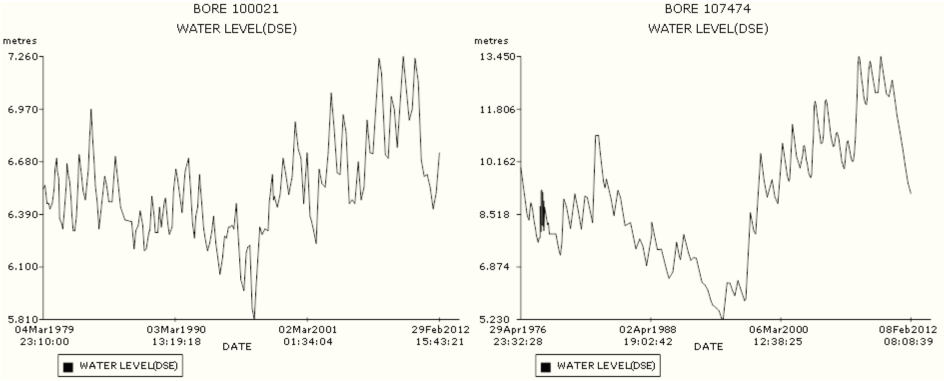

(a) example of moderate groundwater variations **(b)** example of large groundwater variations

Figure 3.8: Examples of field data (port Phillip monitoring site, Australia) showing groundwater level variations. The data is taken from the Victorian Water Resources Data Warehouse, Australia (www.vicwaterdata.net, accessed 25 May 2012). Depths above the sea level (DSE) are shown. Note different scale of y-axis in both figures.

Our objective is to estimate the magnitude of uncertainties in repeated gravity observations caused by temporal variations of water table, soil moisture and imperfect gravity corrections of them. For that purpose a synthetic experiment based on a stochastic forward modeling approach is designed. Random realizations of temporal variability of water table and soil moisture are simulated. To account for the whole range of hydrological scenarios, different degrees of spatial correlation of groundwater variations are considered, varying from tens of meters to several kilometers (Bierkens, personal communication; Hu et al. 2005, Lyon et al. 2006). The reference gravimetric signal induced by hydrological variations is compared with the estimated one and the gravity residuals are computed. Different sampling densities of hydrological observations are considered. The magnitude and composition of the gravity error for various hydrological scenarios is presented.

Simulation approach

The proposed methodology is based on a synthetic experiment which briefly can be summarized as follows:

1. Simulate the reference temporal water table and soil moisture variation.
2. Compute the reference gravity variation for the simulation results of step 1.
3. From the reference water table and soil moisture extract a number of hydrological measurements. Spatially interpolate the measurements to estimate the hydrological variation.
4. Use the results of step 3 to estimate the gravity variation.
5. Compare the reference gravity variation with the estimated one and compute the gravity residuals.

The varied parameters are (explained in more detail later) the correlation scales of groundwater and the density of hypothetical groundwater measurements. Only one scenario for the soil moisture correlation length is considered. For different parameter configurations, steps 1-5 are repeated $N = 100$ times. Finally, the RMSE of N residual gravity fields is calculated.

It is known (Creutzfeldt et al. 2008, Christiansen et al. 2011) that most ($\sim 90\%$) of the hydrology-induced gravitational effect is generated within the close vicinity (a few hundreds of meters) of the gravity measurement location. To illustrate this effect, we express the change in water table by an infinite horizontal slab, i.e., the Bouguer slab. Gravity variation generated by a water (1000 kg/m^3 density) rise of 1 m in a medium with a drainable porosity of 0.25 equals 10.48 μGal regardless of the distance between the gravimeter and the slab. This gravitational attraction can be approximated using a finite-size vertical cylinder model (Fig. 3.9). Fig. 3.10 shows the percentage of the Bouguer plate gravitational attraction generated with the cylinder model for different cylinder radii r and cylinder depths d. It is clear that the larger the cylinder radius the more of the Bouguer slab attraction is recovered and about 90% of the signal is generated within a radius of $50 - 300$ m. This demonstrates the importance of the contribution of a local (or shallow) mass redistribution around the gravimeter on the total gravitational attraction.

Based on this simple sensitivity analysis, we use in the later experiment for the study area a grid of 1 km $\times$ 1 km with a cell size of 10 m $\times$ 10 m $\times$ $\triangle H$. The simulated

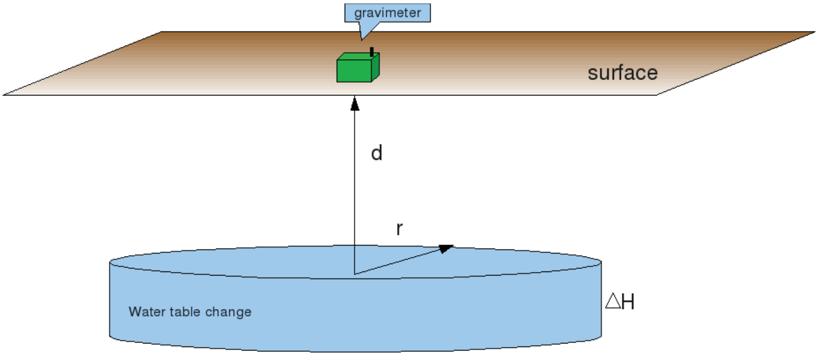

Figure 3.9: Vertical cylinder model. The gravimeter position at the surface is aligned with the cylinder axis.

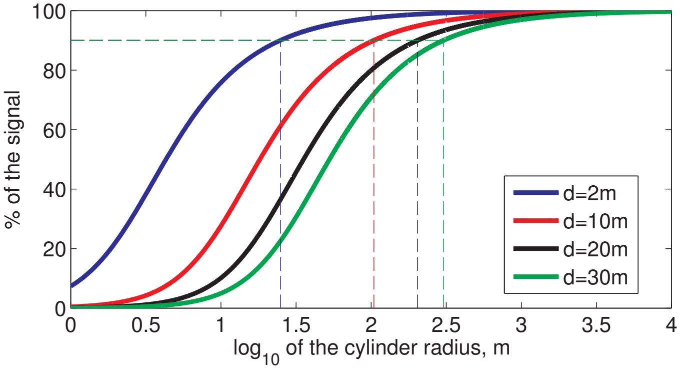

Figure 3.10: Percentage of the Bouguer slab (1 m thick, 0.25 porosity filled with water 1000 kg/m^3 density) gravitational attraction recovered by vertical cylinder model representing groundwater mass change for different cylinder radii r and cylinder burial depth d. The gravimeter position at the surface is aligned with the cylinder axis, see Fig. 3.9.

variables are: the time-lapse rise ($\triangle H$) of the water table and the rise in water content in soil (m of water layer equivalent). For a decrease of these variables the procedure is analogous.

For the simulation of random realizations of water table and soil moisture rise we use the Sequential Gaussian Simulation Method (SGSIM, Remy et al. 2009). A spherical variogram model (see, e.g., Isaaks & Srivastava 1989)

$$f(h) = \begin{cases} c_0 \left[1.5\frac{h}{\theta} - 0.5\left(\frac{h}{\theta}\right)^3\right], & \text{if } h \leq \theta, \\ c_0, & \text{otherwise,} \end{cases} \tag{3.1}$$

where c_0 is the scale parameter, h is the lag distance (in meters) and θ is the variogram range (in meters), is used to model the scales of spatial correlations. Here we assume geometric isotropy, i.e., the variogram range in x- and y-direction is the same. An example of a spherical variogram for different values of θ is shown in Fig. 3.11.

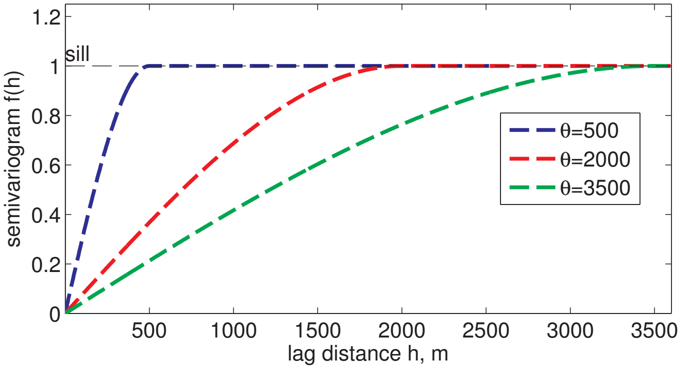

Figure 3.11: Spherical variogram model for different variogram range.

The correlation lengths of the water table variations can vary from tens of meters (Lyon et al. 2006) to tens of kilometers (Hu et al. 2005). A high degree of spatial heterogeneity is likely for shallow water tables (< 2 m) and a higher degree of homogeneity for deep water tables ($> 30 - 50$ m). Three cases for the correlation strength are considered: a "high case" with the variogram range $\theta = 10$ km, "intermediate case" ($\theta = 1$ km) and a "low case" ($\theta = 0.1$ km).

Spatial patterns of soil moisture variations are in general very heterogeneous. Typical correlation lengths are on the order of $0.03 - 0.1$ km (Anctil et al. 2002, Western et al. 2004). In this study we consider only one scenario for correlation lengths of soil moisture with the variogram range equal to $\theta = 0.05$ km.

The magnitude of water table and soil water content rise are randomly generated from a log-normal distribution with probability density function

$$f(x) = \frac{1}{x\sigma\sqrt{2\pi}} \exp\left[-\frac{(\ln x - \mu)^2}{2\sigma^2}\right], \; x > 0, \tag{3.2}$$

where μ denotes the mean and σ denotes the standard deviation of the natural logarithm of the random variable x. The choice of the log-normal distribution is supported by high p-values (Fig. 3.12) of the Kolmogorov-Smirnov goodness of fit test (Massey 1951) to the two real data sets shown in Fig. 3.8. The interpretation of the test results is such that at the significance level of 0.05 there is no reason to reject the hypothesis that the (positive) water table variations follow the log-normal distribution (the p-value is larger than the significance level of 0.05).

We consider three scenarios for the water table variations, which are summarized in Tab. 3.1. In all the cases we use a constant drainable porosity equal to 0.25, which is close to an average among different geological materials (see Tab. 3.2). Note that the gravity signal scales proportionally with density and hence with porosity (see Eq. 2.20 and Eq. 2.23). Therefore, if smaller/larger porosity was used the resulting gravity variations would scale accordingly. Temporal variations of water content in

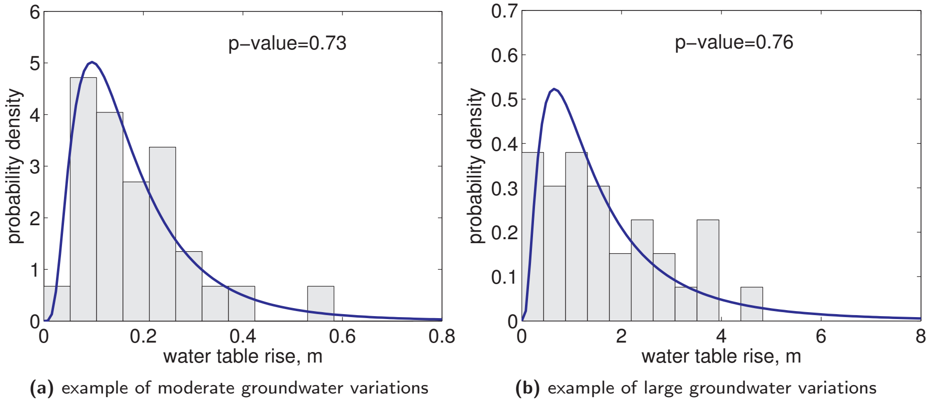

(a) example of moderate groundwater variations **(b)** example of large groundwater variations

Figure 3.12: Goodness of fit evaluation of log-normal distribution to groundwater variation field data. The probability density function is fitted to the positive, approximately 6-months groundwater variations computed for the data shown in Fig. 3.8.

soil can reach 30-40% and more of the soil volume (see, e.g., Loague 1992, Vinnikov et al. 1996). In this study we simulate only one scenario where we set the mean water content rise in 1 m of soil to 0.15 m (this is equivalent to 15 cm of water layer), which can be considered as some average soil moisture variation. In all the cases the standard deviation of the simulated variables is set to 25% of the mean value.

In practice, the soil and the water table changes can be dependent, e.g., the increasing water content in the soil may imply the increasing water table later in time (after the drainage takes place). For this study, however, we do not have a horological model available to model these effects. Therefore, the soil moisture and the water table variations are simulated independently of each other.

Table 3.1: Groundwater level change scenario summary. All values are given in m.

	mean μ	std. σ	variogram range θ	depth
low case	1	0.25	100	2
medium case	2	0.50	1000	10
high case	2	0.50	10000	30

An example of a simulated realization of soil water content rise is presented in Fig. 3.13a. The corresponding gravity variation is shown in Fig. 3.13b. The signal maximum is about 14 μGal and the signal RMSE is about 6 μGal .

Examples of the simulated water table rise are shown in Fig. 3.14. Fig. 3.14a to Fig. 3.14c show the 10 km × 10 km simulation window to visualize the correlation lengths. Fig. 3.14d to Fig. 3.14f show these results in the actual 1 km × 1 km domain used in this study. The temporal gravity variations are presented in Fig. 3.15. Note the signal maximum amplitudes reaching about 22 μGal and the RMSE of about 10 μGal in case of short spatial correlation of water table variations (average water table rise 1 m) and the amplitudes of about 35 μGal and the RMSE of about 26 −

Table 3.2: Representative values of drainable porosity (specific yield) for various geologic materials (Morris & Johnson 1967)

Material	Drainable porosity (%) (Specific Yield)
Gravel, coarse	21
Gravel, medium	24
Gravel, fine	28
Sand, coarse	30
Sand, medium	32
Sand, fine	33
Silt	20
Clay	6
Sandstone, fine grained	21
Sandstone, medium grained	27
Limestone	14
Dune sand	38
Loess	18
Peat	44
Schist	26
Siltstone	12
Till, predominantly silt	6
Till, predominantly sand	16
Till, predominantly gravel	16
Tuff	21

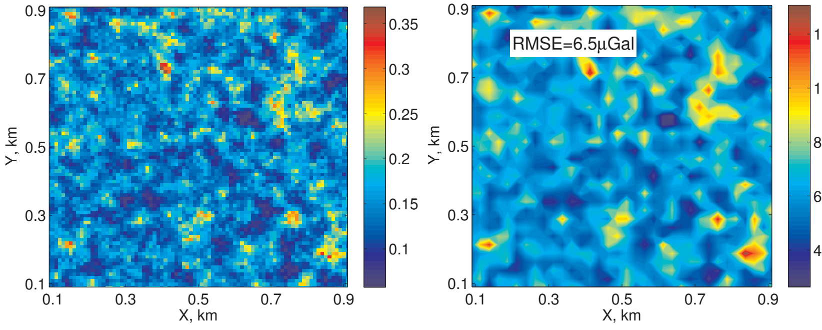

(a) water content change (m) in soil **(b)** gravity field variation, μGal

Figure 3.13: Example of the simulated realization of water-content rise (m) in soil (variogram range 0.05 km). The mean water-content rise is 0.15 m and the water-content rise standard deviation is 0.0375 m (25% of the mean).

28 μGal in the remaining two cases (average water table rise 2 m). The total gravity variation, resulting from the soil water content rise and the water table rise are shown in Fig. 3.16 with the maximum up to 43 μGal and RMSE up to 34 μGal.

The results of the spatial (linear) interpolation of the synthetic measurements of wa-

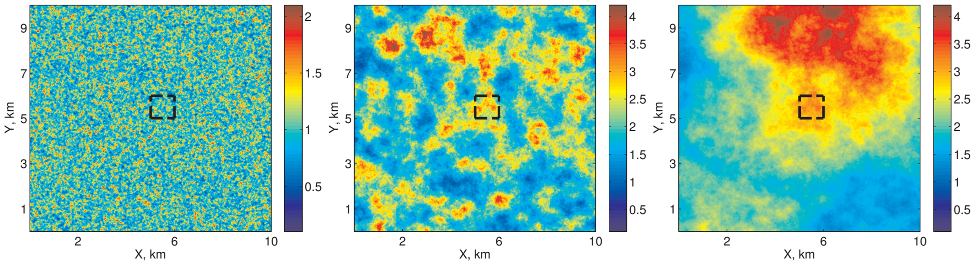

(a) variogram range 0.1 km **(b)** variogram range 1 km **(c)** variogram range 10 km

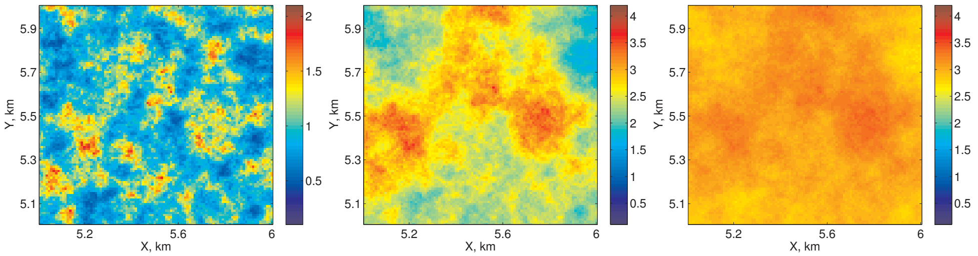

(d) variogram range 0.1 km **(e)** variogram range 1 km **(f)** variogram range 10 km

Figure 3.14: Example of the simulated realizations of water table rise (m) for different lengths of spatial correlations (variogram range) of groundwater. In the top row simulation results for the 10 km × 10 km grid are shown and in the bottom row results for the 1 km × 1 km grid are presented (denoted with black rectangle in the top row figures). The mean water-level change is 1 m in case of variogram range of 0.1 km and 2 m in the remaining cases. In all scenarios the water-level change standard deviation is set to 25% of the mean value.

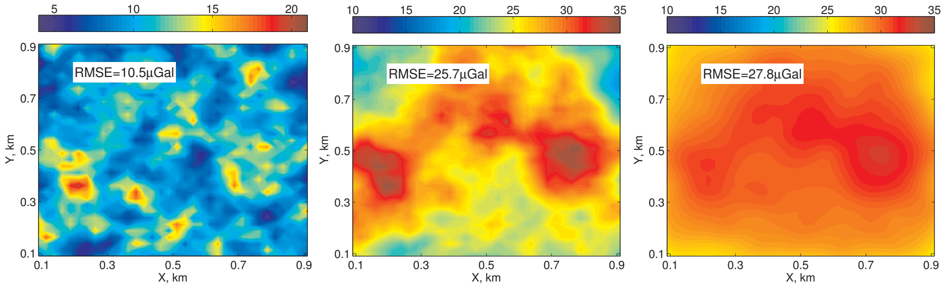

(a) variogram range 0.1 km **(b)** variogram range 1 km **(c)** variogram range 10 km

Figure 3.15: Example of the simulated gravity variation (μGal) caused by water table rise for different correlation lengths (variogram range) of groundwater. The results correspond to the simulated water table rise shown in Fig. 3.14d to Fig. 3.14f.

ter table rise are shown in Fig. 3.17. The results for soil water content change are not displayed here because they are similar to those presented for the shortest correlation length of groundwater. The measurement network is regular, i.e., the distance be-

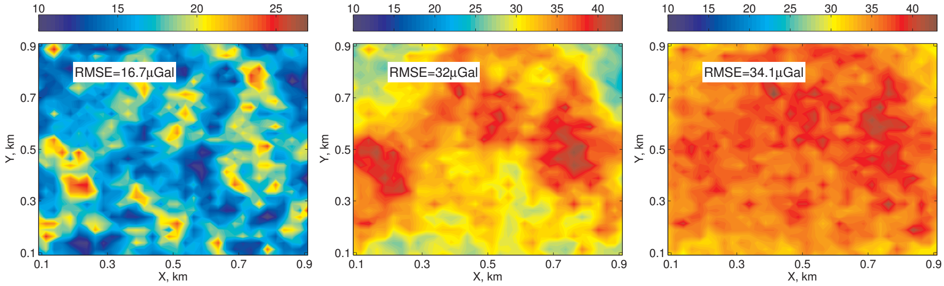

(a) variogram range 0.1km **(b)** variogram range 1km **(c)** variogram range 10km

Figure 3.16: Example of the simulated total gravity variation (μGal) caused by soil moisture and water table rise for different correlation lengths (variogram range) of groundwater. The results correspond to the simulated water content rise in soil shown in Fig. 3.13a and water table rise shown in Fig. 3.14d to Fig. 3.14f.

tween the observations ds is fixed. Different sampling densities are considered, namely $ds = 0.1$ km with 100 measurements in total, $ds = 0.25$ km with 16 measurements in total, $ds = 0.5$ km with 4 measurements in total and $ds = 10$ km with only 1 measurement. As expected, increasing the number of sample data used in the spatial interpolation improves the results: the estimated water table rise and the resulting gravity variation (Fig. 3.18) match the corresponding reference values more closely. Already with a single water table measurements the hydrological signal RMSE can be reduced from 10-26 μGal to about 2-4 μGal (Fig. 3.19). A further increase of the density of measurements could reduce the RMSE to 0.3-2 μGal.

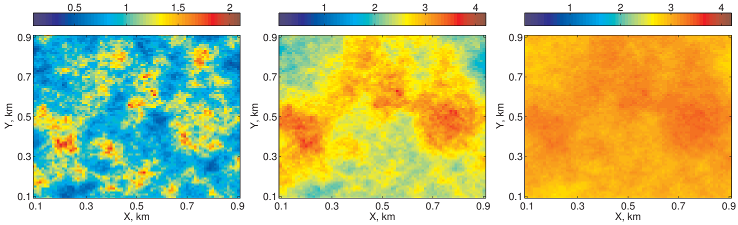

(a) reference, range 0.1 km **(b)** reference, range 1 km **(c)** reference, range 10 km

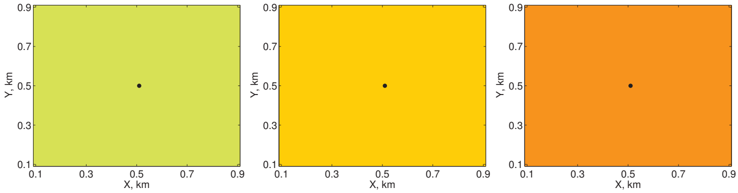

(d) range 0.1 km, ds=1 km **(e)** range 1 km, , ds=1 km **(f)** range 10 km, , ds=1 km

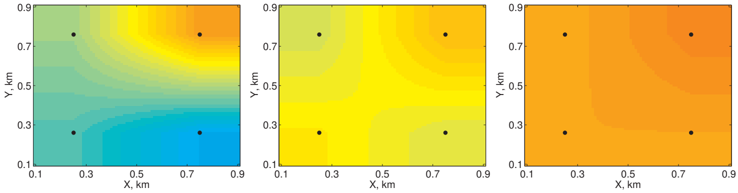

(g) range 0.1 km, ds=0.5 km **(h)** range 1 km, ds=0.5 km **(i)** range 10 km, ds=0.5 km

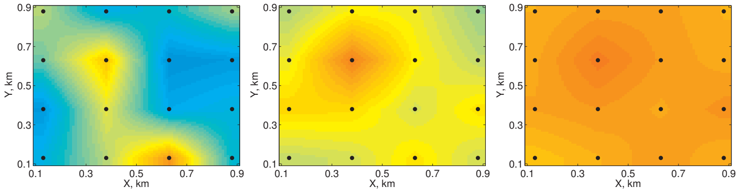

(j) range 0.1 km, ds=0.25 km **(k)** range 1 km, ds=0.25 km **(l)** range 10 km, ds=0.25 km

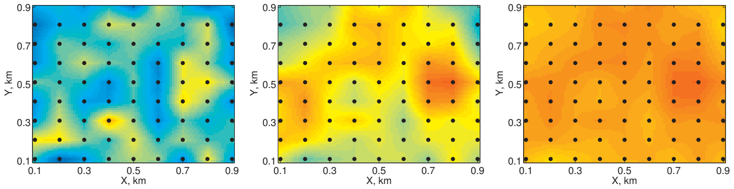

(m) range 0.1 km, ds=0.1 km **(n)** range 1 km, ds=0.1 km **(o)** range 10 km, ds=0.1 km

Figure 3.17: Interpolated water table rise (m) for different groundwater correlation lengths (variogram range) and for various densities of the hypothetical water table observations (black dots). A linear interpolation scheme was used.

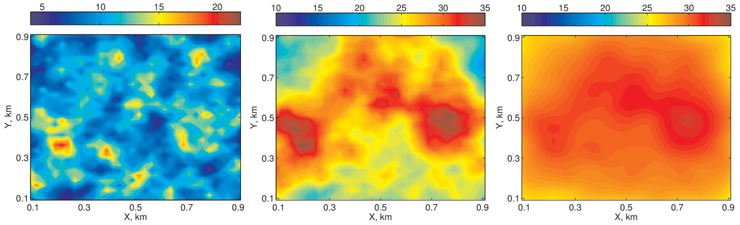

(a) reference, range 0.1 km **(b)** reference, range 1 km **(c)** reference, range 10 km

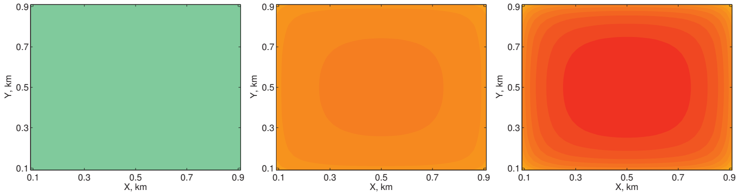

(d) range 0.1 km, ds=1 km **(e)** range 1 km, ds=1 km **(f)** range 10 km, ds=1 km

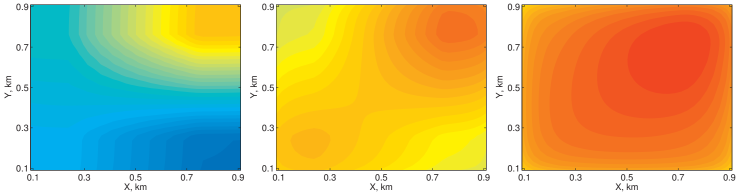

(g) range 0.1 km, ds=0.5 km **(h)** range 1 km, ds=0.5 km **(i)** range 10 km, ds=0.5 km

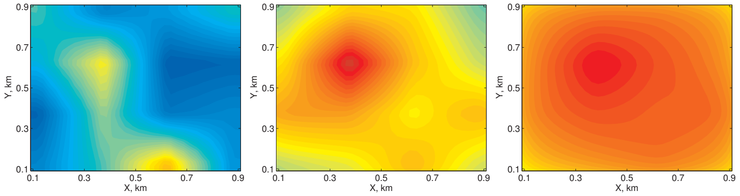

(j) range 0.1 km, ds=0.25 km **(k)** range 1 km, ds=0.25 km **(l)** range 10 km, ds=0.25 km

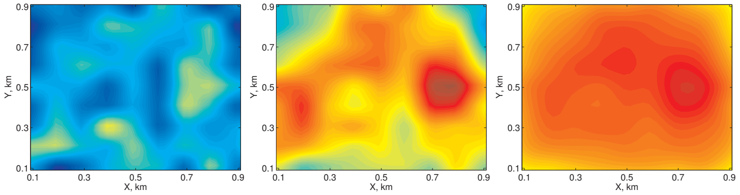

(m) range 0.1 km, ds=0.1 km **(n)** range 1 km, ds=0.1 km **(o)** range 10 km, ds=0.1 km

Figure 3.18: Example of the estimated gravity variation (μGal) caused by water table rise for different groundwater correlation lengths and for various densities of the hypothetical water table observations. The results correspond to the interpolated water table rise shown in Fig. 3.17.

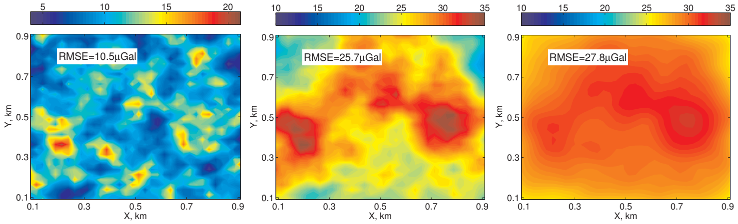

(a) reference, range 0.1 km **(b)** reference, range 1 km **(c)** reference, range 10 km

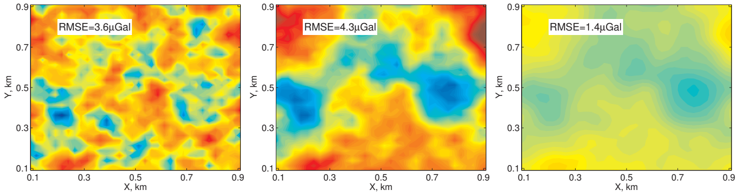

(d) range 0.1 km, ds=1 km **(e)** range 1 km, ds=1 km **(f)** range 10 km, ds=1 km

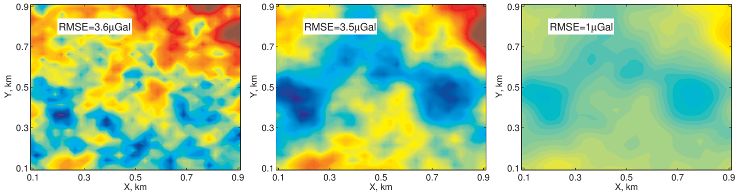

(g) range 0.1 km, ds=0.5 km **(h)** range 1 km, ds=0.5 km **(i)** range 10 km, ds=0.5 km

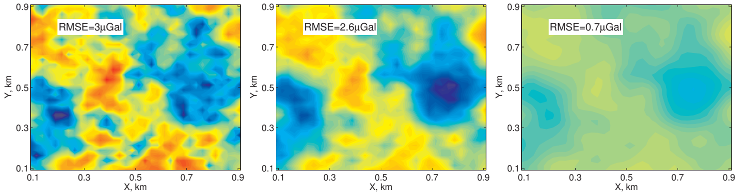

(j) range 0.1 km, ds=0.25 km **(k)** range 1 km, ds=0.25 km **(l)** range 10 km, ds=0.25 km

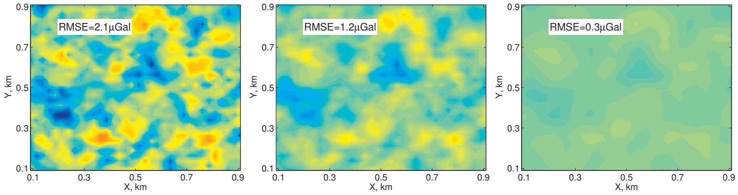

(m) range 0.1 km, ds=0.1 km **(n)** range 1 km, ds=0.1 km **(o)** range 10 km, ds=0.1 km

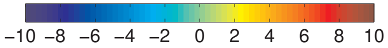

Figure 3.19: Example of the simulated gravity noise realization (μGal) caused by water table rise for different groundwater correlation lengths and for various densities of the hypothetical water table observations. The noise estimates are derived as a difference between hydrological signal estimate (Fig. 3.18d to Fig. 3.18o) and the reference signal (Fig. 3.19a to Fig. 3.19c).

Results

Fig. 3.20 shows an average RMSE of all 100 simulation runs for each of the scenarios considered. The RMSE prior to and after the hydrological signal estimation and correction is displayed. In the case of short correlation lengths of groundwater (Fig. 3.20a) the noise average RMSE is of the order of 3-4 μGal. The major contribution to the error comes from water table variations. Since both soil and groundwater correlation lengths are in the order of tens of meters, decreasing the measurement spacing from 1000 m to 100 m does not significantly reduce the RMSE. For the medium degree of spatial correlation (Fig. 3.20b) the RMSE is within 2-5 μGal. Here, the main contribution originates again from water table variations. However, since the groundwater spatial correlation lengths are larger than the sampling density, increasing the number of water table measurements is effective and leads to a reduction of the RMSE from about 5 to 2 μGal. Under long water table correlation (Fig. 3.20c) the total error is about 2-2.5 μGal and originates mainly from temporal soil moisture variations. The results show that by even using only a single water table measurement the hydrological noise RMSE can be reduced 2-3 times.

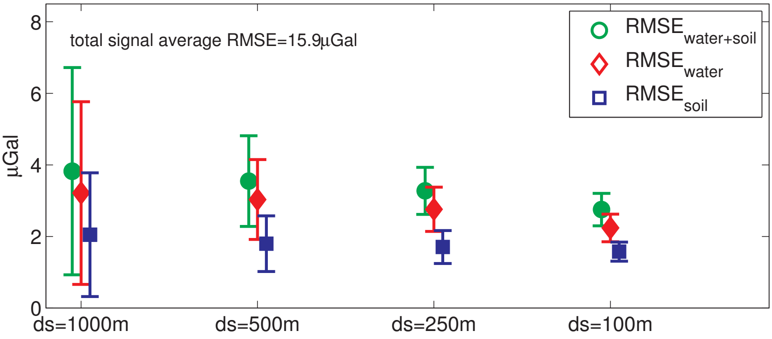

(a) variogram range 0.1km

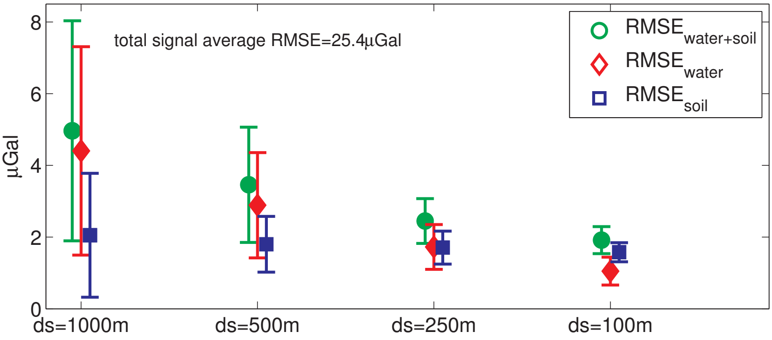

(b) variogram range 1km

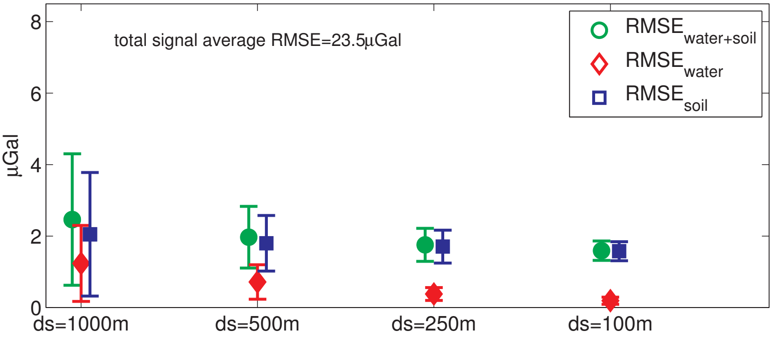

(c) variogram range 10km

Figure 3.20: Average (over 100 realizations) RMSE of gravity residuals for different sampling densities (ds), source of error (water table, soil moisture) and degree of spatial correlation (variogram range) of groundwater. For case a) the mean groundwater-level change of 1 m and for b) and c) of 2 m is assumed. The error bars show $\pm 2 \times \sigma_{RMSE}$ interval.

3.3 Summary

Table 3.3 contains a short summary of the major components contributing to the time-lapse gravimetry uncertainties. It is clear that different operational environments lead to different data acquisition challenges and make some noise sources more relevant than others. For instance, hydrological noise can affect onshore gravimetric surveys whereas it is not a problem in offshore measurements. Similarly, the ocean tide signal is more relevant in offshore gravity campaigns than onshore. For both environments the uncertainty budget is within about $2-6$ μGal which is in good agreement with uncertainty estimates in recent field applications (O. Eiken, personal communication). Certainly, some site-specific factors, such as mass shifts due to reservoir compaction and especially shallow mass variations induced by hydrological processes, may increase the uncertainties. We showed that the influence of hydrological signals can be very large and additional in-situ data are needed to correct for these variations. Already with a single measurements, hydrological noise RMSE induced by water table variations can be reduced 2-3 times, depending on the groundwater correlation lengths. Correction for soil moisture variations may be more challenging due to the short correlation lengths of soil.

Table 3.3: Time-lapse gravimetry noise sources.

source	signal range	residual uncertainty	comment
solid Earth tides	280 μGal	$0.2-0.5$ μGal[1]	
ocean tides	20 μGal	0.2 μGal[1]	
		1.2 μGal[2]	at sea
polar motion	$10-13$ μGal	0.01 μGal[1]	
height changes	$2.2-2.7$ μGal/cm	$0.8-1.3$ μGal[3,4]	underwater
	3.1 μGal/cm	$2-4$ μGal[6]	in the free air
atmospheric effects	0.3 μGal/hPa	$1-2$ μGal[6,7]	
gravimeter	tens of μGal[8]	$1.2-5$ μGal[5]	instrument-dependent
total		$2.5-6.7$ μGal	onshore
		$2.1-5.7$ μGal	offshore
compaction/ subsidence	a few μGal		site-dependent
hydrological effects	20 μGal and more	$2-5$ μGal and more	site-dependent

---

[1] Niebauer et al. (1995)

[2] this estimate is concluded from the results presented by Sasagawa et al. (2008)

[3] Zumberge et al. (2008)

[4] Eiken et al. (2008)

[5] refers to the CG-3, CG-5 relative gravimeters widely used in field applications, (Christiansen et al. 2011)

[6] Ferguson et al. (2008)

[7] Torge (1989)

[8] e.g., instrument drift

Chapter 4

Gravity data inversion for reservoir monitoring and characterization

Inversion of geophysical observations, and gravimetric observations in particular, is an ill-posed problem. Therefore, to stabilize and constrain the solution some sort of regularization must be applied. In classical regularization methods, which are based on the Tikhonov regularization concept, the solution is constrained by applying dedicated stabilizing functionals, which are some mathematical functions of model parameters. An alternative approach is data assimilation, where available observations are merged into a dynamical model of the phenomenon under investigation. In this chapter we discuss inversion/estimation methods used throughout the thesis, namely focusing inversion which belongs to the class of Tikhonov regularization methods. We also introduce two ensemble data assimilation techniques, namely the ensemble Kalman filter and the ensemble smoother. A common framework between the Tikhonov regularization concept and data assimilation is briefly discussed, complemented by illustrative examples of application.

4.1 Introduction

In Chapter 2 we considered various reservoir types and reservoir production processes and performed a forward modeling of the gravimetric signal, i.e., for a given mass redistribution in the reservoir a corresponding gravity field variation was determined. Thus, we were solving the forward problem, which in a general form, can be formulated as

$$\mathbf{F}(\mathbf{x}) \quad = \quad \mathbf{d}, \tag{4.1}$$

where $\mathbf{x} = [x_1, x_2, \ldots, x_M]^T$ is the vector of model parameters (in M-dimensional parameter space), $\mathbf{d} = [d_1, d_2, \ldots, d_N]^T$ denotes the vector of predicted signal (in N-dimensional data space) and $\mathbf{F}$ is the forward modeling operator defining the functional dependence between $\mathbf{x}$ and $\mathbf{d}$. In practice however, the complete subsurface cannot be observed directly and its state must be inferred from indirect observations which are usually contaminated with noise. Therefore, a problem opposite to (4.1) must be solved

$$\mathbf{y} = \mathbf{F}(\mathbf{x}) + \epsilon, \tag{4.2}$$

where $\mathbf{y} = [y_1, y_2, \ldots, y_N]^T$ denotes the noisy observations and $\epsilon = [\epsilon_1, \epsilon_2, \ldots, \epsilon_N]^T$ denotes the observation noise.

To translate the observations into the estimates of unknown parameters at least three things are required: a suitable parametrization, the functional model and the inversion procedure. An example of parametrization in our context, is reservoir domain discretization into a finite set of grid cells (subdomains), with a constant parameter value within each grid cell. The functional model defines the quantitative link between available observations and the model parameters, i.e., it allows to simulate the observations for a given parameter set at prescribed locations. The inversion procedure does the opposite job, i.e., it translates available observations into the parameter estimates.

In general solving the inverse problem (4.2) is not a trivial task. First, because in many cases $\mathbf{F}$ is a nonlinear function of model parameters $\mathbf{x}$. Furthermore, $\mathbf{F}$ may not be known exactly in any closed form. Therefore, in many practical situations one may need to linearize the problem and search for approximate solutions. When the signal is linearly related to the model parameters, one could write

$$\mathbf{A}\mathbf{x} \quad = \quad \mathbf{d} \tag{4.3}$$

where $\mathbf{A}$ is $N \times M$ matrix, often called *design matrix*, *sensitivity matrix* or *Jacobian matrix.*

Another, more fundamental difficulty, is that the inversion of geophysical observations, and gravity observations in particular, is an ill-posed problem. This means that the solution may not exist at all, the solution may not be stable (the two observed data sets, different only within a noise-level, may provide significantly different parameter estimates) and it may not be unique. Therefore, typically some sort of regularization must be applied to obtain any reasonable parameter estimates.

In this chapter we will introduce two regularized inversion (estimation) methods, which will be used throughout the thesis, namely focusing inversion and data assimilation.

Focusing inversion is based on the Tikhonov regularization concept, where some sort of mathematical stabilizer is used to regularize the solution. There are various stabilizers proposed in the literature (for an overview see, e.g., Zhdanov 2002), and some of the traditional choices are the minimum norm and the maximum smoothness stabilizer (see Section 4.3). However, when applying the traditional stabilizers it may be challenging to obtain blocky parameter estimates such as, e.g., the water/gas front position in the reservoir. For such problems, focusing stabilizing functionals can be useful. They offer a mathematical tool to constrain the inversion to models with a compact support and sharp transitions between parameter values. Two types of stabilizers have been proposed for that purpose: the minimum support stabilizing functional and the minimum gradient support stabilizing functional. They will be presented in Section 4.4.

Often, to understand and predict reservoir behavior a numerical model is constructed based on available measurements, assumptions and underlying physics. It incorporates available information from e.g., seismic surveys, geological studies and core samples but also prior knowledge and assumptions based on geologist's and/or reservoir engineer's knowledge and experience with similar fields. The underlying physics of reservoir flow is modeled using physical flow equations (for reservoir flow modeling see Peaceman 1977) discretized in space and time. The reservoir model may contain many uncertain parameters, such as reservoir saturation, pressure, porosity, permeability, structure, initial conditions (fluid contacts) and others, some of which are static and some of which are time-variable. Because the unknowns need to be assigned to every grid cell, their number can easily reach 10^6-10^8 for complex models. Furthermore, the relation between the model parameters and the observations can be nonlinear. For such problems data assimilation methods can be very useful.

Data assimilation, in the context of reservoir engineering is often called "computer-assisted history matching". It offers a methodology to combine available measurements with physically based numerical model predictions. The uncertain parameters of a model are adjusted by comparing real observations with the synthetic data predicted by the numerical model. If the observations do not match the model predictions, the parameters are adjusted accordingly. This process is called history matching. Recently, in reservoir engineering applications the ensemble Kalman filter and ensemble smoother method have been demonstrated to be powerful (Evensen 2007, Aanonsen et al. 2009, Oliver & Chen 2011, Skjervheim et al. 2011) and they will also be applied in this thesis.

We start the chapter with a brief introduction of a Bayesian framework or in other words a statistical regularization concept. Then the classical Tikhonov regularization approach is discussed, followed by the introduction of the focusing inversion stabilizers and a simplified demonstration example. Then, the ensemble Kalman filter and the ensemble smoother methods are presented. For the sake of completeness we introduce also the Kalman filter method and its extension to non-linear problems, namely, the extended Kalman filter method. Subsequently, a common framework between the Tikhonov regularization concept and data assimilation will be briefly discussed, followed by an example of the application of the focusing inversion method and the ensemble Kalman filter method to the parameter estimation in a gas field synthetic case study. Some of the materials in Sections 4.1, 4.2 and 4.6 are based on Ditmar (2010).

4.2 Statistical regularization in the Bayesian framework

The statistical regularization concept (Turchin et al. 1971) is embedded within the Bayesian framework, where the unknown model parameters **x** and measurements **y** are considered as realizations of random variables described by a multivariate probability distribution. The theorem of Bayes states that

$$P(\mathbf{x}|\mathbf{y}) = \frac{P(\mathbf{y}|\mathbf{x})P(\mathbf{x})}{P(\mathbf{y})}, \tag{4.4}$$

where

- $P(\mathbf{x}|\mathbf{y})$ is the posterior probability distribution of model parameters **x** conditioned to available observations **y**;
- $P(\mathbf{y}|\mathbf{x})$ is a likelihood function, i.e., the probability distribution of observations **y** given the model parameter **x**;
- $P(\mathbf{x})$ is the prior probability distribution expressing initial uncertainty of the model parameters **x**;
- $P(\mathbf{y})$ is the probability distribution of the observations **y**.

Typically, the observation errors ϵ are assumed to follow a zero-mean Gaussian distribution. In this case the conditional probability density function (pdf) of observations given model parameter **x** is proportional to

$$P(\mathbf{y}|\mathbf{x}) \propto \exp\left[-\frac{1}{2}(\mathbf{y}-\mathbf{A}\mathbf{x})^T\mathbf{C}_y^{-1}(\mathbf{y}-\mathbf{A}\mathbf{x})\right], \tag{4.5}$$

where $\mathbf{C}_y$ is the data noise covariance matrix and $\propto$ denotes proportionality and where we have assumed that (4.3) is valid, i.e., the model parameters are linearly related to the signal. If the model parameters are also assumed to be Gaussian then

$$P(\mathbf{x}) \propto \exp\left[-\frac{1}{2}(\mathbf{x}-\mathbf{x}_0)^T\mathbf{C}_x^{-1}(\mathbf{x}-\mathbf{x}_0)\right], \tag{4.6}$$

where $\mathbf{x}_0$ is the prior estimate of **x** and $\mathbf{C}_x$ is the parameter covariance matrix. Then the Bayes' theorem allows expressing the pdf of **x** conditioned to available data **y** as

$$P(\mathbf{x}|\mathbf{y}) \propto \exp\left[-\frac{1}{2}(\mathbf{y}-\mathbf{A}\mathbf{x})^T\mathbf{C}_y^{-1}(\mathbf{y}-\mathbf{A}\mathbf{x}) - \frac{1}{2}(\mathbf{x}-\mathbf{x}_0)^T\mathbf{C}_x^{-1}(\mathbf{x}-\mathbf{x}_0)\right], \tag{4.7}$$

or alternatively as

$$P(\mathbf{x}|\mathbf{y}) \propto \exp\left[-J(\mathbf{x})\right], \tag{4.8}$$

where

$$J(\mathbf{x}) = \left[\frac{1}{2}(\mathbf{y} - \mathbf{A}\mathbf{x})^T \mathbf{C}_y^{-1}(\mathbf{y} - \mathbf{A}\mathbf{x}) + \frac{1}{2}(\mathbf{x} - \mathbf{x}_0)^T \mathbf{C}_x^{-1}(\mathbf{x} - \mathbf{x}_0)\right] \tag{4.9}$$

is called the objective function. The most probable estimate of $\mathbf{x}$ is the one for which the conditional pdf given by expression (4.7) attains its maximum, which is equivalent to the minimum of the quadratic objective function $J(\mathbf{x})$. The minimum of J is found by setting its gradient with respect to $\mathbf{x}$ equal to zero. It can be shown that (Oliver et al. 2008)

$$\nabla_x J = \mathbf{C}_x^{-1}(\mathbf{x} - \mathbf{x}_0) + \mathbf{A}^T \mathbf{C}_y^{-1}(\mathbf{A}\mathbf{x} - \mathbf{y}) \tag{4.10}$$

and consequently the estimate of $\mathbf{x}$ is given by

$$\hat{\mathbf{x}} = \mathbf{x}_0 + (\mathbf{C}_x^{-1} + \mathbf{A}^T \mathbf{C}_y^{-1} \mathbf{A})^{-1} \mathbf{A}^T \mathbf{C}_y^{-1}(\mathbf{y} - \mathbf{A}\mathbf{x}_0). \tag{4.11}$$

The solution (4.11) is called the maximum a posteriori (MAP) estimate of $\mathbf{x}$. Thanks to known matrix identities (for the proof see, e.g., Oliver et al. (2008))

$$(\mathbf{C}_x^{-1} + \mathbf{A}^T \mathbf{C}_y^{-1} \mathbf{A})^{-1} \mathbf{A}^T \mathbf{C}_y^{-1} = \mathbf{C}_x \mathbf{A}^T (\mathbf{C}_y + \mathbf{A}\mathbf{C}_x \mathbf{A}^T)^{-1}, \tag{4.12}$$

the MAP estimate of $\mathbf{x}$ can also be written as

$$\hat{\mathbf{x}} = \mathbf{x}_0 + \mathbf{C}_x \mathbf{A}^T (\mathbf{C}_y + \mathbf{A}\mathbf{C}_x \mathbf{A}^T)^{-1}(\mathbf{y} - \mathbf{A}\mathbf{x}_0). \tag{4.13}$$

Note that the use of MAP expression (4.11) requires the solution of a $M \times M$ matrix problem, whereas expression (4.13) involves a $N \times N$ matrix problem. Therefore, the choice of the expression for MAP estimate may be motivated by the numerical efficiency. If $M << N$ then formulation (4.11) can be preferred. If $N << M$ then (4.13) is usually computationally efficient, even if M is large (Oliver et al. 2008).

Statistical regularization of the inverse problem solution requires the specification of the data noise and the model parameter covariance matrices. The noise covariance matrix $\mathbf{C}_y$ acts as a weighting operator giving a lower weight to the more uncertain data. The model parameter covariance matrix $\mathbf{C}_x$ plays a double role: it is the weighting and regularization operator at the same time. It allows a priori knowledge about the parameter to be incorporated into the final solution. Typically, some knowledge about the data noise properties is available because, e.g., accuracy of measuring device is known and the data noise covariance matrix can be approximated. Contrary to that, a limited knowledge about parameter characteristics is often available before any measurements are acquired and specification of the model covariance matrix can be problematic. In such cases regularization techniques can be used, which are based on the Tikhonov regularization concept.

4.3 Tikhonov regularization

The way of solving ill-posed inverse problem, according to the Tikhonov regularization concept (Tikhonov & Arsenin 1977) is based on the minimization of the Tikhonov parametric functional

$$P_\alpha(\mathbf{x}) = m(\mathbf{x}) + \alpha s(\mathbf{x}), \tag{4.14}$$

where

$$m(\mathbf{x}) = \|\mathbf{A}\mathbf{x} - \mathbf{y}\|^2 = (\mathbf{A}\mathbf{x} - \mathbf{y})^T(\mathbf{A}\mathbf{x} - \mathbf{y}) \tag{4.15}$$

is the misfit functional, $s(\mathbf{x})$ is the stabilizing (regularization) functional and α is the regularization parameter. To account for the uncertainties in observations, the misfit functional can be weighted, i.e.

$$m(\mathbf{x}) = \|\mathbf{W}_y\mathbf{A}\mathbf{x} - \mathbf{W}_y\mathbf{y}\|^2 = (\mathbf{A}\mathbf{x} - \mathbf{y})^T{\mathbf{W}_y}^T\mathbf{W}_y(\mathbf{A}\mathbf{x} - \mathbf{y}), \tag{4.16}$$

where $\mathbf{W}_y$ is the observations weighting operator and frequent choice is $\mathbf{W}_y = diag\left[\frac{1}{\sigma}\right]$ with σ being an estimate of observation noise standard deviation. The stabilizing functional $s(\mathbf{x})$ defines a class of models for the inverse problem solution. There are several traditional choices for the stabilizer $s(\mathbf{x})$. The minimum norm stabilizing functional is defined as the squared L_2 norm of the model parameter vector

$$s_{MN}(\mathbf{x}) = \|\mathbf{x}\|^2 = \mathbf{x}^T\mathbf{x}, \tag{4.17}$$

and it usually leads to a relatively smooth image of the inverse model (Zhdanov 2009). In a similar way the maximum smoothness stabilizing functional is defined as

$$s_{max\,SM}(\mathbf{x}) = \|\nabla\mathbf{x}\|^2 = (\nabla\mathbf{x})^T(\nabla\mathbf{x}), \tag{4.18}$$

where $\nabla\mathbf{x}$ denotes the vector of the parameter spatial gradient.

For a unified approach towards regularization with different stabilizers it is convenient to express stabilizer $s(\mathbf{x})$ using L_2 norm of a function of the model parameters

$$s(\mathbf{x}) = \|\mathbf{W}_x\mathbf{x} - \mathbf{W}_x\mathbf{x}_0\|^2 = (\mathbf{x} - \mathbf{x}_0)^T{\mathbf{W}_x}^T\mathbf{W}_x(\mathbf{x} - \mathbf{x}_0), \tag{4.19}$$

where the form of matrix operator $\mathbf{W}_\mathbf{x}$ varies depending on the stabilizer used and some of the examples will be given in one of the following subsections. Using expressions (4.16) and (4.19), the Tikhonov parametric functional (4.14) can be written as

$$P_\alpha(\mathbf{x}) = (\mathbf{A}\mathbf{x} - \mathbf{y})^T{\mathbf{W}_y}^T\mathbf{W}_y(\mathbf{A}\mathbf{x} - \mathbf{y}) + \alpha(\mathbf{x} - \mathbf{x}_0)^T{\mathbf{W}_x}^T\mathbf{W}_x(\mathbf{x} - \mathbf{x}_0). \tag{4.20}$$

The regularized solution can be found by setting the gradient of $P_\alpha(\mathbf{x})$ with respect to $\mathbf{x}$ equal to zero. It can be shown that the least-squares estimate of $\mathbf{x}$ can be expressed as (Zhdanov 2002)

$$\hat{\mathbf{x}} = \mathbf{x}_0 + (\mathbf{A}^T\mathbf{W}_y^T\mathbf{W}_y\mathbf{A} + \alpha\mathbf{W}_x^T\mathbf{W}_x)^{-1}\mathbf{A}^T\mathbf{W}_y^T\mathbf{W}_y(\mathbf{y} - \mathbf{A}\mathbf{x}_0). \tag{4.21}$$

The use of Tikhonov regularization requires the specification of the regularization parameter α, which determines the trade-off between best model fitting to the data and strength of regularization applied to the solution. When a very small α is selected, minimization of the parametric functional (4.14) is equivalent to the minimization of model misfit (4.15) and the solution may not be stable. On the other hand, for a too large α minimization of parametric functional is equivalent to minimization of the stabilizing functional $s(\mathbf{x})$. In this case one may obtain a stable solution but it is determined by a priori knowledge and the stabilizer used. Therefore, the choice of the regularization parameter α strongly influences the final solution. There are several methods available for the regularization parameter selection, e.g., the L-curve method (Hansen & O'Leary 1993) which offers a graphical tool for quasi-optimal selection of α, the Generalized Cross-Validation (GCV) method (Girard 1989, Golub et al. 1979), and the Variance Component Estimation (VCE) method (see, e.g., Koch & Kusche (2002) and references therein) which estimate α explicitly. In this chapter we will use an empirical approach based on adaptive α tuning proposed by Zhdanov (2002). It will be described in Subsection 4.4.3.

4.4 Focusing inversion

Application of traditional stabilizers, such as the minimum norm (4.17) or the maximum smoothness (4.18) stabilizer, is likely to produce smooth parameter estimates, i.e., without sharp contrasts in parameter values. In some cases however, such as in hydrocarbon or mineral exploration, blocky parameter estimates can be desired to describe sharp property transitions within complex geological structures. For such problems focusing stabilizing functionals can be useful. They offer a mathematical tool to constrain the inverse problem solution to models with a compact support and sharp transitions between parameter values. For that purpose two types of stabilizers have been proposed: the minimum support stabilizing functional and the minimum gradient support stabilizing functional.

Focusing inversion was first introduced by Last & Kubik (1983) who proposed the minimum support stabilizer. It was further developed by Portniaguine & Zhdanov (1999), who introduced the minimum gradient support functional. Since its introduction, focusing inversion has been applied in many synthetic studies (Zhdanov & Tolstaya 2004, Zhdanov et al. 2006, Zhdanov 2007, Zhang et al. 2012) and also to various types of geophysical data inversion in field case applications. For instance, Zhdanov et al. (2011a) inverted synthetic electromagnetic observations to estimate a 3D subsurface resistivity model of the Shtokman gas field in the Barents Sea.

Zhdanov et al. (2011b) used the focusing inversion of electromagnetic data to map the salt body structure in the field case in Gulf of Mexico. Čuma et al. (2012) inverted airborne gravity and magnetic data to estimate a large-scale (hundreds of km), 3D distribution of subsurface density and magnetic susceptibility.

Focusing inversion stabilizers are based on the following integral expression applied to the model parameters x

$$\daleth(x) = \int_V \frac{x^2}{x^2 + \beta^2} dv, \tag{4.22}$$

distributed in some 3D physical domain, denoted V. Note that now we consider the parameter as a spatial function of coordinates. To distinguish the notation from the one used in the previous section when the parameter was treated as a vector, we don't use a bold font for x.

Let us denote the support of x as spt_x and define it as the combined closed subdomains of V where $x \neq 0$. Then expression (4.22) can be written as

$$\begin{aligned} \daleth(x) &= \int_{\mathrm{spt}_x} \left[1 - \frac{\beta^2}{x^2 + \beta^2} \right] dv \\ &= \mathrm{V}_x - \beta^2 \int_{\mathrm{spt}_x} \left[\frac{1}{x^2 + \beta^2} \right] dv. \end{aligned} \tag{4.23}$$

From (4.23) we can see that if $\beta \to 0$ then $\daleth(x) \to \mathrm{V}_x$, where V_x denotes the volume of the parameter support. Therefore, the minimum support stabilizing functional is defined as

$$s_{MS}(x) = \daleth(x) = \int_V \frac{x^2}{x^2 + \beta^2} dv, \tag{4.24}$$

where β is called the focusing parameter. From (4.23) and (4.24) it follows that for small β the stabilizer s_{MS} is proportional to the parameter support. Furthermore, parameters in the solution with values close to zero will have negligible contribution to s_{MS} while large parameter values will have contributions close to 1. This allows enhanced solutions with compact parameter support to be produced.

In a similar way the minimum gradient support functional is defined (Portniaguine & Zhdanov 1999)

$$s_{MGS}(\nabla x) = \daleth(\nabla x) = \int_V \frac{(\nabla x)^2}{(\nabla x)^2 + \beta^2} dv, \tag{4.25}$$

where ∇x denotes the spatial parameter gradient. The details of the gradient approximation scheme used in this study are shown in the Appendix A.

Using Eq. (4.23), we can also write

$$s_{MGS}(\nabla x) = \mathrm{V}_{\nabla x} - \beta^2 \int_{\mathrm{spt}_{\nabla x}} \left[\frac{1}{(\nabla x)^2 + \beta^2} \right] dv, \tag{4.26}$$

which shows that for small β the functional $s_{MGS}(\nabla x)$ is proportional to the volume of the parameter gradient support $\mathrm{V}_{\nabla x}$. From expression (4.25) it follows that terms with the parameter gradient nearly zero will have negligible contribution to s_{MGS} while terms with large parameter gradient will have contributions close to 1. This promotes solutions with sharp boundaries because the penalty for large gradients is not excessive (Portniaguine & Zhdanov 1999). The schematic illustration of the focusing inversion is shown in Fig. 4.1.

For the cases when prior knowledge about the parameter values is available, i.e., when

$x_0 \neq 0$, the minimum support functional is given by

$$s_{MS,\,\mathrm{apr}}(x - x_0) = \beth(x - x_0) = \int_V \frac{(x - x_0)^2}{(x - x_0)^2 + \beta^2} dv. \tag{4.27}$$

In this case, the minimization of the functional $s_{MS,\,\mathrm{apr}}$ is equivalent to the minimization of the support of the deviation from a given a priori model x_0. Similarly, we may write for the minimum gradient support stabilizer (Zhdanov et al. 2011a)

$$s_{MGS,\,\mathrm{apr}}(\nabla(x - x_0)) = \beth(\nabla(x - x_0)) = \int_V \frac{(\nabla(x - x_0))^2}{(\nabla(x - x_0))^2 + \beta^2} dv. \tag{4.28}$$

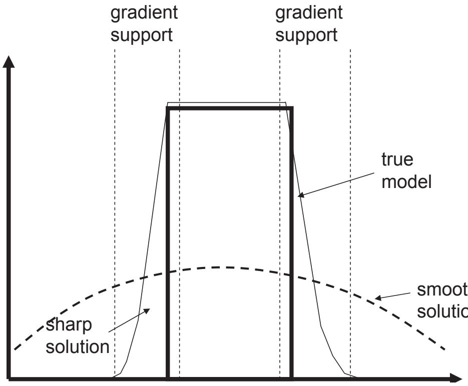

Figure 4.1: Schematic illustration of the sharp inversion with the minimum gradient support stabilizer. After Zhdanov (2002).

4.4.1 Pseudo-quadratic form of the parametric functional

For a unified approach to regularization using different stabilizers, it is convenient to express the functional $s(x)$ as squared L_2 norm of weighted model parameters (Portniaguine & Zhdanov 1999, Zhdanov 2002)

$$s(x) = \int_V (w_x x)^2 dv, \tag{4.29}$$

where w_x is a function of model parameters x taking different forms depending on the stabilizer and where we assumed that $x_0 = 0$. For instance, for the minimum support functional (4.24)

$$w_x^{MS} = \frac{1}{(x^2 + \beta^2)^{1/2}}. \tag{4.30}$$

Similarly, for the minimum gradient support functional (4.25) we want to have

$$s(x) = \int_V (w_x x)^2 dv = \int_V \frac{(\nabla x)^2}{(\nabla x)^2 + \beta^2} dv. \tag{4.31}$$

This is satisfied if

$$w_x^{MGS} = \frac{\nabla x}{((\nabla x)^2 + \beta^2)^{1/2}(x^2 + e^2)^{1/2}}, \tag{4.32}$$

where e is a small number ($e \to 0$) included to avoid a singularity for the points where $x = 0$.

In a practical case when the model parameters are arranged in a column vector $\mathbf{x}$ the functional (4.29) can be written as

$$s(\mathbf{x}) = \|\mathbf{W}_x\mathbf{x}\|^2 = \mathbf{x}^T\mathbf{W}_x^T\mathbf{W}_x\mathbf{x}, \tag{4.33}$$

where $\mathbf{W}_\mathbf{x}$ is a matrix operator of the form

$$\mathbf{W}_x = \mathrm{diag}[w_x], \tag{4.34}$$

i.e., it is diagonal matrix with elements of w_x. Obviously, $\mathbf{W}_x$ depends on the stabilizer used. For instance, for the minimum norm stabilizer,

$$\mathbf{W}_\mathbf{x}^{MN} = I, \tag{4.35}$$

where I is $M \times M$ identity matrix. In case of the maximum smoothness functional,

$$\mathbf{W}_\mathbf{x}^{max\,SM} = \mathrm{diag}\left[\frac{\nabla\mathbf{x}}{(\mathbf{x}^2 + e^2)^{1/2}}\right]. \tag{4.36}$$

For the minimum support functional,

$$\mathbf{W}_\mathbf{x}^{MS} = \mathrm{diag}\left[\frac{1}{(\mathbf{x}^2 + \beta^2)^{1/2}}\right], \tag{4.37}$$

and for the minimum gradient support,

$$\mathbf{W}_\mathbf{x}^{MGS} = \mathrm{diag}\left[\frac{\nabla\mathbf{x}}{((\nabla\mathbf{x})^2 + \beta^2)^{1/2}(\mathbf{x}^2 + e^2)^{1/2}}\right]. \tag{4.38}$$

In case $\mathbf{x}_0 \neq 0$, we have for the minimum support stabilizing functional,

$$\mathbf{W}_\mathbf{x}^{MS,\,\mathrm{apr}} = \mathrm{diag}\left[\frac{1}{((\mathbf{x} - \mathbf{x}_0)^2 + \beta^2)^{1/2}}\right], \tag{4.39}$$

and for the minimum gradient support stabilizer

$$\mathbf{W}_\mathbf{x}^{MGS,\,\mathrm{apr}} = \mathrm{diag}\left[\frac{\nabla(\mathbf{x} - \mathbf{x}_0)}{(\nabla(\mathbf{x} - \mathbf{x}_0)^2 + \beta^2)^{1/2}((\mathbf{x} - \mathbf{x}_0)^2 + e^2)^{1/2}}\right]. \tag{4.40}$$

If $\mathbf{W}_\mathbf{x}$ is independent of $\mathbf{x}$ then the functional (4.34) is quadratic. When $\mathbf{W}_\mathbf{x}$ is a function of model parameters, as, e.g., in case of the minimum support or the minimum gradient support stabilizers, the functional (4.34) is not quadratic. For that reason, it is called ”pseudo-quadratic” (Zhdanov 2002).

4.4.2 Focusing parameter choice rule

The choice of the parameter β in the focusing inversion method influences the sharpness (compactness) and stability of the obtained solution. A too large focusing parameter β may produce smooth images (Blaschek et al. 2008), whereas extremely small values of β may result in a singular behavior (division by zero) of the functional and an unstable solution. Zhdanov & Tolstaya (2004) proposed an empirical approach for focusing parameter selection which resembles the L-curve method. Their idea is to consider the plot of the normalized stabilizing functional for a range of values of the focusing parameter β and for a given priori estimate x_0 (Fig. 4.2). If prior knowledge about $\mathbf{x}$ is absent then $\mathbf{x}_0$ could be obtained from, e.g., a smooth inversion with the minimum norm stabilizer. The quasi-optimal value of the focusing parameter β_{opt} is found as the point of the maximum curvature (quasi L-corner point). For $\beta < \beta_{opt}$ the value of the stabilizer changes rapidly with decreasing parameter β. For $\beta > \beta_{opt}$ the stabilizer decreases more slowly. For that reason, values of β near the point of maximum curvature are considered to be close to optimal.

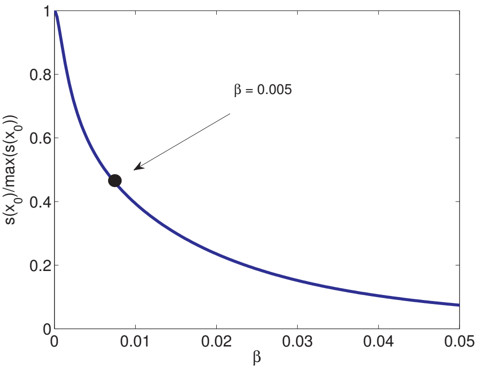

Figure 4.2: Schematic illustration of the focusing parameter empirical selection. After Zhdanov & Tolstaya (2004).

4.4.3 Re-weighted regularized conjugate gradient optimization scheme

In order to find the inverse problem solution by minimization of the parametric functional (4.14), various approaches can be used. For instance, one could apply directly the least-squares expression (4.21) for the regularized parameter estimate. However, this approach is not that useful when, e.g., the forward modeling operator is large and/or the regularization operator is a function of model parameters which are to be determined. Therefore, iterative methods are more frequently used, among which the gradient-based ones, such as quasi-Newton methods (Oliver et al. 2008) or conjugate gradient methods.

In order to minimize the parametric functional (4.14) we follow the approach proposed by Portniaguine & Zhdanov (1999) and Zhdanov (2002), which is called the re-weighted regularized conjugate gradient method (RRCG). In this approach the variable regularization operator $\mathbf{W}_x = \mathbf{W}_{x_n}$ is pre-computed before every iteration using the solution obtained in the previous iteration. During one iteration process this operator is fixed as a constant matrix. The RRCG algorithm is summarized as follows (Zhdanov 2002)

$$\begin{aligned}
\mathbf{r}_n &= \mathbf{A}\mathbf{x}_n - \mathbf{y}, \\
\mathbf{s}_n &= \mathbf{W}_{x_n}(\mathbf{x}_n - \mathbf{x}_0), \\
\mathbf{l}_n^{\alpha_n} &= \mathbf{A}^T\mathbf{W}_y^2\mathbf{r}_n + \alpha_n\mathbf{W}_{x_n}\mathbf{s}_n, \\
\beta_n^{\alpha_n} &= \|\mathbf{l}_n^{\alpha_n}\|^2/\|\mathbf{l}_{n-1}^{\alpha_{n-1}}\|^2, \quad \widetilde{\mathbf{l}}_n^{\alpha_n} = \mathbf{l}_n^{\alpha_n} + \beta_n^{\alpha_n}\widetilde{\mathbf{l}}_{n-1}^{\alpha_{n-1}}, \quad \widetilde{\mathbf{l}}_0^{\alpha_0} = \mathbf{l}_0^{\alpha_0} \\
\widetilde{k}_n^{\alpha_n} &= \left(\widetilde{\mathbf{l}}_n^{\alpha_n T}\mathbf{l}_n^{\alpha_n}\right) / \left[\widetilde{\mathbf{l}}_n^{\alpha_n T}\left(\mathbf{A}^T\mathbf{W}_y^2\mathbf{A} + \alpha\mathbf{W}_{x_n}^2\right)\widetilde{\mathbf{l}}_n^{\alpha_n}\right], \\
\mathbf{x}_{n+1} &= \mathbf{x}_n - \widetilde{k}_n^{\alpha_n}\widetilde{\mathbf{l}}_n^{\alpha_n}.
\end{aligned} \tag{4.41}$$

The iteration process is terminated if the misfit condition is satisfied, i.e., if

$$\|\mathbf{r}_n\|^2 \leq \delta, \tag{4.42}$$

where δ is the data noise level.

Because the solution is re-weighted after every iteration, the stabilizing functional, in some instances, can increase from iteration to iteration. To assure convergence of the parametric functional to the global minimum, Zhdanov (2002) proposed to damp the regularization parameter α proportionally to the increase of the stabilizer

$$\alpha_{n+1} = \begin{cases} \alpha_n, & \text{if } \gamma \leq 1 \\ \alpha_n/\gamma, & \text{if } \gamma > 1, \end{cases} \tag{4.43}$$

where

$$\gamma = \frac{s(\mathbf{x}_{n+1})}{s(\mathbf{x}_n)} = \frac{(\mathbf{x}_{n+1} - \mathbf{x}_0)^T\mathbf{W}_{x_{n+1}}^2(\mathbf{x}_{n+1} - \mathbf{x}_0)}{(\mathbf{x}_n - \mathbf{x}_0)^T\mathbf{W}_{x_n}^2(\mathbf{x}_n - \mathbf{x}_0)}. \tag{4.44}$$

Then, the product of the regularization parameter and the stabilizing functional decreases or does not change

$$\alpha_{n+1}s(\mathbf{x}_{n+1}) = \begin{cases} \alpha_n s(\mathbf{x}_{n+1}) = \alpha_n\gamma s(\mathbf{x}_n), & \text{if } \gamma \leq 1 \\ \alpha_n s(\mathbf{x}_{n+1})\gamma = \alpha_n s(\mathbf{x}_n), & \text{if } \gamma > 1. \end{cases} \tag{4.45}$$

If the convergence rate is slow, Zhdanov (2002) proposed to decrease α further with

$$\alpha'_{n+1} = q\alpha_{n+1}, \; q < 1 \text{ if } \|\mathbf{W}_y\mathbf{r}_n\|^2 - \|\mathbf{W}_y\mathbf{r}_{n+1}\|^2 < 0.01\|\mathbf{W}_y\mathbf{r}_n\|^2, \tag{4.46}$$

where, based on empirical experiments, values of $q \in (0.5; 0.9)$ are used. Note, however, that a damping of α using condition (4.46) decreases the magnitude of the regularization applied to the solution. If α is reduced too quickly, the minimization of the parametric functional may turn into the minimization of the model misfit, and weakly-regularized solution may be obtained. We will demonstrate this effect in Subsection 4.4.4.

Following Zhdanov (2002) we run the first iteration without regularization. This result is used to determine the initial value of the regularization parameter α which assures the balance (equality) between the model misfit term $m(\mathbf{x})$ and the stabilizing term $\alpha s(\mathbf{x})$ at the start of inversion process. Equating $m(\mathbf{x})$ with $\alpha s(\mathbf{x})$ gives the initial value of α

$$\alpha_1 = \frac{\|\mathbf{W}_y\mathbf{A}\mathbf{x}_1 - \mathbf{W}_y\mathbf{y}\|^2}{\|\mathbf{W}_{x_1}\mathbf{x}_1 - \mathbf{W}_{x_1}\mathbf{x}_0\|^2}. \tag{4.47}$$

4.4.4 Example

A simple 2D density model is considered for the application of the focusing inversion of gravity data. The model domain is discretized into 20×20 cubes, each of dimension 100×100×100 m. The distance from the surface to the model top layer is 350 m. The true model (Fig. 4.3a) contains two rectangular bodies consisting of 3×3×1 cubes (300×300×100 m) with a density contrast of -50 kg/m^3 with respect to the homogenous background density.

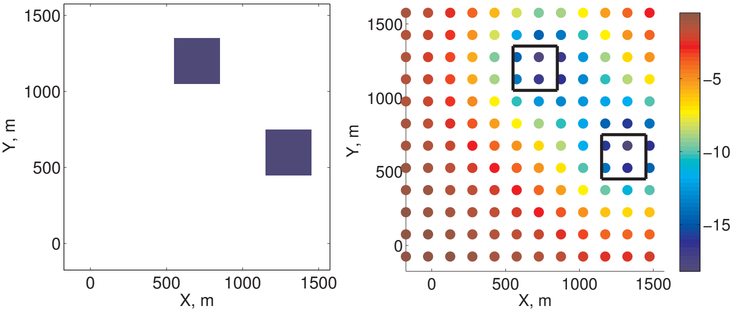

(a) true model **(b)** gravity observation grid

Figure 4.3: Layout of the true model (Fig. 4.3a) and layout of the gravity observation (μGal) grid (Fig. 4.3b). The density contrast in Fig. 4.3a with respect to a homogenous background is -50 kg/m^3 (shown in dark blue). In Fig. 4.3b the black rectangles show the boundaries of the true model.

Synthetic residual gravity measurements are simulated on a regular grid of dimension 12×12 with measurement spacing of 150 m in x- and y-direction (Fig. 4.3b). The maximum gravity variation for the true model is about -18 μGal. The synthetic data are contaminated with zero-mean uncorrelated Gaussian noise with 5 μGal standard deviation.

We perform both the regularized focusing inversion and the unregularized least-squares model fit to the synthetic gravity data to estimate the subsurface density anomaly. The unregularized least-square solution could be directly determined by using Eq. (4.21), with α set equal to zero. Here, we want to apply the lower/upper bound constrains on the estimated parameter values

$$\begin{aligned} x_i &= x_{min} \text{ if } x_i < x_{min}, \\ x_i &= x_{max} \text{ if } x_i > x_{max}, \text{ for } i = 1, \ldots, 400, \end{aligned} \tag{4.48}$$

where

$$\mathbf{x} = [x_1, x_2, \ldots, x_{400}]^T, \tag{4.49}$$

and $x_{min} = -50$ kg/m^3 and $x_{max} = 0$ kg/m^3. Therefore, the use of iterative methods, such as the conjugate gradient scheme is more convenient in this case. Furthermore, it provides a unified framework for the comparison of results in case of the regularized and the unregularized solutions.

Fig. 4.4 shows the results of the focusing inversion compared to the least-squares solution without regularization. In both cases, the a priori model is $\mathbf{x}_0 = \mathbf{0}$ and the observation weighting operator (see eqn. 4.16)

$$\mathbf{W}_y = \text{diag}\left[\frac{1}{\sigma}\right], \tag{4.50}$$

has been used, which is a diagonal matrix with σ=5 μGal. For the focusing inversion with the minimum support stabilizer, the regularization operator (4.37) is used and for the inversion with the minimum gradient support functional operator (4.38) is applied. The regularization parameter α is adjusted (decreased) after every 10-th iteration using condition (4.43). The focusing parameter β is chosen based on the empirical method described in Subsection 4.4.2 and is set to $\beta = 0.5$ kg/m^3, which is 1% of the density contrast in the true model.

The application of the minimum support stabilizer resulted in a significantly more compact parameter support distribution as compared to the unregularized least-squares parameter estimate (Fig. 4.4a, Fig. 4.4b). The minimum gradient support inversion gave not only a compact support, but also a sharp-boundary solution (Fig. 4.4b). Nevertheless, many iterations were required to obtain focused images. For instance in case of the minimum support inversion, 717 iterations were performed. For a comparison, the unregularized least-squares inversion scheme converged after already 6 iterations. Fig. 4.5 shows the parametric functional convergence for the inversion with the minimum support stabilizer. We observe that after about 300 iterations the regularization term played a major role, and the minimization of the parametric functional $P_\alpha(\mathbf{x})$ was driven by the minimization of the stabilizing functional $s(\mathbf{x})$. The regularization parameter α remained almost unchanged during the iteration process (Fig. 4.5b). If we attempt to increase the speed of convergence by damping α with a parameter $q = 0.8$ (originally $q = 1$) then the results shown in Fig. 4.6 are obtained. We notice that the convergence speed is improved almost an order of magnitude (Fig. 4.7). Nevertheless, due to the fast damping of α and, consequently, small contribution of the stabilizing functional $s(\mathbf{x})$ to the minimization of the parametric functional $P_\alpha(\mathbf{x})$, the final solution is very smooth.

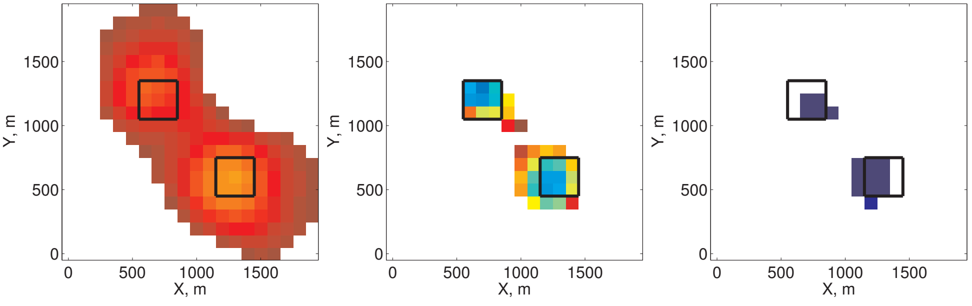

(a) least-squares **(b)** minimum support **(c)** minimum gradient support

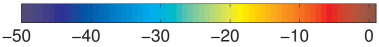

Figure 4.4: Example of the focusing gravity inversion results for a simple 2D density model (kg/m^3). Only the values greater than -2kg/m^3 are shown. The regularization parameter α is adjusted after every 10-th iteration using condition (4.43). The focusing parameter β is set equal to 0.5 kg/m^3 in this case. The black contour shows the boundaries of the true model.

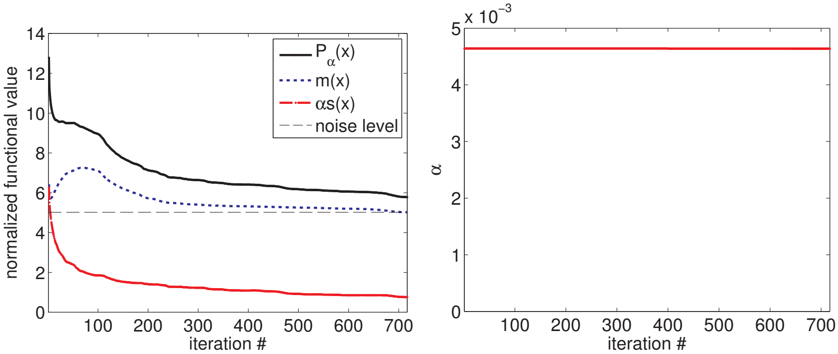

(a) parametric functional **(b)** regularization parameter α, log scale

Figure 4.5: Example of the parametric functional convergence for the minimum support gravity inversion. $P_\alpha(x)$ denotes the parametric functional, $m(x)$ denotes the misfit term and $\alpha s(x)$ denotes the regularization term. The results are shown for the inverse solution presented in Fig. 4.4b. The regularization parameter α is adjusted after every 10-th iteration using condition (4.43). The changes (decrease) of α are to small to be visible. The focusing parameter β is set equal to 0.5 kg/m^3.

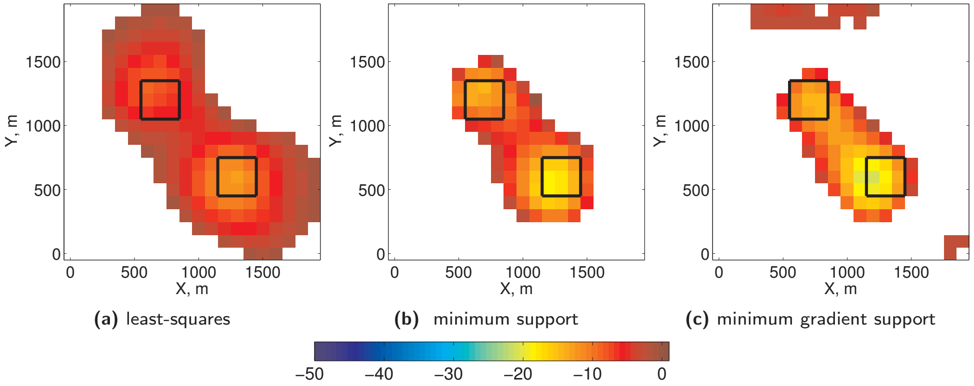

(a) least-squares **(b)** minimum support **(c)** minimum gradient support

Figure 4.6: Example of the focusing gravity inversion results for a simple 2D density model (kg/m^3). Only the values greater than -2kg/m^3 are shown. The regularization parameter α is adjusted (decreased) after every 10-th iteration using conditions presented in equations (4.43)-(4.46). The damping coefficient $q = 0.8$ and the focusing parameter β is set equal to 0.5 kg/m^3 in this case. The black contour shows the boundaries of the true model.

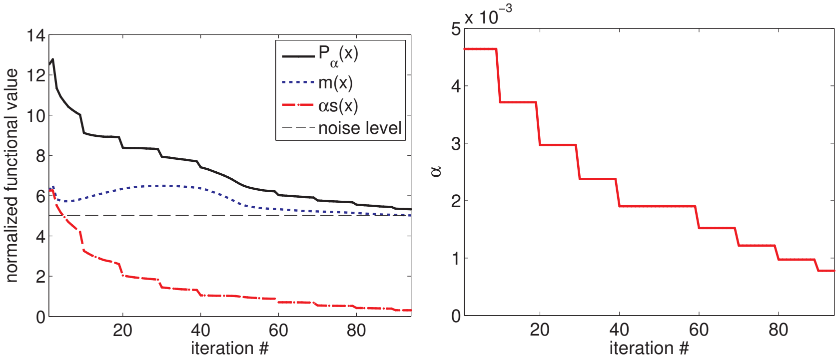

(a) parametric functional **(b)** regularization parameter α, log scale

Figure 4.7: Example of the parametric functional convergence for the minimum support gravity inversion. The results are shown for the inverse solution presented in Fig. 4.6b. The regularization parameter α is adjusted (decreased) after every 10-th iteration using conditions presented in equations (4.43)-(4.46). The damping coefficient $q = 0.8$ and the focusing parameter β is set equal to 0.5 kg/m^3.

4.4.5 Summary

Focusing inversion is an attractive regularization method for inverse problems where the solution of interest is characterized by a compact parameter support and/or sharp property transitions in parameter values. Two types of stabilizers, namely, the minimum support and the minimum gradient support stabilizer can be used for such problems. The minimum support stabilizer promotes focused solutions with a compact parameter support. The minimum gradient support stabilizer allows obtaining estimates with sharp transitions in parameter values. To demonstrate this, both stabilizers were applied to a simple 2D gravity inverse problem where the unknown parameter was a subsurface density anomaly. For a comparison, the unregularized least-square inversion was performed. The focusing inversion provided solutions, which were much more compact and closer to the blocky-structure model. Contrary to that, very smooth and blurred density anomaly estimates were obtained from the least-squares model fit.
The focusing inversion method with the minimum support stabilizer will be applied to the field case feasibility study in Chapter 5.

4.5 Data assimilation

4.5.1 Introduction

Data assimilation (computer-assisted history matching) methods can be used for system state or combined system state and parameter estimation problems. In the context of this research the system states refer to, e.g., reservoir pressure, saturations, density and the parameters are, e.g., porosity and permeability. In this section we will introduce two data assimilation techniques, namely the ensemble Kalman filter (EnKF) and the ensemble smoother (ES), which will be applied in this thesis.

The ensemble Kalman filter was introduced by Evensen (1994), and has since recently been applied for state- and parameter-estimation problems in the petroleum industry. In one of the first EnKF applications, Nævdal et al. (2002) updated the permeability field to history match and forecast a 2D near-well reservoir model. The range and complexity of synthetic experiments with the EnKF was extended quickly. Gu & Oliver (2005) estimated permeability and porosity using production data for the 3D PUNQ-S3 model. Liu & Oliver (2005) applied the EnKF to update facies boundaries, and Seiler et al. (2010) estimated the top and bottom reservoir horizons. In a recent publication, Chang et al. (2010) investigated the applicability of the EnKF to the problem of coupled fluid flow and geomechanics. They assimilated jointly production and subsidence data and found improved estimates of reservoir permeability and Young's-modulus fields. Encouraging results of many synthetic studies have stimulated the use of EnKF for real-field cases. Bianco et al. (2007) applied the EnKF to history match the Zagor reservoir model and to update the uncertain porosity field. Evensen et al. (2007) assimilated production data from a North Sea reservoir to update model parameters, including porosity, permeability, fault transmissibilities, and depths of initial fluid contacts. An overview of other field-case studies using the EnKF can be found in Aanonsen et al. (2009) and in Oliver & Chen (2011) and an extensive literature overview of Kalman filtering (general) applications is included in Evensen (2007). The EnKF method is briefly introduced in Subsection 4.5.4 of this Chapter. Further theoretical details of the EnKF can be found in Evensen (2007) and practical implementation aspects are discussed in Evensen (2003).

The EnKF is a sequential Monte Carlo simulation-based method where an ensemble of models are propagated forward and updated each time new measurements become available. This makes the EnKF capable of uncertainty assessment and uncertainty propagation and real-time model updating. However, the sequential nature of the EnKF may require restarts (either from the start of the simulation or from the previous time step) of the ensemble models (why the restarts may be required will explained in more detail in Subsection 4.5.6). For complex large-scale reservoir systems this may lead to a significant computational load. Furthermore, dealing with structural model (reservoir horizons, thickness, fault locations, etc.) updates resulting in changes of the numerical grid may not be straightforward using the EnKF. Therefore, the ensemble Smoother (ES) has recently been considered as an alternative approach for reservoir history-matching. The ES differs from the EnKF by computing one global update in the time-space domain rather than updating the models recursively as the EnKF does. Thus, when using the ES frequent model restarts are not necessary and computational time can be significantly reduced. The ES was proposed by van Leeuwen & Evensen (1996) and its performance for a reservoir history-matching problem was recently evaluated by Skjervheim et al. (2011). Skjervheim et al. (2011) used a 3D synthetic example based on the real sector model and also a real North Sea field application to test the performance of both the ES and the EnKF. In the synthetic case production data (oil rates and water cuts) and 4D seismic data (cumulative two-way travel times) were assimilated to estimate reservoir permeability and porosity fields. Fairly similar results were obtained using both methods. The major difference was the quantification of the associated uncertainty: the EnKF-based uncertainty estimate was slightly smaller than the one obtained with the ES. In a real case study they history-matched the production data (oil and water rates) and updated the reservoir structure (top and bottom horizons). Also in this case the results were rather similar, but the ES required significantly less computational time, i.e., about 10% of that used by the EnKF because a large number of recursive model restarts could be avoided. However, based on these studies they could not conclude that one method is better than the other.

The ensemble Kalman filter and the ensemble smoother methods are briefly introduced in Subsections 4.5.4 and 4.5.5, respectively. For completeness we start with a brief sketch of the Kalman filter and and its extension to non-linear problems, namely, the extended Kalman filter method.

4.5.2 Kalman filter

The Kalman filter (KF) is an optimal sequential assimilation method for linear system dynamics and Gaussian assumptions about the system and measurement noise (see Evensen 2007, Oliver et al. 2008, Heemink et al. 2010). The optimality refers to the minimization of analysis errors with respect to the true state. The KF is based on sequential updating of system state using a predictor-corrector approach. For a particular time step when measurements become available a prediction of the system state is made using estimates from the previous time step. The mismatch between observed and predicted data is used to update (correct) the modeled system state and produce forecasted state for the next assimilation time. Furthermore, the statistics of estimation/prediction error can be determined and propagated forward. This allows the quality of the estimates to be assessed.

For a linear system a stochastic state space representation is defined as follows

$$\mathbf{x}_{k+1} = \mathbf{F}_k\mathbf{x}_k + \mathbf{B}_k\mathbf{u}_k + \mathbf{w}_k \tag{4.51}$$

$$\mathbf{y}_k = \mathbf{H}_k\mathbf{x}_k + \mathbf{v}_k, \tag{4.52}$$

where k is the time-index, $\mathbf{x}$ denotes the state of the system, $\mathbf{F}$ is the linear forward operator of the system state, $\mathbf{B}$ is the control input operator, $\mathbf{w}$ denotes the zero-mean Gaussian system noise with covariance $\mathbf{C}_{w_k}$, $\mathbf{y}$ denotes the noisy observations, $\mathbf{H}$ is the linear measurement operator relating the system state to the observations, and $\mathbf{v}$ denotes the zero-mean Gaussian measurement noise with covariance $\mathbf{C}_{y_k}$.

The initial conditions are assumed to be Gaussian with

$$\mathbf{x}_0^a = \mathbf{x}_0 \tag{4.53}$$

$$\mathbf{C}_{x_0}^a = \mathbf{C}_{x_0}, \tag{4.54}$$

where $\mathbf{x}_0$ denotes the mean, $\mathbf{C}_{x_0}$ is the covariance matrix of the Gaussian distribution, and $\mathbf{x}^a$ denotes the analyzed (updated) estimate. It is assumed that the system noise process, the measurement noise and the initial condition distribution are mutually independent.

For an optimal state estimate, the Kalman filter combines sequentially information provided by the model with available measurements. A two-stage process is applied where the first stage is the system state forecast

$$\mathbf{x}_k^f = \mathbf{F}_{k-1}\mathbf{x}_{k-1}^a + \mathbf{B}_{k-1}\mathbf{u}_{k-1} \tag{4.55}$$

$$\mathbf{C}_{x_k}^f = \mathbf{F}_{k-1}\mathbf{C}_{x_{k-1}}^a\mathbf{F}_{k-1}^T + \mathbf{C}_{w_{k-1}}, \tag{4.56}$$

where $\mathbf{x}_k^f$ is the forecast of the system state at time t_k, $\mathbf{C}_{x_k}^f$ is the forecasted state covariance matrix, and $\mathbf{C}_{x_k}^a$ is the analyzed state covariance matrix. In the next step, the model information is combined with available measurements using

$$\mathbf{x}_k^a = \mathbf{x}_k^f + \mathbf{K}_k(\mathbf{y}_k - \mathbf{H}_k\mathbf{x}_k^f), \tag{4.57}$$

where the weighting term $\mathbf{K}_k$ is called the Kalman gain, defined as

$$\mathbf{K}_k = \mathbf{C}_{x_k}^f\mathbf{H}_k^T(\mathbf{H}_k\mathbf{C}_{x_k}^f\mathbf{H}_k^T + \mathbf{C}_{y_k})^{-1}. \tag{4.58}$$

The state covariance matrix provides an estimate of the analysis errors, and is updated using

$$\mathbf{C}_{x_k}^a = (I - \mathbf{K}_k\mathbf{H}_k)\mathbf{C}_{x_k}^f. \tag{4.59}$$

There are several ways to derive the Kalman filter estimation scheme summarized in Eqs. (4.57)-(4.58), see Jaźwinski (1970) for more details. It can be obtained as a posterior variance minimizing scheme (minimization of the trace of the analyzed state covariance matrix) or as a sequential least-square estimate embedded within the Bayesian framework (Oliver et al. 2008, Evensen 2007).

4.5.3 Extended Kalman filter

The Kalman filter provides optimal state estimates for linear system dynamics and Gaussian assumptions about the noise processes. In nonlinear cases, however, with (for simplicity we assume $\mathbf{B}_k = 0$)

$$\mathbf{x}_{k+1} = \mathbf{f}_k(\mathbf{x}_k) + \mathbf{w}_k, \tag{4.60}$$

where $\mathbf{f}$ denotes the nonlinear forward operator or

$$\mathbf{y}_k = \mathbf{h}_k(\mathbf{x}_k) + \mathbf{v}_k, \tag{4.61}$$

where $\mathbf{h}$ denotes the nonlinear measurement operator, the KF estimation scheme is not applicable.

An ad hoc extension of KF to (weakly) nonlinear problems is based on determining approximate linear operators

$$\mathbf{x}_{k+1} \approx \mathbf{A}_k\mathbf{x}_k + \mathbf{w}_k, \tag{4.62}$$

where $\mathbf{A}_k$ is the tangent linear operator (Jacobian matrix) of $\mathbf{f}_k(\mathbf{x}_k)$. In a similar way the relation between observations and system state can be linearized

$$\mathbf{y}_k \approx \mathbf{H}_k\mathbf{x}_k + \mathbf{v}_k. \tag{4.63}$$

This approach is known as extended Kalman filter (EKF). Due to the inherent approximations it provides sub-optimal state estimates (Jaźwinski 1970, Evensen 2007, Oliver et al. 2008). In addition, for large-scale problems not only the storage and forward propagation of the state covariance matrix, but also the approximation of the Jacobian matrices can be expensive.

4.5.4 Ensemble Kalman filter

To overcome some of the shortcomings of KF and EKF another sequential data assimilation method can be used, namely the ensemble Kalman filter (EnKF), proposed by Evensen (1994). The EnKF is a Monte Carlo implementation of KF, which approximates the state covariance matrix using a finite set of randomly generated system states, and where the ensemble mean is considered as the best-guess estimate of the state. Consequently, there is no need to linearize the dynamic system equations, because the state covariance matrix is not explicitly propagated forward, but is approximated from the ensemble of system states. Thus, the state covariance matrix does not need to be stored. This makes the EnKF attractive for nonlinear models and large-scale problems.

In the following we introduce the EnKF notation as will be used throughout the thesis. In particular, we consider a joint parameter and state estimation problem instead of state estimation problem as in the traditional KF formulation. This means that the state vector will be augmented with uncertain static parameters, which are simultaneously solved for together with the model state (Evensen 2007).

The EnKF algorithm, similarly to the classical KF, uses three major steps: initialization, forecast and update. The EnKF is initialized by generating an ensemble of model states, where typically $40 - 200$ members are used in reservoir engineering applications. We denote the matrix holding the ensemble of augmented state vectors at time t_k as

$$\boldsymbol{\Psi}_k = \left[\psi_{k,1}, \psi_{k,2}, \ldots, \psi_{k,N_e}\right], \tag{4.64}$$

where N_e is the number of ensemble members and $\psi_{k,j},\ j = 1, \ldots, N_e$ are the augmented ensemble state vectors, i.e.,

$$\psi_{k,j} = \left[\mathbf{x}_{k,j}^T, \theta_{k,j}^T, g(\mathbf{x}_{k,j}, \theta_{k,j})^T\right]^T. \tag{4.65}$$

In Eq. 4.65 $\mathbf{x}$ denotes the system state (e.g., pressure, saturations), θ denotes the static parameters (e.g., permeability, porosity) and $g(\mathbf{x}_{k,j}, \theta)$ denotes the simulated data, which in general can be nonlinear function of the state $\mathbf{x}$ variables and the static parameters θ. Note that in (4.65) the predicted data are explicitly included in the augmented state vector. This is a common approach in EnKF reservoir engineering applications, which allows to linearly relate predicted observations $\mathbf{y}$ to the augmented state vector ψ even in a nonlinear case, and still use the recursive KF scheme.
In the forecast step all the ensemble members are propagated forward to the next time when measurements are available

$$\psi_{k,j}^f = \mathbf{f}(\psi_{k-1,j}^a), \tag{4.66}$$

where $\mathbf{f}(\cdot)$ denotes the nonlinear forward modeling operator. In context of this research $\mathbf{f}(\cdot)$ stands for simulator of reservoir flow. The superscript a denotes analyzed (updated) ensemble member realization obtained according to

$$\psi_{k,j}^a = \psi_{k,j}^f + \mathbf{K}_k(\mathbf{y}_{k,j} - \mathbf{H}_k\psi_{k,j}^f), \tag{4.67}$$

where $\mathbf{K}_k$ is the ensemble Kalman gain, $\mathbf{H}_k = [\mathbf{0}, \mathbf{I}]$ is the measurement operator extracting predicted data from the ensemble state vector, $\mathbf{0}$ is a $N \times M$ matrix filled with zeros, and $\mathbf{I}$ denotes the $N \times N$ identity matrix. Burgers & Evensen (1998) showed that in order to obtain proper error covariance of the analyzed state, random perturbations must be added to the observations, i.e

$$\mathbf{y}_{k,j} = \mathbf{y}_k + \epsilon_j,\ j = 1, \ldots, N_e, \tag{4.68}$$

where ξ_j is a random perturbation drawn from the same distribution as the measurement error, i.e., zero-mean Gaussian with covariance matrix $\mathbf{C}_{y_k}$. The ensemble Kalman gain is analogous to (4.58) and is given by

$$\mathbf{K}_k = \mathbf{C}_{\Psi_k}^f \mathbf{H}_k^T (\mathbf{H}_k \mathbf{C}_{\Psi_k}^f \mathbf{H}_k^T + \mathbf{C}_{y_k})^{-1}, \tag{4.69}$$

but in this case the state covariance matrix is approximated from

$$\mathbf{C}_{\Psi_k}^f = \frac{\mathbf{L}_k \mathbf{L}_k^T}{N_e - 1}, \tag{4.70}$$

where

$$\mathbf{L}_k = \mathbf{\Psi}_k^f - \overline{\mathbf{\Psi}}_k^f = \mathbf{\Psi}_k^f(\mathbf{I} - \mathbf{1}_{N_e}), \tag{4.71}$$

and

$$\overline{\mathbf{\Psi}}_k^f = [\overline{\psi}_k^f, \overline{\psi}_k^f, \ldots, \overline{\psi}_k^f], \tag{4.72}$$

with

$$\overline{\psi}_k^f = \frac{1}{N_e}\sum_{j=1}^{N_e} \psi_{k,j}^f. \tag{4.73}$$

In Eq. (4.71), $\mathbf{I}$ is the $N_e \times N_e$ identity matrix and $\mathbf{1}_{N_e}$ is a $N_e \times N_e$ matrix with all elements equal to $1/N_e$. Using (4.70) the ensemble Kalman gain can be written as

$$\mathbf{K}_k = \mathbf{L}_k(\mathbf{H}_k\mathbf{L}_k)^T \left[(\mathbf{H}_k\mathbf{L}_k)(\mathbf{H}_k\mathbf{L}_k)^T + (N_e - 1)\mathbf{C}_{y_k}\right]^{-1}, \tag{4.74}$$

which typically is computationally more efficient because the state covariance matrix does not need to be stored.

Following Evensen (2007) it can be shown that the updated ensemble is a combination of the forecast ensemble members. To simplify the notation, we skip the time index k. Let us define the ensemble of innovation vectors as

$$\mathbf{Y}' = \mathbf{Y} - \mathbf{H}\mathbf{\Psi}^f, \tag{4.75}$$

where $\mathbf{Y} = [\mathbf{y}_1, \mathbf{y}_2, \ldots, \mathbf{y}_{N_e}]$ is a matrix holding the ensemble of perturbed measurements. Let

$$\mathbf{S} = \mathbf{H}\mathbf{L}, \tag{4.76}$$

and

$$\mathbf{M} = \mathbf{S}\mathbf{S}^T + (N_e - 1)\mathbf{C}_y. \tag{4.77}$$

Then, using (4.74), the update equation can be written as (Evensen 2007)

$$\begin{aligned}
\mathbf{\Psi}^a &= \mathbf{\Psi}^f + \mathbf{L}\mathbf{S}^T\left(\mathbf{S}\mathbf{S}^T + (N_e - 1)\mathbf{C}_y\right)^{-1}\mathbf{Y}' \\
&= \mathbf{\Psi}^f + \mathbf{\Psi}^f(\mathbf{I} - \mathbf{1}_{N_e})\mathbf{S}^T\mathbf{M}^{-1}\mathbf{Y}' \\
&= \mathbf{\Psi}^f\left(\mathbf{I} + (\mathbf{I} - \mathbf{1}_{N_e})\mathbf{S}^T\mathbf{M}^{-1}\mathbf{Y}'\right) \\
&= \mathbf{\Psi}^f\left(\mathbf{I} + \mathbf{S}^T\mathbf{M}^{-1}\mathbf{Y}'\right) \\
&= \mathbf{\Psi}^f\mathbf{X},
\end{aligned} \tag{4.78}$$

where $\mathbf{X} = \left(\mathbf{I} + \mathbf{S}^T\mathbf{M}^{-1}\mathbf{Y}'\right)$ is called the transformation matrix. In (4.78), Eq. (4.71) was used together with $\mathbf{1}_{N_e}\mathbf{S}^T \equiv \mathbf{0}$ (note that the ensemble mean is removed in 4.71). Equation (4.78) shows that the updated ensemble members are a combination of the forecasted ensemble members, and hence, by applying this result recursively in time, are the combination of the initial ensemble members. This clearly shows that the EnKF solution is searched for in the space spanned by the initial ensemble members. Thus, unless the true model is contained in this space it is not possible to obtain a true model solution from any combination of ensemble members. We will demonstrate this with a simplified example in Subsection 4.6.1.

4.5.5 Ensemble smoother

The Ensemble smoother (ES), introduced by van Leeuwen & Evensen (1996), differs from the EnKF by computing one global update in the time-space domain rather than performing recursive updates as the EnKF does. Let us define the ensemble matrix of a joint state from time t_0 to time t_m

$$\widetilde{\boldsymbol{\Psi}}^f = \begin{bmatrix} \boldsymbol{\Psi}_0^f \\ \boldsymbol{\Psi}_2^f \\ \vdots \\ \boldsymbol{\Psi}_m^f \end{bmatrix}. \tag{4.79}$$

In an analogous way as in (4.71), the ensemble perturbation matrix is defined as

$$\widetilde{\mathbf{L}} = \widetilde{\Psi}^f - \overline{\widetilde{\Psi}}^f = \widetilde{\Psi}^f(\mathbf{I} - \mathbf{1}_{N_e}). \tag{4.80}$$

The time-space ensemble of perturbed measurements is stored in

$$\widetilde{\mathbf{Y}} = \begin{bmatrix} \mathbf{Y}_1 \\ \mathbf{Y}_2 \\ \vdots \\ \mathbf{Y}_m \end{bmatrix}, \tag{4.81}$$

and the time-space measurement operator is given by

$$\widetilde{\mathbf{H}} = \begin{bmatrix} \mathbf{H}_1 \\ \mathbf{H}_2 \\ \vdots \\ \mathbf{H}_m \end{bmatrix}. \tag{4.82}$$

In analogy with (4.75), (4.76) and (4.77), the ensemble of innovation vectors

$$\widetilde{\mathbf{Y}}' = \widetilde{\mathbf{Y}} - \widetilde{\mathbf{H}}\widetilde{\boldsymbol{\Psi}}^f, \tag{4.83}$$

measurements of ensemble perturbations

$$\widetilde{\mathbf{S}} = \widetilde{\mathbf{H}}\widetilde{\mathbf{L}}, \tag{4.84}$$

and the matrix

$$\widetilde{\mathbf{M}} = \widetilde{\mathbf{S}}\widetilde{\mathbf{S}}^T + (N_e - 1)\widetilde{\mathbf{C}}_y \tag{4.85}$$

are defined, where $\widetilde{\mathbf{C}}_y$ is the error covariance matrix of all measurements from time t_0 to time t_m. Using this notation, the ES update equation can be expressed as

$$\begin{aligned} \widetilde{\boldsymbol{\Psi}}^a &= \widetilde{\boldsymbol{\Psi}}^f + \widetilde{\mathbf{L}}\widetilde{\mathbf{S}}^T \left(\widetilde{\mathbf{S}}\widetilde{\mathbf{S}}^T + (N-1)\widetilde{\mathbf{C}}_y\right)^{-1} \widetilde{\mathbf{Y}}' \\ &= \widetilde{\boldsymbol{\Psi}}^f + \widetilde{\boldsymbol{\Psi}}^f(\mathbf{I} - \mathbf{1}_{N_e})\widetilde{\mathbf{S}}^T\widetilde{\mathbf{M}}^{-1}\widetilde{\mathbf{Y}}' \end{aligned}$$

$$\begin{aligned} &= \widetilde{\boldsymbol{\Psi}}^f \left(\mathbf{I} + (\mathbf{I} - \mathbf{1}_{N_e}) \widetilde{\mathbf{S}}^T \widetilde{\mathbf{M}}^{-1} \widetilde{\mathbf{Y}}' \right) \\ &= \widetilde{\boldsymbol{\Psi}}^f \left(\mathbf{I} + \widetilde{\mathbf{S}}^T \widetilde{\mathbf{M}}^{-1} \widetilde{\mathbf{Y}}' \right) \\ &= \widetilde{\boldsymbol{\Psi}}^f \widetilde{\mathbf{X}}. \end{aligned} \tag{4.86}$$

4.5.6 Discussion

For linear systems and Gaussian assumptions about the noise processes, KF, EnKF and ES will result in the same solution for the same inputs and an infinitely large number of ensemble members (Evensen 2007). For nonlinear problems, the KF is not suitable and the EnKF and the ES can be used. In practice, their application provides approximations to the optimal solution because of the limited number of ensemble members that can be afforded. Furthermore, in case of highly non-Gaussian (e.g., multimodal, skewed) parameter distribution, the probability density function (pdf) of the final estimate may converge to a Gaussian-like pdf because only two statistical moments, i.e., the mean and the variance, are used in the update step. For that reason, various transformations (e.g., logarithmic to the permeability field) are applied to assure that the prior parameter pdf is close to Gaussian. Other alternative is to use particle filters, which approximate the evolution of the complete parameter pdf (see, e.g., van Leeuwen 2009, Vossepoel & van Leeuwen 2007). However, many particles (ensemble members) may be required (often more than 1000) what for large and complex models is (nowadays) computationally expensive.

Another issue in the use of EnKF is the inconsistency problem, which may arise when the static and dynamic variables are combined together in a state vector. By consistency it is meant that the state estimates (e.g., pressures, saturations) obtained using the filter are the same as those we would obtain if we re-run the model with the corresponding static parameter estimates (e.g. permeability, porosity) from time zero with a given initial state. The limited number of ensemble members and the linear EnKF update step may not always guarantee that the physically meaningful relationship between the static and dynamic variables is preserved after the update (see, e.g., Emerick & Reynolds 2011). This means, for instance, that resulting permeability estimates may not be physically consistent with the estimates of pressure and/or saturation. Furthermore, negative values of pressure or saturation can be obtained. To mitigate this problem, the reservoir simulator can be restarted from time zero with the latest estimates of the static parameters to compute new realizations of the dynamic variables (Thulin et al. 2007). In this case only the static parameters are updated. This approach solves the consistency problem, but it may be computationally expensive for complex and large-scale models.

4.6 The common framework

In the previous section we discussed two approaches for the estimation of uncertain model parameters (or system state). In the first one, more traditional approach based on the Tikhonov regularization concept, the estimates of uncertain parameters are determined in the inversion process using available observations and, to constrain

the solution, some sort of mathematical regularization. Usually, no distinction is made between static parameters and dynamic variables and the unknowns are simply called model parameters. Thus, the model parameters to be determined can be, e.g., values of porosity or density for every grid cell of a reservoir model. The second approach, called data assimilation (or computer-assisted history matching), estimates a system state by combining information provided by available measurements and the physical model (here, reservoir flow simulator) forecast. Thus, the term ”model” has a broader meaning here: it refers not only to a set of uncertain parameters (as in the classical inversion), but also includes the physics (discretized flow equations, boundary conditions and constraints) of phenomena under investigation. Usually, a distinction is made between state variables and static parameters. Depending on the implementation approach, only the static parameters can be estimated whereas values of the time-variable state variables (pressures, saturations, densities) are simulated from the model given the updated parameters or both, the state variables and static parameters, can be estimated simultaneously.
In this section we will try to show some of the similarities and differences between these two approaches, especially in the context of regularization.

Let us recall the MAP estimate of $\mathbf{x}$ derived within the Bayesian framework

$$\hat{\mathbf{x}} = \mathbf{x}_0 + \mathbf{C}_x\mathbf{A}^T(\mathbf{C}_y + \mathbf{A}\mathbf{C}_x\mathbf{A}^T)^{-1}(\mathbf{y} - \mathbf{A}\mathbf{x}_0). \tag{4.87}$$

For a comparison the generalized least-square solution following from minimization of the Tikhonov parametric functional (4.20) is

$$\hat{\mathbf{x}} = \mathbf{x}_0 + (\mathbf{A}^T\mathbf{W}_y^T\mathbf{W}_y\mathbf{A} + \alpha\mathbf{W}_x^T\mathbf{W}_x)^{-1}\mathbf{A}^T\mathbf{W}_y^T\mathbf{W}_y(\mathbf{y} - \mathbf{A}\mathbf{x}_0). \tag{4.88}$$

If we define

$$\mathbf{P}_x = \alpha\mathbf{W}_x^T\mathbf{W}_x, \tag{4.89}$$

and

$$\mathbf{P}_y = \mathbf{W}_y^T\mathbf{W}_y, \tag{4.90}$$

then (4.88) can be written as

$$\hat{\mathbf{x}} = \mathbf{x}_0 + (\mathbf{A}^T\mathbf{P}_y\mathbf{A} + \mathbf{P}_x)^{-1}\mathbf{A}^T\mathbf{P}_y(\mathbf{y} - \mathbf{A}\mathbf{x}_0). \tag{4.91}$$

Using again the matrix identities (4.12), the Eq. (4.91) can be expressed as

$$\hat{\mathbf{x}} = \mathbf{x}_0 + \mathbf{P}_x\mathbf{A}^T(\mathbf{P}_y + \mathbf{A}\mathbf{P}_x\mathbf{A}^T)^{-1}(\mathbf{y} - \mathbf{A}\mathbf{x}_0). \tag{4.92}$$

Finally, let us recall the Kalman filter update equation

$$\mathbf{x}_k^a = \mathbf{x}_k^f + \mathbf{C}_{x_k}^f\mathbf{H}_k^T(\mathbf{C}_{y_k} + \mathbf{H}_k\mathbf{C}_{x_k}^f\mathbf{H}_k^T)^{-1}(\mathbf{y}_k - \mathbf{H}_k\mathbf{x}_k^f), \tag{4.93}$$

where k is the time index.
From the above we can see that the generalized least-squares estimate can be written in the same form as the MAP estimate derived within the Bayesian framework. Note however, that in these cases regularization of the solution is performed from a

different point of view, i.e., in Eq. (4.92) the matrix $\mathbf{P}_x$ acts purely as a numerical operator and takes various forms depending on the stabilizer used, whereas the model covariance matrix $\mathbf{C}_x$ in Eq. (4.87), acting also as regularization operator, has a statistical meaning. The Kalman filter, and hence EnKF and ES, are closely related to the statistical regularization concept. In the EnKF and ES, however, the model (or state) covariance matrix is not explicitly specified, but is approximated from the prior ensemble. We showed that in this case the true solution is searched for in the space spanned by the prior ensemble members, which provide a regularization of the solution. We will demonstrate this with a simple example in Subsection 4.6.1.

4.6.1 Example

A 2D synthetic gas-reservoir model extending from 0 to 3000 m in both the x- and y-directions with a uniform 75 × 75 × 50 m grid-cell size is considered. The distance from the reservoir top to the free surface is 1700 m. The reservoir gas production causes pressure drop and water influx through the western reservoir boundary (Fig. 4.8a). Because the reservoir permeability (Fig. 4.8b) is heterogenous, the water front (Fig. 4.8a) does not propagate uniformly. Further details of this model setup will be given in Chapter 6. Here, we consider the problem of the reservoir density-change estimation (and hence, implicitly, the water-front position) given observations of temporal gravity variations after 1500 days of the gas production. There are in total 1600 uncertain density change values to determine (40×40 model grid size) and 900 gravity observations available, separated by about 166 m in x- and y-direction. A zero-mean Gaussian noise with 5μGal standard deviation is added to contaminate the synthetic gravity data. Three approaches will be used to estimate the density variation, namely, the unregularized least-squares model fit, the focusing inversion, and the ensemble Kalman filter.

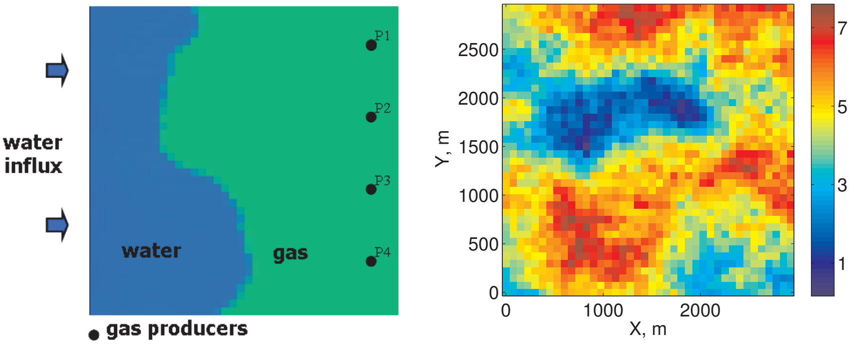

(a) reservoir saturation at 3500 days **(b)** permeability, log of mdarcy

Figure 4.8: The reservoir model permeability field and the corresponding saturation at 3500 days. Initially (at time t=0) the reservoir is saturated with gas only.

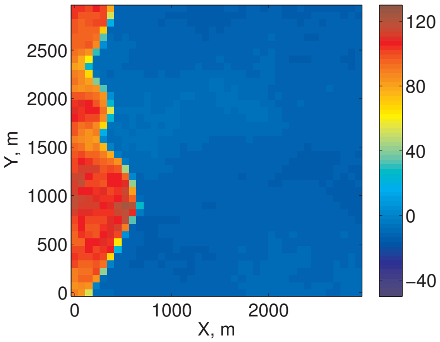

Figure 4.9: Density change (kg/m^3) between time t=0 and t=1500 days for the reference model. The negative density variation is caused by gas takeout and the positive density variation by water influx.

The ensemble Kalman filter setup

The use of the ensemble Kalman filter requires the specification of the initial ensemble which spans the parameter space where the solution is searched for. To generate the ensemble representing the temporal density variation, we apply the following procedure. A set of 100 different realizations of the permeability field is used as input to the physical model of the gas reservoir which, subsequently, is run forward for 1500 days using the reservoir simulator. How the initial ensemble of different permeability fields was created will be explained in detail in Chapter 6. An example of the generated permeability field realizations is shown in Fig. 4.10 and an example of the corresponding density changes is shown in Fig. 4.11.

The focusing inversion setup

Similarly as in the previous section, we apply both the minimum support and the minimum gradient support inversion. In both cases, the focusing parameter β is set equal to 120 kg/m^3 $\times 10^{-2}$ i.e., to about 1% of the density change induced by the water/gas replacement. Again the re-weighted regularized conjugate gradient scheme (4.41) is applied with adjusting the regularization parameter α at every iteration using condition (4.43).

Density change estimates

The estimates of density change are shown in Fig. 4.12. To evaluate quantitatively the results we first estimate the water front position. They estimates are derived from the density change maps by reading the contour line with the specified density change threshold. In this study we assume that a threshold of 20 kg/m^3 defines the boundaries of the water front. Susequently, the RMSE of the water front position is calculated.

The unregularized least-squares estimate is significantly smoother and far from the true model (shown in Fig. 4.9) compared to the other cases. The front position RMSE is 581 m in this case. The minimum support and the minimum gradient

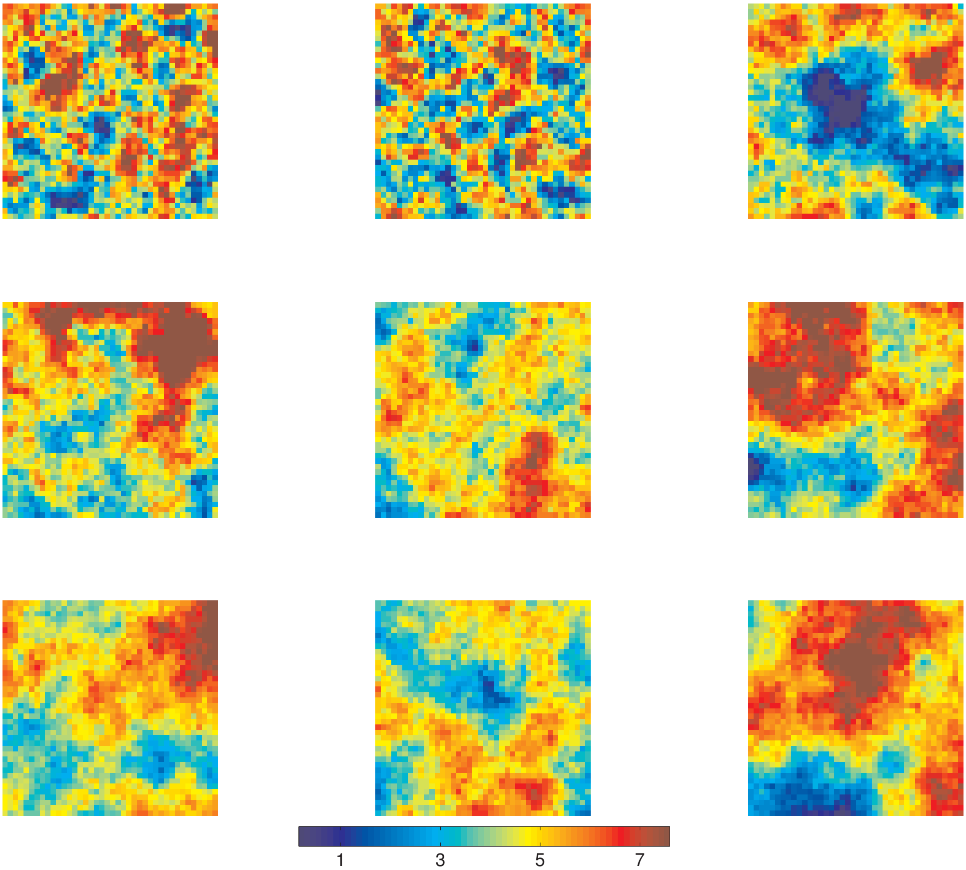

Figure 4.10: Example of the initial permeability fields (natural logarithm scale, mdarcy).

support solutions are fairly similar with the RMSE of 325 m and 316 m, respectively. Compared to the EnKF solution (mean of the 100 updated ensemble members), which gives the lowest front position RMSE of 218 m, the focusing inversion results are slightly overshooting the reference density change in the southern part of the reservoir. Because the EnKF is based on the Monte Carlo approach it provides additionally uncertainty estimates for the solution which are shown in Fig. 4.13. We can see that the standard deviation (std) of the density change estimate is reduced by about 40% compared to the initial ensemble uncertainty spread.

The case with incorrect initial ensemble

We showed in (4.78) that the EnKF solution (the updated ensemble) is searched for in the space spanned by the initial (prior) ensemble members, i.e., it is a linear combination of them. This provides not only very strong regularization of the EnKF inversion but also means that it may not be possible to obtain a reasonable solution if the initial ensemble members are specified incorrectly. We will demonstrate this with a simple example applying some changes to the current experiment setup. Previously,

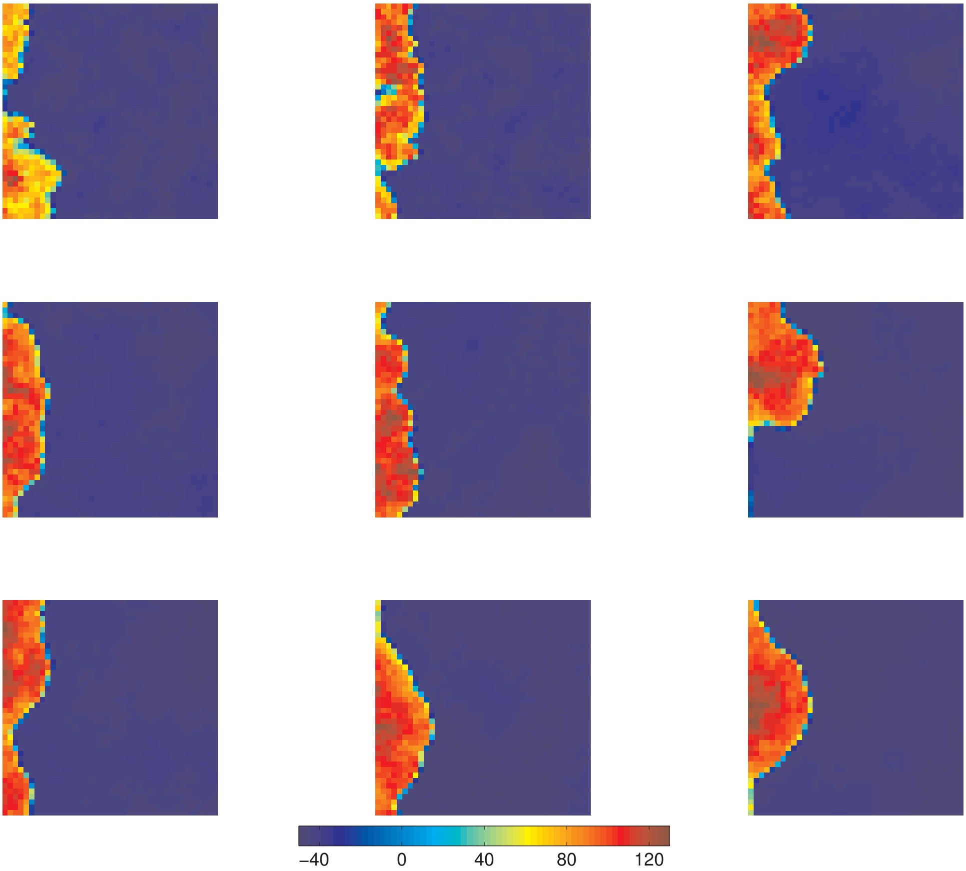

Figure 4.11: Examples of the initial ensemble members (density change in kg/m^3 from time t=0 to time t=1500 days) used in the EnKF history matching. The density change is obtained by running the reservoir simulator model with different permeability field (shown in Fig. 4.10) for each ensemble member.

it was assumed that the aquifer water can enter the reservoir via the western reservoir boundary. All the prior ensemble members were constrained to this assumption while generating initial predictions of the subsurface density changes. Suppose now that we assume the water influx from the South while the reference model is unchanged, i.e., water enters the reservoir from the West. The example of ”incorrect” prior ensemble members is show in Fig. 4.14 and the corresponding subsurface density change estimate in Fig. 4.15. It’s clear that in this case it is not possible to obtain accurate results, because as it is schematically shown in Fig. 4.15b, the true solution is not contained in the space spanned by the initial ensemble members.

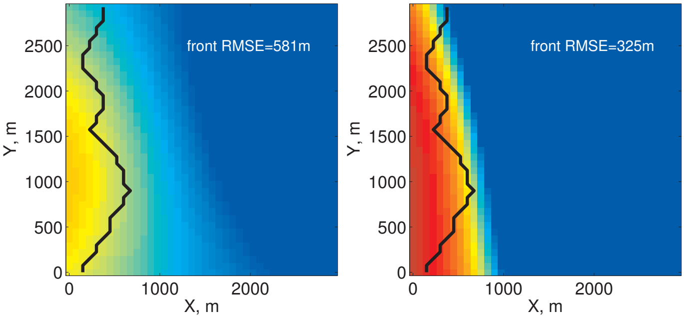

(a) least-squares **(b)** minimum support

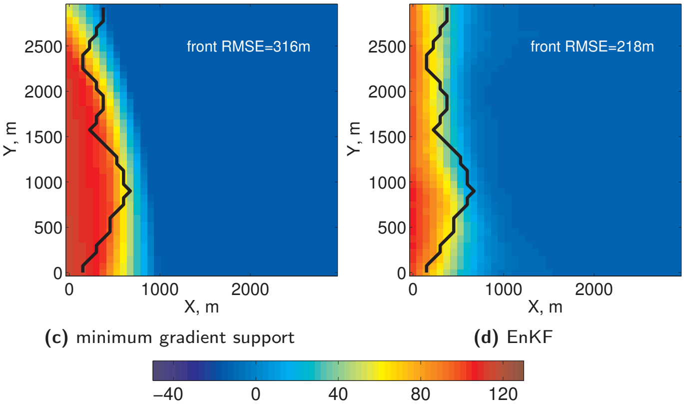

(c) minimum gradient support **(d)** EnKF

Figure 4.12: The reservoir density (kg/m^3) change estimates (from t=0 to t=1500 days) caused by reservoir gas production and water influx. The black contour shows the true water front position.

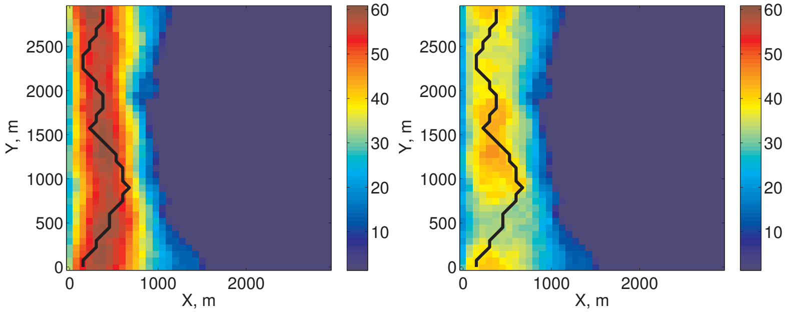

(a) density change std., initial ensemble **(b)** density change std., updated ensemble

Figure 4.13: Standard deviation of the density change estimates (kg/m^3) for the initial and the updated ensemble members.

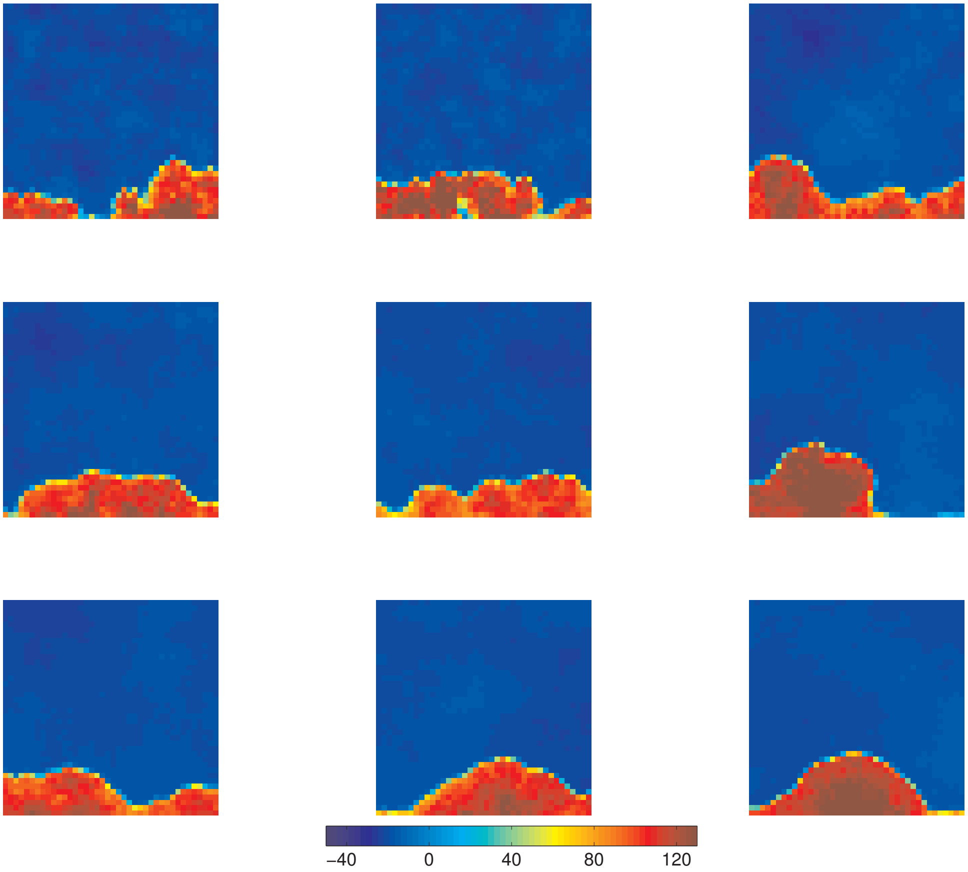

Figure 4.14: Examples of the incorrect prior ensemble members (density change in kg/m^3 from time t=0 to time t=1500 days) used in the EnKF history matching.

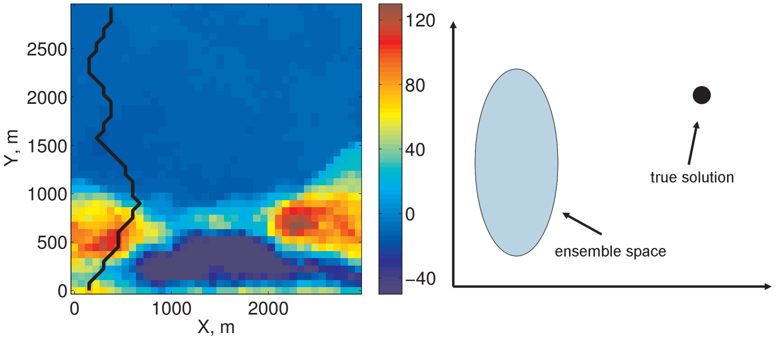

(a) EnKF solution

(b) schematic illustration of incorrect initial ensemble space

Figure 4.15: Example of the gravity inversion for reservoir density change estimate (kg/m^3) in case of incorrect prior ensemble members. The black curve shows the true water front position.

4.7 Bias-aware data assimilation

4.7.1 Introduction

A frequent assumption in reservoir engineering applications of data assimilation is that there are no model errors and the measurement errors are purely random, typically drawn from a zero-mean Gaussian distribution. The first assumptions implies that for a set of correct input parameters the true signal can be predicted perfectly by running the numerical model. The second assumption implies that there is no systematic component in the measurement noise.

However, the numerical model even for perfectly correct input parameters may not be able to accurately simulate the true data. Model errors may originate from e.g., too coarse parametrization (too large grid blocks) or linearization and numerical approximations applied to solve a system of physical equations. Another source of errors relates to the unrepresented model physics and poorly known boundary conditions, such as, e.g., aquifer support. Therefore, the model errors can arise both as random as well as systematic. Similarly, errors in measurements may have different origins and some of them are, e.g., data processing or influence of the environmental processes. In Chapter 3 of the thesis we have shown that gravimetric observations can be affected by spatio-temporal variations of groundwater which can add a correlated signal to the measured gravity variation.

In data assimilation a systematic part of the model or the measurement errors is called a bias. Dee & Da Silva (1998) showed that the Kalman filtering scheme for any Kalman gain **K** (see, e.g., Eq. 4.58) will result in a biased analysis if the model and/or observations are biased. On the other hand, the influence of a bias on analysis results can be large, especially in case of severely ill-posed problems. Therefore, there is a need for bias-aware data assimilation schemes where systematic error components are taken into account properly.

Various authors have investigated bias estimation in data assimilation framework. Jaźwinski (1970) proposed the state augmentation approach for model bias estimation, i.e., the model bias is estimated simultaneously with the state variables. Friedland (1969) introduced an alternative approach where the bias estimation is decoupled from the state estimation and showed that it is algebraically equivalent to the Kalman filter for the augmented system. Dee & Da Silva (1998) extended the work of Friedland to the sequential bias estimation and state correction for the bias influence. De and Da Silva discussed extensively estimation of model bias. Recently, Lea et al. (2008) used the Bayesian formulation to derive an analysis scheme for a joint estimation of observation and model bias in sequential data assimilation. This scheme will be introduced in this chapter. For an overview of general bias estimation theory see, e.g., Dee (2005).

The information about the presence of bias can be obtained from innovations, i.e., a difference between the model predictions of observations and the actual observations (Ménard 2010)

$$\langle \mathbf{y} - \mathbf{H}\mathbf{x}^f \rangle, \tag{4.94}$$

where $\mathbf{y}$ denotes the observations, $\mathbf{H}$ is the measurement operator, $\mathbf{x}^f$ denotes the forecasted state and $\langle \cdot \rangle$ denotes the mean. The non-zero mean innovations indicate the presence of bias. However, they do not distinguish the source of a bias, therefore additional knowledge is needed to discriminate the bias origin which can be the model, the observations or both. The constraints on the bias can be incorporated through the prior information about the possible source of bias and its characteristics. In next section we introduce the bias-aware data assimilation methodology following Ménard (2010).

4.7.2 Bias-aware assimilation scheme

Let us introduce first the notation for the observation and the model bias

$$\begin{aligned} \mathbf{x}^f &= \mathbf{x}^t + \mathbf{e}^t + \varepsilon^f \\ \mathbf{y} &= \mathbf{H}\mathbf{x}^t + \mathbf{b}^t + \varepsilon^o \\ \mathbf{e}^f &= \mathbf{e}^t + \varepsilon^e \\ \mathbf{b}^f &= \mathbf{b}^t + \varepsilon^b, \end{aligned} \tag{4.95}$$

where $\mathbf{x}^f$ is the forecasted state, $\mathbf{x}^t$ is the true state, $\mathbf{e}^t$ is the true model bias, ε^f are the random forecast errors of the state with covariance matrix $\mathbf{C}_x^f$, $\mathbf{y}$ denotes the observations, $\mathbf{H}$ is the measurement operator, $\mathbf{b}^t$ is the true observation bias, ε^o is the random measurement noise with covariance matrix $\mathbf{C}_y$, $\mathbf{e}^f$ is the forecasted model bias, ε^e are the random errors of model bias forecast with covariance matrix $\mathbf{Q}_e$, $\mathbf{b}^f$ is the observation bias forecast, $\mathbf{b}^t$ is the true observation bias and ε^b denotes the random errors of the observation bias forecast with covariance matrix $\mathbf{S}_b^f$.
The following three assumptions are needed to derive analysis equations in the presence of both the observation and the model bias (see, e.g., Ménard 2010)

- the observations $\mathbf{y}$ are independent of the model bias $\mathbf{e}$, i.e.

$$P(\mathbf{y}|\mathbf{x}, \mathbf{b}, \mathbf{e}) = P(\mathbf{y}|\mathbf{x}, \mathbf{b}), \tag{4.96}$$

- the model state $\mathbf{x}$ is independent of the observation bias $\mathbf{b}$, i.e.

$$P(\mathbf{x}|\mathbf{b}, \mathbf{e}) = P(\mathbf{x}|\mathbf{e}), \tag{4.97}$$

- the model bias $\mathbf{e}$ is independent of the observation bias $\mathbf{b}$, i.e.

$$P(\mathbf{b}, \mathbf{e}) = P(\mathbf{e}|\mathbf{b})P(\mathbf{b}) = P(\mathbf{b})P(\mathbf{e}), \tag{4.98}$$

where P denotes the probability density function.
The above assumptions are used to find the maximum a posteriori (MAP) estimate of the state, the observation and the model bias given available observations and a priori information about the state and the biases. Using the Bayes' theorem

$$P(\mathbf{x}, \mathbf{b}, \mathbf{e}|\mathbf{y}) = \frac{P(\mathbf{y}|\mathbf{x}, \mathbf{b}, \mathbf{e})P(\mathbf{x}, \mathbf{b}, \mathbf{e})}{P(\mathbf{y})}. \tag{4.99}$$

and

$$P(\mathbf{x},\mathbf{b},\mathbf{e}) = P(\mathbf{x}|\mathbf{b},\mathbf{e})P(\mathbf{b}|\mathbf{e})P(\mathbf{e}). \tag{4.100}$$

Using (4.100) and the assumptions (4.96)-(4.98) the expression (4.99) reduces to

$$P(\mathbf{x},\mathbf{b},\mathbf{e}|\mathbf{y}) = \frac{P(\mathbf{y}|\mathbf{x},\mathbf{b})P(\mathbf{x}|\mathbf{e})P(\mathbf{b})P(\mathbf{e})}{P(\mathbf{y})}. \tag{4.101}$$

Under the Gaussian assumptions for the noise processes the sequential formulation (the time index is skipped) of the solution for (4.101) is given by (for derivation details see Ménard 2010)

$$\begin{aligned} \mathbf{x}^a &= \mathbf{x}^f - \mathbf{e}^a + \mathbf{K}\left[\mathbf{y} - \mathbf{b}^a - \mathbf{H}\left(\mathbf{x}^f - \mathbf{e}^a\right)\right], && (4.102)\\ \mathbf{K} &= \mathbf{C}_x^f\mathbf{H}^T\left(\mathbf{H}\mathbf{C}_x^f\mathbf{H}^T + \mathbf{C}_y\right)^{-1}, && (4.103) \end{aligned}$$

which requires the knowledge of analyzed bias estimates $\mathbf{e}^a$ and $\mathbf{b}^a$. The model bias estimate $\mathbf{e}^a$ is obtained from

$$\begin{aligned} \mathbf{e}^a &= \mathbf{e}^f - \mathbf{L}\left[\mathbf{y} - \mathbf{b}^a - \mathbf{H}\left(\mathbf{x}^f - \mathbf{e}^f\right)\right], && (4.104)\\ \mathbf{L} &= \mathbf{Q}_e^f\mathbf{H}^T\left(\mathbf{H}\mathbf{C}_x^f\mathbf{H}^T + \mathbf{H}\mathbf{Q}_e^f\mathbf{H}^T + \mathbf{C}_y\right)^{-1}, && (4.105) \end{aligned}$$

and the observation bias estimate from

$$\begin{aligned} \mathbf{b}^a &= \mathbf{b}^f - \mathbf{M}\left[\mathbf{y} - \mathbf{b}^f - \mathbf{H}\left(\mathbf{x}^f - \mathbf{e}^f\right)\right], && (4.106)\\ \mathbf{M} &= \mathbf{S}_b^f\left(\mathbf{H}\mathbf{C}_x^f\mathbf{H}^T + \mathbf{H}\mathbf{Q}_e^f\mathbf{H}^T + \mathbf{C}_y + \mathbf{S}_b^f\right)^{-1}. && (4.107) \end{aligned}$$

This coupled system is solved by first estimating the observation bias with (4.106) then by updating the model bias with (4.104) and finally using this estimates to update the state estimate with (4.102).

Further in the thesis we will use the ensemble formulation for the scheme (4.102)-(4.106). This means that apart from the state covariance matrix $\mathbf{C}_x^f$ the bias covariance matrices $\mathbf{Q}_e^f$ and $\mathbf{S}_b^f$ will be approximated using a finite set of N_e ensemble realizations

$$\mathbf{e}_k^f = \left[e_{k,1}^f, e_{k,2}^f, \ldots, e_{k,N_e}^f\right], \tag{4.108}$$

and

$$\mathbf{b}_k^f = \left[b_{k,1}^f, b_{k,2}^f, \ldots, b_{k,N_e}^f\right], \tag{4.109}$$

with

$$\begin{aligned} e_{k,j}^f &= \mathbf{f}_e(e_{k-1,j}^a), && (4.110)\\ b_{k,j}^f &= \mathbf{f}_b(b_{k-1,j}^a), && (4.111) \end{aligned}$$

where $\mathbf{f}_e$ and $\mathbf{f}_b$ denote some function describing the model and the observation bias evolution, respectively and $j = 1, \ldots, N_e$. The model bias covariance matrix is approximated from

$$\mathbf{Q}_{e_k}^f = \frac{\mathbf{L}_{e_k}\mathbf{L}_{e_k}^T}{N_e - 1}, \tag{4.112}$$

where

$$\mathbf{L}_{e_k} = \mathbf{e}_k^f(\mathbf{I} - \mathbf{1}_{N_e}), \tag{4.113}$$

an analogously the observation bias covariance matrix

$$\mathbf{S}_{b_k}^f = \frac{\mathbf{L}_{b_k}\mathbf{L}_{b_k}^T}{N_e - 1}, \tag{4.114}$$

where

$$\mathbf{L}_{b_k} = \mathbf{b}_k^f(\mathbf{I} - \mathbf{1}_{N_e}). \tag{4.115}$$

In (4.113) and (4.115) $\mathbf{I}$ is $N_e \times N_e$ identity matrix and $\mathbf{1}_{N_e}$ is $N_e \times N_e$ matrix with all elements equal to $1/N_e$.

An example of application of this methodology to estimate both the observation and the model bias in gravity data assimilation will be shown in Chapter 8 of the thesis.

4.8 Summary

Focusing inversion and two data assimilation methods, namely the ensemble Kalman filter and the ensemble smoother, were discussed in this chapter.

Focusing inversion belongs to the family of mathematical regularization techniques based on the Tikhonov regularization concept. In focusing inversion, constraints to the solution are incorporated using specific stabilizing functionals, namely the minimum support and the minimum gradient support stabilizers, which promote focused solutions with sharp transitions in parameter values. It requires tuning/estimation of the regularization parameter α and the focusing parameter β, which balance the tradeoff between the model fit to the observations and the strength of regularization. Focusing inversion can be used for both linear and nonlinear problems. However, in the nonlinear case one needs to determine the tangent linear operator. For large scale problems this can become computationally expensive. Furthermore, no explicit distinction is made between time-dynamic and static parameters, and all the unknowns are treated in the same way regardless of their nature. The unknowns are simply called parameters, which are estimated from the available observations at a particular moment in time. The estimate obtained at a given moment does not explicitly influence the estimates obtained later.

In the EnKF and ES, which belong to the class of ensemble data assimilation techniques, regularization of the solution is performed in a statistical sense, embedded within the Bayesian framework. The state covariance matrix, which acts as a regularization operator, is approximated from a finite set of ensemble members, which span the space in which the solution is searched for. The EnKF and the ES are suitable methods for nonlinear problems and parameter/state estimation of time-dynamic nature. A numerical model of the phenomenon under investigation, acting as a forward operator, is, however, needed to simulate synthetic data and to propagate forward the ensemble members. The updated estimates combine the model predictions with the information contained in the assimilated observations. Usually, a distinction is made between state variables and static parameters. Depending on the implementation approach, only the static parameters (e.g., porosity and permeability) can be estimated whereas the values of the time-variable states (pressures, saturations, and densities) are simulated from the model given the updated parameters, or the state variables and the static parameters can be estimated simultaneously. There is no need to linearize the problem because the state covariance matrix is approximated from the evolving ensemble. In the EnKF the ensemble members are continuously updated whenever new observations are available. Hence, the estimate obtained at a given moment influences the estimate at a later moment. Similarly in the ES, where all the data are matched simultaneously, the previous solution is affected by the future observations, because of the cross correlations between the parameter/state and the observations acquired at different moments in time. Furthermore, provided that the prior information about the source and the characteristic of the systematic errors (called bias) in the model and/or the observations is available, the data assimilation scheme can be extended with the explicit estimation-correction scheme of these errors. Both the focusing inversion method and the EnKF and the ES are attractive inversion/estimation methods and they will be used throughout the thesis.

Chapter 5

Gravimetric monitoring of a Carbonate Field in the North of Oman: a feasibility study

This Chapter summarizes findings of the feasibility study on gravimetric monitoring of the Thermally-Assisted Gas-Oil Gravity Drainage (TA-GOGD) process at a carbonate field in the North of Oman. The monitoring objective is time-evolution of the heat-front position. The study includes quantification of the expected changes in the temporal gravity signal resulting from the reservoir mass redistribution induced by the TA-GOGD process. These estimates are based on the synthetic data predicted from the reservoir model of realistic complexity developed for the field. Furthermore, using historical groundwater measurements, the estimates of noise in gravity data related to the specific hydrological conditions in the field are considered. It is shown that hydrological signals can be a very significant source of noise affecting the gravimetric monitoring of the field. Therefore, it is investigated under which conditions the hydrological influences can be minimized. For this purpose a set of hypothetical scenarios is evaluated, where various densities of the water-level observation wells are simulated. Finally, we perform a focusing inversion of the gravimetric observations and analyze the achievable accuracy of heat-front position estimates under the specific hydrological conditions.
Major findings included in this chapter have been submitted for a publication (Glegola et al. n.d.).

5.1 The carbonate field in the North of Oman

The field is a highly fractured carbonate containing heavy (16°API gravity) and viscous (200-220 cP) oil. The reservoir is a very shallow (∼300 m below the surface), dome-shaped structure (Fig. 5.1) of about 6 km × 3 km extent. It has high porosity of about 30% and low matrix permeability of 5-15 milidarcy (Hartemink et al. 1997). The main reservoir production mechanism is Gas-Oil Gravity Drainage.

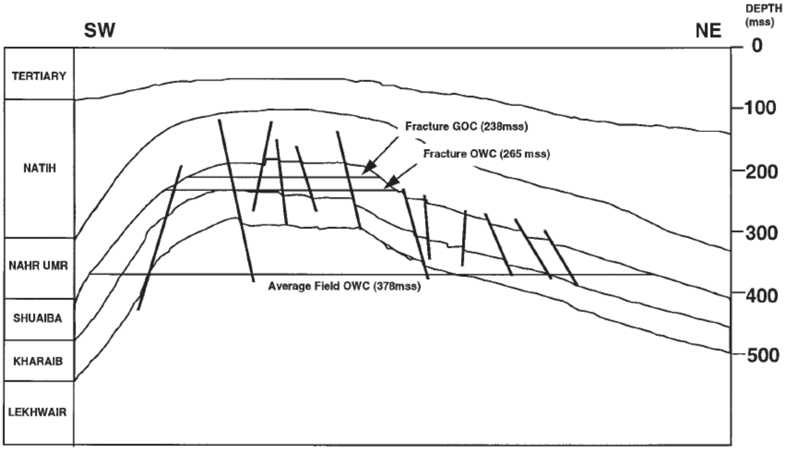

Figure 5.1: Cross-section of the considered field in Oman, after Hartemink et al. (1997).

5.1.1 Gas-Oil Gravity Drainage (GOGD)

GOGD is a hydrocarbon recovery process applied to fractured reservoirs, particulary carbonates. It is based on the density difference between oil and gas and a natural mechanism where gravity is a major driving force. The GOGD process occurs when gas is introduced into a highly fractured reservoir formation and a fracture gas cap is established. When the oil in the matrix is above the fracture gas-oil contact (FGOC) a lack of hydrodynamic equilibrium causes gravity forces to drain the oil down the matrix (see Fig. 5.2). In the absence of vertical flow barriers the oil drainage takes place entirely down the matrix until it reaches the location of the FGOC. As a result an oil rim is established in the fracture system from which the oil can be produced (Penney et al. 2007). The mathematical description of the GOGD process can be found in Hagoort (1980).

The effectiveness, i.e., the oil drainage rates of the GOGD process strongly depends on the properties of oil and the properties of the reservoir rock. Heavy and viscous oils will be drained at lower rates. Similarly, low matrix permeability may slow down the oil drainage. Finally, density and connectivity of the fracture network have a strong impact on the overall drainage distribution. In the field example considered in this study oil is relatively dense and viscous and, therefore, low production rates from the GOGD process were achieved. Consequently, the GOGD was expected to recover only 3-5% of the oil in place. Therefore, to enhance the field production Thermally-Assisted GOGD (TA-GOGD) has been implemented.

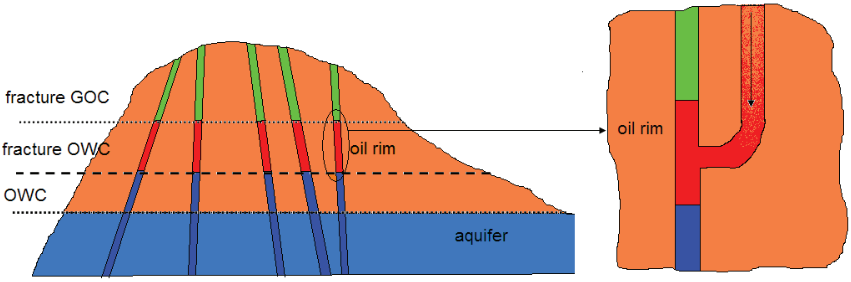

Figure 5.2: Schematic view of the GOGD process, after Penney et al. (2007). The green color denotes gas, the red is oil and the blue denotes water. GOC stands for Gas-Oil Contact and OWC stands for Water-Oil Contact.

5.1.2 Thermally-Assisted Gas-Oil Gravity Drainage (TA-GOGD)

In the TA-GOGD process, steam is injected to heat up the oil in the matrix (Fig. 5.3) and to accelerate the GOGD recovery. The heat is transferred from fractures into the rock matrix by conduction. The steam releases its heat, condenses, and flows down the fractures as hot water. The heated oil becomes less viscous and drains at accelerated rates, where the rate yield is proportional to the viscosity reduction. An increase in the reservoir temperature results in the development of gas volumes in the matrix. The gas originates from the reservoir oil and the connate water vaporization. Another important effect induced by the heat transfer is thermal expansion of the reservoir fluids. In the result some of the oil is squeezed out of the matrix into the fracture system (Boerrigter & van Dorp 2009, Bychkov et al. 2008).
In the field example considered here, heating the matrix rock through the steam injection is expected to increase the GOGD rate by a factor of about 100 (Habsi et al. 2008). The full field scale TA-GOGD is the world's first project of this type.

5.2 Temporal gravity variations

5.2.1 Gravity field variations caused by TA-GOGD

The effectiveness of the TA-GOGD strongly depends on the fracture density and distribution. The fractures are means to provide steam and, hence, heat into the reservoir, which determines to a large extent the oil drainage rates and drainage areas. As a result of the TA-GOGD process application, the movable oil in the matrix will be replaced by a mixture of steam and hydrocarbon gases (Fig. 5.4). This will create

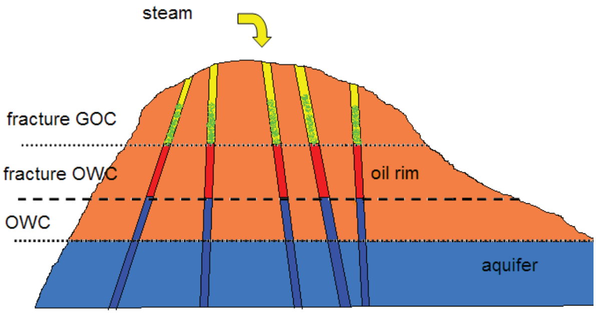

Figure 5.3: Schematic view of the TA-GOGD process, after Penney et al. (2007). The yellow color denotes steam, the green color denotes gas, the red is oil and the blue denotes water. GOC stands for Gas-Oil Contact and OWC stands for Water-Oil Contact.

a negative variation in the reservoir formation density since the oil is denser than the steam and hydrocarbon gases. Consequently, the reservoir density change will lead to local gravity field variations. Therefore, measurements of the temporal gravity changes could be used to make inference about density/mass redistribution due to TA-GOGD.

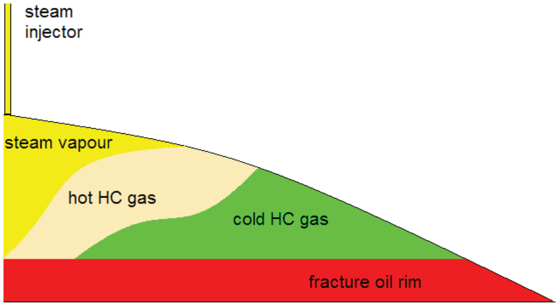

Figure 5.4: Schematic illustration of the distribution of injected steam, after Penney et al. (2007).

To estimate the time-lapse gravity variations resulting from the field production with TA-GOGD we perform a numerical study. We use numerical model outputs provided by the field operating asset. The synthetic data are obtained by running forward a realistic complexity reservoir model, consisting of 157×102×9 cells, which was developed for the field. The model simulates steam injection and oil production and is propagated forward for a period of 10 years, i.e., from year 2010 to year 2020. After every 5 years of the simulation, the predicted reservoir phase densities and the saturations are extracted. The time evolution of the reservoir phase saturation is shown in Fig. 5.5. As a result of the oil drainage caused by the TA-GOGD process, a significant gas cap with a fairly regular, circular shape at the top of the reservoir structure will develop. The gas saturation will gradually increase in time and will be distributed mostly in the top 4 reservoir layers. The gas/oil displacement will lead to the time-lapse density changes with a predicted maximum amplitude after 10 years

of reservoir production of about 120 kg/m^3 (Fig. 5.6).
The other data provided by the field asset team for the simulation of the gravity signal include the reservoir model porosity, the reservoir model grid geometry, and the elevation of the surface.

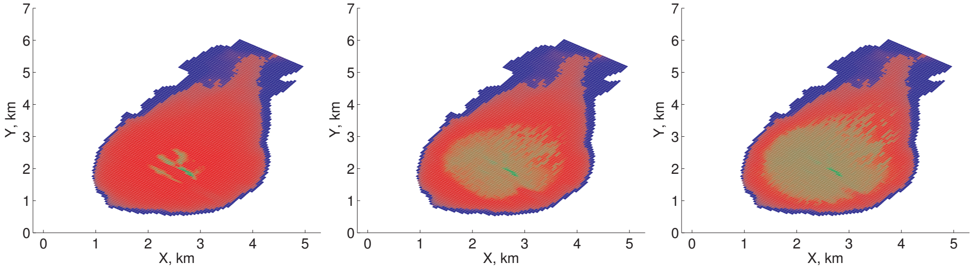

(a) year 2010 **(b)** year 2015 **(c)** year 2020

Figure 5.5: The reservoir model saturation in time, top view. The green color denotes gas, the red color is oil and the blue color denotes water.

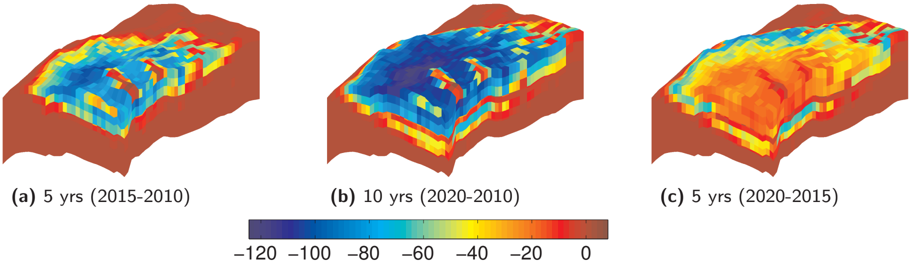

(a) 5 yrs (2015-2010) **(b)** 10 yrs (2020-2010) **(c)** 5 yrs (2020-2015)

Figure 5.6: Simulated time-lapse density change (kg/m^3) after 5 and 10 years of the field production. Cross-sections through the reservoir parts with major time-lapse density changes are shown.

For the computation of the gravimetric signal the analytical solutions for the gravitational attraction of a rectangular prism are applied (see Chapter 2). Since the reservoir model grid is composed of irregular cells rather than prisms, a model grid approximation is performed after the reservoir model simulation. Each cell in the original grid is approximated by 4 rectangular prisms (Fig. 5.7). This means that the grid refinement is performed in the proportion 1:2 in x- and y-directions, respectively. The grid cell size is reduced from about 50×50 m to about 25×25 m.

The time-lapse gravimetric signal is simulated on a regular observation grid containing 552 observation points (Fig. 5.8). The measurement separation distance is fixed and equal to about 150 m, which is close to half of the reservoir depth. Three gravimetric surveys are simulated: the baseline survey in 2010, the first monitoring survey in

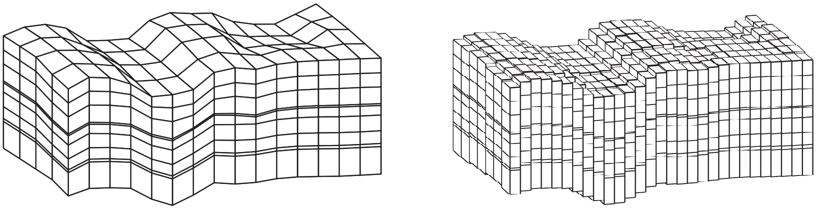

(a) the original model grid **(b)** the model grid approximated by prims

Figure 5.7: Reservoir model grid representation. Only a part of the whole grid is shown.

2015 and the second monitoring survey in 2020. Subsequently, two time-lapse gravity variations are determined: the 5 years difference between the first monitoring survey and the baseline survey (2015-2010) and the 10 years difference between the second monitoring survey and the baseline survey (2020-2010). The predicted time-lapse gravity variation is shown in Fig. 5.9. The signal amplitudes are 84 μGal for the 2015-2010 difference and 148 μGal for the 2020-2010 difference. They are significantly above the typical measurement uncertainty, which is in the order of 5 μGal.

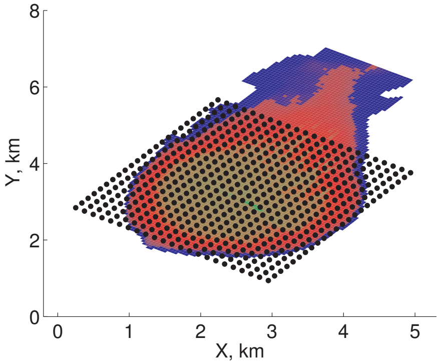

Figure 5.8: Schematic layout of the field gravity measurement network (black dots). The measurement spacing is regular with about 150 m in x- and y-direction. The gravity observation network is compared to the reservoir layout (in the background).

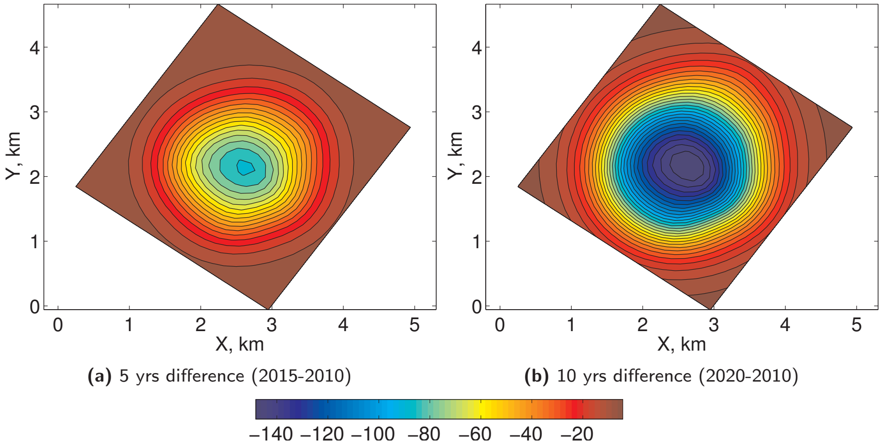

(a) 5 yrs difference (2015-2010) **(b)** 10 yrs difference (2020-2010)

Figure 5.9: Simulated time-lapse gravity variation induced by the TA-GOGD process after 5 (a) and 10 (b) years of the reservoir production. One contour interval is 5 μGal.

5.2.2 Field estimates of the gravity data noise

In order to estimate the gravity data noise levels under the specific conditions of the Oman field, three gravity test surveys with CG5 relative gravimeter were performed by the reservoir operating asset. The relative gravity measurements were made in August, September and October 2010 with about 100 stations per survey (Fig. 5.10). The observational-noise estimates are determined by computing the mean and the standard deviation of the time-lapse difference data sets, i.e., September-August, October-August and October-September. Prior to the calculation of the statistics, the data outliers are removed. An outlier is defined to be the time-lapse difference exceeding 30 μGal in the absolute sense.

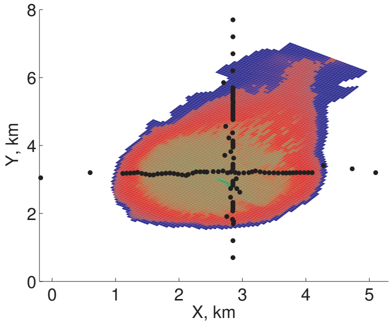

Figure 5.10: Measurement network layout for the gravity observational-noise test survey in the Oman field. Black dots denote the location of gravity stations. The reservoir layout is shown in the background.

The field estimates of gravity data observational noise are presented in Tab. 5.1 and Fig. 5.11. As can clearly be seen, the noise estimates based on the difference data with

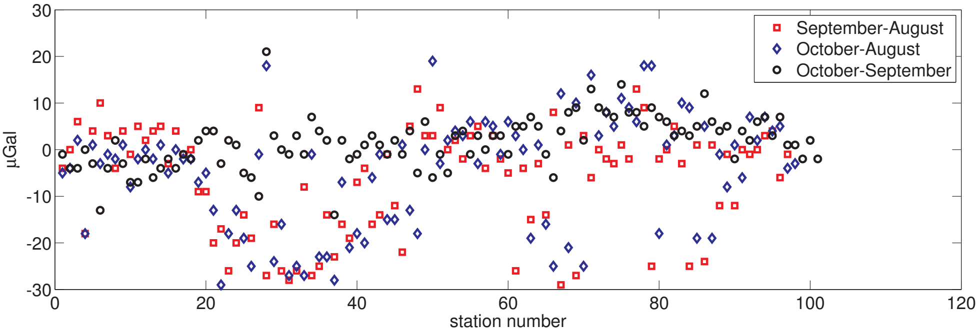

Figure 5.11: Gravity time-lapse data representing the observational noise, μGal.

the August survey as the baseline show unsatisfactory results. The mean differences seem to be biased by about 5μGal whereas the standard deviations are high: in the order of 11-12 μGal. Significantly improved estimates are obtained for the time-lapse data of the October and September surveys: the mean difference is less than 2 μGal and the standard deviation of the difference is close to 5 μGal, which is not far from the typical uncertainty of the gravity field measurements. The poor quality of the August survey could be due to many reasons such as instrument drift, insufficient accuracy of the instrument positioning in the vertical direction, inaccurate application of gravity data corrections, etc. Therefore, it should be further investigated at the data processing stage.

Table 5.1: Summary statistics of time-lapse difference data.

	September-August	October-August	October-September
# of outliers	3	1	1
mean (μGal)	-6.2	-4.6	1.6
std. (μGal)	11.3	12.1	5.5

5.2.3 Hydrological signal estimates

The specific conditions in the field include a dynamic hydrological environment. Fig. 5.12 shows that temporal variations in groundwater levels in the order of 10 m are possible. The variations are partly due to the natural recharge and discharge processes and partly due to the extraction and the disposal of production water. Therefore, a detailed modeling of gravimetric signal resulting from the groundwater variations may be crucial to properly assess the feasibility of gravimetric monitoring of the TA-GOGD at the field.

Since a detailed hydrological model of the field was not available for this study we followed a stochastic approach to investigate the potential contributions of the hydrological signal to the observed time-lapse gravity changes. Our simulation is based on the observed variability in the groundwater field data. The available measurements are a time series of water levels at observation wells in the field. From these data

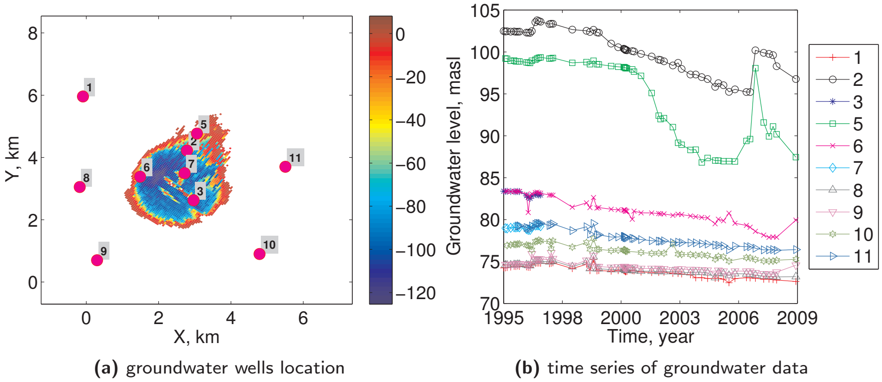

(a) groundwater wells location (b) time series of groundwater data

Figure 5.12: Groundwater data for the field in Oman. In (a) location of the groundwater observation wells is compared to the location of the predicted time-lapse density change (kg/m^3) in the reservoir after 10 years of production (2020-2010).

we extract 2 snapshots between which significant changes in the groundwater levels occurred. The first sample S_1 are the water level measurements at 01.04.2002 and the second sample S_2 is taken at 18.04.2008. Further, the difference of the two readings, i.e., $\delta S = S_2 - S_1$ is determined. The data show a decrease in the water table reaching several meters at some observation wells (Tab. 5.2).

Table 5.2: Groundwater level change sample data.

well number	1	2	5	6	8	9	10	11
water level change (m)	-0.85	-0.05	-7.21	-2.92	-0.61	-0.67	-1.04	-1.22

The time-lapse water level changes δS are used to constrain the stochastic simulation of the groundwater-level variations. The realizations are generated in such a way that the well data are matched. For this purpose the Direct Sequential Simulation (DSSIM) method (Remy et al. 2009) is applied. To account for the uncertainties related to the properties of the aquifer (e.g., aquifer continuity) we considered different scales of the spatial correlation for the groundwater variations and used the variogram range of about 7.5, 15 and 30 km. Furthermore, for every case, 50 simulation runs are performed, giving in total 150 different stochastic realizations of the water-level change. Two examples of the generated realizations are shown in Fig. 5.13. To translate the hydrological variation into the gravimetric signal we use a homogenous drainable aquifer porosity of 0.12 and an aquifer water density of 1000 kg/m^3. The resulting hydrological signal is shown in Fig. 5.14. As can be seen, the modeled groundwater changes can result in correlated gravity signal with amplitudes up to 30-50 μGal. The root-mean-square error (RMSE) of the total hydrological signal, which is determined as

$$RMSE_{hydr.signal} = \sqrt{\frac{1}{552}\sum_{i=1}^{552}\left(\Delta g_i^{W,T}\right)^2} \tag{5.1}$$

where $\Delta g^{W,T}$ is the true temporal gravity change due to groundwater variation, is in the order of 15-26 μGal in this case.

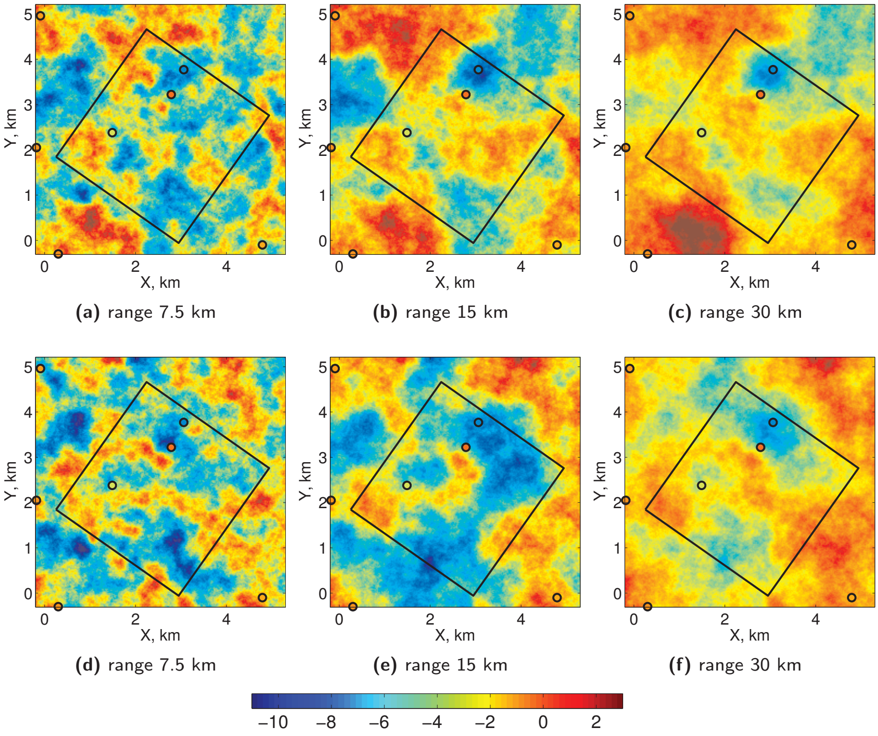

(a) range 7.5 km **(b)** range 15 km **(c)** range 30 km

(d) range 7.5 km **(e)** range 15 km **(f)** range 30 km

Figure 5.13: Two examples of the simulated time-lapse groundwater variation (m) for different groundwater correlation scales. In the top row results of the first simulation run are shown and in the bottom row of the second run, respectively. The black rectangle denotes the boundaries of the gravity measurement network. The black circles denote the location of the conditioning well-data.

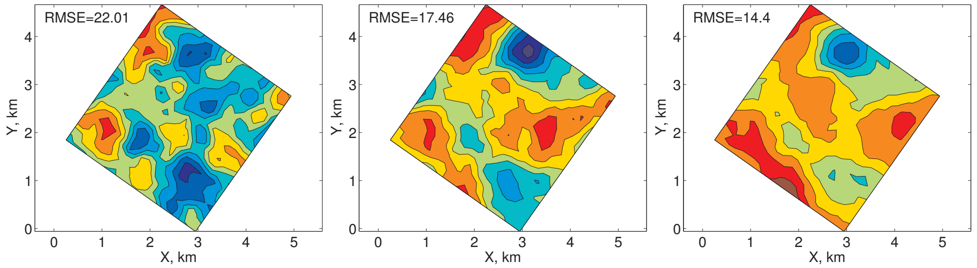

(a) range 7.5 km **(b)** range 15 km **(c)** range 30 km

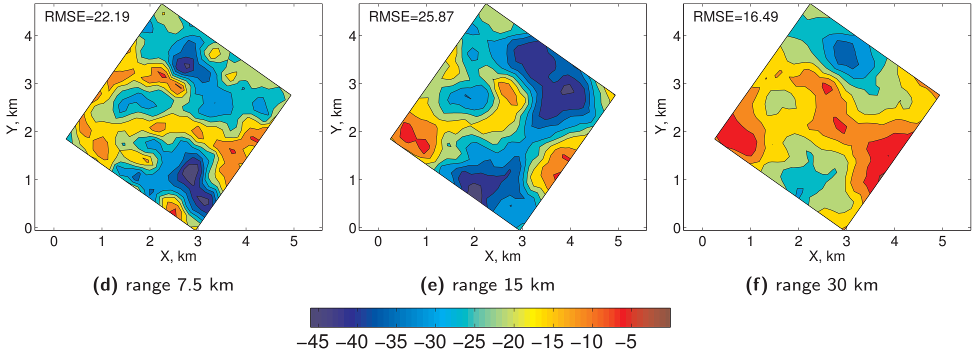

(d) range 7.5 km **(e)** range 15 km **(f)** range 30 km

Figure 5.14: Examples of the simulated hydrological signal realizations. One contour interval is 5 μGal. The RMSE is computed using Eq. (5.1).

5.2.4 Hydrological noise estimates

We showed in Chapter 3 that using spatial interpolation of water level measurements the hydrological gravity signal caused by temporal variations of groundwater can be estimated. Subsequently, this estimate can be subtracted from the observed gravity data to remove the unwanted hydrological influences. In practice, however, not all of this signal can be removed because of the limited number of hydrological data. Therefore, a residual signal, i.e., the difference between the signal estimate and the true signal, will constitute the hydrological gravity noise remaining in the data.

In order to investigate the potential influences of the hydrological noise on gravimetric monitoring of the TA-GOGD process in the considered field we simulate a number of hypothetical scenarios. First, we assume that the stochastic realizations of the groundwater variations generated in Section 5.2.3, and based on the field sample data, serve as the true (reference) values, which are used to generate the true hydrological gravity signal. Next we attempt to estimate this signal using spatial interpolation of hypothetical groundwater measurements. Here, we consider three scenarios where various densities of groundwater measurements are simulated ranging from 6 × 6 grid and 36 observations to 24 × 24 grid and 576 observations (see Tab. 5.3).

The results of the spatial interpolation of the synthetic groundwater data are shown in Fig. 5.15. As expected, with increasing number of hydrological measurements a more detailed picture of the unknown groundwater variation can be recovered.

Table 5.3: Density of the synthetic measurements of groundwater for the field in Oman.

	36 obs. wells 6 × 6 grid	144 obs. wells 12 × 12 grid	576 obs. wells 24 × 24 grid
separation distance in x- and y-direction (m)	860	470	240

The interpolated groundwater measurements are subsequently used to estimate the unknown hydrological signal (Fig. 5.16) and to compute the hydrological noise as the difference between the signal estimate and the actual signal (Fig. 5.17). Comparing Fig. 5.14 with Fig. 5.17 we can observe that already with 36 groundwater observation wells the amplitudes of the hydrological gravity noise can be reduced 2-3 times, i.e., from about 30-45 μGal to about 10-25 μGal. Nevertheless, the remaining spatial correlations in the noise are still present in this case. This is especially true for the shortest correlation range of the groundwater, i.e., 7.5 km. With a denser groundwater observation network most of the unwanted hydrological signal could be removed. For instance, with 144 groundwater measurements the remaining noise amplitudes are below 10-14 μGal in case of a 7.5 km variogram range and below 5-7 μGal for 15 km and 30 km variogram range, respectively. For the most idealized scenario of 576 measurements, the noise amplitude is below 3-5 μGal. These results are further quantified by computing the RMSE values of the hydrological noise from

$$RMSE_{hydr.noise} = \sqrt{\frac{1}{552}\sum_{i=1}^{552}\left(\Delta g_i^{W,E} - \Delta g_i^{W,T}\right)^2} \tag{5.2}$$

where $\Delta g^{W,E}$ is the estimated and $\Delta g^{W,T}$ is the true temporal gravity change due to groundwater variation, respectively. The above procedure to generate the gravimetric noise is repeated for every simulated conditional realization (50 runs × 3 cases of groundwater correlation) of groundwater level change and for each of the three scenarios for the density of well observations. The combination of all the cases gives in total (50 stochastic realizations of groundwater × 3 cases of groundwater correlation scales × 3 cases of groundwater observation well density) 450 different hydrological noise realizations. These realizations are subsequently used to contaminate the 5 year and 10 year predicted time-lapse gravity variation (Fig. 5.9) resulting from the reservoir production. The average (over 50 simulation runs) RMSE values of the simulated hydrological signal and hydrological noise are shown in Tab. 5.4. With already a 6 × 6 groundwater observation grid, the average RMSE is significantly reduced, i.e., from about 17-22 μGal to about 3-7 μGal. Further increasing the density of groundwater observation wells would lead to average RMSE of about 2-5 μGal in case of 144 observation wells and 1-2 μGal in case of 576 wells.

Additionally to the hydrological noise, the observational noise, related to the instrument operation and data processing, is simulated and added to the data. Here, based on the field noise estimates (Fig. 5.11), we assume 5 μGal uncorrelated zero-mean Gaussian noise. For each gravity survey data (i.e., at 2010, 2015 and 2020) we add a set of random values simulated from that distribution. To account for the sensitivity of

Table 5.4: Average (over 50 simulation runs) RMSE (μGal) of the simulated hydrological signal and hydrological noise for the field in Oman. The results are presented for different correlation scales of groundwater (variogram range) and for different density of the hypothetical groundwater measurements.

	range 7.5 km	range 15 km	range 30 km
$\overline{RMSE}_{hydr.signal}$	21.50	21.20	16.70
$\overline{RMSE}_{hydr.noise}$, 36 obs.	7.40	5.00	3.29
$\overline{RMSE}_{hydr.noise}$, 144 obs.	4.56	2.90	1.90
$\overline{RMSE}_{rhydr.noise}$, 576 obs.	2.19	1.43	0.98

the results to the observational noise, 50 different sets of random values are simulated.

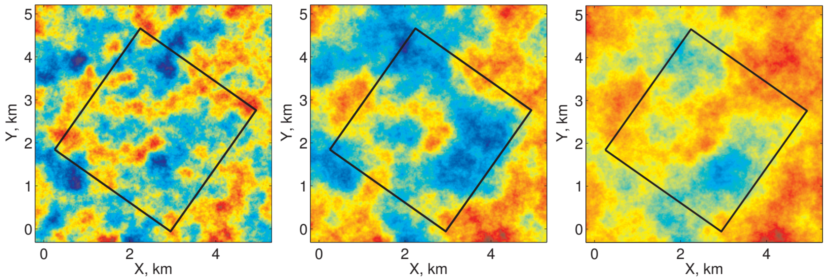

(a) range 7.5 km, reference **(b)** range 15 km, reference **(c)** range 30 km, reference

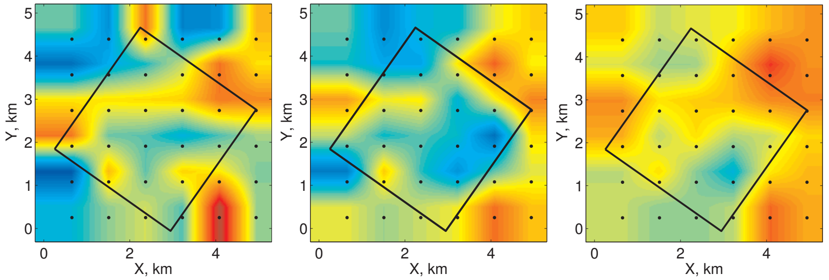

(d) range 7.5 km, 36 obs. **(e)** range 7.5 km, 36 obs. **(f)** range 7.5 km, 36 obs.

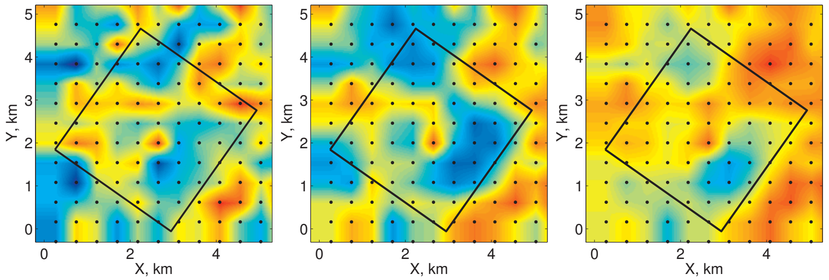

(g) range 15 km, 144 obs. **(h)** range 15 km, 144 obs. **(i)** range 15 km, 144 obs.

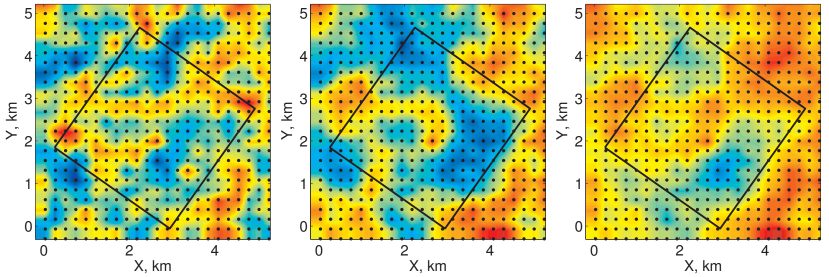

(j) range 30 km, 576 obs. **(k)** range 30 km, 576 obs. **(l)** range 30 km, 576 obs.

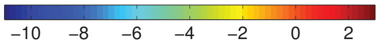

Figure 5.15: Interpolated groundwater variation (m) for different groundwater correlation scales (variogram range) and for various densities of the hypothetical observation wells of groundwater (black dots). Linear interpolation was used. The black rectangle denotes the boundaries of the gravity measurement network.

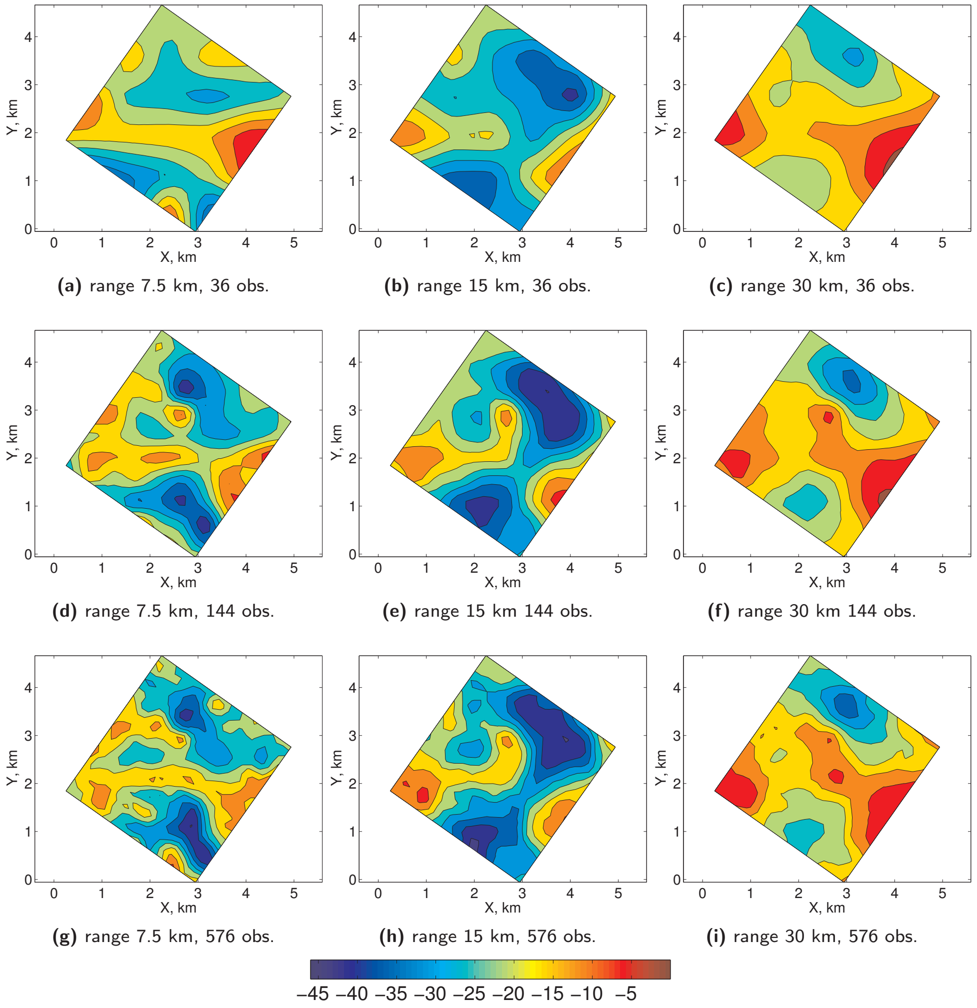

(a) range 7.5 km, 36 obs. **(b)** range 15 km, 36 obs. **(c)** range 30 km, 36 obs.

(d) range 7.5 km, 144 obs. **(e)** range 15 km 144 obs. **(f)** range 30 km 144 obs.

(g) range 7.5 km, 576 obs. **(h)** range 15 km, 576 obs. **(i)** range 30 km, 576 obs.

Figure 5.16: Examples of the estimated hydrological signal realizations for different correlation scales of groundwater and for different density of groundwater measurements. One contour interval is 5 μGal.

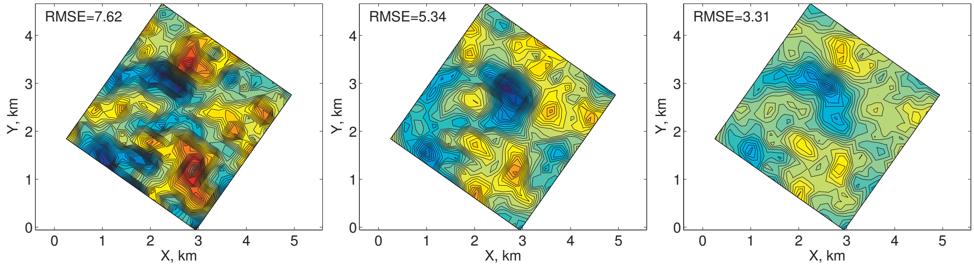

(a) range 7.5 km, 36 obs. **(b)** range 15 km, 36 obs. **(c)** range 30 km, 36 obs.

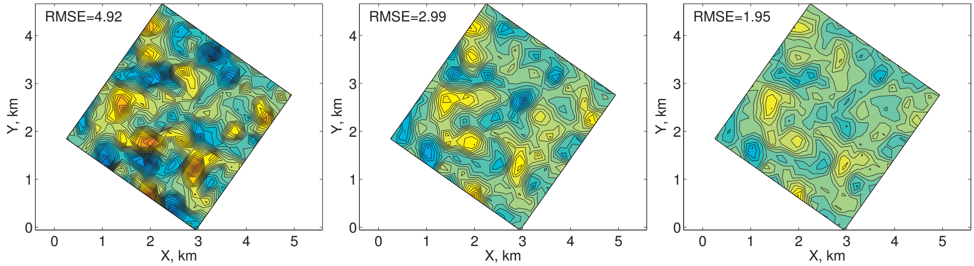

(d) range 7.5 km, 144 obs. **(e)** range 15 km, 144 obs. **(f)** range 30 km, 144 obs.

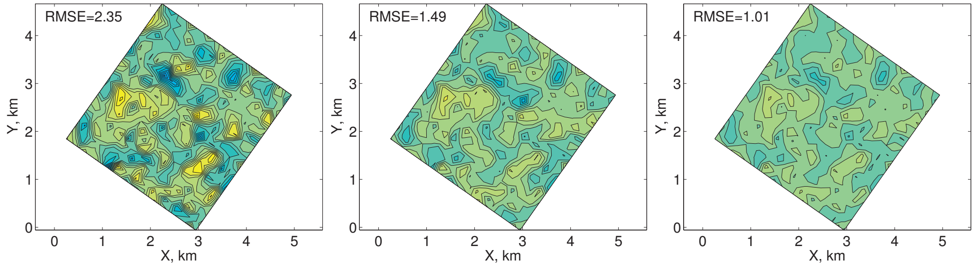

(g) range 7.5 km, 576 obs. **(h)** range 15 km, 576 obs. **(i)** range 30 km, 576 obs.

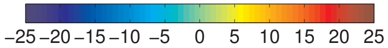

Figure 5.17: Examples of the hydrological noise realizations for different correlation scales of groundwater and for different density of groundwater measurements. One contour interval is 1 μGal. The RMSE is computed using Eq. (5.2).

5.3 Gravity data inversion for heat-front monitoring

To investigate the feasibility of gravimetric monitoring of TA-GOGD in the considered field, the focusing inversion of the synthetic gravimetric observations with the minimum support stabilizer is performed (see Chapter 4 for details of the methodology). We assume that the target of gravimetric monitoring is a time-evolution of the heat-front. In the interior of the evolving heat-front, the mixture of steam and hot hydrocarbon gases (see Fig. 5.4) will gradually substitute the oil in the reservoir rock matrix. Since oil is denser than steam and hydrocarbon gases, negative time-lapse variation in the reservoir bulk density will occur. The decrease in the reservoir bulk density will induce negative time-lapse variations in the local gravity field, which as we showed in Section 5.2, should be significantly above the expected uncertainy of gravimetric measurements in the field. Therefore, gravimetric observations can be a source of information about the heat-front evolution.

Because the direct inversion of gravity data for the spatial position of the heat-front is a challenging and non-linear problem, a simplified two-step approach is followed. In the first step, the gravity data are inverted to estimate the time-lapse density change in the reservoir. Then the inverse problem becomes linear because the density change and the gravity change are linearly dependent, i.e., the time-lapse gravimetric signal scales proportionally with the temporal density variation (see Chapter 2). Here, since surface gravimetric observations offer limited vertical resolution, we solve a 2D linear inverse problem instead of a 3D. The uncertain parameters are the vertical averages of the time-lapse reservoir density change. To reduce the number of parameters, the recovered density change is represented on a coarser grid than the original fine-scale grid used to simulate the time-lapse gravity observations (see Fig. 5.7). The upscaling is 6:1 (Fig. 5.18), in both x- and y-direction, so that the upscaled grid consists of 30×22×1 prisms, each of 150×150×130 m size.

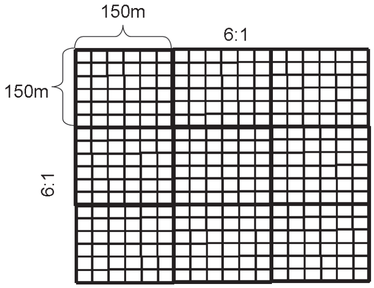

Figure 5.18: Grid upscaling.

In the second step, the heat-front position is estimated. It is derived from the inverted density change maps by reading the contour line with the specified density change threshold. In this study we assume that a threshold of -20 kg/m^3 defines the boundaries of the heat front. This choice follows from a simplified approximation. Note that at the edge of the heat front the time-lapse density variation is about -90 kg/m^3

(see Fig. 5.6) and only the first two layers are affected. If we take the average over 9 layers, this gives about -20 kg/m^3. The application of this procedure to the reference (true) average time-lapse density change in the reservoir after 5 and 10 years of production results in the heat-front positions shown in Fig. 5.19.

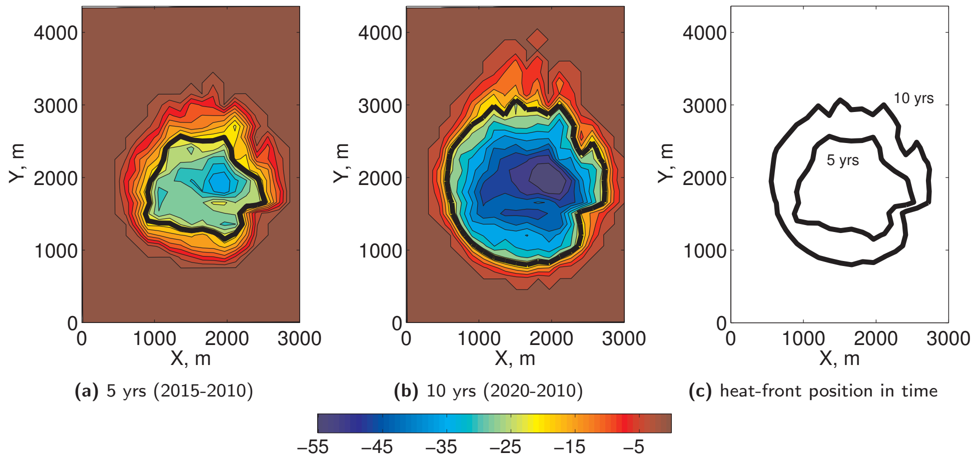

(a) 5 yrs (2015-2010)

(b) 10 yrs (2020-2010)

(c) heat-front position in time

Figure 5.19: Time-lapse average density change after 5 (a) and 10 (b) years of the reservoir production. The black lines define the heat-front position and are the average density change contours (c) at -20 kg/m^3.

In this feasibility study we investigate the conditions under which the gravimetric monitoring in the considered field can provide a given accuracy of the heat-front position recovery. For this purpose various scenarios concerning the noise contaminating the gravity data are considered. First we consider a scenario when only the 5 μGal uncorrelated (in space and time) Gaussian observational noise is added to the data. An example of the heat-front recovery in this case is shown in Fig. 5.20. When additionally to the observational noise the total hydrological signal (the signal without any corrections) is present in the data, the heat-front estimation is significantly less accurate (Fig. 5.21) with errors in the front position in the order of 500-800 m. More importantly, we analyze the scenarios when an attempt is made to estimate and subsequently remove the hydrological influences from the gravity data, i.e., the case when additionally to the observational noise the hydrological noise (the difference between the hydrological signal estimate and the true signal) is added to the data. An example of the heat-front estimation in this case is shown in Fig. 5.22. Comparing Fig. 5.22 with Fig. 5.21 we can observe that hydrological signal corrections based on 12×12 groundwater observation wells significantly improved the accuracy of the front position estimate in this case. Other scenarios for the density of groundwater observation wells and scenarios for the scales of spatial correlation of groundwater are also considered. In total 450 gravity inversion experiments are run (50 stochastic realizations of groundwater × 3 cases of groundwater correlation scales × 3 cases of groundwater observation well density).

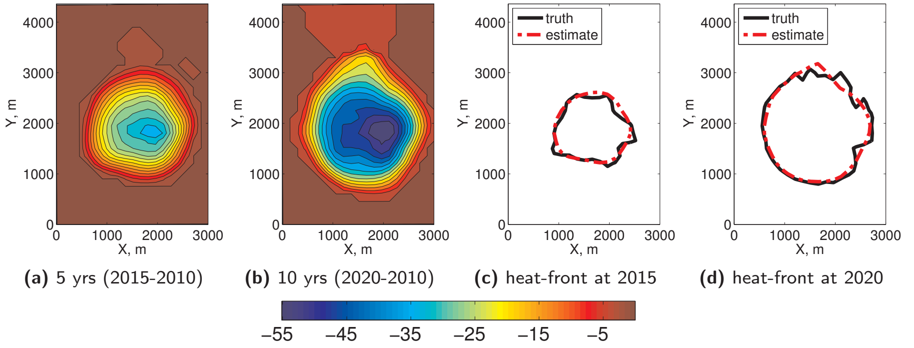

(a) 5 yrs (2015-2010) **(b)** 10 yrs (2020-2010) **(c)** heat-front at 2015 **(d)** heat-front at 2020

Figure 5.20: Time-lapse average density change estimate (a-b) for the field in Oman in the case when 5 μGal Gaussian observational noise is added to the gravity data. In c) and d) the recovered heat-front positions are shown.

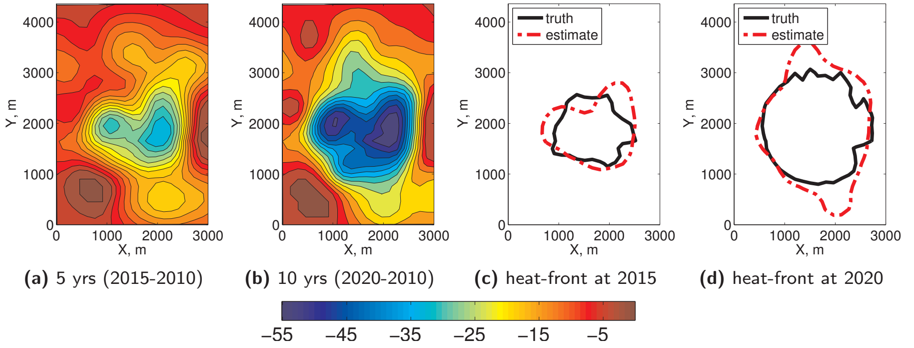

(a) 5 yrs (2015-2010) **(b)** 10 yrs (2020-2010) **(c)** heat-front at 2015 **(d)** heat-front at 2020

Figure 5.21: Time-lapse average density change estimate (a-b) for the field in Oman. The gravity data are contaminated with 5 μGal Gaussian observational noise and additionally with the total hydrological signal, which is not removed from the gravity data. The hydrological signal (Fig. 5.14e) corresponds to the case of 15 km variogram range used to simulate the conditional groundwater variation. In c) and d) the recovered heat-front positions are shown.

To evaluate the results in a quantitative way, the recovered heat-front positions are compared with the true ones by computing spatial statistics. Between the front estimate and the true front the maximum closest distance d is determined (see Fig. 5.23). Then for a particular scenario (i.e., observation well density and groundwater correlation scales) the error statistics based on the 450 simulation runs are computed, i.e.

$$d_{min} = min\{d_1, ..., d_{450}\},$$

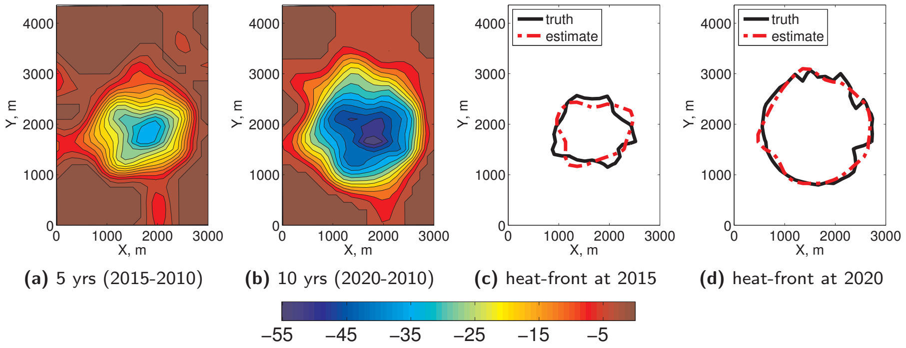

(a) 5 yrs (2015-2010) **(b)** 10 yrs (2020-2010) **(c)** heat-front at 2015 **(d)** heat-front at 2020

Figure 5.22: Time-lapse average density change estimate (a-b) for the field in Oman. The gravity data are contaminated with 5 μGal Gaussian observational noise and additionally with the hydrological signal which is subsequently estimated and removed from the gravity data. The hydrological signal (Fig. 5.14e) corresponds to the case of 15 km variogram range used to simulate the conditional groundwater variation. The hydrological signal estimate (Fig. 5.16e) is obtained from the spatial interpolation of 144 groundwater measurements. In c) and d) the recovered heat-front positions are shown.

$$d_{avg} = \frac{1}{450}\sum_{i=1}^{450} d_i,$$

$$d_{max} = max\{d_1, ..., d_{450}\}$$

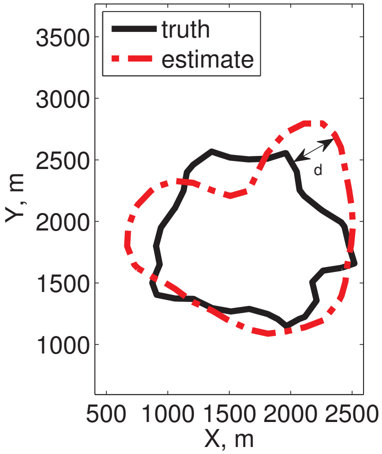

Figure 5.23: Schematic illustration of the error computation for the heat-front position estimate.

5.3.1 Results

In Fig. 5.24 to Fig. 5.28 the heat-front position estimates are shown and Tab. 5.5 to Tab. 5.7 contain the summary of the front recovery errors. The results are presented for three cases: the case when gravity data are contaminated with 5 μGal observational Gaussian noise only; the case when additionally to the observational noise the total (without any corrections) hydrological signal is added and the case when additionally to the observational noise the hydrological noise is added, i.e., the difference between the hydrological signal estimate and the actual signal. The hydrological noise is generated under various scenarios with respect to the correlation scales of groundwater and the number of groundwater observation wells used to estimate and subsequently remove the hydrological signal.

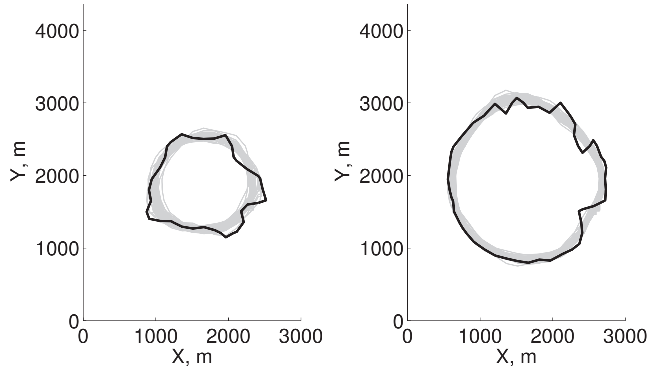

(a) heat-front at 2015 **(b)** heat-front at 2015

Figure 5.24: Heat-front estimates for the case when only the 5 μGal Gaussian observational noise is contaminating the data.

In the most favorable scenario (Fig. 5.20), i.e., in the case when only the observational Gaussian noise is present in the data, the average error in the front position estimate is about 160 m after 5 years of the reservoir production and about 140 m after 10 years, respectively. More accurate front position estimates in the latter case are expected, because the 10 year time-lapse gravity variation is significantly stronger than the 5 year variation (see Fig. 5.9). Furthermore, it can be observed that the front-position estimates are rather smooth, i.e., the small-scale local heterogeneities in the propagation of the true front were not recovered.

When additionally to the observational noise the total hydrological signal is added to the gravity data the recovered front position estimates are very erroneous (Fig. 5.25). For some cases, e.g., the case of 7.5 km and 15 km variogram range, the average error is about 200-500 m larger than in the case when groundwater signal does not contaminate the data (see Tab. 5.6). Furthermore, more accurate (in the average sense) 5-year than 10-year results can be observed in this case. Large inaccuracies in the 10-year front recovery result from the overlap of the actual front position with the severe negative groundwater variations, exceeding 7 m, around well #5 (see Tab. 5.2, Fig. 5.12, Fig. 5.13 and Fig 5.25e).

The front position estimates are significantly improved when the hydrological influences are estimated and removed from the data (Fig. 5.26 to Fig. 5.28). With already 36 groundwater observations (6×6 grid), the estimation error is reduced by about 150-550 m. Further increasing the density of water level measurements brings the accuracy of the estimates close to the case when only the observational noise is present in the data. For instance in the case of 12×12 grid of groundwater wells and the most challenging case of 7.5 km variogram range of groundwater, the average error in the front estimation is 10-40 m larger (202 compared to 163, or 147 compared to 138, see Tab. 5.5) than in the hydrological signal-free scenario. With a grid of 24×24 wells these differences are smaller than 10 m.

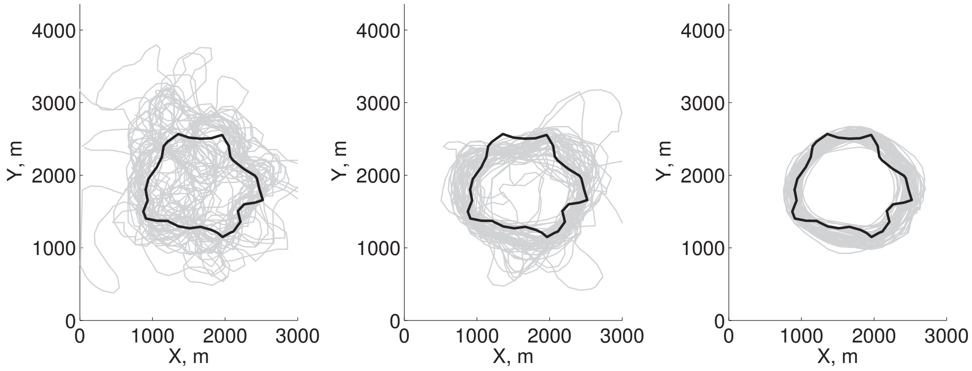

(a) range 7.5 km **(b)** range 15 km **(c)** range 30 km

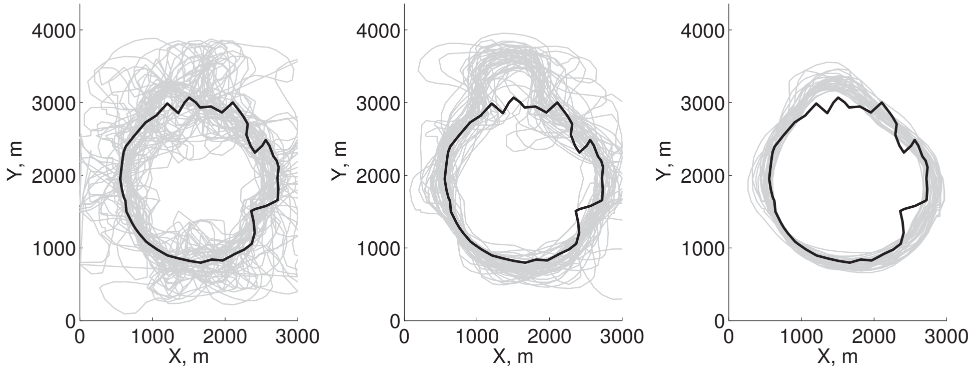

(d) range 7.5 km **(e)** range 15 km **(f)** range 30 km

Figure 5.25: Heat-front estimates for different correlation scales of groundwater. In this case no hydrological signal is removed from the data. The top row shows the results for the front position after 5 years of the reservoir production (front in 2015) and the bottom row after 10 years (front in 2020), respectively. The true heat-front position is shown in black, the grey color denotes the position estimates.

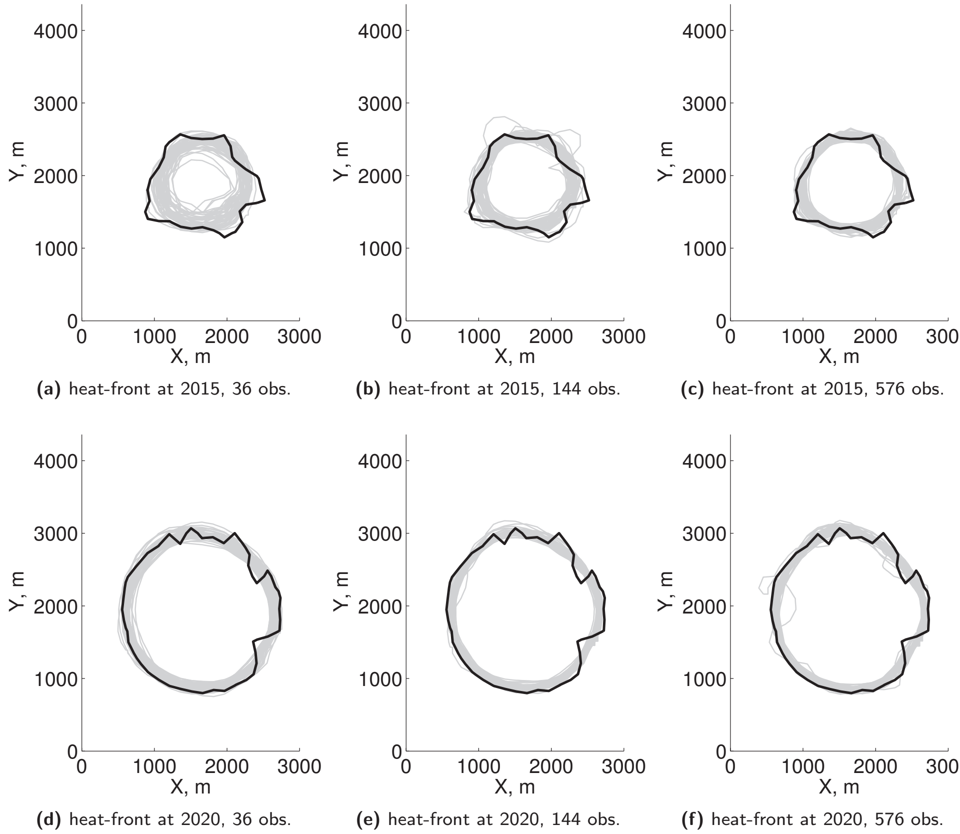

(a) heat-front at 2015, 36 obs. **(b)** heat-front at 2015, 144 obs. **(c)** heat-front at 2015, 576 obs.

(d) heat-front at 2020, 36 obs. **(e)** heat-front at 2020, 144 obs. **(f)** heat-front at 2020, 576 obs.

Figure 5.26: Heat-front estimates for a 7.5 km variogram range of groundwater and various densities of the hypothetical observation wells of groundwater. The true heat-front position is shown in black, the grey color denotes the position estimates.

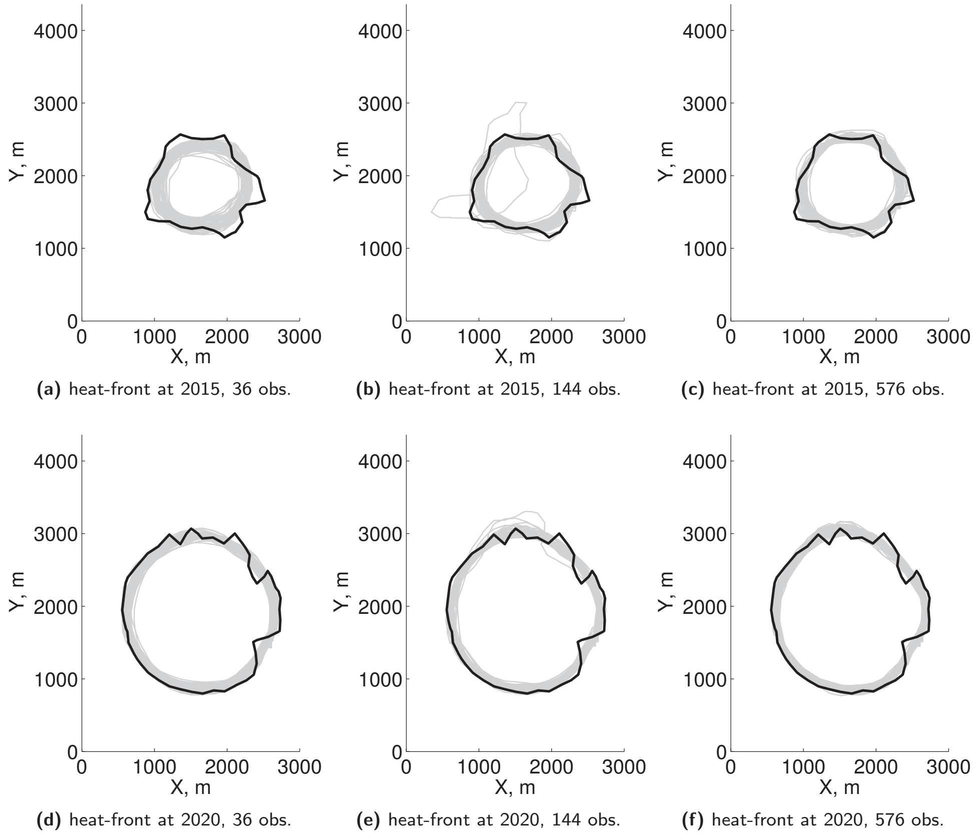

(a) heat-front at 2015, 36 obs. **(b)** heat-front at 2015, 144 obs. **(c)** heat-front at 2015, 576 obs.

(d) heat-front at 2020, 36 obs. **(e)** heat-front at 2020, 144 obs. **(f)** heat-front at 2020, 576 obs.

Figure 5.27: Heat-front estimates for a 15 km variogram range of groundwater and various densities of the hypothetical observation wells of groundwater. The true heat-front position is shown in black, the grey color denotes the position estimates.

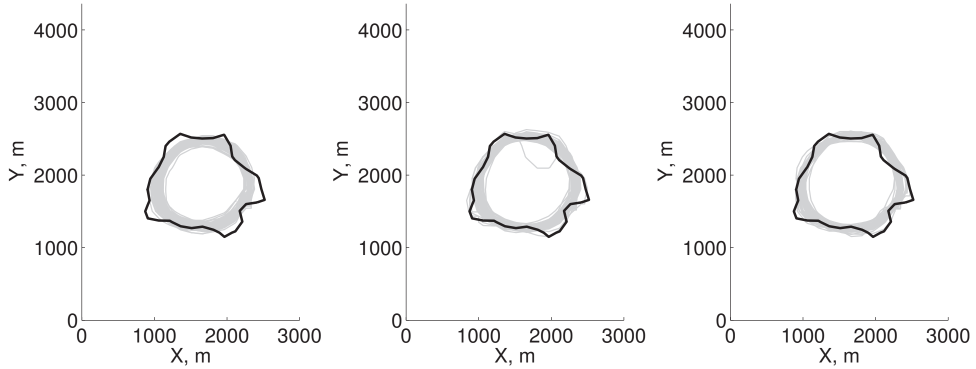

(a) heat-front at 2015, 36 obs. **(b)** heat-front at 2015, 144 obs. **(c)** heat-front at 2015, 576 obs.

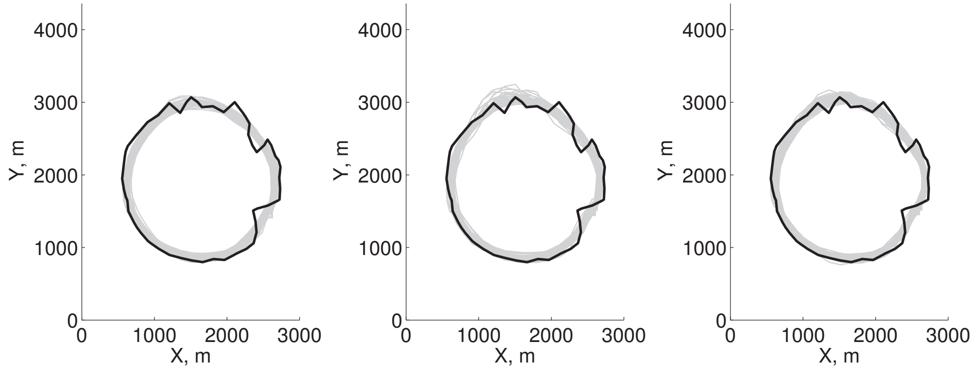

(d) heat-front at 2020, 36 obs. **(e)** heat-front at 2020, 144 obs. **(f)** heat-front at 2020, 576 obs.

Figure 5.28: Heat-front estimates for a 30 km variogram range of groundwater and various densities of the hypothetical observation wells of groundwater. The true heat-front position is shown in black, the grey color denotes the position estimates.

Table 5.5: Accuracy [d_{min} d_{avg} d_{max}] of the heat-front position estimates (m) for a 7.5 km variogram range of groundwater.

	36 obs.	144 obs.	576 obs.	no hydr. sig.	sig. not corr.
at 2015	161 **252** 403	130 **202** 379	104 **170** 218	105 **163** 207	254 **620** 1398
at 2020	124 **157** 198	127 **147** 225	116 **145** 342	113 **138** 197	298 **707** 1177

Table 5.6: Accuracy [d_{min} d_{avg} d_{max}] of the heat-front position estimates (m) for a 15 km variogram range of groundwater.

	36 obs.	144 obs.	576 obs.	no hydr. sig.	sig. not corr.
at 2015	163 **225** 289	115 **192** 566	113 **168** 213	105 **163** 207	184 **412** 1088
at 2020	128 **148** 200	122 **148** 343	114 **140** 191	113 **138** 197	266 **637** 1125

Table 5.7: Accuracy [d_{min} d_{avg} d_{max}] of the heat-front position estimates (m) for a 30 km variogram range of groundwater.

	36 obs.	144 obs.	576 obs.	no hydr. sig.	sig. not corr.
at 2015	151 **199** 246	114 **176** 338	117 **165** 210	105 **163** 207	117 **216** 357
at 2020	125 **143** 180	121 **146** 225	114 **139** 195	113 **138** 197	174 **299** 529

5.3.2 Alternative scenario - unexpected heat-front distribution

The predicted steam distribution, and hence the heat-front propagation, coming from the reservoir model is characterized by a fairly regular round shape. It is interesting to investigate if different shapes of the heat front and, hence, alternative scenarios for the oil drainage areas could be inferred from gravity data inversion. Since a dynamic model of the reservoir that could be used to create such scenarios is not available for this study, a simplified approach is followed. We use the average time-lapse density change (Fig. 5.19a and Fig. 5.19b) as predicted by the reservoir model and apply to it an image transformation, i.e., a scaling and a shearing. The transformed image (Fig. 5.29a and Fig. 5.29b) may represent scenario when the steam/heat distribution in the reservoir is affected by different than expected subsurface characterization, e.g., presence of sealing faults or an alternative distribution of fractures. In the particular case that we consider, the steam cloud moves preferentially into the south-east direction.

To demonstrate that gravimetric observations can be a source of information about the propagation of the heat front, one scenario is presented. The synthetic gravity data are contaminated with 5 μGal Gaussian observational noise and additionally with hydrological noise. The hydrological noise results from the groundwater signal estimation and correction using a 12×12 grid of water level measurements and assumed variogram range of groundwater of 15 km (Fig. 5.17e). The results clearly show (Fig. 5.29c and Fig. 5.29d), that gravimetric monitoring can provide information about the heat-front evolution in this case.

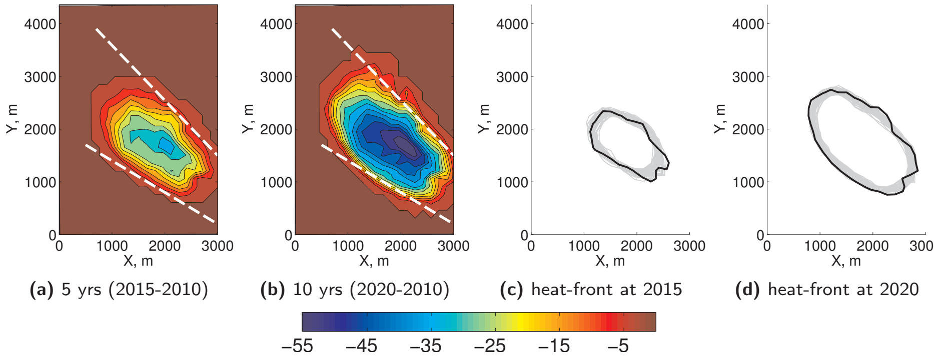

(a) 5 yrs (2015-2010) **(b)** 10 yrs (2020-2010) **(c)** heat-front at 2015 **(d)** heat-front at 2020

Figure 5.29: Heat-front estimates in case of an alternative oil drainage distribution. In (a-b) the average time-lapse density change (kg/m^3) in the reservoir is shown. The white dashed lines indicate the position of the hypothetical sealing faults. In (c-d) the heat-front position estimates (in grey) are compared to the true front (in black). The synthetic gravity data were contaminated with 5 μGal Gaussian observational noise and with the hydrological noise shown in Fig. 5.17b. This noise results from hydrological signal corrections based on 36 groundwater measurements. The assumed groundwater variogram range was 15 km.

5.3.3 Summary

In this study the feasibility of gravimetric monitoring of TA-GOGD process for one of the fields in Oman was investigated. We applied the focusing inversion method to synthetic time-lapse gravity observations. The minimum support stabilizer was used to assure a compact distribution of the inverted density change model. From the time-lapse density change estimate the heat-front position was determined.

We showed that the density redistribution and hence the time-evolution of the heat front in the field has the potential to be monitored with time-lapse gravimetric observations. The predicted gravity signal amplitudes are very strong: about 80 μGal and 150 μGal after 5 and 10 years of production, respectively. They are significantly above the 5 μGal observed noise in the field. However, we showed also that the gravimetric measurements can be to a large extent influenced by the hydrological signal resulting from spatio-temporal groundwater variations. Using a set of stochastic simulations constrained to the groundwater field data, we demonstrated that large groundwater level changes can produce correlated gravity signal with amplitudes up to 30-50 μGal. In such a case the inversion of gravity data for the front propagation monitoring can be very challenging. The resulting front position errors can reach several hundreds of meters (200-700 m). However, by applying corrections based on hydrological measurements, the accuracy of gravimetric heat-front monitoring can be significantly improved. With already 36 groundwater observations (6×6 grid) the estimation error in the front position can be reduced by about 150-550 m compared to the case when no hydrological signal is removed from the data. Further increasing the density of water level measurements to about 100-200 could bring the accuracy of the estimates close to the case when only the observational noise is present in the data. The average achievable accuracy was about 140-160 m in this case.

5.4 Conclusions and recommendations

We demonstrated that gravimetric monitoring of TA-GOGD in the considered field has a great potential. The heat-front evolution could be monitored with best accuracy in the order of 140-160 m, which is comparable to half of the reservoir depth. Such accuracy can provide information about the shape of the front, whereas the smaller-scale (below 150 m) local heterogeneities in the propagation of the front may not be recovered. Furthermore, due to groundwater variations, the total error in the estimation of the front position can reach 200-700 m and more. Therefore, a more detailed study should follow addressing the specific hydrological conditions. It is recommended to use a hydrological model that was developed for the field to predict the groundwater variations. The model should be calibrated to the available hydrological measurements. Forward model simulations would result in the predicted groundwater states in off-well locations. A number of extreme and typical cases could be further considered with respect to aquifer properties and the amplitudes of the groundwater variations. The possibilities to remove the unwanted hydrological signal in gravity data is another issue to be investigated. For instance, the placement of additional observational wells can be optimized. By simulating a number of different scenarios a quantitative assessment of the feasibility of gravimetric reservoir monitoring for the field could be achieved.

In the future research, other production effects such as subsidence or uplift due to thermal rock expansion should also be considered and the benefits of a joint inversion of gravity and surface deformation data for heat-front monitoring investigated.

Chapter 6

Case study 1–Gravimetric monitoring of water influx into a gas reservoir: a 2D numerical study with the ensemble Kalman filter

Water influx into gas fields can reduce recovery factors by $10 - 40\%$. Therefore, information about the magnitude and spatial distribution of water influx is essential for the efficient management of water-drive gas reservoirs. Time-lapse gravimetry may provide a direct measure of mass redistribution below the surface, yielding in this way additional and valuable information for reservoir monitoring.

In this chapter, we investigate the added value of gravimetric observations for monitoring water-influx into a gas field. For this purpose we use data assimilation with the ensemble Kalman filter (EnKF). For a simplified gas reservoir model, we assimilate the synthetic gravity measurements and estimate the reservoir permeability. The updated reservoir model is used to predict the water front position. We consider a number of possible scenarios, making various assumptions on the level of gravity measurement noise and the distance from the gravity observation network to the reservoir formation. The results show that with increasing gravimetric noise and/or distance, the updated model permeability becomes smoother and its variance higher. Finally, we investigate the effect of a combined assimilation of gravity and production data. In the case when only production observations are used, the permeability estimates far from the wells can be erroneous, despite a very accurate history match of the data. In the case when both production and gravity data are combined within a single data assimilation framework, we obtain a considerably improved estimate of the reservoir permeability and an improved understanding of the subsurface mass flow. These results illustrate the added value of gravimetric observations for monitoring water influx and they show also that gravimetric and production observations can be complementary.

The content of this chapter is to a large extent based on the results published in (Glegola et al. 2012a).

6.1 Introduction

Most hydrocarbon reservoirs are surrounded by aquifers. When reservoir fluids are produced, a pressure gradient develops which may cause water influx from a neighboring aquifer to the reservoir formation. In practice, because of a lack of measurements and consequently limited knowledge about aquifer properties (porosity, permeability, thickness, and extent), large uncertainties in estimating water influx are common (Dake 2001). For water-drive gas fields, water influx may have very significant implications affecting the field production. Because gas can be trapped by encroaching water, the recovery factors for water-drive gas reservoirs can be significantly lower than for volumetric (no water influx) reservoirs produced by gas expansion. The gas recovery factor for water-drive gas fields can range between $50 - 70\%$, whereas volumetric gas reservoirs have an ultimate recovery of $80 - 90\%$ (Ahmed 2006). This implies that the information about the magnitude and spatial distribution of water influx can be crucial for the efficient management of water-drive gas reservoirs. Time-lapse (4D) gravimetry, which provides a direct measure of mass redistribution below the surface, has a potential to yield complementary and valuable information in this context.

Reservoir monitoring is one of the key components of closed-loop reservoir management (see Chapter 1), which is recently receiving growing attention in the petroleum industry . The concept is based on continuous or real-time updating of reservoir model (Jansen et al. 2009) to optimize field operations and improve its long-term production. The states (pressures, saturations) and/or parameters (permeability, porosity) of reservoir models are updated by data assimilation methods. A number of studies have shown that the EnKF is suitable for this purpose. The EnKF is a sequential Monte Carlo method where an ensemble of models is propagated in time and updated when new measurements become available (see Chapter 4 for details). This makes the EnKF suitable for real-time model updating based on frequent input streams of monitoring data. In reservoir engineering applications of data assimilation, typically, reservoir models are updated using production measurements (i.e., well-fluid rates and bottomhole pressures) and other data, mostly time-lapse seismic. The advantage of assimilating time-lapse seismic data resides essentially in the large spatial coverage of the data, making it possible to determine location-specific production-induced changes and constrain the assimilation results. Also, time-lapse gravimetric measurements could be considered, especially in cases where time-lapse seismic data offer limited resolution, are difficult to acquire or are simply too costly. Particularly in processes involving a moving gas/liquid contact (e.g., gas and water), time-lapse gravimetric measurements have a potential to provide an additional source of spatial information (see Chapter 2).

In this chapter, we investigate the added value of time-lapse gravimetric measurements for monitoring of water influx into a gas reservoir. For this purpose, a simplified gas-reservoir model with a lateral aquifer influx is used. The synthetic time-lapse surface-gravity observations are assimilated with the EnKF to update the static reservoir parameters (permeability) and determine improved estimates of the water front position. The assimilation process is sequential, i.e., the reservoir models (ensemble members) are updated whenever new observations become available. To evaluate the sensitivity of the results to the experiment setup and to understand the limitations of the gravimetric technique, different scenarios are investigated. For instance, various assumptions about the level of gravimetric noise and the distance from the gravity stations to the reservoir formation are considered. Finally, the effect of a combined assimilation of gravity and production data is examined.

6.2 2D gas reservoir model

We consider a synthetic 2D gas-reservoir model extending from 0 to 3000 m in both the x- and y-directions with a uniform 75 × 75 × 50 m grid-cell size. There are four active gas wells: P1, P2, P3, and P4, producing at maximum gas-rate constraint of 1.5×10^6 m^3/d and at minimum bottomhole pressure (BHP) constraint of 40×10^5 Pa. We consider an active aquifer along the western reservoir border, which leads to a lateral water influx when the reservoir pressure decreases (Fig. 6.1a).

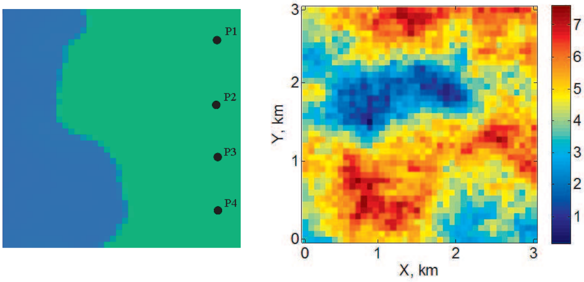

(a) reservoir saturation at 3500 days

(b) reference permeability field

Figure 6.1: Reservoir saturation after 3500 days of simulation (a) and the corresponding reference permeability ($\ln(k)$, where k is the permeability in milidarcies) field (b). In Fig. 6.1a the blue color denotes water, green is gas and the black dots denote the four gas producers.

For simplicity, we assume that the permeability is the main uncertain model parameter, while the porosity is determined using a deterministic functional dependency

$$\phi_i = \frac{\ln(200k_i)}{50}, \tag{6.1}$$

where ϕ_i denotes grid-cell porosity and k_i is grid-cell permeability in milidarcies. A similar approach to relate these two parameters through a deterministic relationship was used by Bianco et al. (2007) for the field-case EnKF application. The permeability there was expressed as a function of porosity, and the dependence was determined using geological information from the core and log data. The poro-perm relationship we use here is close to the one determined for limestone at the Wellington West field (Oliver et al. 2008). The reference permeability field in Fig. 6.1b was generated using a sequential Gaussian simulation (SGSIM) method (Remy et al. 2009), with an isotropic spherical variogram model with a range of 35 grid cells (or 2625 m). Fig. 6.1a

illustrates how the heterogeneities in the permeability field cause an inhomogeneous water front propagation.
The initial ensemble members were generated with the SGSIM method using the same isotropic spherical variogram model and applying a set of values for the variogram range. More precisely, we simulated $N_e = 100$ unconditional permeability fields consisting of five groups with 20 members each, and using variogram ranges of 5, 15, 25, 35, and 45 cells (or 375, 1125, 1875, 2625, and 3375 m), respectively. In practice, not only the magnitude of permeability values is uncertain, but also the scale and location of spatial patterns that may determine the reservoir flow behavior. Therefore, we use different variogram ranges while generating the initial ensemble members to account for the geostatistical uncertainty related to the correlation scales of the unknown permeability field. Examples of one permeability realization for members for each variogram range are shown in Fig. 6.2.

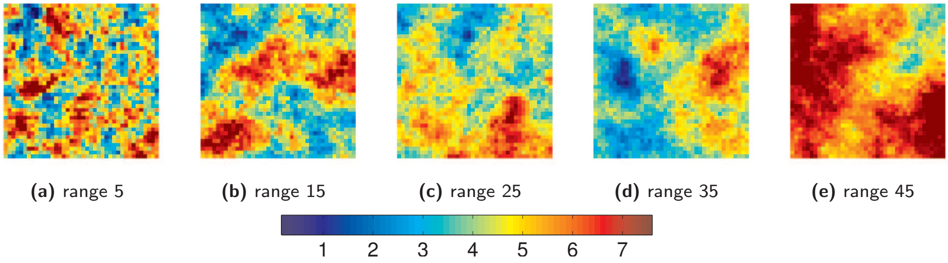
(a) range 5 **(b)** range 15 **(c)** range 25 **(d)** range 35 **(e)** range 45

Figure 6.2: Examples of permeability field realizations (ln(k), where k is the permeability in milidarcies) for different variogram ranges (number of grid blocks).

In this study, the ensemble mean is considered as the best estimate of the reference field. Fig. 6.3 shows the prior ensemble mean and variance. The initial uncertainty over the permeability field is large: the mean is almost constant, with little to no spatial patterns, and the ensemble variance is high (of the same order as the parameter mean value).

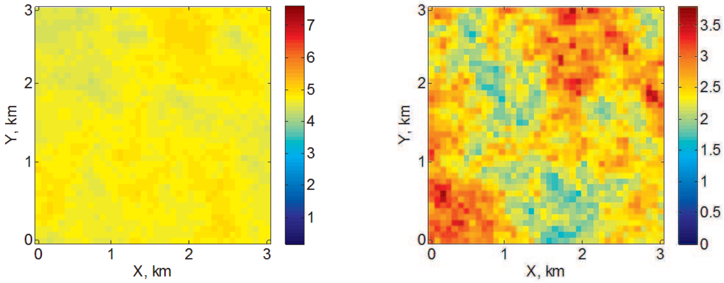
(a) ensemble mean **(b)** ensemble variance

Figure 6.3: The initial ensemble mean and the initial ensemble variance of the permeability field (ln(k), where k is the permeability in milidarcies).

We assimilate the time-lapse gravimetric observations and production data with the EnKF to update the reservoir permeability field and produce improved estimates of the water front position. The reservoir model is propagated forward using a reservoir simulator. To assure physical consistency between the static (permeability) and dynamic variables (pressure, saturation), after each update of the ensemble members, we rerun the reservoir simulator from time zero. Therefore, our problem is reduced to the static parameter estimation only. The state vector consists of a static log-transformed permeability and the synthetic measurements. The following three cases with different input data are considered: only gravity data, only production data, and both types of data. To better understand the influence of gravimetric measurements on the permeability estimate, we start the study with a sensitivity analysis. In the later part, we perform a number of twin experiments using both gravity and production measurements.

6.3 Data assimilation results

6.3.1 Sensitivity to gravimetric observations

The gravity data are assimilated after 1500, 2500, and 3500 days of the reservoir production. The gravity network extends one kilometer beyond (from −1000 m to 4000 m in x- and y-directions) the reservoir boundaries, and contains 900 equally distributed observation points separated by approximately 166 m. The resolution of gravimetric measurements, i.e., the ability to separate two signal-source features (e.g., two zones with mass redistribution in the reservoir) that are close together, is related to the distance (denoted further as *dist*) from the gravity observation network to the signal source. The ratio of the distance to the size (width and length) of the signal source influences to a large extent the capabilities of gravimetric observations to provide spatial information. More precisely, when the distance is much larger than the lateral extension of the body (i.e., the zone with spatial mass redistribution in the reservoir), the resulting gravitational attraction will not differ significantly from the gravitational attraction of a point mass. In such a case, the gravimetric observations will not add spatial information. Therefore, a range of values for *dist*, namely 1.0 km, 1.7 km, and 2.5 km, will be used (Fig. 6.4). To keep the reservoir conditions for all the scenarios similar, we fix the reservoir depth at 2.5 km and move up and down the gravity network by changing the value of variable *dist*. We assume uncorrelated (in space and time), zero-mean Gaussian gravity measurement noise. Here, we investigate two cases: a highly optimistic level of measurement noise with a standard deviation $\sigma_\epsilon = 2\ \mu$Gal and a more realistic noise level with $\sigma_\epsilon = 5\ \mu$Gal. The assumed noise is for a single survey, which means that the temporal gravity variations are computed (we omit here the observation point index) as

$$\triangle g_k = (g_k + X_k) - (g_0 + X_0), \tag{6.2}$$

where $\triangle g_k$ is the temporal gravity variation determined as a difference between the baseline survey at time t_0 and the monitoring survey at time t_k and X_k are the random vectors sampled from a zero-mean Gaussian distribution with the diagonal covariance matrix filled with σ_ϵ^2 entries. The combination of assumptions about observation distance and measurement noise standard deviation provides six scenarios. The most optimistic one combines $\sigma_\epsilon = 2$ μGal with *dist* $= 1$ km and the most pessimistic one $\sigma_\epsilon = 5$ μGal with *dist* $= 2.5$ km. The noise added to the synthetic gravity data is consistent, in a statistical sense, with the gravity noise assumptions used in the EnKF.

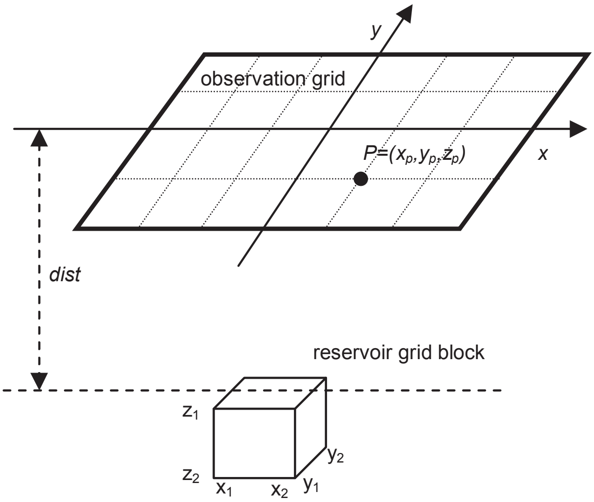

Figure 6.4: Schematic illustration of the acquisition of gravimetric data. The reservoir cells are represented by a number (40×40) of rectangular prisms.. The distance *dist* from the gravity observation network to the reservoir top is varied by shifting the network up and down. We consider *dist* $= 1$ km, *dist* $= 1.7$ km and *dist* $= 2.5$ km. P stands for the gravity observation point.

Fig. 6.5 shows the reference (true) time-lapse mass change after 3500 days of gas production and water influx. The gas takeout creates negative and the water influx creates positive mass variations. In our experiment, water density is approximately

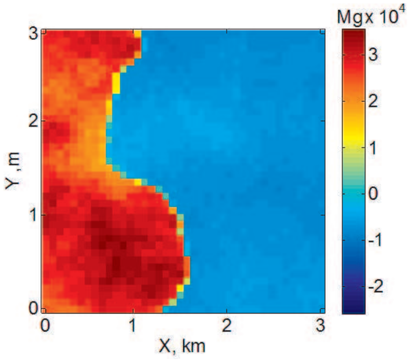

Figure 6.5: Mass change between time t=0 and t=3500 days for the reference model.

six times larger than the density of gas, and, as a consequence, a large mass increase can be observed in the western part of the reservoir where gas is being replaced by water. In the remaining part, the mass change is negative, but its magnitude is much smaller. Therefore, most of the gravimetric signal originates from the waterflooded areas. Consequently, one should expect more accurate permeability estimates in the reservoir regions crossed by the water front. This is confirmed in Fig. 6.6, where the time evolution of the mean of the ensemble log-permeability fields for the two extreme scenarios is presented.

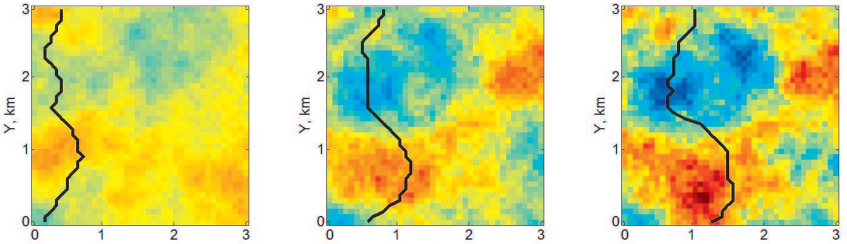

(a) t=1500 days **(b)** t=2500 days **(c)** t=3500 days

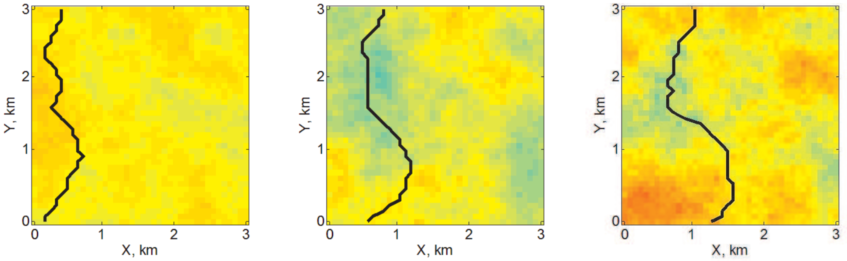

(d) t=1500 days **(e)** t=2500 days **(f)** t=3500 days

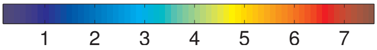

Figure 6.6: The mean ensemble permeability field ($\ln(k)$, where k is the permeability in milidarcies) after different update times. The black curve denotes the reference water front position at that particular time. In the top row the results for the scenario with $\sigma_\epsilon = 2$ μGal and *dist* $= 1$ km are shown and in the bottom row the results for the scenario with $\sigma_\epsilon = 5$ μGal and *dist* $= 2.5$ km.

In the optimistic scenario ($\sigma_\epsilon = 2$ μGal and *dist* $= 1$ km), some of the key parameter features in the waterflooded regions (e.g., location of the high permeability zone) could be reasonably well estimated already after the first update at 1500 days. After the next model updates, the parameter estimate further improves also in the areas, which were not crossed by the water front. This is because gravity field variations induced by gas takeout are larger than the assumed noise level for the two last update times. In the pessimistic scenario ($\sigma_\epsilon = 5$ μGal and *dist* $= 2.5$ km), the mean permeability estimate is significantly less accurate. The parameter estimate becomes smoother. The location of the high permeability zone could be estimated to some extent only at the latest assimilation time at 3500 days and only for the reservoir regions crossed by the front. This is mainly because of the relatively large distance from the gravity observation network to the reservoir top compared to the reservoir size. In this case, the true gravity variation caused by gas takeout is less than the assumed 5 μGal standard deviation of the measurement noise. The maximum variation of the true time-lapse signal is approximately 3 μGal at 1500 days, 7 μGal at 2500 days, and 12 μGal at 3500 days. This is larger than the assumed noise level only at the latest assimilation time (3500 days), making it possible to recover the main permeability features in the western reservoir part.

Fig. 6.7 shows examples of representative ensemble members after the final update. The initial members consist of five groups, each generated with a different variogram range (5, 15, 25, 35, and 45 cells or 375, 1125, 1875, 2625, and 3375 m) and each having 20 members. A comparison of Fig. 6.2 with Fig. 6.7 shows how much the correlation lengths were altered. For the optimistic scenario, the update was significant, and even the members with initially very short variogram ranges seem to match the reference field correctly. This case shows a high information content added by gravity observations. In the other scenario, the results are less promising. The spatial structure of the individual members is not improved significantly.

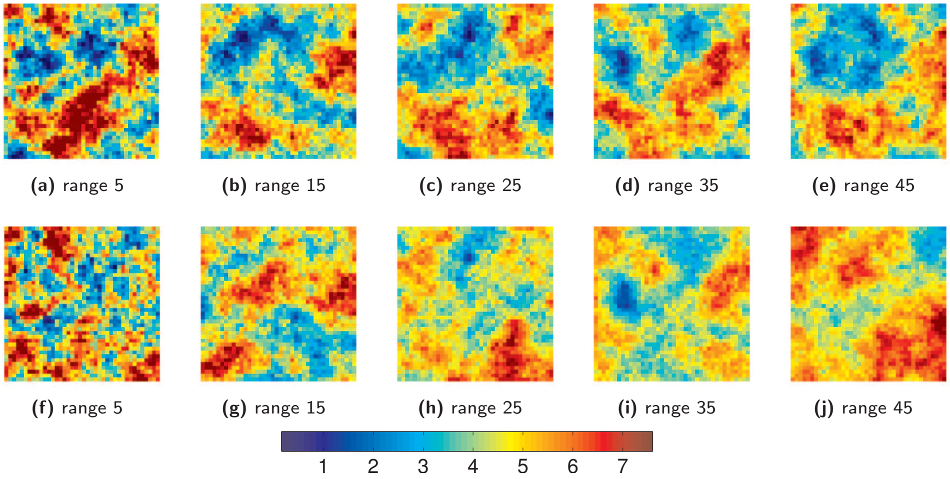

(a) range 5 **(b)** range 15 **(c)** range 25 **(d)** range 35 **(e)** range 45

(f) range 5 **(g)** range 15 **(h)** range 25 **(i)** range 35 **(j)** range 45

Figure 6.7: Representative ensemble members (the same as in Fig. 6.2) after the final update at t=3500 days. In the top row the results for the scenario with $\sigma_\epsilon = 2$ μGal and $dist = 1$ km are shown and in the bottom row the results for the scenario with $\sigma_\epsilon = 5$ μGal and $dist = 2.5$ km.

Fig. 6.8 shows how the ensemble variance of the permeability is reduced in time. As expected, in the optimistic scenario it is significantly lower than in the less favorable scenario. The variance is reduced not only in the waterflooded areas, but also in the negative mass change zone. On the other hand, in the pessimistic scenario, the model is mostly updated in the regions crossed by the water front, leaving very high uncertainty over the possible permeability structures in the remaining part of the reservoir formation.

In Fig. 6.9, we present a brief summary of the results for all the six scenarios consid-

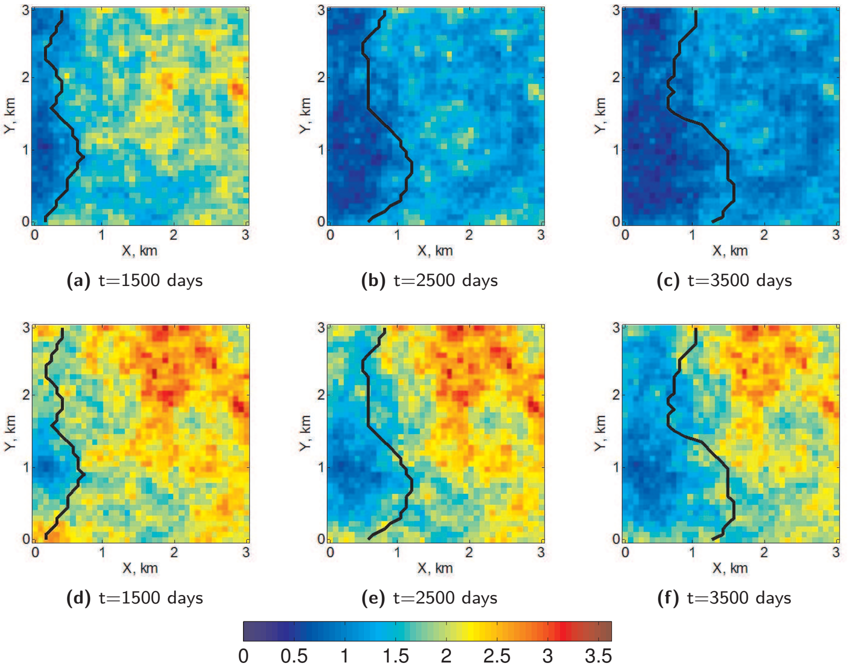

(a) t=1500 days **(b)** t=2500 days **(c)** t=3500 days

(d) t=1500 days **(e)** t=2500 days **(f)** t=3500 days

Figure 6.8: The variance of the ensemble field ($\ln(k)$, where k is the permeability in milidarcies) after different update times. In the top row the results for the scenario with $\sigma_\epsilon = 2$ μGal and $dist = 1$ km are shown and in the bottom row the results for the scenario with $\sigma_\epsilon = 5$ μGal with $dist = 2.5$ km are presented. The black curve denotes the reference water front position at that particular time.

ered. It shows the root mean square error (RMSE) of the estimated mean permeability field as well as the correlation between the estimated mean and reference permeability fields. The results are presented separately for the waterflooded and dry areas. As expected, the RMSE is reduced more for the reservoir region crossed by the water front than for the remaining part of the reservoir. The RMSE rapidly decreases after the first assimilation of gravity data and then either slightly increases or remains stable. The correlation coefficient shows in general a gradual improvement with a maximum value of approximately 0.8. For the regions which were not crossed by the front, these estimates are not significantly improved except for the smallest distance to the reservoir.

To evaluate the history match of the reservoir model, we restart the reservoir simulator with the updated mean permeability field to determine the estimate of the water front position. Fig. 6.10 shows that in the optimistic scenario, the water front configuration could be tracked very well throughout all the assimilation times. The estimate matches the truth closely, and the initial average standard deviation of the water front position is reduced from approximately 380 m to approximately 150 m after the final update. For the pessimistic scenario, the front position is reasonably matched only after the last assimilation time. Here, the average standard deviation

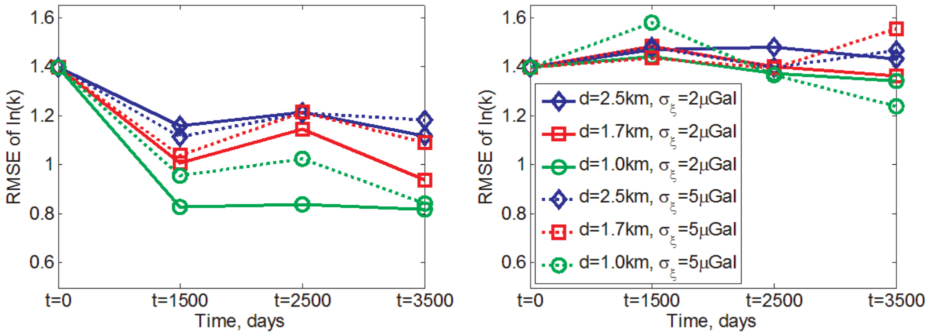

(a) RMSE, front crossed **(b)** RMSE, front not crossed

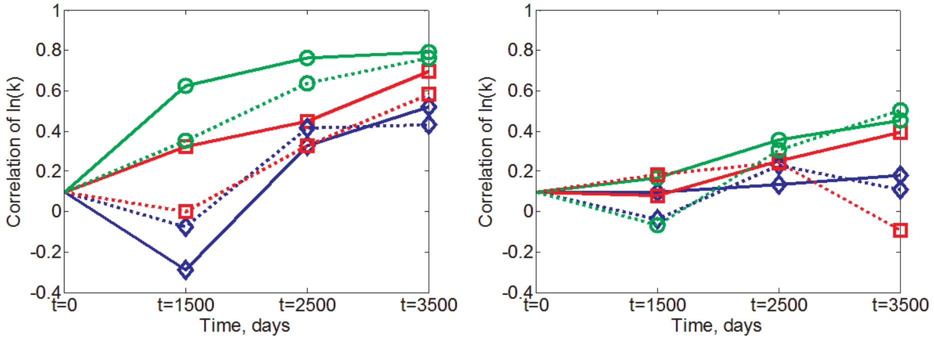

(c) corr., front crossed **(d)** corr., front not crossed

Figure 6.9: The RMSE (top row) and correlation coefficient (bottom row) in time for the all the scenarios considered. In the left column results for reservoir regions crossed by the water front are shown and in the right column for the remaining part of the reservoir. Note that the reservoir region crossed by the front changes in time.

is reduced to approximately 290 m.

Fig. 6.11 shows the RMSE between the reference and estimated water front position at 3500 days. The RMSE is reduced from approximately 300 m to approximately $90 - 110$ m in the case of $dist = 1$ km , and for the remaining cases to values between $190 - 210$ m. Such a difference is caused by the fact that only for $dist = 1$ km the main low permeability zone in the middle of the reference field (see Fig. 6.1b) was recovered. For the remaining cases, only the high permeability zone in the region crossed by the front was estimated reliably. It is important to note that these two extreme permeability zones determine to a large extent the position of the water front at 3500 days.

The effect of increasing the noise from 2 μGal to 5 μGal seems to be limited. Despite some differences in the permeability estimate (compare the final RMSE and correlation values in Fig. 6.9), the reproduced positions of the water front are fairly similar. This is because of the physical properties of the flow: the main pattern of the flow is

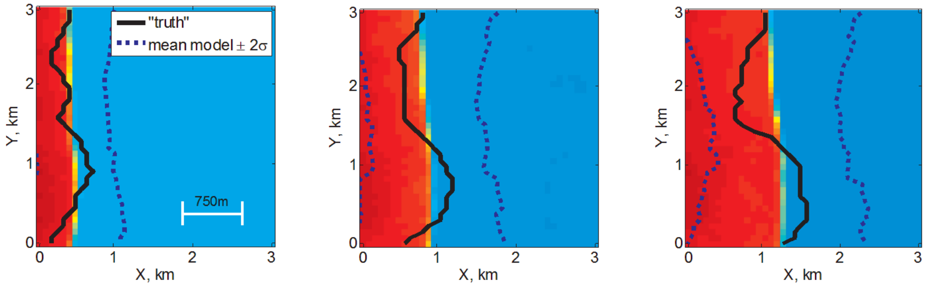

(a) t=1500 days **(b)** t=2500 days **(c)** t=3500 days

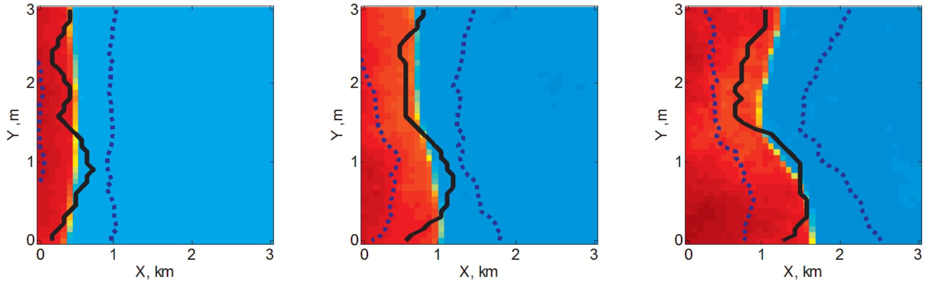

(d) t=1500 days **(e)** t=2500 days **(f)** t=3500 days

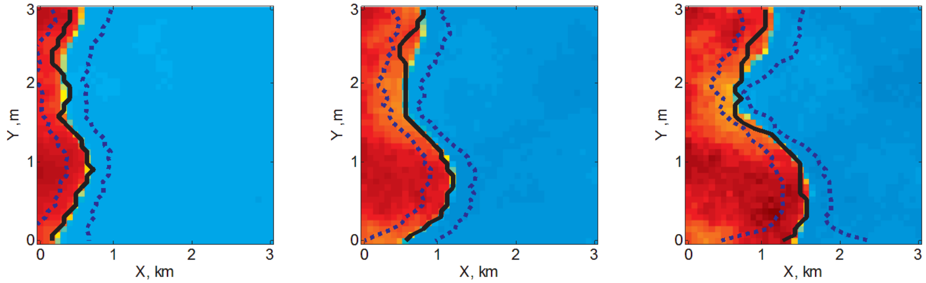

(g) t=1500 days **(h)** t=2500 days **(i)** t=3500 days

Figure 6.10: Mass change estimates in time with respect to the initial conditions. In the top row results for the initial ensemble members (no assimilation of gravimetric observations) are shown. In the middle row results for the scenario with $\sigma_\epsilon = 5$ μGal and $dist = 2.5$ km and in the bottom row results for the scenario with $\sigma_\epsilon = 2$ μGal and $dist = 1$ km are presented. The black curve denotes the reference water front position, the blue dotted curve is the estimated front position $\pm 2\sigma$, where σ is the ensemble members standard deviation of the front position. The color scale is the same as in Fig. 6.5.

relatively insensitive to small scale random perturbations of the permeability. Therefore, because the time-lapse gravity is sensing temporal mass variations induced by the flow, we should not expect that the permeability estimate fits the reference model in the pixel-wise sense.

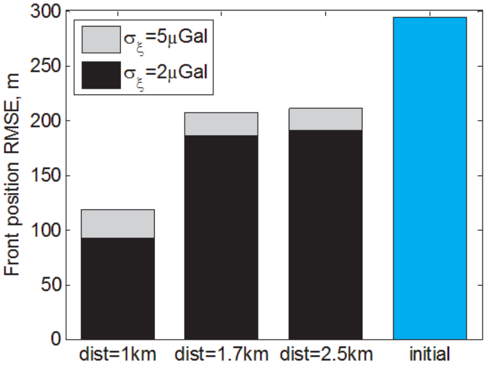

Figure 6.11: The RMSE of the estimated water front position for time 3500 days.

We simulated the synthetic gravity observations on a relatively dense network consisting of 900 stations with approximately 166 m measurement spacing. In practice, however, a coarser gravity measurement network is more common. To test the impact of the survey design, we repeated the experiment with the most optimistic ($\sigma_\epsilon = 2$ μGal, $dist = 1$ km) and most pessimistic ($\sigma_\epsilon = 5$ μGal, $dist = 2.5$ km) scenarios using only 100 gravity stations with 500 m measurement spacing. In Fig. 6.12, the final permeability estimate and its ensemble variance are presented. The parameter estimate is similar to the case with 900 gravity observation points (see Fig. 6.6), but, as expected, the parameter variance scales with the inverse square root of a number of data points, and therefore, is approximately $2 - 3$ times larger (see Fig. 6.8).

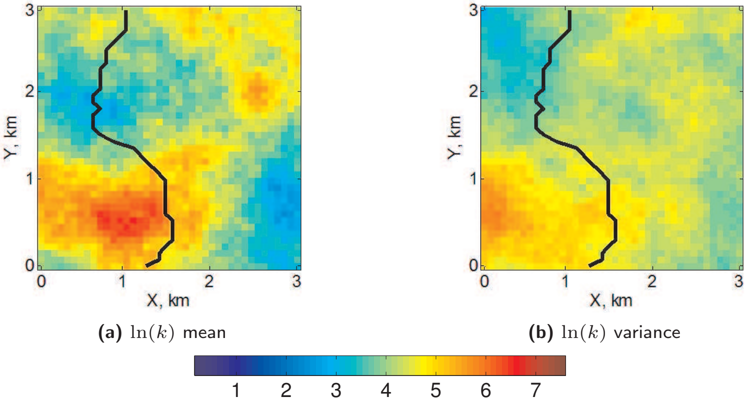

(a) $\ln(k)$ mean

(b) $\ln(k)$ variance

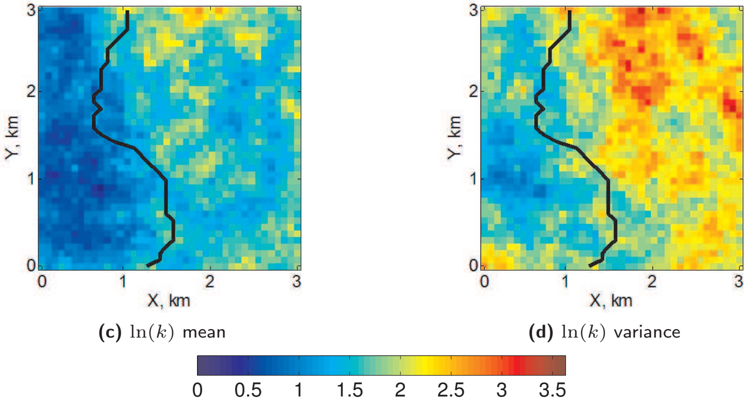

(c) $\ln(k)$ mean

(d) $\ln(k)$ variance

Figure 6.12: The ensemble mean (top row) of $\ln(k)$ and the ensemble variance (bottom row) of $\ln(k)$ after final assimilation of 100 gravity observations at t=3500 days (k is the permeability in milidarcies). In the left column the results for the scenario with $\sigma_\epsilon = 2$ μGal and $dist = 1$ km (a-c) and in the right column with $\sigma_\epsilon = 5$ μGal and $dist = 2.5$ km (b-d) are shown, respectively.

6.3.2 Joint assimilation of production and gravity data

In this section, we investigate the effect of assimilation of the gravity and production data on the permeability and the water front position estimates. We simulate 900 gravity observations, and consider the scenario where the distance from the gravity observation network to the reservoir top is $dist = 1.7$ km and the gravity measurement noise standard deviation is $\sigma_\epsilon = 5$ μGal. Compared to the scenarios analyzed in the previous section, this configuration can be considered as intermediate with respect to the parameter *dist* while the noise level stays at the upper bound of the range.

The data assimilation window is as before from time 0 to 3500 days. Production measurements are the gas rate and BHP from the four producers and are generated by running the reference model and adding 5% zero-mean Gaussian noise to the synthetic observations. As in the previous experiment, the noise assumptions used for the EnKF algorithm are consistent with the actual noise contaminating the data. The production data are assimilated every 90 days, and, as in the previous section, the time-lapse gravity data are assimilated at 1500, 2500, and 3500 days.

Localization

The limited number of ensemble members may lead to spurious correlations in the approximation of the state covariance matrix. This problem is especially common when the covariances between single measurements, such as well production data, and the parameters of the whole reservoir grid are inferred. In Fig. 6.13, the cross-correlation between the production data of the producer P1 and reservoir (log–) permeability for a different number of ensemble members is plotted.

For 100 ensemble members we observe some strong correlation patterns located far from the producer which are not present when the number of ensemble members is doubled. As a result of the inaccurate covariance approximation, the corresponding Kalman gain estimate may lead to the parameter updates in the region of no real influence of a particular observation. To resolve this problem, covariance localization is often applied by using the Schur product of the state covariance matrix with the localization function (Hamill et al. 2001, Houtekamer & Mitchell 2001). Then the Kalman gain is calculated (we omit the time index) as

$$\mathbf{K} = (\rho \circ \mathbf{C}_\Psi^f)\mathbf{H}^T \left[\mathbf{H}(\rho \circ \mathbf{C}_\Psi^f)\mathbf{H}^T + \mathbf{C}_y\right]^{-1}, \tag{6.3}$$

where $\circ$ represents the Schur product (i.e., the element-wise matrix product). We use the distance-based localization function (Furrer & Bengtsson 2007)

$$\rho(h) = \frac{1}{1 + (1 + f(0)^2/f(h)^2)/N_e}, \tag{6.4}$$

where f is the covariance function, h is the distance, and N_e is the number of ensemble members. We model the covariance between production data and permeability using the exponential covariance function

$$f(h) = \exp(-3h/\theta), \tag{6.5}$$

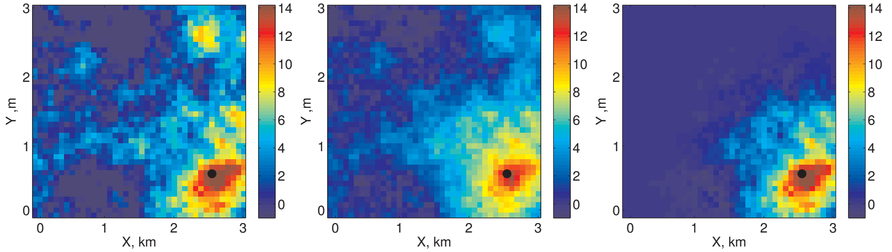

(a) BHP, $N_e = 100$ **(b)** BHP, $N_e = 200$ **(c)** BHP, $N_e = 100$, localization

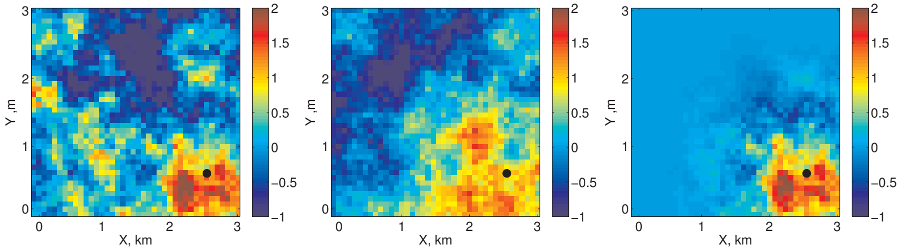

(d) GAS, $N_e = 100$ **(e)** GAS, $N_e = 200$ **(f)** GAS, $N_e = 100$, localization

Figure 6.13: Example of cross-correlation between $\ln(k)$ and BHP (k is the permeability in milidarcies) at time 270 days, and between gas rate and $\ln(k)$ at time 1800 days. In the left column the results for 100 ensemble are shown, in the middle column the results for 200 ensemble members are shown and in the right column the results with 100 ensemble members in case of localization are shown, respectively. The black dot denotes the position of the producer P1.

where θ is the correlation range. To localize the production data, we use $\theta = 1500$ m. The corresponding covariance function $f(h)$ and the localization function $\rho(h)$ are shown in Fig. 6.14. The example of localized covariances is presented in Fig. 6.13c-6.13f.

In Fig. 6.15 the cross-correlation between (log–) permeability and gravity data is presented for time $t = 3500$ days and two different gravity observation points.

First, we can observe that the results for 100 ensemble members slightly underestimate the cross-covariance compared to the case with 200 ensemble members. Furthermore, it is interesting to note that the cross-correlation pattern coincides with the reservoir mass redistribution pattern (see Fig. 6.5), i.e., the cross-correlation is positive for the waterflooded regions (crossed by the water front) with the positive mass change and is negative for the regions affected by gas takeout (negative mass change). This is because the higher the permeability (and hence the porosity via relation (6.1)) in the waterflooded part of the reservoir the more the positive mass change in those regions and the stronger the positive temporal gravity variation. Similarly, the higher the permeability (porosity) in the regions affected by gas takeout the larger the negative mass change there and the larger the negative variation in the local gravity field. Hence, it is clear that the correlation between gravity and reservoir permeability (porosity) is not only a function of distance (from observation point to the reservoir

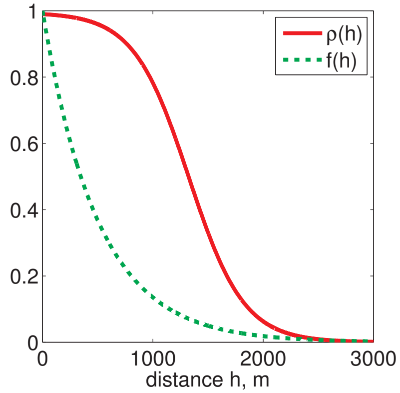

Figure 6.14: The permeability covariance function $f(h)$ and the localization function $\rho(h)$ for $\theta = 1500$ m.

body) but also depends on the subsurface mass redistribution pattern which, in practice, is uncertain. Therefore, a distance-based localization is not applicable in this case because, when using a fixed cut-off radius, physically meaningful correlations could be tempered. From that reason, and also due to the fact that with already 100 members a reasonable approximation of the cross-covariance is obtained, no localization of gravity data is used in this study.
To investigate the contribution of the production and gravity data to the permeability estimate, we consider four cases with different data being assimilated: only production data with and without localization; only gravity data; and production data with localization and gravity data. Fig. 6.16 shows the history match to the synthetic data for the producer P1. The predicted data result from re-running the reservoir model from time zero with the final estimates of the permeability field. In all cases, except the scenario where only the gravity data are assimilated, the history match is satisfactory. The measurement predictions from the updated members and from the mean model follow the reference predictions very closely. As expected, when localization is applied, the spread of the ensemble predictions slightly increases. This spread is reduced when additionally gravity data are used. For the other producers, we observed very similar results.

In Fig. 6.17, the final permeability estimates are shown. We see that despite a very similar history match of the production data, they are significantly different. This demonstrates clearly the non-uniqueness of the problem we deal with. When only the production data are assimilated, the permeability estimates are acceptable only for the regions within a range of approximately 1500 m from the wells. When no localization is applied, the estimate in the more distant regions is inaccurate. On the other hand, localization prevents any significant updates there. When only the gravity data are used, some of the main features of the permeability can only be recovered for the regions crossed by the water front. Combining both data sets gives satisfactory results for the whole reservoir grid. Fig. 6.18 shows how the accuracy of the permeability estimate translates into matched and forecasted positions of the water front. It is clear

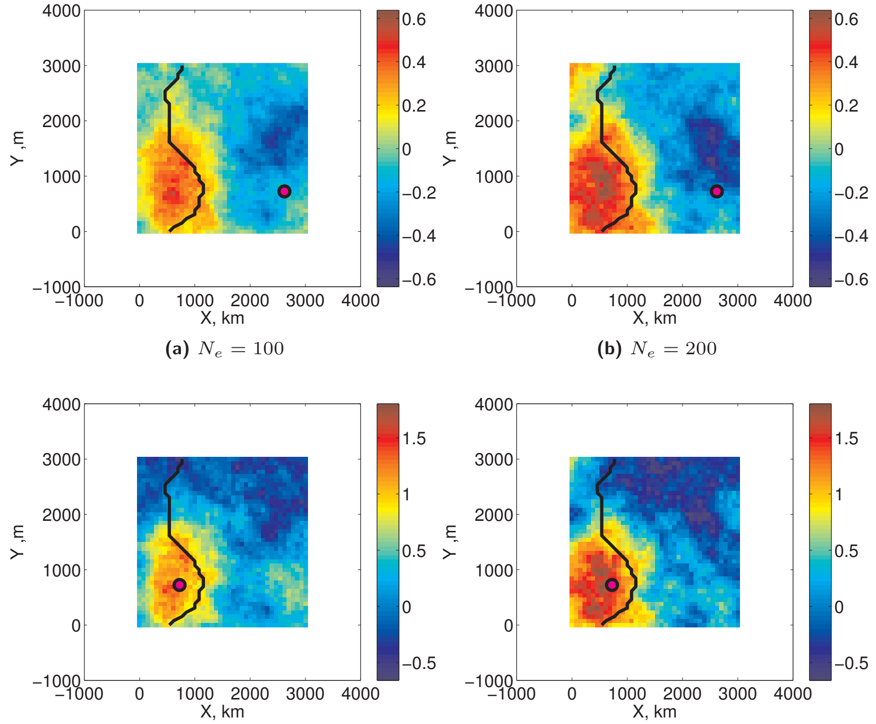

(a) $N_e = 100$ **(b)** $N_e = 200$

(c) $N_e = 100$ **(d)** $N_e = 200$

Figure 6.15: Example of cross-correlation between $\ln(k)$ and gravity data (k is the permeability in milidarcies) at time 3500 days. In the left column the results for 100 ensemble are shown and in the right column the results for 200 ensemble members. The black curve denotes the water front position at that time. The pink dot denotes the position of the gravity station.

that production data alone cannot provide sufficient information to track the water front position accurately. Only when the gravity data are used the front position can be history matched. Furthermore, the scenario combining both data types gives the most accurate results in terms of the forecasted front positions, as shown in Fig. 6.19.

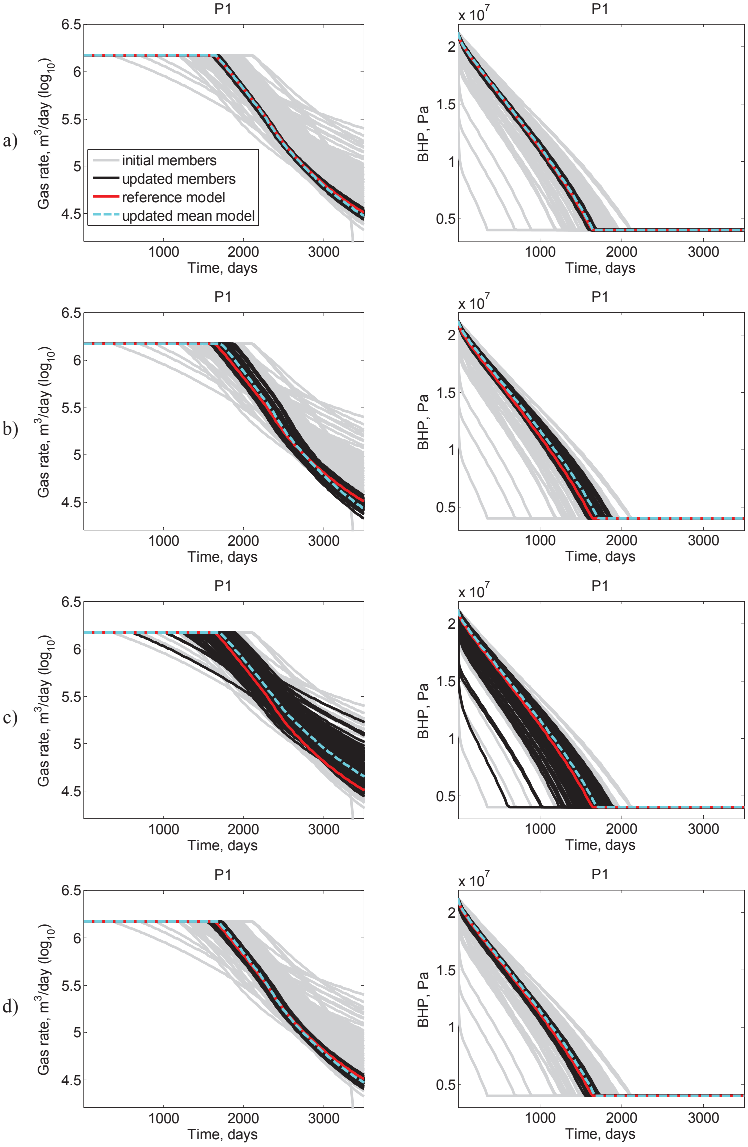

Figure 6.16: History-match to production data versus different data assimilated: a) only production data without localization; b) only production data with localization; c) only gravity data; d) both types of data with localization of the production data. The predicted data result from re-running the reservoir model from time zero with the final (and initial) estimates of the permeability field.

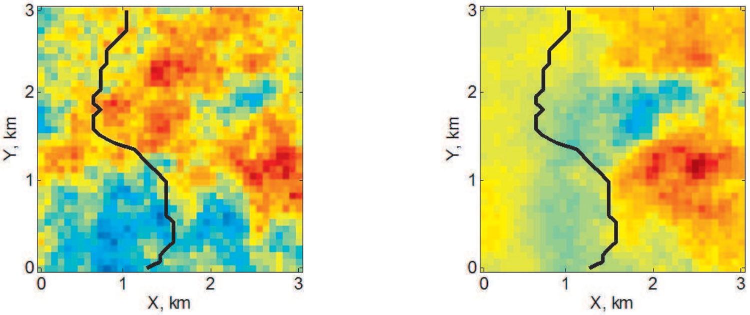

(a) only prod. data

(b) only prod. data + localization

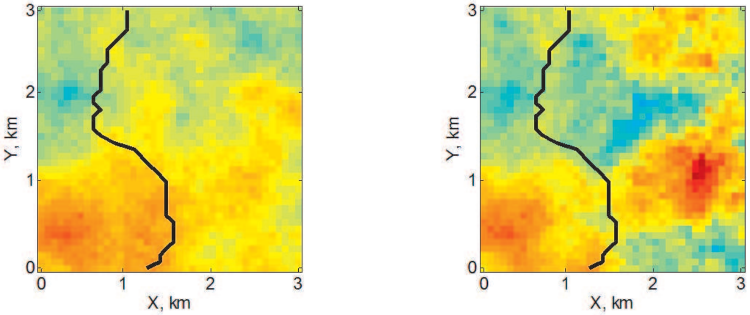

(c) only gravity data

(d) gravity and prod. data + localization

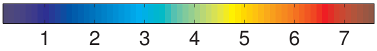

Figure 6.17: The mean ensemble $\ln(k)$ field (k is the permeability in milidarcies) after the final update at 3500 days versus different data assimilated.

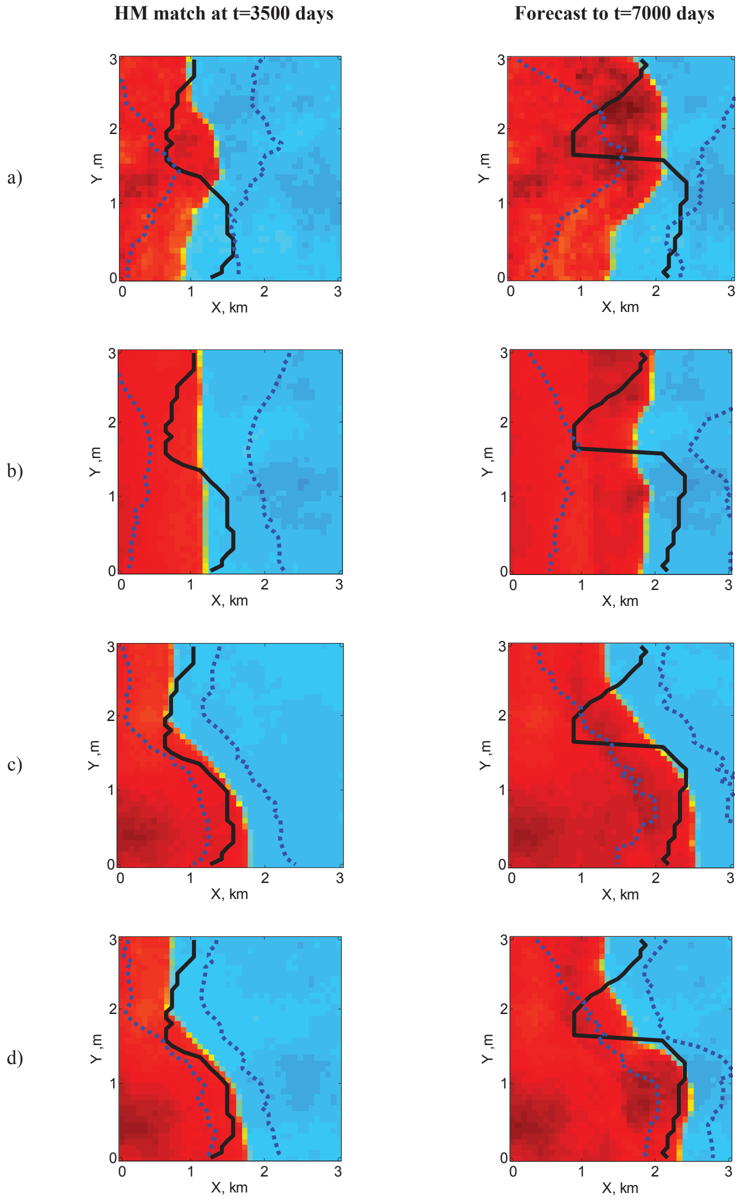

Figure 6.18: Mass change estimates with respect to the initial conditions for different data assimilated: a) only production data without localization: b) only production data with localization; c) only gravity data; d) both types of data with localization of the production data. The black curve denotes the reference water front position, the blue dotted curve is the estimated front position $\pm 2\sigma$, where σ is the ensemble members standard deviation of the front position. The color scale is the same as in Fig. 6.5.

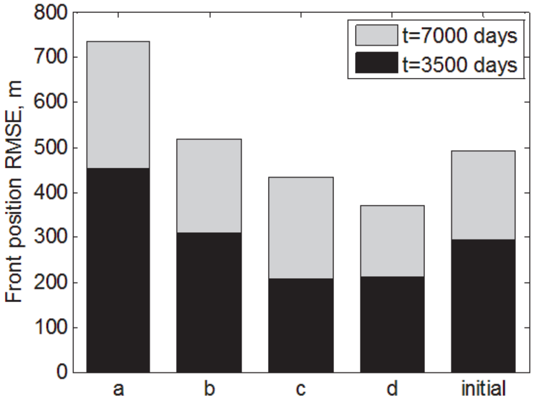

Figure 6.19: The RMSE of the estimated water front position at the end of a history match (3500 days) and for the model forecast (7000 days) versus different data assimilated: a) only production data without localization; b) only production data with localization; c) both types of data without localization; d) both types of data with localization of the production data.

6.3.3 Discussion

To simplify our experiments, we made a number of assumptions. For instance, for the assimilation of gravity data with the EnKF, we assumed perfectly known statistical properties of the measurement noise. We simulated stationary and spatially uncorrelated Gaussian noise with a known covariance structure. The covariance matrix that describes measurement uncertainty was fully consistent with the actual noise added to the synthetic data. This guaranteed an optimal performance of the filter. In practice, however, the noise can be correlated. Moreover, the noise characteristics are uncertain and may not match the assumptions used for the EnKF algorithm. Using the Lorenz-96 model with 40 variables, Miyoshi et al. (2009) showed that the analysis results could be deteriorated when the assumed noise covariance matrix is inconsistent with the actual noise contaminating the data. Because gravity measurements reflect the overall mass changes, many environmental processes and especially spatiotemporal hydrological variations can contaminate gravity data with correlated noise (see Chapter 3 of the thesis and, e.g., Glegola et al. 2009). Therefore, it requires further research to assess how the filter performance can be degraded by errors in the stochastic model, how this affects the added value of gravity data, and how to estimate the unknown gravity noise characteristics properly.

We based our experiments on a simplified 2D gas reservoir model, where a deterministic relationship was used between the porosity and the permeability fields, and the aquifer support was fixed and perfectly known. To investigate the added value of gravity in a more realistic setting, in Chapter 7, we extend our study to a more realistic 3D case, where not only porosity and permeability are uncertain parameters, but also aquifer support characteristics and reservoir structure are considered unknown.

6.4 Summary

In this chapter, we investigated the added value of time-lapse gravimetric observations for the monitoring of water influx into a gas reservoir. We assimilated synthetic gravity and production data with the EnKF method to estimate the reservoir permeability and to predict the water front position. We started with a sensitivity study using the gravity data only. By varying the level of gravity measurement noise and the distance to the reservoir, we found that an increase in the noise level and/or distance leads to a smoother parameter estimate with a higher variance. We demonstrated how the subsurface mass redistribution induced by the water influx, and sensed by time-lapse gravity, can be translated into a better knowledge about the reservoir permeability with the EnKF inversion. The updated permeability can be further used to improve forecasts of the actual mass redistribution and to decrease the uncertainty about the water front configuration. We showed that the RMSE of the water front position can be reduced even for deep reservoirs and realistic noise levels in gravity data. The added value of gravity data has clearly been demonstrated. On the other hand, when only the production data were used, the permeability field could not be estimated accurately in the regions distant from the producers. Consequently, very erroneous estimates of the water front position were obtained. We showed that despite a satisfactory history match of production data, without additional information, here provided by the gravity data, the inferred reservoir state may be very far from the truth. We demonstrated that production and time-lapse gravity observations are complementary sources of information, which, when combined within a data assimilation framework, can provide a considerably improved picture of reservoir permeability and a better understanding of the subsurface mass redistribution.

Chapter 7

Case study 2–History-matching time-lapse surface gravity and well pressure data for estimating gas field aquifer support: a 3D numerical study with the ensemble smoother

In this chapter we investigate the added value of gravimetric observations for gas field production monitoring and aquifer support estimation. We perform a numerical study with a realistic 3D gas field model which contains a large and complex aquifer system. The aquifer support along with other reservoir parameters, i.e., porosity, permeability, and reservoir top and bottom horizons are simultaneously estimated using the ensemble smoother (ES). We consider three cases where only gravity, only pressure and both gravity and pressure data are assimilated. We show that a combined estimation of the aquifer support with the permeability field, porosity field and reservoir structure is a very challenging and non-unique history matching problem, where gravity certainly has an added value. Pressure data alone may not discriminate between different reservoir scenarios. Combining pressure and gravity data may help reducing the non-uniqueness problem and provides not only an improved gas and water production forecast and gas-in-place evaluation but also a more accurate reservoir state description. The content of this chapter is to a large extent based on (Glegola et al. 2012b).

7.1 Introduction

Water influx is an important factor influencing production of gas reservoirs in many aspects. First, the encroaching water can trap and/or bypass gas volumes and, therefore, can reduce the ultimate field recovery. Secondly, an aquifer influx can lead to an early water breakthrough causing well operational problems (see, e.g., Veeken et al. 2000). In some cases, a high degree of pressure support provided by a strong aquifer may extend the reservoir life and turn out to be beneficial. The actual gas yield depends on the interplay of aquifer flooding characteristics (such as aquifer size, residual gas saturation, volumetric sweep) and the level of a reservoir abandonment pressure (Dake 2001). Furthermore, characterization of a reservoir drive mechanism (volumetric depletion or water-drive) and a reliable estimation of the amount of water influx is crucial for an accurate gas reserves estimation. Gas initially in place (GIIP) is commonly derived by means of the material balance analysis where the cumulative water influx is one of the relevant input parameters. In practice however, due to the lack of measurements, large uncertainties about aquifer characteristics and, consequently, about water influx are common. No direct measurements of aquifer properties are available and they must be inferred from other, mostly pressure data. It may be challenging to discriminate between a larger gas reservoir with no aquifer support and a smaller gas reservoir with much aquifer activity since both may provide a similar pressure response, especially the in early reservoir life. Diamond & Ovens (2011) showed how ambiguous interpretations of results of a gas material balance analysis can arise when compartmentalized or water-drive reservoirs are considered. The deviation from an idealized tank-like reservoir behavior may be caused by non-homogenous pressure communication and/or by water influx from a surrounding aquifer. Pressure data alone may not be sufficient to uniquely discriminate between these two scenarios and there is a need for complementary information. Time lapse (4D) gravimetry, which is a direct measure of a subsurface mass redistribution, has the potential to provide independent and valuable information on water influx into a gas reservoir.

Often, in computer-assisted history matching applications one updates reservoir model states, e.g., pressures and saturations, static reservoir parameters such as permeability and porosity, and since recently, also fluid contacts and structural parameters. Although large uncertainties are associated with the reservoir aquifer characteristics, the aquifer support is typically fixed and assumed to be known in history-matching experiments. For gas fields however, the influence of aquifer support can be very significant and, therefore, it should be appropriately accounted for in reservoir history-matching workflows. In this chapter we extend the work presented in Chapter 6 where gravimetric observations were assimilated with the EnKF for water influx monitoring into a gas field. On a simplified 2D gas reservoir model it was shown how mass redistribution in the subsurface, as directly sensed by gravimetry, can be translated through the EnKF inversion into an improved estimation of the reservoir permeability field and, consequently, into the estimation of the water front position. In Chapter 6 the permeability field was considered the only uncertain parameter whereas the aquifer support was fixed and assumed perfectly known. In this chapter, we present a more realistic synthetic 3D example inspired by some of the North Sea gas fields. This 3D example is not an exact copy of an existing field but reflects some of the typical

North Sea gas field features like: a clustered and limited number of wells, seasonal variability in gas production, and the uncertainty over the aquifer support. The key field uncertainties addressed in this study are not only the permeability field but also the porosity field, reservoir structural parameters and foremost the aquifer support characteristics. The reference field (or the truth case) includes an explicitly modeled complex, heterogeneous aquifer system and contains about 60000 cells, whereas the ensemble models contain only the field fraction with the gas reservoir and consist of about 5000 cells each. Note that the ensemble members do not contain an aquifer explicitly; the aquifer response is modeled as boundary conditions using an analytical aquifer model. Mostly due to the computational efficiency we use the ES rather than the EnKF as an assimilation method. We compare scenarios where only gravity, only production and both production and gravity data are assimilated. The added value of gravity data is evaluated in the context of various reservoir engineering aspects, such as reservoir characterization, reservoir state description, forecast reliability and gas reserves estimation.

In this chapter we investigate the added value of time-lapse gravimetry for a gas reservoir characterization and monitoring. We start with an overview of the modeling workflow for the aquifer support estimation. Then, the setup of a comprehensive 3D gas field model and data assimilation results with and without gravity data are shown and discussed. Next, the sensitivity of the results on gravity data noise assumptions and the magnitude of aquifer modeling errors are presented.

7.2 The Modeling Workflow

Fig. 7.1 illustrates the conceptual workflow for estimating an aquifer support along with other reservoir parameters such as those related to a reservoir structure (e.g., top and bottom horizons) or petrophysical properties (e.g., permeability and porosity). In the first step of the workflow, the prior uncertainty over the aquifer is modeled. Since in practice aquifer systems can be very large, complex structures with many uncertainties, a complete, grid block-based aquifer modeling and property estimation is very challenging. Therefore, a semi-analytical approach is proposed for the aquifer support estimation. This approach combines a 1D analytical model response to simulate the amount of water influx into the reservoir with a gridlock-based simulation of that water flow within the reservoir. The aquifer water influx simulation is based on an ”in-house” version of the Van Everdingen-Hurst Unsteady-State (Van Everdingen & Hurst 1949) analytical model which is fully integrated in the reservoir simulator that we use. The Van Everdingen-Hurst methodology provides exact solutions to diffusivity equations used for the water influx calculations and, therefore, is considered a correct technique for the water influx modeling (Ahmed 2006). However, the approach proposed here for the aquifer support estimation is general and, depending on the availability, other analytical aquifer models (e.g., the pot aquifer model and Carter-Tracy water influx model, see, e.g., Ahmed 2006) can also be applied.

We start by generating the ensemble realizations of the primary aquifer parameters, i.e., aquifer size (length, width, thickness) and 1D distribution of petrophysical properties (permeability, porosity and compressibility). The realizations are used as

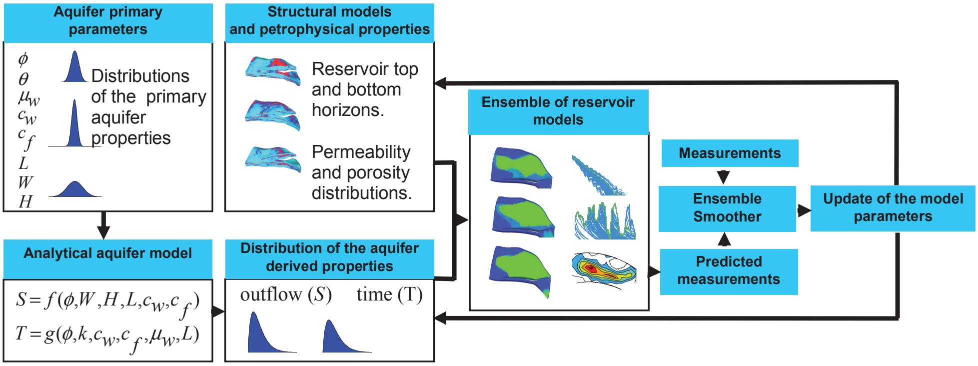

Figure 7.1: The workflow for estimation of an aquifer support and other reservoir parameters.

input to the analytical aquifer model to compute the distribution of aquifer response parameters. The approximation of the aquifer influence is represented by two model-derived parameters, i.e., aquifer outflow S and aquifer time T, which are functions of the primary aquifer parameters.[1] The parameter S (m^3/bar) describes how much cumulative outflow corresponds to the pressure drop, whereas T (day) describes how fast the aquifer reacts to the reservoir pressure change. For every grid block at the reservoir boundaries the 1D aquifer model simulates the amount of water entering the reservoir through that grid block as reservoir pressure drops. The aquifer response is computed assuming a linear water-drive (a box aquifer model, Ahmed 2006). In practice, infinitely many combinations of the basic aquifer properties exist which can result in the same aquifer behavior. Therefore, in our experiments we estimate directly the relevant aquifer response parameters rather than the primary aquifer parameters. Another step in the workflow includes the structural and petrophysical prior uncertainty modeling. The initial uncertainty over the reservoir structure is expressed by alternative realizations of reservoir top and bottom horizons. The other structural parameters (e.g., faults) are not considered in this study. Therefore, only a subset of the possible uncertainty in the reservoir structure is addressed. For a simulation and estimation of the reservoir top and bottom horizons we follow the approach proposed by Seiler et al. (2010). The alternative reservoir top and bottom horizons are simulated around the base-case model, which typically would be a result of seismic data processing and interpretation. The inputs to the simulation algorithm are the base-case reservoir top and bottom together with the associated uncertainty estimate and the correlation structure. The model structure is updated with an "elastic grid" approach as used in Seiler et al. (2010). The reservoir grid is stretched appropriately to match the reservoir top and bottom keeping the number of grid blocks fixed. Further, the initial ensemble of reservoir models is propagated forward with the reservoir simulator. Based on the mismatch between the synthetic and measured data, the ensemble models are updated accordingly with the ES equations (see Chapter 4).

---

[1] due to copyrights the exact equations cannot be shown

7.3 3D gas field model

A synthetic 3D gas reservoir model (Fig. 7.2) is considered. The field is a dipping half-dome structure containing the gas reservoir at the top, which is surrounded by a large aquifer system. The field, which includes the reservoir and the aquifer, is characterized by heterogeneous permeability and porosity (Fig. 7.3) which affects the amount of water influx into the reservoir and its spatial distribution. The dimensions of the field model are about 55 × 19 km, the average thickness is about 80 m, the average depth (distance to the formation top) is about 1250 m. The model is represented with $139 \times 48 \times 9$ grid blocks. The gas reservoir has dimensions of about 15×5 km and the aquifer area is about 900 km^2. The reservoir is produced with 8 gas wells operating under fixed, cycling production conditions which reflects typical seasonal gas demand variations, i.e., the field is produced at higher rates during the winter than during the summer months. The maximum water production constraint is 6000 m^3/day. The well flow is constrained to a minimal bottomhole pressure of 40 bar[2] and whenever the well flow pressure drops below this level the producer gas rate is reduced accordingly.

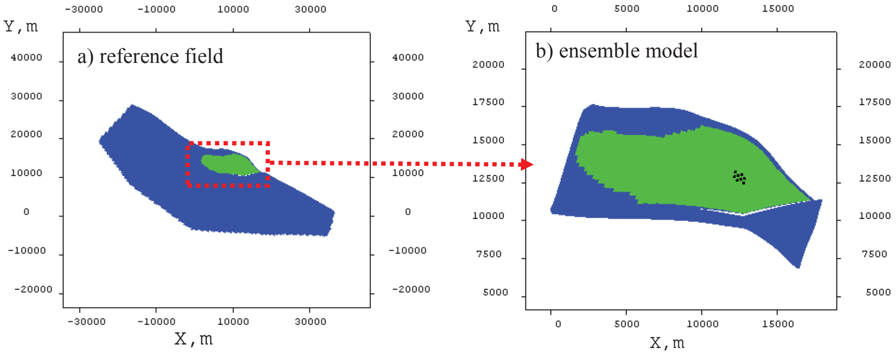

Figure 7.2: Layout of the reference field (a) and the reservoir model used for ensemble members simulation (b). The blue color denotes water and the green is gas. The reference field contains the gas reservoir and the grid block-based aquifer system which is not present in the ensemble model. There, the aquifer support is simulated with the analytical model. The black dots denote the location of gas producers.

In this experiment we use 197 ensemble members. For all the ensemble members the aquifer support, i.e., the amount of water influx into the reservoir, is simulated with the proposed semi-analytical approach (Fig. 7.1). Consequently, the ensemble members are constructed with less grid blocks, namely 38 × 14 × 9 and essentially contain only the gas saturated field fraction (see Fig. 7.2). The initial realizations of

---

[2] 1 bar=14.5038 PSI

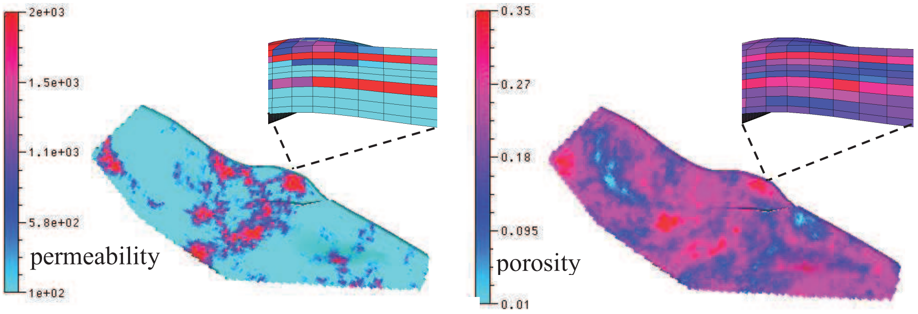

Figure 7.3: The permeability (in milidarcies) and the porosity field of the reference model. In the upper right corner the cross-section through the small part (7 grid blocks) of the field is shown.

the aquifer input parameters are sampled from uniform distribution with statistics summarized in Tab. 7.1. The alternative realizations of the reservoir top and bottom horizons are simulated assuming 10 m (standard deviation) uncertainty of the base-case model and are conditioned to well picks data. All realizations are generated with the Sequential Gaussian Co-Simulation (SGCOSIM) method (Remy et al. 2009) with an isotropic spherical variogram model with 10 cells range (about 3.9 km) and the correlation between the top and bottom horizons of 0.6. Preserving to some degree a correlation between the generated top and bottom structure deviations allows maintaining the overall reservoir thickness. The generated realizations are shown in Fig. 7.4.

Table 7.1: Parameter range for the prior uncertainty modeling of the aquifer. These parameters are 1D and are inputs to the analytical aquifer model that we use.

	porosity ϕ	permeability k	total aquifer compressibility $(c_f + c_w)$	length (H)	width (W)	thickness (W)
min	0.05	1 mdarcy	8×10^{-5}/bar	1.5 km	0.5 km	20 m
max	0.35	500 mdarcy	3×10^{-4}/bar	150 km	50 km	200 m

The reference permeability and porosity distributions are generated with the SGCOSIM method using a spherical variogram model with a range of 14 cells (about 5.5 km) in x and y-direction and a range of 3 cells (about 26 m) in z-direction. To correlate the permeability and porosity fields, again a 0.6 correlation was used. We assume a laterally isotropic permeability distribution and set the vertical permeability to 20% of the horizontal permeability value. Similarly as for the reference field, the initial ensemble permeability and porosity realizations were simulated with the SGCOSIM method. To account for the uncertainty in the correlation structure of the permeability and porosity fields, the variogram range was randomly selected from

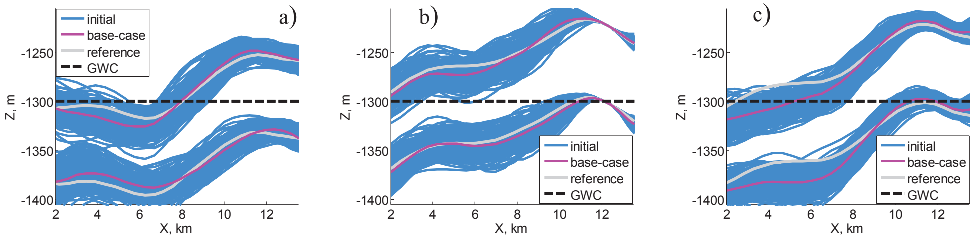

Figure 7.4: Three different cross-sections (along x-direction) through the reservoir structure: a) through the northern part of the reservoir; b) through the middle part of the reservoir; c) through the southern part of the reservoir. The pink line indicates the base-case structure used to generate the initial ensemble members shown in blue and the reference structure is shown in grey. The GWC is indicated by the black dashed line.

the Gaussian distribution with the mean of 10 cells (about 3.9 km) and standard deviation of 3 cells (about 1.2 km). The variogram range in z-direction was fixed to 3 cells (about 26 m). To correlate the prior ensemble porosity and permeability fields 0.6 correlation was used.

The unknowns in the state vector contain the log-transformed permeability field, porosity field, reservoir top and bottom deviations, log-transformed aquifer strength, log-transformed aquifer time, the temporal mass change and the cumulative water influx into the reservoir. The history-matching window spans a period of about 7 years. The production data consist of the flowing bottom-hole pressure available each 30 days. Here, we assume zero-mean Gaussian measurement errors with 1 bar standard deviation. The time-lapse gravity data are available after about 3, 5 and 7 years. There are in total 96 stations simulated (Fig. 7.5), with a fixed spacing of about 1200 m, which is comparable to the reservoir depth. The maximum temporal gravity variation for the reference model is 4, 10 and 15 μGal after 3, 5 and 7 years, respectively. Note however, that this signal is a sum of two major counteracting effects: a positive change in gravity caused by the water influx and a negative change in gravity due to gas takeout. In practice, the negative gravitational effect of gas takeout is not of interest because the amount of gas produced is known to a high accuracy. Therefore the gas takeout effect can be estimated and subtracted from the observed data leaving the gravitational effect of the water influx as the signal to be analyzed (see, e.g., Eiken et al. 2008). In our case the strongest variation in gravity due to gas takeout is -4, -7 and -10 μGal after 3, 5 and 7 years, respectively. Consequently, the maximum gravity variation caused by water influx is about 8, 17 and 25 μGal after 3, 5 and 7 years, respectively. Furthermore, in reality there will be a small negative gravity variation (nearby reservoir/aquifer interface) caused by aquifer pressure drop and, consequently, density decrease of the aquifer water. However, such effect typically is rather minor (see, e.g., Stenvold et al. 2008). In our example it accounts for less than 2% of the signal of interest and, therefore, it is ignored in forward modeling of gravimetric data for the ensemble members. The single-survey measurement

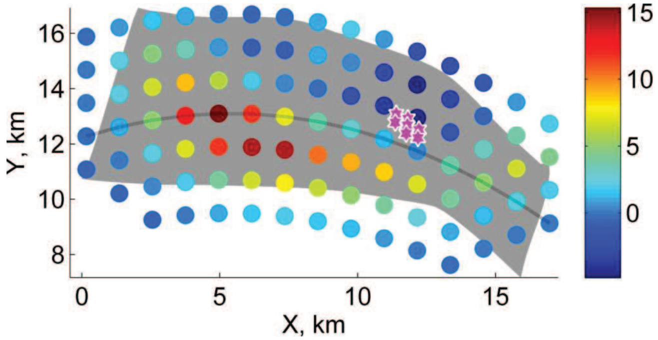

Figure 7.5: Temporal gravity variation (μGal) after 7 years of the reservoir production. The location of gravity stations is shown with colored circles and the layout of the gas reservoir is shown in grey. The pink stars denote the position of gas producers. The black curve indicates the stations which were selected to plot the gravity shown later in this chapter.

noise is uncorrelated (in space and time) and simulated from a zero-mean Gaussian distribution with 2 μGal standard deviation. Consequently, the standard deviation of temporal gravity noise is about 2.83 μGal, which is close to the best achievable precision of relative gravimetric measurements (Zumberge et al. 2008, Alnes et al. 2011).

7.4 Results

7.4.1 The data history-match

In Fig. 7.6 the history-match of the pressure and gravity data for the three assimilation scenarios is presented. It shows the predictions from the initial and updated ensemble members compared to the noisy measurements. The ensemble predictions result from re-running the ensemble members from time zero with the initial and final parameter estimates. The assimilation of the pressure observations provides a very reasonable pressure history-match. On the other hand, when only the gravity data are assimilated the spread in the pressure predictions is very large and not significantly different from the spread in the initial model predictions. Combining both, gravity and pressure data, improves slightly the overall data-match compared to the case when only the pressure data are assimilated. The history-match to the time-lapse gravity observations after 7 years of gas production is shown for the cross-section along the x-direction through the middle of the reservoir (Fig. 7.5). The initial uncertainty is large, spanning about 100 in the time-lapse signal variation. The updated models match the noisy data reasonably well when the gravity observations are assimilated.

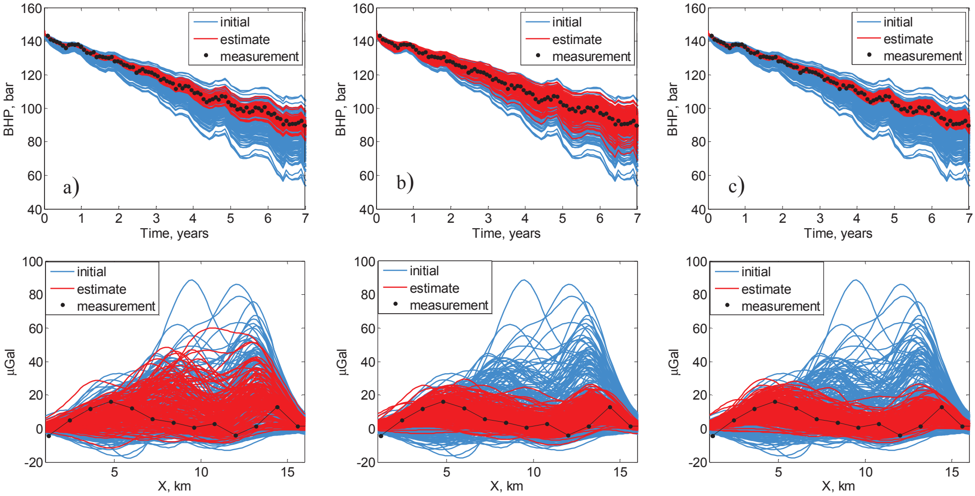

Figure 7.6: History-match to the noisy pressure (top row) and the noisy gravity (bottom row) data: a) only the pressure data are assimilated; b) only the gravity data are assimilated; c) both, the pressure and gravity are jointly assimilated. The predicted data result from re-running the reservoir models from time zero with the updated parameters. The time-lapse gravity data are computed as the difference between the gravity survey after 7 years of the reservoir production and the baseline survey at the start of the simulation. The data x-profile through the middle of the field is shown (see Fig. 7.5).

7.4.2 Static parameter estimates

Fig. 7.7 shows the first layer of the reference permeability and the reference porosity fields. The ensemble mean of the initial and the final permeability and porosity fields for all the scenarios considered are shown in Fig. 7.8. The permeability and porosity fields are not recovered accurately. When only the pressure data are used the final mean estimate is close to the prior parameter mean, despite the reasonable pressure data-match (Fig. 7.6). We obtained similar results for the remaining 8 layers, not shown here. With the assimilation of 4D gravity data, some of the permeability and porosity features in the first layer of the reference fields seem to be captured, e.g., the high-permeability zone in the south-west part of the reservoir where a large part of the aquifer water was distributed. We showed in Chapter 6 that reservoir permeability estimates based on history-matching 4D gravity should be more accurate in the reservoir regions affected by large temporal mass variations. This is also confirmed here. Nevertheless, for some of the other reservoir layers the estimates based on the assimilation of gravity data were not significantly improved. This is because the time-lapse gravity observations offer a limited 3D resolution, i.e., they reflect the overall mass variation integrated over all reservoir layers, but cannot provide information about the vertical mass redistribution.

Fig. 7.9 shows depth residual maps (the ensemble mean minus the reference surface) of

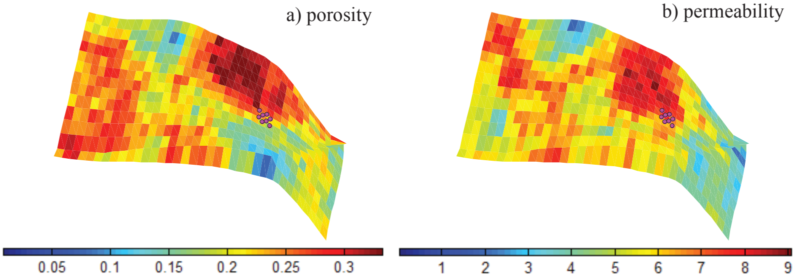

Figure 7.7: The first layer of the porosity and the permeability (ln(k) where k is the permeability in milidarcies) field of the reference model. The pink dots denote the location of the gas producers.

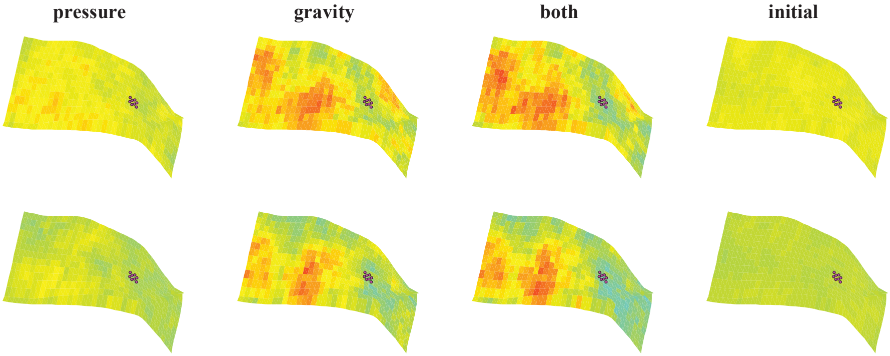

Figure 7.8: The mean ES estimates of the porosity field (top row) and the permeability field (bottom row) for different data assimilation scenarios (the first layer is shown). The color scale is the same as in Fig. 7.7. The pink dots denote the location of the gas producers.

the initial and the updated reservoir top and bottom horizons. Because the alternative reservoir horizons were conditioned to the well picks data, the residual surfaces are close to zero around the well location. At some distant off-well locations, e.g., west- and south-west reservoir regions, large negative residuals of the reservoir top and the reservoir bottom for the mean of the initial members can be observed. This means that at those locations the initial reservoir models are, on average, positioned deeper than the reference structure. The mismatch there does not decrease when the pressure data are assimilated. When gravity data are history-matched the mean of the updated models is matching the reference structure more closely there. Nevertheless, not all of the reservoir regions where significantly updated. This can be seen in Fig. 7.11 where two cross-sections through the reservoir structure for one particular ensemble member are shown: one cross-section through the reservoir region affected by a large time-lapse mass variation due to the water/gas displacement and the other through the region which was not waterflooded. It can clearly be seen that no significant structure updates were performed in the latter part of the reservoir. The final estimate of the reservoir structure is erroneous there and close to the initial values.

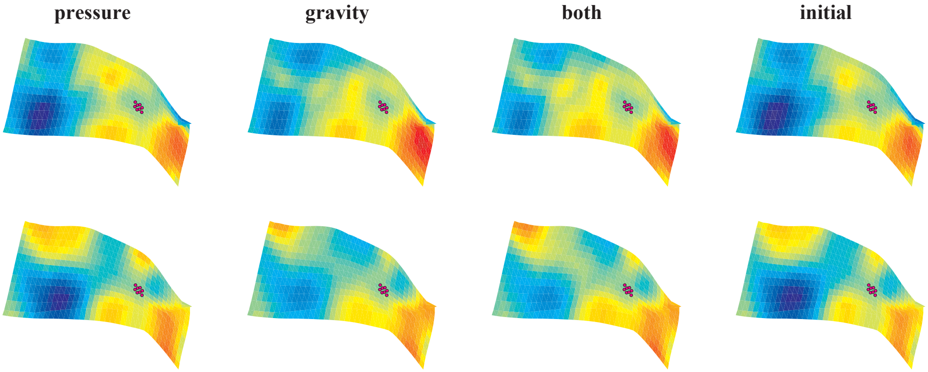

Figure 7.9: Depth residual maps of the reservoir top (top row) and bottom (bottom row) horizons (the ensemble mean minus the reference surface) for different data assimilation scenarios. The pink dots denote the location of the gas producers.

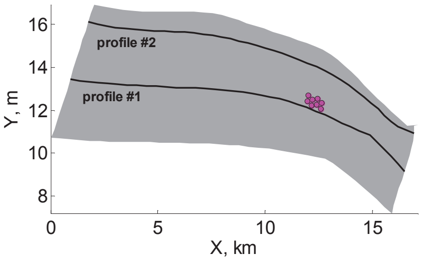

Figure 7.10: Location of two different profiles used for structure cross-section plots shown in Fig. 7.11.

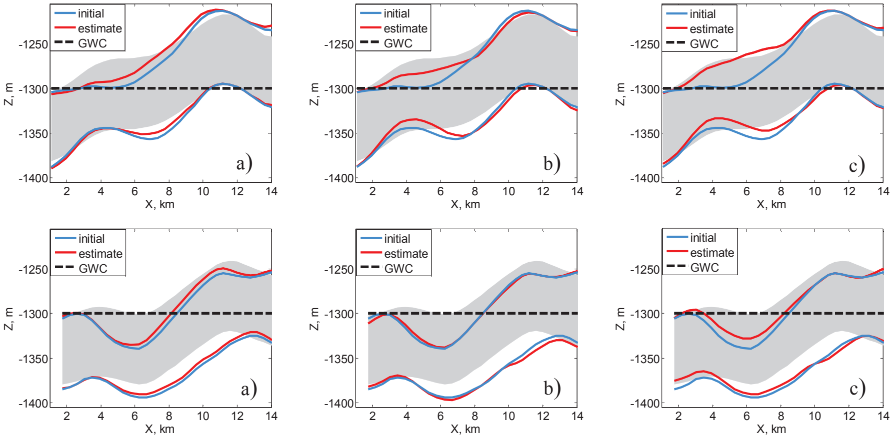

Figure 7.11: The two different cross-sections through the reservoir structure for one particular model realization are shown: the top row profile #1; the bottom row profile #2, see Fig. 7.10. The blue lines indicate the initial structure, the red lines delineate the updated structure and the layout of the reference structure is shown in grey. The GWC is indicated by the black dashed line. The top row shows the cross-section through the reservoir region affected by the large mass variation due to water influx and the bottom row through the region not affected by the water influx (see Fig. 7.12). The columns correspond to the different data assimilation scenarios: a) only the pressure data are assimilated; b) only the gravity data are assimilated, and c) both, the gravity and the pressure data are jointly assimilated.

7.4.3 Monitoring water influx

In Fig. 7.12 the ensemble mean of the total (sum over the 9 reservoir layers) 7-year time-lapse mass change estimate is shown. The mass change estimate results from the ES update and not from the reservoir model re-run from time zero with the updated static parameters. In Fig. 7.12 the green and red colors denote the major positive temporal mass variation and hence highlight the reservoir regions affected by the influx of the aquifer water. The mean estimate based on the pressure data only is inaccurate with the severe overshooting and underestimation of the actual mass influx. The assimilation of gravity data improved very significantly the overall mass change estimates, especially in the western and southern part of the reservoir. Fig. 7.13 shows the direct ES cumulative water influx estimates for the end of the data assimilation period, i.e., after about 7 years. The spread in the initial model predictions is large with a standard deviation of 24.8 Mm^3. It is reduced to 11.5 Mm^3 when the pressure data are assimilated, though the final results tend to overestimate the reference value. The mean estimate is 43.8 Mm^3 compared to the reference value of 32.4 Mm^3. The uncertainty reduction is large and the estimate is much more accurate when the gravity observations are used. The mean is 32.3 Mm^3 and the standard deviation is 1.4 Mm^3. When both the pressure and the gravity data are jointly matched, these results do not change very much. In this case the mean is

32.6 Mm^3 and the standard deviation is 1.3 Mm^3. A significant added value of gravity data for cumulative water influx estimates is expected because the amount of cumulative water influx is directly sensed by gravity observations.

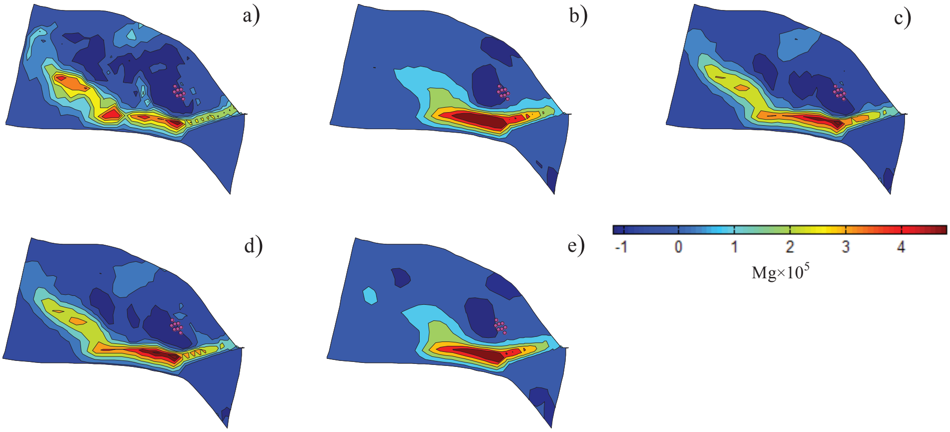

Figure 7.12: The temporal mass variation after 7 years of gas production and water influx. In a) the reference mass variation is shown; in b), c) and d) the mean of the final ES estimates for different data assimilation scenarios is presented: only the pressure data are assimilated (b); only the gravity data are assimilated (c) and both, the pressure and the gravity data are jointly assimilated (d). In e) the mean of the prior models is shown. The pink dots denote the location of the gas producers.

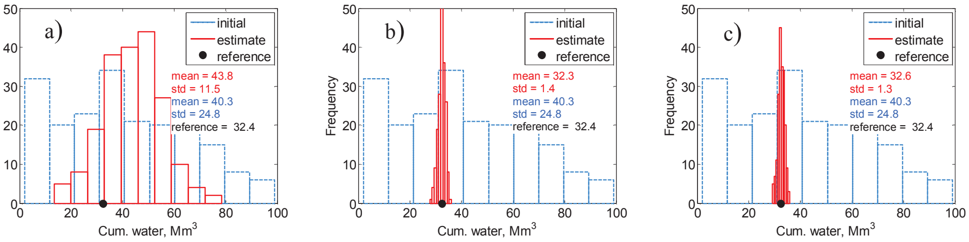

Figure 7.13: The ES cumulative water influx estimates versus different data assimilation scenarios: a) only the pressure data are assimilated; b) only the gravity data are assimilated, and c) the pressure and the gravity data are jointly assimilated.

7.4.4 Gas Initially in Place (GIIP) estimates

We estimate GIIP volumes by two approaches; one is based on the ES-updated models and the other one is based on material balance analysis. The GIIP estimates in the first approach (Fig. 7.14) are derived by computing the volumes of gas above the GWC in the reservoir models containing the final estimates of the reservoir top and bottom horizons and of the reservoir porosity. Note that in this case no material balance analysis is applied and the uncertainly in the GIIP volumes is mostly related to the uncertainty in the reservoir porosity and the top and bottom horizons. The reference GIIP, which is equal to 55.5 Gm^3, is about 10% larger than the ensemble-mean GIIP prediction from the initial models, which is equal to 50.7 Gm^3. This is because the base-case structure that was used to generate the alternative reservoir top and bottom horizons is a few meters deeper at some off-well locations than the reference structure (see Fig. 7.4). Since the initial GWC is fixed as homogenous for all the ensemble members, the prior reservoir models positioned deeper than the reference structure will underestimate the actual GIIP volumes. When only pressure data are assimilated, the mean GIIP estimate is 53.1 Gm^3 and the initial standard deviation is reduced from 4.9 Gm^3 to 2.4 Gm^3. When only gravity data are used, the mean GIIP is 56.1 Gm^3 and the standard deviation of the GIIP estimate is equal to about 4.3 Gm^3. The joint assimilation of pressure and gravity data, results in a compact GIIP distribution with the standard deviation of 1.3 Gm^3, and the mean GIIP estimate equal to 56.6 Gm^3.

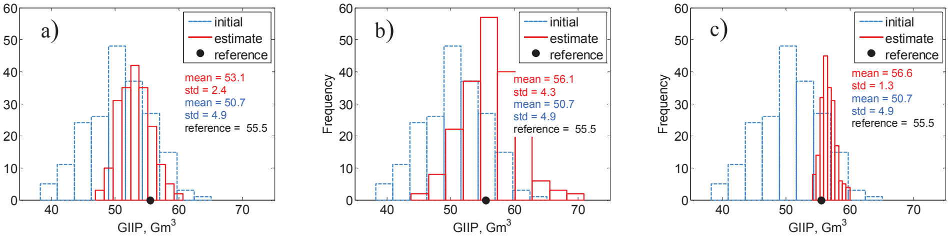

Figure 7.14: The GIIP estimates versus different data assimilation scenarios; a) only the pressure data are assimilated; b) only the gravity data are assimilated; c) the pressure and the gravity data are jointly assimilated. The estimates are obtained by computing the initial gas volumes in the updated reservoir models.

Volumetric material balance analysis results

The second approach is based on the commonly used volumetric material balance analysis where the cumulative water influx is one of the relevant input parameters. Here, for the cumulative water influx we substitute the direct ES estimates and for the GIIP calculation we apply the Havlena-Odeh formulation which can be expressed as (Dake 2001)

$$G_pB_g + W_p = G(B_g - B_{gi}) + GB_{gi}\left(\frac{c_wS_{wc} + c_f}{1 - S_{wc}}\right)\Delta P + We. \qquad (7.1)$$

In Eq. (7.1) G_p is the cumulative gas produced at surface (standard) conditions, B_g and B_{gi} are the gas formation volume factors at the current and initial reservoir pressure, W_p is the cumulative water production at reservoir conditions, G is the gas initially in place, c_w is the compressibility of reservoir water and c_f is the pore volume compressibility, S_{wc} is the connate water saturation, ΔP is the reservoir pressure difference between the initial conditions and the current state, and W_e is the cumulative water influx to the reservoir at reservoir conditions. Rearranging the terms in Eq. (7.1), the GIIP can be expressed as

$$G = \frac{F - W_e}{E_g + E_{fw}}, \tag{7.2}$$

where

$$F = G_p B_g + W_p, \tag{7.3}$$

$$E_g = B_g - B_{gi}, \tag{7.4}$$

$$E_{fw} = B_{gi}\left(\frac{c_w S_{wc} + c_f}{1 - S_{wc}}\right)\Delta P. \tag{7.5}$$

Often the term E_{fw} can be omitted since typically $E_{fw} \ll E_g$. In our example $E_{fw} \approx 0.5\% E_g$, there is no water produced ($W_p = 0$) and, therefore, the GIIP is computed from

$$G = \frac{F - W_e}{E_g}, \tag{7.6}$$

with $F = G_p B_g$. After 7 years of the field production (end of the history matching window) we have: $G_p = 23.3$ Gm^3, $B_g = 0.0129$ and $B_{gi} = 0.0081$.

In Eq. (7.6) except for the cumulative water influx, other input variables can also be uncertain, even though they can be measured directly. These uncertainties can originate from measurement errors of pressure or gas rates, PVT laboratory experiments or representativeness of well samples for the whole field. To account for some of them we add 1% zero-mean Gaussian noise to the measured cumulative gas produced and 4% zero-mean Gaussian noise to the formation volume factors (for the uncertainty scales in reservoir fluid description see Meisingset 1999) .

The GIIP estimates based on the material balance analysis are presented in Fig. 7.15. In this case the cumulative water influx is the major uncertain parameter influencing to a large extent the GIIP volumes (see Eq. 7.6). When only the pressure data are used the mean GIIP is lower than the reference value of 55.5 Gm^3 by about 2 Gm^3 and the ensemble standard deviation is reduced from the initial 5.3 Gm^3 to 2.5 Gm^3. The assimilation of gravity data provided better cumulative water influx estimates (see Fig. 7.13). In the result, the GIIP differs only by about 0.3 Gm^3 from the reference value and the ensemble standard deviation is reduced to about 0.7 Gm^3. Comparing Fig. 7.14 with Fig. 7.15, we observe that fairly similar estimates of the GIIP were obtained using different approaches, especially for the case when only the pressure data were matched and the case when both, the pressure and the gravity data, were used. In both cases, the joint assimilation of pressure and gravity data provided the most accurate results, and the benefits of a joint data inversion were clearly visible in the model-based GIIP estimates. When only the gravity observa-

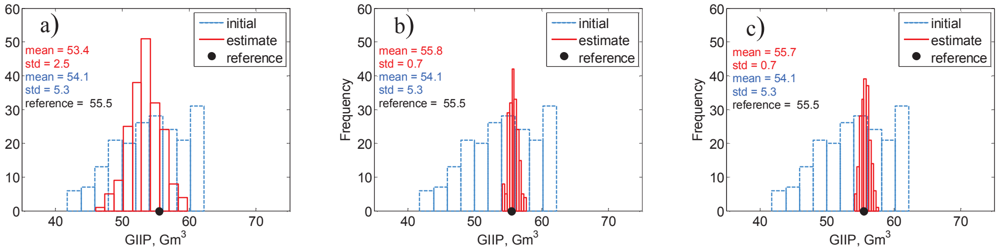

Figure 7.15: The GIIP estimates for different data assimilation scenarios; a) only the pressure data are assimilated; b) only the gravity data are assimilated; c) the pressure and gravity data are jointly assimilated. The estimates are obtained from the material balance analysis.

tions were matched, more accurate estimates of the GIIP followed from the material balance analysis compared to the model-based results. We explain this by accurate total water influx estimates derived from the gravity data inversion and a limited ability to accurately update all the static reservoir parameters in this case. It is difficult to judge which approach for the GIIP determination is more suitable because both methods were applied under certain assumptions. For the material balance analysis the total water influx was the major uncertain parameter, and the average reservoir pressure drop was representative for the whole reservoir formation. On the other hand, in the model-based approach GWC position and lateral extent of the reservoir structure were fixed, and only the top and bottom horizons were tuned. Thus, only a part of the possible structural uncertainty was modeled. It requires further research in more complex settings to evaluate strengths and weaknesses of the two approaches. Nevertheless, we demonstrated that in both cases gravity data assimilation a clear added value.

7.4.5 Field production forecasts

The forecasts of the field gas and water production rates from 7 to 14 years are shown in Fig. 7.16. The reference gas production rate and the predictions from the initial and the final ensemble members are compared to the predicted gas demand, and it is uncertain if the field is capable of producing at the desired gas rates during the specified forecast period. The accuracy of production forecasts is further evaluated by computing the root-mean square error for the forecasted cumulative gas production

$$RMSE_G = \sqrt{\frac{1}{N_e}\sum_{j=1}^{N_e}\left(G^j_{cum} - G^{ref}_{cum}\right)^2}, \tag{7.7}$$

and for the forecasted cumulative water production

$$RMSE_W = \sqrt{\frac{1}{N_e}\sum_{j=1}^{N_e}\left(W^j_{cum} - W^{ref}_{cum}\right)^2}, \tag{7.8}$$

where G denotes gas, W denotes water and N_e is the number of ensemble members. The predicted gas production rates from the initial models are inaccurate with RMSE (Fig. 7.16) of 4.8 Gm^3. Some of the initial models show a severe drop in the gas production indicating the end of the reservoir life after only 9 years. On the other hand there are also models predicting high rates up to 14 years. This uncertainty is to a large extent reduced with the assimilation of pressure data. The rates of the updated models match the reference rate more closely and the RMSE of the forecasted cumulative gas production is reduced to 1.5 Gm^3 in this case. When only gravity data were assimilated the forecast accuracy is also improved, but the effect is smaller compared to the results when only pressure data were assimilated. Combining both, pressure and gravity data does further improve the results and gives RMSE of 1.1 Gm^3. Therefore, we may conclude that mostly matching the pressure data influenced the gas production forecast improvement in this case. On the other hand, the reference field does not produce any water during the forecast interval. Contrary to that, there are many initial ensemble members giving high field water production rates reaching 3000 m^3/day and more (see Fig. 7.16). The assimilation of pressure measurements improves the water rates predictions and the RMSE of forecasted cumulative water production is reduced from 2010.8 $\times$ 10^3 m^3 to 718.5 $\times$ 10^3 m^3. However, there are still many final members predicting a water breakthrough after $9-10$ years with rates up to 500 m^3/day and more. Matching the gravity data gives more accurate water production forecast, where only a few members show any water production. The RMSE is drastically reduced to 32.0 $\times$ 10^3 m^3.

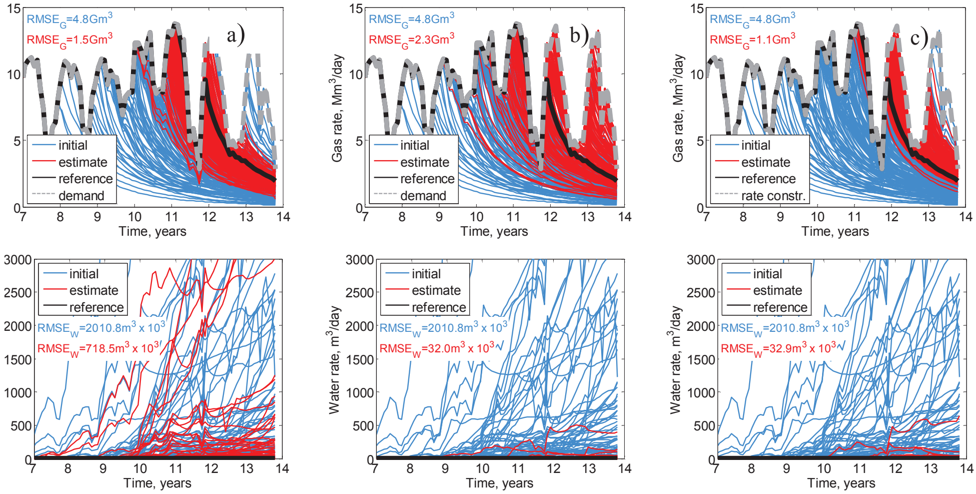

Figure 7.16: The forecasts of the field gas (top row) and water (bottom row) production from 7 to about 14 years for different data assimilation scenarios; a) only the pressure data are assimilated; b) only the gravity data are assimilated; c) the pressure and the gravity data are jointly assimilated. The estimates are obtained by re-running the reservoir model from time zero with the final parameter estimates. The grey line denotes the predicted gas demand.

A combined assimilation of pressure and gravity data does not change the results noticeably. Therefore, we may conclude that matching the gravity data improved to a large extent the forecast of water production in this case. These results show the complementarity of pressure and gravity measurements, which, when combined can provide more accurate gas and water production forecast.

7.4.6 The non-uniqueness

In the previous sections we showed that in the case when only the pressure data were assimilated, despite the reasonable pressure history-match, the static parameter estimates were inaccurate. Furthermore, the dynamic variables important for reservoir monitoring, i.e., the cumulative water influx and the temporal mass variations, were also erroneous. Nevertheless, the gas production forecasts resulting from the reservoir model re-run from time zero with inaccurate static parameters was quite acceptable. These results show the non-uniqueness of the history-matching problem. There are four uncertain parameters that we update, namely permeability, porosity, reservoir structure, and aquifer support which can all explain the pressure data mismatch. For instance, a lower permeability reservoir will experience a quicker pressure drop. However, a similar effect could be obtained with a thinner reservoir structure, with smaller volumes of gas above the GWC or a reservoir with smaller pore volume. Finally, the reservoir pressure behavior can be very sensitive to the aquifer support. It is clear that the interplay of all these parameters determines the pressure as measured in the wells. Furthermore, many combinations exist which may give the same pressure response. Therefore, the pressure data alone cannot discriminate between different reservoir scenarios as illustrated in Fig. 7.17, where the data assimilation results for one of the ensemble members are shown. In both cases when only the pressure data or the pressure data in combination with gravity data are used the pressure history-match and the pressure forecast are very accurate. Nevertheless, the estimates of the aquifer support are significantly different in these two cases. Results based on pressure data only suggest large and strong aquifer (large values of the parameters and) and high water influx rates, whereas results based on both pressure and gravity data show much weaker aquifer support. In the first case the permeability is significantly underestimated (compare with Fig. 7.8) around the well region limiting the pressure communication with the reservoir boundary (this region is shown with the dashed circle in Fig. 7.17d-f)). Therefore, to compensate for a too low permeability there the aquifer needs to "push" harder to match the pressure as sensed in the wells. Consequently, the well pressure is matched but the actual amount of water influx, which is not seen in the wells, is substantially overestimated. Because gravity observations can sense the subsurface mass redistribution and hence the water/gas displacement directly, a joint assimilation of gravity and pressure data can provide more adequate solution in this case.

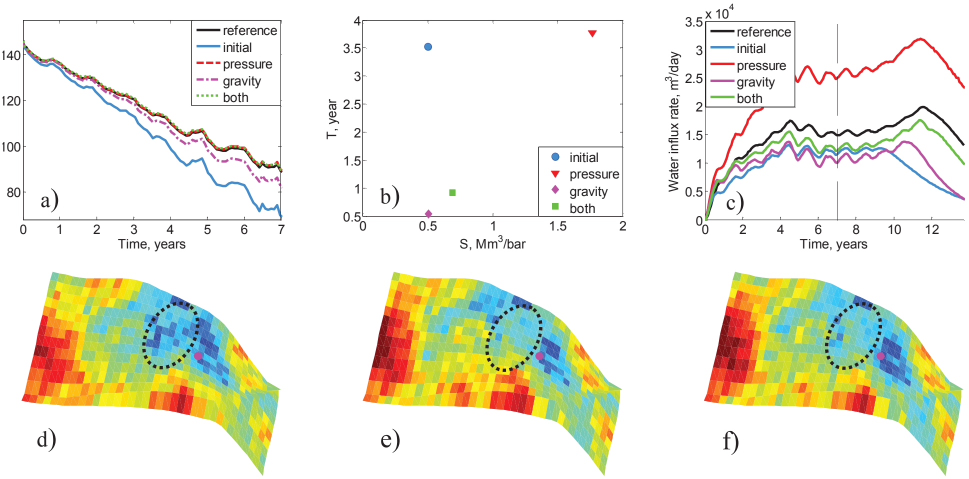

Figure 7.17: The data assimilation results for one particular model realization and various assimilation scenarios. a) shows the pressure history-match for one of the producers; b) shows the parameter estimates for the analytical aquifer model; c) shows the corresponding estimate of the water influx rate obtained by re-running the updated ensemble models from time zero and d-f present the 1st layer of the updated permeability field (ln(k) where k is the permeability in milidarcies): d) only the pressure data are assimilated; e) only the gravity data are assimilated; f) the pressure and gravity data are assimilated. The pink dot denotes the location of the producer. Because the aquifer for the reference field is not modeled with the analytical approach, no reference values are shown in b).

7.4.7 Sensitivity to gravimetric noise

To simulate gravimetric observations we assumed uncorrelated, zero-mean, 2 μGal Gaussian measurement noise. Such noise levels for a single gravity survey are in principle achievable but they should be considered rather as a best-case scenario. Therefore, to investigate the sensitivity of the results on the gravity data noise assumptions we increased the single survey gravity noise (standard deviation) to a more pessimistic value of 5 μGal what results in about 7 μGal for the time-lapse gravity noise. Here, we consider the case when the pressure and the gravity data are jointly assimilated. Fig. 7.18 shows the field gas and the field water production forecasts and the GIIP estimates based on the material balance analysis. Comparing Fig. 7.18 with Fig. 7.15c) and Fig. 7.16c) we observe that increasing the gravity noise did not influence the results dramatically. The gas production forecast remaines almost unchanged and the water production forecast becomes less accurate with a RMSE increasing from 32.9×10^3 m^3 to 82.9×10^3 m^3. Due to the larger uncertainty in the cumulative water influx estimates (not shown here) where the standard deviation increased from 1.3 Mm^3 to 2.5 Mm^3, the standard deviation of the GIIP estimates increased (derived from Eq. 7.6) from 0.7 Gm^3 to 0.9 Gm^3.

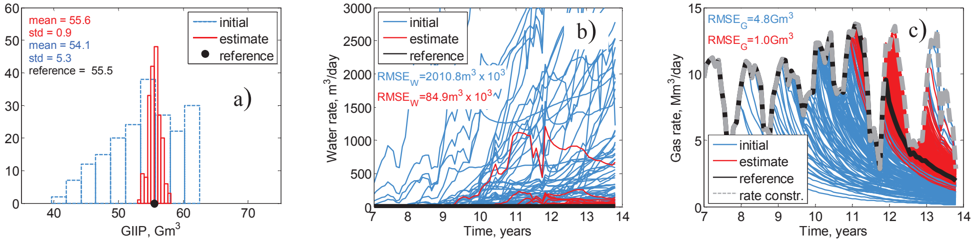

Figure 7.18: The GIIP estimates obtained from the material balance analysis (a) and the forecasts of the field water (b) and gas (c) production from 7 to about 14 years. The case with a joint assimilation of the pressure and the gravity data is shown. The gravity observations are contaminated with a 5 μGal Gaussian noise in this case. The water and gas rate estimates are obtained by re-running the reservoir model from time zero with the final parameter estimates. In Fig. 7.18c) the grey line denotes the predicted gas demand.

7.4.8 The aquifer modeling error

We perform a data assimilation experiment to investigate if the reference model output can be matched using the analytical aquifer response. To find the best possible parameter estimates of the aquifer model, we assimilate jointly the noise-free pressure and the noise-free gravity data, and estimate the parameters of the aquifer model while keeping the other parameters (porosity, permeability and reservoir structure) fixed and set to the correct values of the reference model. Fig. 7.19 shows the predicted outputs from the reference model: the well pressure for one of the producers and the gravity variation profile. The reference model outputs are compared with the predicted data from the final model, which results in the lowest RMSE over all data. The RMSE for all the pressure data available (8 producers) is 1.4 bar and the RMSE for all the gravity data available (after 3, 5 and 7 years) is 1.9 μGal. The predicted data mismatch could partly be explained by the limitations of the analytical aquifer model to accurately simulate the dynamic response of the 3D reference aquifer, partly by limitations of the data assimilation to find the exact parameter estimates of the analytical aquifer, and partly by the limited information content of the output data about the aquifer properties. Unfortunately, at this stage it is not clear, which effect contributes the most.

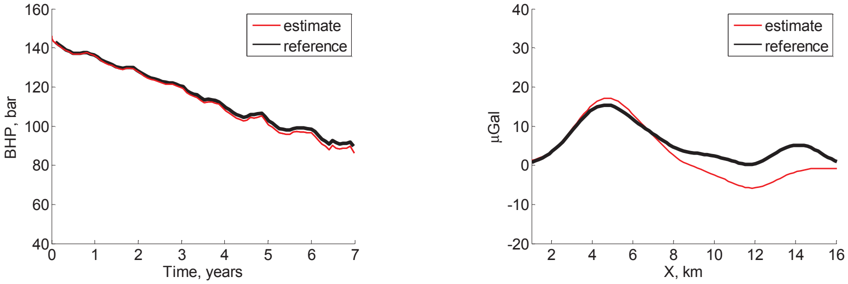

Figure 7.19: The predicted outputs from the reference model (black): the well pressure (a) for one of the producers and the 7-year gravity variation profile (b). The gravity profile from Fig. 7.5 is shown. In red the predicted data from the updated model is presented, for which the RMSE over all data is the smallest.

7.5 Discussion and conclusions

The purpose of this study was to investigate the added value of gravimetric observations for history-matching a gas field. Gravity and pressure data were assimilated with the ES to infer the aquifer support characteristics, to update the static reservoir model, and to estimate the GIIP volumes. We used the analytical approach for modeling of the water influx, which made the estimation of the aquifer support possible with using just a few parameters, compared to the thousands and more parameters in case of the grid block based property estimation. However, a more detailed investigation of the aquifer modeling errors should follow to investigate in detail the limitations of the proposed approach. Furthermore, only a subset of the actual structural uncertainty has been modeled in our experiments. For instance, no faults in the gas reservoir were considered, which could potentially create reservoir compartments, non-homogenous fluid contacts and much more complex reservoir pressure behavior. We believe that such scenarios are very interesting for future research.

We showed that history-matching a gas field with only pressure data may provide highly non-unique solutions because several parameter combinations can explain the reservoir pressure behavior observed in the wells. Then, it is hardly possible to find at the same time accurate estimates of aquifer support and reservoir structure or permeability. Therefore, additional information is needed. Time-lapse gravimetric observations are complementary to pressure data because they can sense the subsurface mass changes and infer aquifer support. We showed that a joint assimilation of pressure and gravity data can provide more constrained inverse solutions and result not only in improved gas and water production forecast but also gives more accurate reservoir reserves evaluation and reservoir state description.

Chapter 8

Case study 3–Bias-aware data assimilation

In this chapter we show an example of an application of the bias-aware data assimilation methodology introduced in Chapter 4. We perform synthetic experiments based on the 2D gas reservoir model already used in the data assimilation in Chapter 6. Similarly as in Chapter 6, we assimilate gravity data to estimate the reservoir permeability and the reservoir mass redistribution. This time, however, we consider not only random noise in the observations but also systematic errors (biases) in both the observations and the forward model.

8.1 Introduction

In reservoir engineering applications of data assimilation an assumption is often made that the forward model is error-free and that the observation errors are zero-mean and purely random. We also followed this approach in the synthetic 2D case study in Chapter 6. It is known, however, that both the model and the observation errors can arise as random as well as systematic. The numerical model may not be capable of predicting the true signal perfectly even if the best possible set of the model parameters was given. The model errors may occur due to, e.g., too coarse parametrization (too large grid blocks), linearization, and numerical approximations. The errors can also be caused by unrepresented model physics and poorly known boundary conditions, such as, e.g., an aquifer support (see Chapter 7). Similarly, observation errors can have many sources. The examples include the instrument, the data processing procedures, and the influence of environmental processes (see Chapter 3).

In Chapter 4 we described briefly the extension of the ensemble-based data assimilation methods used in this thesis to include explicit modeling and estimation of systematic errors in the model and the observations, referred to as bias. In this chapter we show the application of this methodology in the context of gravity data assimilation. First, we introduce the experiment setup. Next, the origin and characteristics of observation and model bias are presented. In the subsequent section, we describe the bias-evolution models used in the data assimilation scheme. The assimilation results are discussed after that. The chapter is finalized with a brief summary.

8.2 Experiment setup

8.2.1 2D gas field model

We consider the 2D gas reservoir model already used in the data assimilation experiments in Chapter 6 (see Fig. 6.1). To recall, the model is represented as a $3000\times3000\times50$ m box divided into 40×40 grid blocks with dimensions of $75\times75\times50$ m. The distance from the reservoir top to the free surface is set equal to 1700 m. To simplify the analysis, this time we consider the assimilation of gravity data only. We use a 5000×5000 m regular gravity observation grid with 100 stations separated by 500 m in x- and y-direction. Similarly as before, the history-matching window spans a period of 3500 days and the observations are assimilated at 1500 days, 2500 days and 3500 days. Apart from the observation bias (discussed in Section 8.2.2), a 2 μGal (std) uncorrelated (in time and space) zero-mean Gaussian noise is added to the observations. The noise is added to the single-survey data which means that the standard deviation of the time-lapse gravity noise is $\sqrt{2^2+2^2} \approx 2.83$ μGal.

The unknown parameters are the grid-block permeabilities and the cumulative water influx into the reservoir. We apply the EnKF method with 100 ensemble members and use the same as in Chapter 6 initial ensemble realizations of the permeability field (see Fig. 6.2). The estimates of the water-front position are obtained by running forward the reservoir model with the updated permeability field. Porosity is updated by applying the deterministic relationship between the permeability and the porosity

(see Eq. 6.1).
Three cases are analyzed with respect to the presence of bias: only the observation bias, only the model bias, and both the observation and the model bias.

8.2.2 Biases

The observation bias

The observation bias may have many sources and some one of them relate to gravity data acquisition and data processing procedures. For instance, in time-lapse gravimetry based on relative measurements, such as, e.g., offshore gravimetry, the relative readings must be tied to reference stations. The reference stations need to be located far enough from the target, i.e., the reservoir, so they are not affected by the signal of interest. Tying the field relative measurements to those at the reference stations allows comparing measurements in time despite of the gravimeter drift. However, since measurements, including those at the reference stations, are always affected by some kind of noise, this procedure may introduce a random offset (called zero-level uncertainty, see Eiken et al. 2008) to time-lapse gravity differences. In this study this offset will be considered as observation bias.
The observation bias, the zero-level uncertainty, is a random constant shifting the whole gravity variation map up or down. Therefore, to model the evolution of the observation bias b we use

$$b^f_{k,j} = \beta_{k,j}, \tag{8.1}$$

where $b^f_{k,j}$ denotes the observation bias forecast for the ensemble member j, $j = 1, \dots, N_e$, k is the time index, $k = 1, \dots, N_s$ where N_s denotes the number of assimilation time steps, and $\beta_{k,j}$ is a random number sampled from the Gaussian distribution, i.e, $\beta_{k,j} \sim N(0, \sigma_b)$, where σ_b denotes the standard deviation. Based on the field estimates (Eiken et al. 2008) we use $\sigma_b = 2$ μGal for the observation bias modeling.

The model bias

Hydrology can introduce a model bias into history-matching gravimetric observations since accurate information on hydrological processes at a site is rarely available. Consequently, the observed gravity variations, which contain the hydrological signal (see Chapter 3), cannot be predicted correctly. Thus, the model predictions of the observed data can be biased because of the undermodeling error (Fig 8.1). The gravity signal variations caused by the groundwater-level changes will define the model bias in this study.
To generate realistic realizations of the model bias, we use outputs of a hydrological model of a catchment area located in the southern part of the Netherlands. Figure 8.2 presents the predicted groundwater levels in terms of the mean highest groundwater table and the mean lowest groundwater table in the catchment. A difference between these two levels of more than 2 m at some locations can be observed. Because the hydrological model domain is larger than the extent of the gravity computation grid of

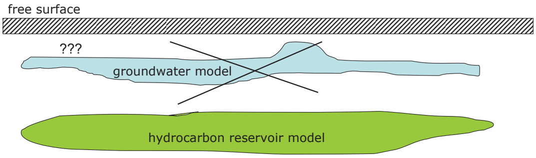

Figure 8.1: Schematic illustration of the model bias originating from undermodeling. The observed gravity variations are caused by overall mass changes, i.e., those in the hydrocarbon reservoir and in the shallow subsurface. However, the hydrological model for the shallow subsurface is not available and only the numerical model of the reservoir can be used. Consequently, the predicted gravity variations are biased because they do not contain the hydrological signal.

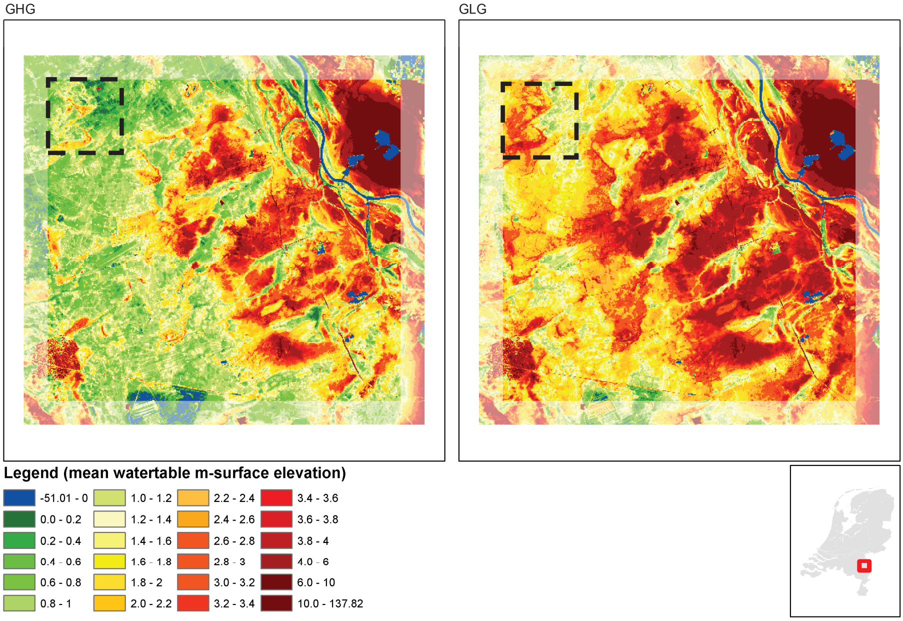

Figure 8.2: The mean highest groundwater table (abbreviated GHG, left figure) and mean lowest groundwater table (abbreviated GLG, right figure) predicted by the hydrological model of the Netherlands, in meters below the surface elevation. Courtesy of G. Hendriksen, Deltares. The black rectangle shows the location of data subset used in this study.

the reservoir, i.e., 575 km^2 compared to 25 km^2, only a subset of the available hydrological data, shown with the dashed rectangle in Fig. 8.2, is used. Three snapshots of the hydrological noise are taken (Fig. 8.3a–Fig. 8.3c) to contaminate the gravimetric observations at the assimilation times at 1500, 2500 and 3500 days. Compared to the true signal from the reservoir (Fig. 8.4) the hydrological noise is of the same magnitude (up to 20 μGal) but opposite in sign. Furthermore, the true signal is aligned mostly with the propagating water front whereas the hydrological noise is distributed over the whole gravity observation grid and it is characterized by a mixture of short and long-range spatial correlations. The hydrological noise will partly mask the signal of interest where the two signals overlap.

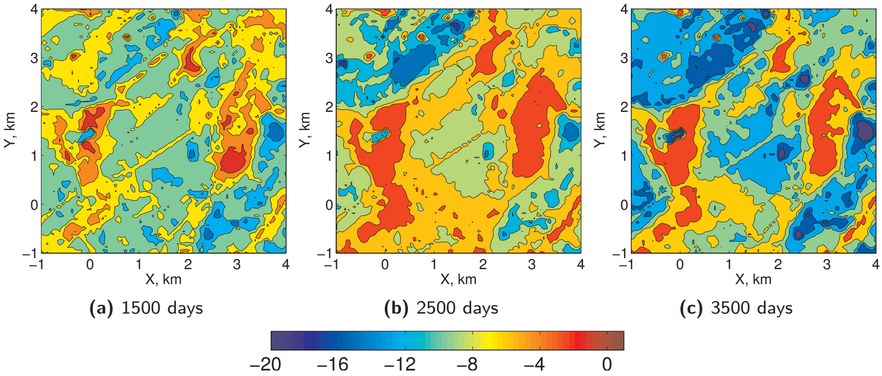

(a) 1500 days **(b)** 2500 days **(c)** 3500 days

Figure 8.3: Examples of predicted gravity field variations (μGal) resulting from the groundwater level changes in the catchment area shown in Fig. 8.2.

A simple modeling approach is used to propagate forward the model bias. It is based on the observation that the spatial pattern of the natural groundwater variations is relatively stable in time (Fig. 8.3). It mostly depends on the terrain topography and the subsurface characterization such as, rock/soil type, porosity, permeability etc., and these parameters do not change in time rapidly. Certainly, the magnitude of the groundwater changes is variable and relates to, e.g., the amount of precipitation. At a given location, for different time epochs, the temporal groundwater level changes with respect to a baseline state can be both positive and negative. Consequently, as shown in Fig. 8.3, the pattern of hydrological gravity noise may stay similar but its sign may flip. Therefore, to propagate forward the model bias e, we use

$$e^f_{k,j} = \gamma_{k,j} e^a_{k-1,j}, \tag{8.2}$$

where $\gamma_{k,j} \sim N(0, \sigma_e)$ and the superscript a stands for the analyzed (updated) estimate. In this way the bias structure estimate obtained in step $k-1$ is fixed in the bias forecast for the k^{th} assimilation step. Because the sign of the true bias may flip from update to update, the updated bias estimate from step $k-1$ is multiplied with a random constant to produce the forecast for step k. In this way there is higher chance that the true bias is included in the space spanned by the ensemble of bias models. In this study we use $\sigma_e = 2$.

The initial ensemble members of the model bias are generated with the Sequential Gaussian simulation method (SGSIM) with a spherical variogram. To include the uncertainty about the correlation lengths of the true model bias, a number of cases for the variogram range (θ) is considered, i.e., $\theta = 2.5$ km, 5 km, 7.5 km, 12.5 km and 17.5 km. For each variogram range we simulate 20 members giving in total 100 initial realizations for the model bias. The representative examples of the initial model bias realizations are shown in Fig. 8.5.

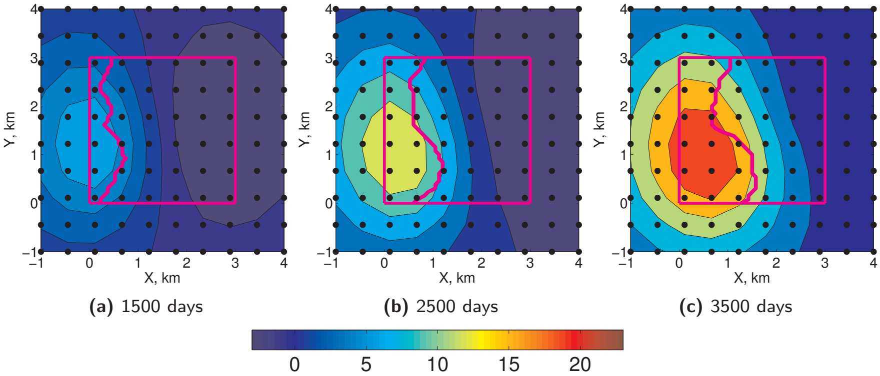

(a) 1500 days **(b)** 2500 days **(c)** 3500 days

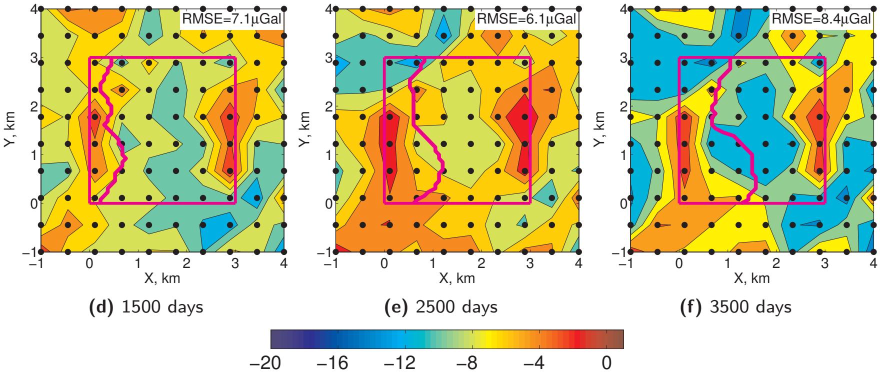

(d) 1500 days **(e)** 2500 days **(f)** 3500 days

Figure 8.4: The reference (true) time-lapse gravity variations caused by the reservoir mass redistribution (top row) and the model bias resulting from the groundwater mass changes (bottom row). The values are in (μGal). The model bias simulation is based on the hydrological model outputs shown in Fig. 8.2. The black dots show the location of the gravity observation points. The pink rectangle shows the reservoir layout and the pink curve shows the position of the true water front.

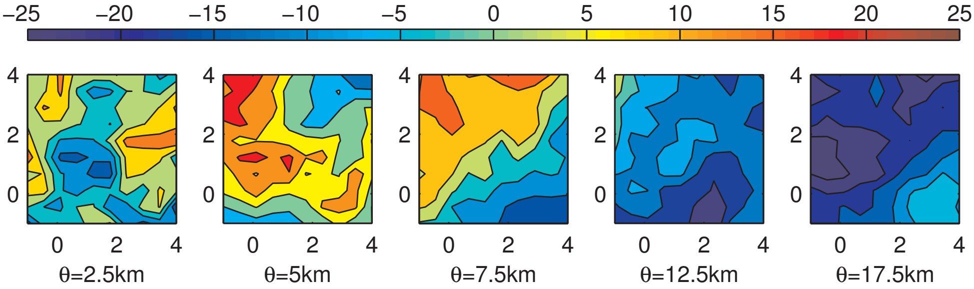

Figure 8.5: Examples of the initial realizations of the model bias for different variogram range θ. The representative ensemble members are shown. The values are in μGal.

8.3 Results

8.3.1 Bias-free estimates

Figure 8.6 and Fig. 8.7 show the final (after 3500 days) estimates in the bias-free case. The estimates result from assimilation of gravimetric observations contaminated by a 2 μGal zero-mean Gaussian noise only. Therefore, they will serve as a reference for the results in the cases when additionally the observation, the model or both biases enter the system.

Fig. 8.6c shows the final permeability estimate. Compared to the reference (true) permeability (Fig. 8.6a), only the major high-permeability zone is recovered. How the permeability estimate translates into the estimate of the reservoir mass change, and hence into the estimate of the water-front position, is shown in Fig. 8.7. Because only some of the main parameter features were captured, the water-front position estimate is not perfectly aligned with the true front. Despite this the front position RMSE is reduced significantly, from the initial value of about 300 m (see Fig. 6.11) to about 188 m. A large added value of the gravity data can be seen in the estimates of the cumulative water influx (Fig. 8.7b). In this case, the mean of the updated members, which is equal to 19.4 Mm^3, is very close to the reference value of 20.1 Mm^3. Furthermore, a significant reduction of the uncertainly in the total water influx can be observed, i.e., the ensemble standard deviation is reduced from 4.6 Mm^3 to 0.5 Mm^3.

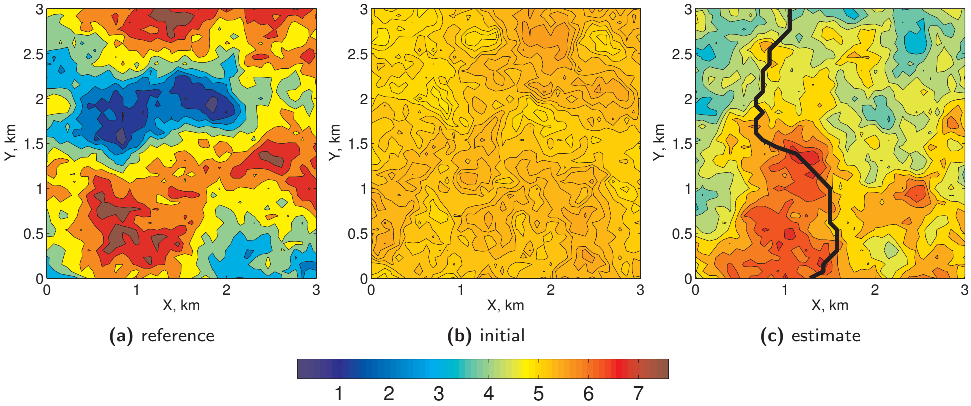

(a) reference **(b)** initial **(c)** estimate

Figure 8.6: The reference permeability field (a), the initial permeability field (b) and the final estimate of the permeability field (c) in the bias-free scenario. The values are in milidarcies. The black curve shows the reference water-front position at the final update time (3500 days).

8.3.2 Bias-blind estimates

The bias-blind estimates are shown in Fig. 8.8. In this case the presence of the bias in observations and/or the model is ignored and the classical EnKF scheme is applied

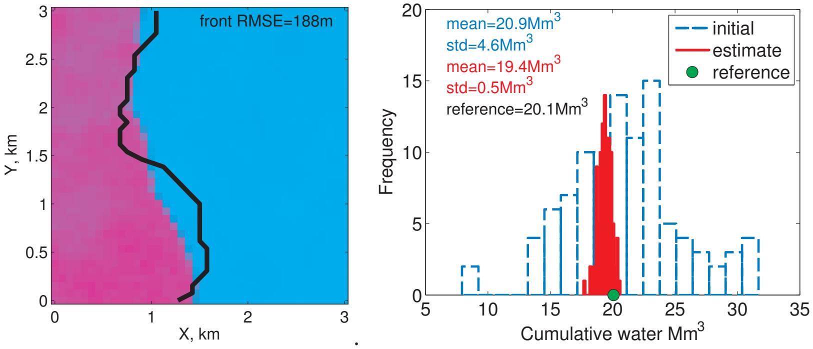

(a) water influx distribution **(b)** cumulative water influx

Figure 8.7: The estimates of the reservoir mass variation (a) and of the total water influx (b) in the bias-free scenario. The results for the final update time (3500 days) are shown. In Fig. 8.7a the dark pink color shows the water mass distribution. The black curve shows the reference water-front position at that time.

(see Chapter 4 for details). Three cases are analyzed for the presence of the bias, namely, only the observation bias, only the model bias and both biases at the same time.

Fig. 8.8a shows the final permeability estimate in case of the first scenario. The negative observation bias, equal to -4.48 μGal, shifts the observed gravity variation map down. For a comparison, the maximum amplitude of the true signal is about 22 μGal. Consequently, the observed gravity variations are significantly lower than the true ones which results in severely overshooted permeability field estimates. For instance, in the western part of the reservoir, where most of the water influx is distributed, the permeability field is underestimated. This is because the gas replacement by water creates positive mass variations and, as a result, positive gravity changes. To match the observed gravity, which is smaller than the true one, the permeability field needs to be reduced to allow for less water influx. The opposite holds for the eastern part of the reservoir from where most of the gas is produced. There, the gas takeout leads to the negative mass changes and hence to the negative gravity field variations. Since the observed gravity variation is smaller (larger in the absolute sense) than the true one, the permeability is enhanced to allow for more mass takeout. The strongly erroneous permeability estimate results in an inaccurate prediction of the water-front position with a RMSE of about 478 m (Fig. 8.8d). The destructive influence of the observation bias is also visible in the cumulative water influx estimates (Fig. 8.8g). The total amount of water influx is underestimated by more than 25% with respect to the reference value.

Introduction of the model bias, which in this case is the negative gravity variation caused by the groundwater decrease, has similar consequences. However, due to the larger signal amplitude, reaching about -14 μGal, the influence on the estimates is stronger. The front-position RMSE is equal to 887 m in this case and the cumulative water influx estimate is underestimated by more than 50% with respect to the reference value. The scenario where both the observation and the model bias are present, results in very large errors, especially in the water influx estimates (Fig. 8.8i), underestimated by about 67% with respect to the reference value.

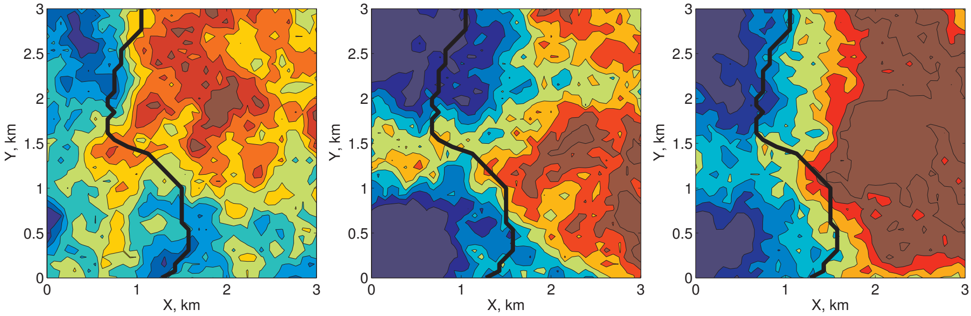

(a) observation bias only **(b)** model bias only **(c)** both biases

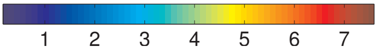

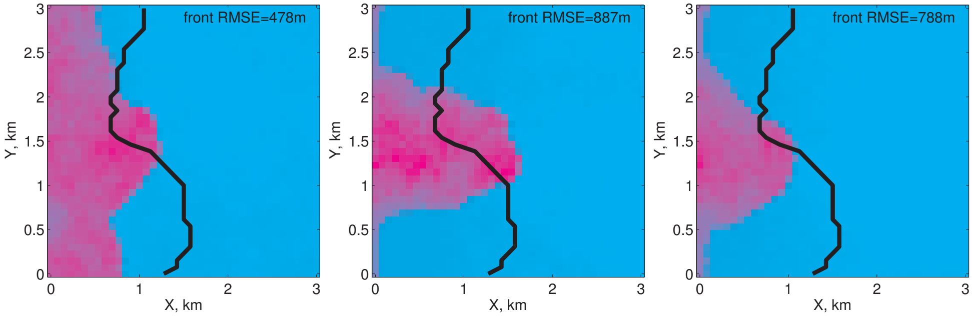

(d) observation bias only **(e)** model bias only **(f)** both biases

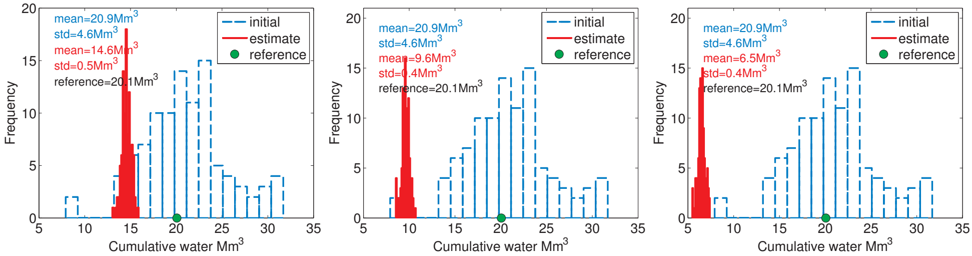

(g) observation bias only **(h)** model bias only **(i)** both biases

Figure 8.8: The final (at 3500 days) estimates in the bias-blind scenario. The first row shows the permeability (in milidarcies) estimates, the middle row shows the estimates of the reservoir mass variation and the bottom row shows the cumulative water influx estimates. In Fig. 8.8d-8.8f the dark pink color shows the water mass distribution. The black curve shows the reference water-front position at that time.

8.3.3 Bias-aware estimates

Fig. 8.9 shows the results of the bias-aware gravity data assimilation. The permeability field estimates are significantly less overshooted compared to those when the biases are completely ignored (compare Fig. 8.8a-8.8c with Fig. 8.9a-8.9c). Especially in the case of the observation bias (Fig. 8.9a) the permeability estimate is not far from the one in the bias-free scenario (Fig. 8.6c). In case of model bias the permeability is less accurate. More accurate estimates in the first case are expected because the observation bias is smaller in magnitude than the model bias. Furthermore, the observation bias is a constant number whereas the model bias is a spatially-variable signal which is much more difficult to estimate. Despite this, the estimates of the water-front position are significantly improved compared to the bias-blind results. The front-position RMSE is reduced several significantly (see Tab. 8.1), i.e., from $500 - 800$ m to about 200 m. Also the estimates of the total water influx are significantly better compared to the bias-blind results. The ensemble mean in all the bias-aware cases is close to the reference value. In case of the observation bias the the ensemble standard deviation of the total water influx is equal to 0.7 Mm^3 and in case of the model bias is equal to 1.4 Mm^3. When both biases are present, as expected, the uncertainty on total water influx is the highest and equal to 1.6 Mm^3. We observed a similar relationship between the variances of the permeability field estimates (not shown here).

Table 8.1: Summary statistics of parameter estimates. The reference cumulative water influx is equal to 20.1 Mm^3.

	RMSE water front (m)	water influx est. (Mm^3)	water influx std (Mm^3)
bias-free	188	19.4	0.5
obs. bias-blind	478	14.6	0.5
model bias-blind	887	9.6	0.4
both bias-blind	788	6.5	0.4
obs. bias-aware	208	18.6	0.7
model bias-aware	212	18.7	1.4
both bias-aware	234	19.3	1.6

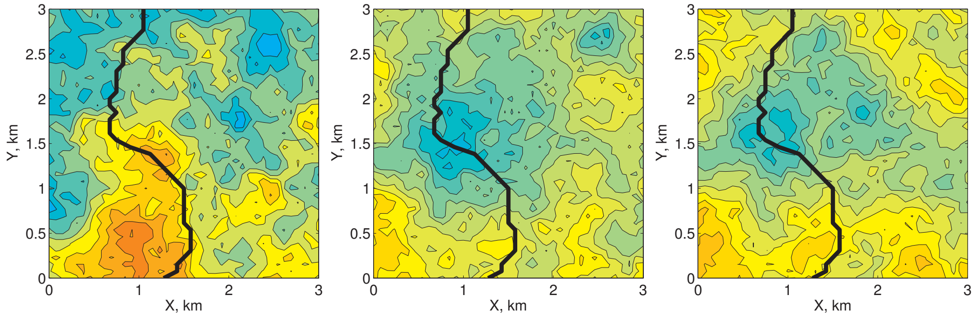

(a) observation bias only **(b)** model bias only **(c)** both biases

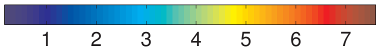

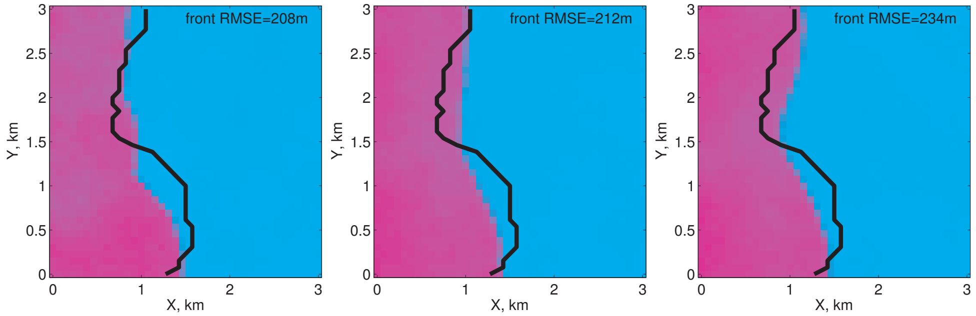

(d) observation bias only **(e)** model bias only **(f)** both biases

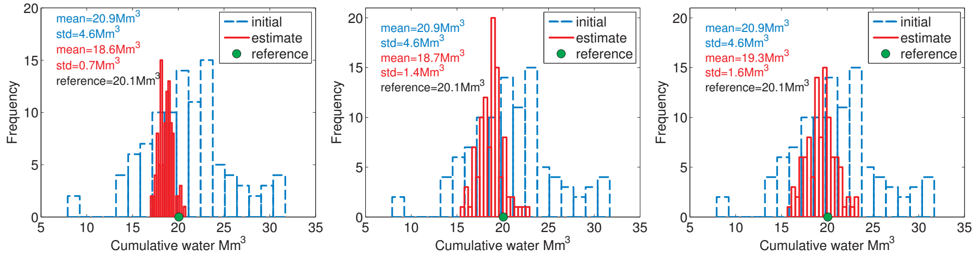

(g) observation bias only **(h)** model bias only **(i)** both biases

Figure 8.9: The final (at 3500 days) estimates in the bias-aware scenario. The first row shows the permeability (in milidarcies) estimates, the middle row shows the estimates of the reservoir mass variation and the bottom row shows the cumulative water influx estimates. In Fig. 8.9d-8.9f the dark pink color shows the water mass distribution. The black curve shows the reference water-front position at that time.

8.3.4 Bias estimates

The estimates of the observation bias are shown in Fig. 8.10. This time we present the results for all the assimilation times, i.e., 1500, 2500 and 3500 days. In all the cases the reference observation bias is within the spread of the updated ensemble members. Also a significant reduction of uncertainty on the bias can be observed. The standard deviation of the initial ensemble is reduced from 2 to about 0.5 μGal.

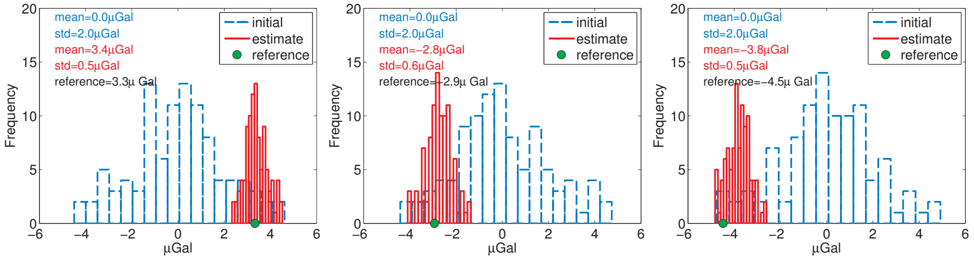

(a) 1500 days **(b)** 2500 days **(c)** 3500 days

Figure 8.10: The observation bias estimates at different data assimilation times. In this case only the observation bias was present.

The model bias estimates are presented in Fig. 8.11. Most of the bias features were recovered reasonably, e.g., the location of the signal low/high values. The estimate RMSE is reduced 2-3 times, i.e., from $6-8$ μGal (Fig. 8.4) to $2-3$ μGal.

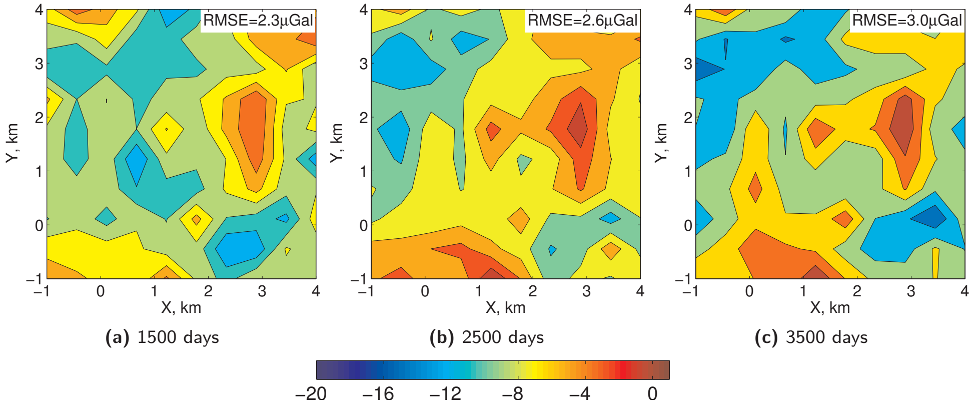

(a) 1500 days **(b)** 2500 days **(c)** 3500 days

Figure 8.11: The model bias estimates at different data assimilation times. In this case only the model bias was present.

The results are less accurate when both biases are present at the same time. The updated estimates of the observation bias (Fig. 8.12) are not very different from the initial values. In all the time steps the reference observation bias is underestimated by about $1-2$ μGal. The model bias estimates (Fig. 8.13) seem to preserve the main signal trend, e.g., the location of the signal low/high values, however they are overshoothed. This suggests that a part of the constant observation bias was absorbed by the model bias estimate.

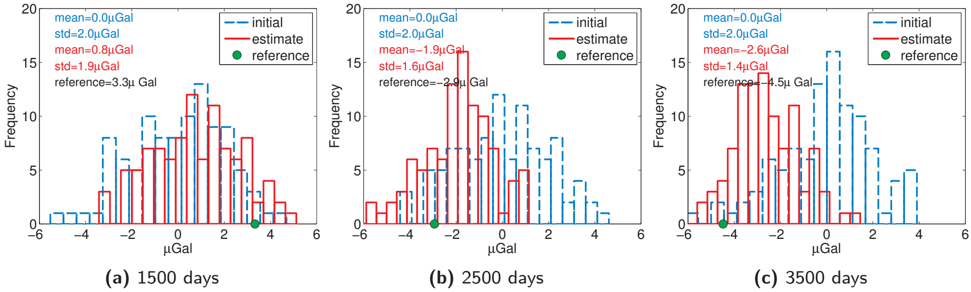

(a) 1500 days **(b)** 2500 days **(c)** 3500 days

Figure 8.12: The observation bias estimates at different data assimilation times in case when both the observation and the model bias were present

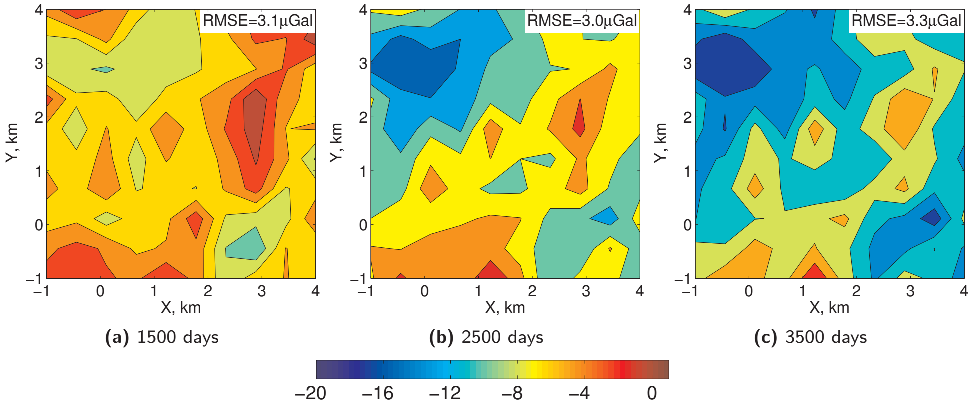

(a) 1500 days **(b)** 2500 days **(c)** 3500 days

Figure 8.13: The model bias estimates at different data assimilation times in case when both the observation and the model bias were present

Figure 8.14 shows the $x-$profile at about $y = 1.3$ km through the gravity variation maps for all three assimilation times. The predictions from the prior ensemble members, the reference signal and the biased signals are shown. The presence of the observation bias, which is a random constant, leads to an offset in the observations but they are still contained within the spread of the ensemble predictions. When the model bias is added, the observed signal is very different not only from the reference signal, but also from the ensemble predictions. It is more spatially variable and significantly smaller. When both biases are combined, the observed gravity is even more outstanding. Thus, in all the cases the innovations (see Chapter 4 for more details), i.e., the difference between the model predictions of the observations and the actual observations, provide information about the presence of biases. The innovations, however, do not distinguish the bias source. We incorporate the constraints on the bias source and the spatio-temporal bias characteristics through the prior information. The bias model forecasts are used to approximate the bias error covariance matrices which define the space where bias estimates are searched for. Thus, it is important that the space spanned by the bias error covariances and the state error covariances are different. This is in fact the case in the considered example. Figure 8.15 shows the model bias (hydrological noise in gravity) and the state (gravity signal from the reservoir) normalized covariance estimates at 3500 days. One row of the covariance matrices is displayed, and the correlation as a function of distance is shown. Clearly, the two covariances are different. The signal (state) covariance matrix shows high correlation at close distances and the correlation decays to zero at about 2.8 km. Note that this is consistent with the spatial characteristics of the true signal (Fig. 8.4c). The model bias covariance shows slightly lower correlation at close distances but higher correlation at larger distances. This seem to be consistent with the characteristics of the hydrological signal defining the true bias (see Fig. 8.3 and Fig. 8.4).

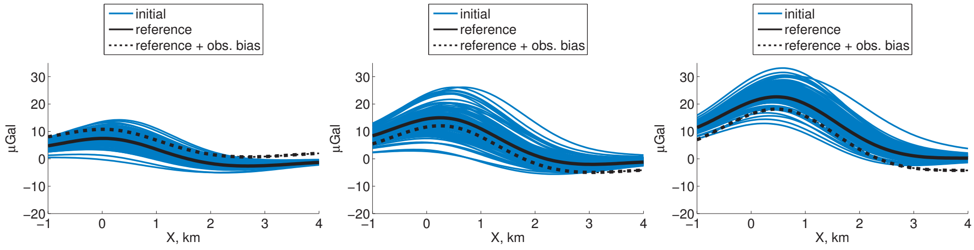

(a) 1500 days **(b)** 2500 days **(c)** 3500 days

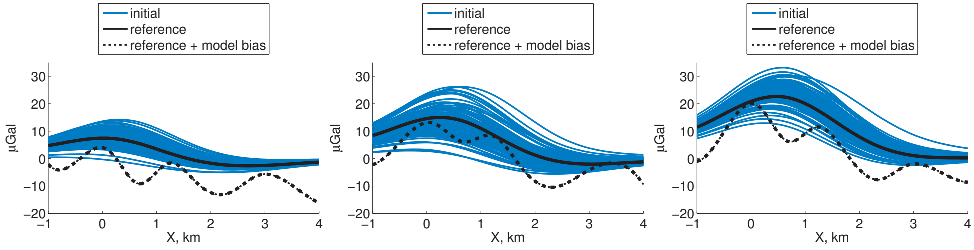

(d) 1500 days **(e)** 2500 days **(f)** 3500 days

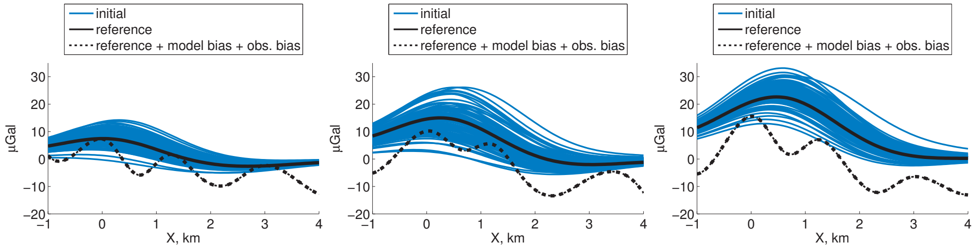

(g) 1500 days **(h)** 2500 days **(i)** 3500 days

Figure 8.14: The $x-$profile at about $y = 1.3$ km through the time-lapse gravity variations: (a-c) only the observation bias is present; (d-f) only the model bias is present; (g-i) both biases are present.

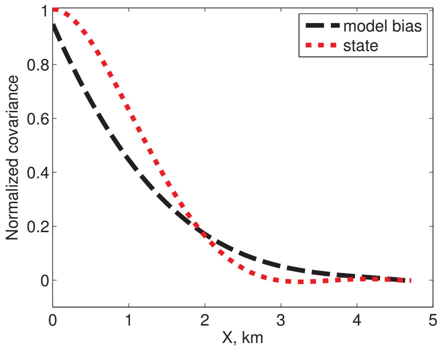

Figure 8.15: One row of the normalized estimate of the error covariance matrices of the state and of the model bias. The covariance as a function of distance is shown.

8.4 Summary

In reservoir history matching, often the assumption is made that the forward model predictions and the observations are unbiased, i.e., that there are no systematic errors. In this study we considered the case where the model and the observation errors arise both as random as well as systematic. For this purpose, a synthetic example of gravity data assimilation for gas field monitoring and characterization was used. Our definitions of the observation and the model bias relate to some practical problems in time-lapse gravimetry. The observation bias was defined as a random offset in the observed time-lapse gravity variations. The model bias was defined as the gravity signal variations caused by the groundwater mass changes. To generate realistic model bias realizations, a hydrological model of the real catchment area was used.

We showed that the influence either of the observation bias or the model bias on assimilation results can be very severe and can lead to a large state/parameter under/overestimation. This is because the inversion of gravimetric observations, like inversion of other geophysical observations, is a severely ill-posed problem. A bias-aware data assimilation methodology can be used when the model and/or observations are likely to be biased. The information about the presence of bias can be obtained from innovations, but to distinguish the bias source, which can be the model, the observations, or both, additional information is needed. The constraints on the bias origin and the bias characteristics can be incorporated through the prior information. The bias error covariances provide the spatial bias information, and the temporal characteristics are included in the bias-evolution models. We showed that by using a bias-aware data assimilation methodology, the bias can be estimated separately from the state and that the deteriorating bias influence on the assimilation results can be to a large extent mitigated. However, the presence of bias implies more uncertain parameter estimates (larger variance) compared to the bias-free scenario. In future studies the applicability of bias-aware data assimilation to other model/observation bias types, such as, e.g., errors in boundary conditions modeling, should be investigated.

Chapter 9

Conclusions and recommendations

9.1 Conclusions

- Time-lapse gravimetry is a promising areal monitoring technique for reservoirs containing fluids with high density contrasts, e.g., gas and water or oil and steam. For large and shallow reservoirs, stronger 4D signals can be observed as compared to small and deep reservoirs. Therefore, the monitoring of shallow reservoirs is especially promising.

- Borehole gravimetry can be used for near well monitoring, within a few tens of meters from the well. Time-lapse gravity gradiometry has the potential to be useful for shallow targets.

- Hydrological variations can be the major source of noise affecting onshore time-lapse gravimetry. Therefore, hydrological observations, in particular groundwater levels, need to be acquired along with gravity data and used to correct for hydrological influences. Already with a single groundwater measurement the hydrological signal can be estimated to some extent, thus reducing the hydrological noise.
  Soil moisture can also add a few μGal to the hydrological signal. However, correcting observed gravity for the influence of soil moisture variations can be very challenging due to soil spatial heterogeneity and its short correlation lengths.

- Gravimetric monitoring of steam injection in the shallow, heavy oil reservoir in the North of Oman has a great potential. The heat-front evolution could be monitored with best accuracy in the order of 140-160 m, which is comparable to half of the reservoir depth. However, we showed also that the gravimetric measurements can be to a large extent influenced by the hydrological signal resulting from spatio-temporal groundwater variations. The front position errors can reach 200-700 m compared to 140-160 m when the hydrological noise is not present. Using field groundwater data we showed that by applying corrections based on the hydrological measurements, the accuracy of gravimetric heat-front monitoring can be significantly improved. With already 36 groundwater observations (6×6 grid) the front-position error can be reduced to about 150-250 m. Further increasing the density of groundwater measurements to about 100-200 brings the accuracy of the estimates close to the case with only the observational noise present in the data, i.e. to about 140-160 m.

- Time-lapse gravimetry is useful for the monitoring of spatial mass redistribution in the reservoir. Large-scale mass variations are easier to monitor than small-scale ones. One of the most promising and useful applications of time-lapse gravimetry is monitoring the amount and spatial distribution of water influx into a gas field.
- The subsurface mass redistribution induced by the water influx, and sensed by time-lapse gravimetry, can be translated into a better knowledge about reservoir parameters and aquifer characteristics using data assimilation. The improvement in spatial parameter estimates can be expected foremost in the regions affected by reservoir mass variations. Gravimetric observations have an added value for the estimation of large-scale patterns (high/low zones) of permeability and porosity fields. They can also contribute to a better understanding of the aquifer dynamics.
- The non-uniqueness of the gravity data inversion for, e.g., permeability estimates, is not only driven by the non-uniqueness of gravimetric observations, but is additionally influenced by an intrinsic non-uniqueness of the reservoir fluid flow.
- The non-uniqueness of the history-matching problem can be partly mitigated by a proper problem parametrization. For instance, instead of a complex 3D aquifer model, analytical solutions can be used, provided that they offer a reasonable approximation of the aquifer behavior.
- Production data assimilation can provide more accurate estimates in near-well regions compared to distant locations. Long-distance spurious correlations may deteriorate the accuracy of estimates at large distances from the wells. The influence of spurious correlations can be reduced with the application of covariance localization methods. Distance-based localization is not suitable for localizing gravity data. This is because the correlation between static parameters, such as permeability, and gravimetric observations, is not only a function of distance but also depends on the mass flow pattern, which in fact is one of the major uncertainties.
- Production data and time-lapse gravity observations are complementary sources of information, which, when combined within a data assimilation framework, can provide a considerably improved picture of reservoir permeability and a better understanding of the subsurface mass redistribution. Furthermore, the joint assimilation of pressure and gravity data results in improved gas and water production forecasts and gives a more accurate reservoir reserves evaluation and reservoir state description.

- Higher gravity measurement random noise-levels lead to smoother parameter estimates with a higher variance.

- In the context of gravity data inversion for hydrocarbon reservoir monitoring and characterization, data assimilation methods, in particular the EnKF and the ES, can be more attractive than classical inversion techniques based on the Tikhonov regularization concept. Firstly, because in data assimilation the prior knowledge can easily be integrated and used to regularize the solution in a physically-based way. Secondly, because it facilitates the integration (joint inversion) of different data types even in a non-linear case.

- The influence either of the observation bias or the model bias on assimilation results can be very severe and can lead to a large state/parameter under/overestimation. This is because the inversion of gravimetric observations, like inversion of other geophysical observations, is a severely ill-posed problem. A bias-aware data assimilation methodology can be used when the model and/or observations are likely to be biased. We showed that by using a bias-aware data assimilation methodology, the bias can be estimated separately from the state and that the deteriorating bias influence on the assimilation results can be to a large extent mitigated. However, the presence of bias implies more uncertain parameter estimates (larger variance) compared to the bias-free scenario.

9.2 Recommendations

- The added value of field-wide, continuous gravity measurements for reservoir monitoring and characterization should be investigated. Gravity sensors have been developed and low-drift (or drift-free), inexpensive gravimeters may become available in the future. A grid of permanently installed gravimeters could provide not only enhanced reservoir monitoring information but also could add to a better understanding of environmental processes affecting gravity observations at a site, such as hydrology.

- Monitoring shallow targets, such as heavy oil reservoirs, with gravity gradiometry may be feasible. Therefore, the added value of gravity gradiometry for monitoring shallow reservoirs and a joint assimilation of gravity and gravity gradient measurements with reservoir production data should be investigated.

- In this research geomechanical effects such as subsidence due to reservoir compaction or uplift due to thermal rock expansion have not been taken into account. Subsidence and gravity observations in the context of gas field monitoring can be a source of complementary information. Gas production causes reservoir pressures to drop, which may induce surface/seabed subsidence, and the gas takeout leads to negative variations in the local gravity field. On the other hand aquifer pressure support may reduce the magnitude of subsidence and aquifer water influx causes positive variations in the local gravity field. In this context, integration of gravity and subsidence data has the potential to be useful for reservoir compartments detection and inference about aquifer support.

- The added value of a joint assimilation of 4D gravity and 4D seismic data for gas field monitoring should be investigated. Both gravity and seismic observations are sensitive to reservoir saturation changes (i.e., gas vs water) and their joint inversion may provide a better constrained reservoir history match.

Appendix: Parameter spatial gradient approximation

In order to approximate the parameter spatial gradient we use the 8-point approximation scheme (see Fig. 9.1). For every grid cell the absolute differences in the parameter values with respect to the parameter values in neighboring cells are determined. The gradient is taken as the maximum of these differences. Of course at the edges the scheme is appropriately adjusted, depending on the number of neighboring cells (Fig. 9.1b). The mathematical formulation of this scheme is shown in Eq. (9.1).

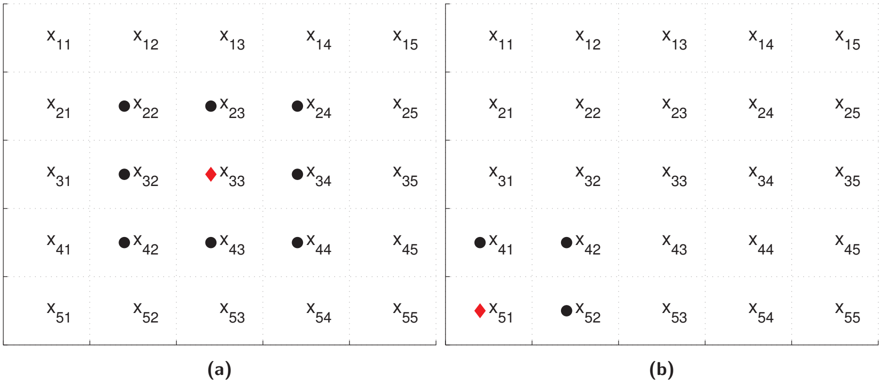

Figure 9.1: Schematic illustration of the numerical spatial gradient calculation. The red diamond denotes the grid cell for which the gradient is computed and the black circles denote the grid cells which are taken into account to approximate the gradient.

$$
\nabla \mathbf{x}_{ij} =
\begin{cases}
\max\{|\mathbf{x}_{ij}-\mathbf{x}_{i+1,j-1}|, |\mathbf{x}_{ij}-\mathbf{x}_{i+1,j}|, |\mathbf{x}_{ij}-\mathbf{x}_{i+1,j+1}|, |\mathbf{x}_{ij}-\mathbf{x}_{i,j+1}|, \\
|\mathbf{x}_{ij}-\mathbf{x}_{i-1,j+1}|, |\mathbf{x}_{ij}-\mathbf{x}_{i-1,j}|, |\mathbf{x}_{ij}-\mathbf{x}_{i-1,j-1}|, |\mathbf{x}_{ij}-\mathbf{x}_{i,j-1}|\}, \text{ for } i<n, j<m \\[2ex]
\max\{|\mathbf{x}_{ij}-\mathbf{x}_{i+1,j}|, |\mathbf{x}_{ij}-\mathbf{x}_{i+1,j+1}|, |\mathbf{x}_{ij}-\mathbf{x}_{i,j+1}|\}, \text{ for } i=1,\ j=1 \\[2ex]
\max\{|\mathbf{x}_{ij}-\mathbf{x}_{i-1,j}|, |\mathbf{x}_{ij}-\mathbf{x}_{i-1,j+1}|, |\mathbf{x}_{ij}-\mathbf{x}_{i,j+1}|\}, \text{ for } i=n,\ j=1 \\[2ex]
\max\{|\mathbf{x}_{ij}-\mathbf{x}_{i-1,j}|, |\mathbf{x}_{ij}-\mathbf{x}_{i-1,j-1}|, |\mathbf{x}_{ij}-\mathbf{x}_{i,j-1}|\}, \text{ for } i=n,\ j=m \\[2ex]
\max\{|\mathbf{x}_{ij}-\mathbf{x}_{i+1,j}|, |\mathbf{x}_{ij}-\mathbf{x}_{i,j-1}|, |\mathbf{x}_{ij}-\mathbf{x}_{i+1,j-1}|\}, \text{ for } i=1,\ j=m \\[2ex]
\max\{|\mathbf{x}_{ij}-\mathbf{x}_{i+1,j}|, |\mathbf{x}_{ij}-\mathbf{x}_{i+1,j+1}|, |\mathbf{x}_{ij}-\mathbf{x}_{i,j+1}|, |\mathbf{x}_{ij}-\mathbf{x}_{i-1,j}|, |\mathbf{x}_{ij}-\mathbf{x}_{i-1,j+1}|\}, \\
\text{for } 1<i<n,\ j=1 \\[2ex]
\max\{|\mathbf{x}_{ij}-\mathbf{x}_{i+1,j}|, |\mathbf{x}_{ij}-\mathbf{x}_{i+1,j-1}|, \\
|\mathbf{x}_{ij}-\mathbf{x}_{i,j-1}|, |\mathbf{x}_{ij}-\mathbf{x}_{i-1,j}|, |\mathbf{x}_{ij}-\mathbf{x}_{i-1,j-1}|\}, \text{ for } 1<i<n,\ j=m \\[2ex]
\max\{|\mathbf{x}_{ij}-\mathbf{x}_{i+1,j}|, |\mathbf{x}_{ij}-\mathbf{x}_{i+1,j-1}|, \\
|\mathbf{x}_{ij}-\mathbf{x}_{i,j-1}|, |\mathbf{x}_{ij}-\mathbf{x}_{i,j+1}|, |\mathbf{x}_{ij}-\mathbf{x}_{i+1,j+1}|\}, \text{ for } i=1,\ 1<j<m \\[2ex]
\max\{|\mathbf{x}_{ij}-\mathbf{x}_{i-1,j}|, |\mathbf{x}_{ij}-\mathbf{x}_{i-1,j-1}|, \\
|\mathbf{x}_{ij}-\mathbf{x}_{i,j-1}|, |\mathbf{x}_{ij}-\mathbf{x}_{i,j+1}|, |\mathbf{x}_{ij}-\mathbf{x}_{i-1,j+1}|\}, \text{ for } i=n,\ 1<j<m
\end{cases}
\tag{9.1}
$$

Bibliography

Aanonsen, S. I., Nævdal, G., Oliver, D. S., Reynolds, A. C. & Vallès, B. (2009), 'The ensemble kalman filter in reservoir engineering-a review.', *SPE Journal* **14**(3), 393–412. SPE-117274-PA.

AhmadZamri, A. F., Musgrove, F. W., Bridle, I. M., Angelich, M. T. & Van den Bosch, R. (2009), Successful reservoir monitoring with 4D microgravity at Ras Laffan, state of Qatar, International Petroleum Technology Conference, Doha, Qatar.

Ahmed, T. (2006), *Reservoir Engineering Handbook , third edition*, Elsevier Inc.

Alawiyah, S., Santoso, D., Kadir, W. G. A. & Matsuoka, T. (2011), Time-lapse microgravity application for estimating fluid density changes of multilayer reservoir using dsmvd technique, International Petroleum Technology Conference, Bangkok, Thailand.

Alixant, J. & Mann, E. (1995), In-situ residual oil saturation to gas from time-lapse borehole gravity, SPE Annual Technical Conference and Exhibition : formation evaluation and reservoir geology, Dallas TX, USA.

Allis, R. G. & Hunt, T. M. (1986), 'Analysis of exploitation-induced gravity changes at wairakei geothermal field', *Geophysics* **51**(8), 1647–1660.

Alnes, H., Eiken, O., Nooner, S., Sasagawa, G., Stenvold, T. & Zumberge, M. (2011), 'Results from Sleipner gravity monitoring: Updated density and temperature distribution of the CO2 plume', *Energy Procedia* **4**(0), 5504–5511.

Alnes, H., Eiken, O. & Stenvold, T. (2008), 'Monitoring gas production and CO2 injection at the Sleipner field using time-lapse gravimetry', *Geophysics* **73**(6), WA155–WA161.

Amalvict, M., Hinderer, J., Mäkinen, J., Rosat, S. & Rogister, Y. (2004), 'Long-term and seasonal gravity changes at the strasbourg station and their relation to crustal deformation and hydrology', *Journal of Geodynamics* **38**(3–5), 343–353. Time Varying Gravimenty, GGP, and Vertical Crustal Motions.

Anctil, G., Mathieu, R., Parent, L. ., Viau, A. A., Sbih, M. & Hessami, M. (2002), 'Geostatistics of near-surface moisture in bare cultivated organic soils', *Journal of Hydrology* **260**, 30–37.

Baker, T. F. & Bos, M. S. (2003), 'Validating earth and ocean tide models using tidal gravity measurements', *Geophysical Journal International* **152**(2), 468–485.

Battaglia, M., Gottsmann, J., Carbone, D. & Fernandez, J. (2008), '4D volcano gravimetry', *Geophysics* **73**(6), WA3–WA18.

Bianco, A., Cominelli, A., Dovera, L., Naevdal, G. & Valles, B. (2007), 'History matching and production forecast uncertainty by means of the ensemble kalman filter: A real field application', *Proceedings of EUROPECEAGE Conference and Exhibition, London, U.K* .

Biegert, E., Ferguson, J. & Li, X. (2008), '4D gravity monitoring — introduction', *Geophysics* **73**(6), WA1–WA2.

Biegert, E. & Witte, S. (2001), 4-D monitoring using gravity and gravity gradients, EAGE 63rd Conference and Technical Exhibition, Amsterdam, The Netherlands,.

Blaschek, R., Hordt, A. & Kemna, A. (2008), 'A new sensitivity-controlled focusing regularization scheme for the inversion of induced polarization data based on the minimum gradient support', *Geophysics* **73**(2), F45–F54.

Boerrigter, P. & van Dorp, J. (2009), Advances in understanding thermally assisted GOGD, 15th European Symposium on Improved Oil Recovery, Paris, France.

Bonafede, M. & Mazzanti, M. (1998), 'Modelling gravity variations consistent with ground deformation in the campi flegrei caldera (italy)', *Journal of Volcanology and Geothermal Research* **81**(1-2), 137–157.

Bos, M. & Baker, T. (2005), 'An estimate of the errors in gravity ocean tide loading computations', *Journal of Geodesy* **79**, 50–63.

Bosch, W., Savcenko, R., Flechtner, F., Dahle, C., Mayer-Grr, T., Stammer, D., Taguchi, E. & Ilk, K.-H. (2009), 'Residual ocean tide signals from satellite altimetry, grace gravity fields, and hydrodynamic modelling', *Geophysical Journal International* **178**(3), 1185–1192.

Boy, J. P., Gegout, P. & Hinderer, J. (2002), 'Reduction of surface gravity data from global atmospheric pressure loading', *Geophysical Journal International* **149**(2), 535–546.

Boy, J. P., Hinderer, J. & Gegout, P. (1998), 'Global atmospheric loading and gravity', *Physics of The Earth and Planetary Interiors* **109**(3-4), 161–177.

Brady, J., Hare, J., Ferguson, J., Seibert, J., Klopping, F., Chen, T. & Niebauer, T. (2008), Results of the world's first 4D microgravity surveillance of a waterflood-Prudhoe Bay, Alaska, SPE Annual Technical Conference and Exhibition, San Antonio, Texas.

Burgers, J. G. & Evensen, G. (1998), ‘Analysis Scheme in the Ensemble Kalman Filter’, *Monthly Weather Review* **126**(6), 1719–1724.

Bychkov, A., Verlaan, M., Boerrigter, P., van Heel, T. & van Dorp, J. (2008), Steam injection into fractured carbonates the physical recovery mechanisms analyzed and upscaled, Abu Dhabi International Petroleum Exhibition and Conference, Abu Dhabi, UAE.

Chang, H., Chen, Y. & Zhang, D. (2010), ‘Data assimilation of coupled fluid flow and geomechanics using the ensemble kalman filter.’, *SPE Journal* **15**(2), 382–394. SPE-118963-PA.

Chapin, D. (1998), ‘Gravity instruments; past, present, future’, *The Leading Edge* **17**(1), 100–112.

Christiansen, L., Lund, S., Andersen, O. B., Binning, P. J., Rosbjerg, D. & Bauer-Gottwein, P. (2011), ‘Measuring gravity change caused by water storage variations: Performance assessment under controlled conditions’, *Journal of Hydrology* **402**(1-2), 60–70.

Creutzfeldt, B., Güntner, A., Klügel, T. & Wziontek, H. (2008), ‘Simulating the influence of water storage changes on the superconducting gravimeter of the geodetic observatory Wettzell, Germany’, *Geophysics* **73**(6), WA95–WA104.

Crossley, D., Hinderer, J. & Rosat, S. (2002), ‘Using atmosphere-gravity correlation to derive a time-dependent admittance’, *Bulletin d’ Informations Marees Terrestres, Roy. Obs. Belgium* **136**, 10809–10820.

Čuma, M., Wilson, G. A. & Zhdanov, M. S. (2012), ‘Large-scale 3d inversion of potential field data’, *Geophysical Prospecting* .

Dake, L. (2001), *The Practice of Reservoir Engineering (Revised Edition)*, Elsevier Science Ltd.

Dee, D. P. (2005), ‘Bias and data assimilation’, *Quarterly Journal of the Royal Meteorological Society* **131**(613), 3323–3343.

Dee, D. P. & Da Silva, A. M. (1998), ‘Data assimilation in the presence of forecast bias’, *Quarterly Journal of the Royal Meteorological Society* **124**(545), 269–295.

Diamond, P. & Ovens, J. (2011), Practical aspects of gas material balance: Theory and application., SPE EUROPEC/EAGE Annual Conference and Exhibition, Vienna, Austria. Paper SPE 142963-MS.

DiFrancesco, D. (2002), Time lapse gravity gradiometry for reservoir monitoring, EAGE 64th conference and exhibition, Florence, Italy.

DiFrancesco, D. (2007), Advances and challenges in the development and deployment of gravity gradiometer systems, EGM 2007 International Workshop Innovation in EM, Grav. and Mag. Methods:a new Perspective for Exploration, Capri, Italy.

Ditmar, P. (2010), ‘Inverse problems’, Lecture notes. Delft University of Technology, The Netherlands.

Droujinine, A., Vasilevsky, A. & Evans, R. (2007), ‘Feasibility of using full tensor gradient (ftg) data for detection of local lateral density contrasts during reservoir monitoring’, *Geophysical Journal International* **169**(3), 795–820.

Eiken, O. & Stenvold, T. (2005), ‘Gravimetric and seafloor subsidence monitoring-a reservoir management tool’, SPE Offshore Beregen One Day Seminar.

Eiken, O., Stenvold, T., Zumberge, M., Alnes, H. & Sasagawa, G. (2008), ‘Gravimetric monitoring of gas production from the Troll field’, *Geophysics* **73**(6), WA149–WA154.

El-Gelil, M. A., Pagiatakis, S. & El-Rabbany, A. (2008), ‘Frequency-dependent atmospheric pressure admittance of superconducting gravimeter records using least squares response method’, *Physics of the Earth and Planetary Interiors* **170**(1-2), 24–33.

Emerick, A. A. & Reynolds, A. C. (2011), ‘History matching a field case using the ensemble kalman filter with covariance localization’, *SPE Reservoir Evaluation and Engineering* **14**(4), 423–432.

Evensen, G. (1994), ‘Sequential data assimilation with a nonlinear quasi-geostrophic model using monte carlo methods to forecast error statistics.’, *Journal of Geophysical Research* **99**(C5), 10143–10162.

Evensen, G. (2003), ‘The ensemble kalman filter: Theoretical formulation and practical implementation.’, *Ocean Dynamics* **53**(4), 343–367.

Evensen, G. (2007), *Data Assimilation: The Ensemble Kalman Filter*, Springer-Verlag Berlin Heidelberg.

Evensen, G., Hove, J., Meisingset, H. C., Reiso, E., Seim, K. S. & Espelid, S. O. (2007), Using the enkf for assisted history matching of a north sea reservoir model., SPE Reservoir Simulation Symposium, Houston. Paper SPE 106184.

Ferguson, J. F., Chen, T., Brady, J., Aiken, C. L. V. & Seibert, J. (2007), ‘The 4D microgravity method for waterflood surveillance: Part II gravity measurements for the Prudhoe Bay reservoir, Alaska’, *Geophysics* **72**(2), I33–I43.

Ferguson, J. F., Klopping, F. J., Chen, T., Seibert, J. E., Hare, J. L. & Brady, J. L. (2008), ‘The 4D microgravity method for waterflood surveillance: Part 3 — 4D absolute microgravity surveys at Prudhoe Bay, Alaska’, *Geophysics* **73**(6), WA163–WA171.

Fjar, E., Holt, R., Horsrud, P., Raaen, A. & Risnes, R. (2008), *Petroleum Related Rock Mechanics (2nd Edition)*, Elsevier.

Friedland, B. (1969), ‘Treatment of bias in recursive filtering’, *Automatic Control, IEEE Transactions on* **14**(4), 359 – 367.

Furrer, R. & Bengtsson, T. (2007), ‘Estimation of high-dimensional prior and posterior covariance matrices in Kalman filter variants’, *Journal of Multivariate Analysis* **98**(2), 227–255.

Girard, A. (1989), ‘A fast ’Monte-Carlo cross-validation’ procedure for large least squares problems with noisy data’, *Numerische Mathematik* **56**, 1–23.

Glegola, M., Ditmar, P., Bierkens, M. F. P., Arts, R. & Vossepoel, F. C. (2009), Estimation of the time-lapse gravity errors due to water table and soil moisture variations., SEG Expanded Abstracts 28, 976, Houston, USA.

Glegola, M., Ditmar, P., Hanea, R. G., Eiken, O., Vossepoel, F. C., Arts, R. & Klees, R. (2012b), ‘History-matching time-lapse surface gravity and well pressure data with ensemble smoother for estimating gas field aquifer support: a 3D numerical study.’, *SPE Journal* **17**(4). SPE-161483-PA.

Glegola, M., Ditmar, P., Hanea, R. G., Vossepoel, F. C., Arts, R. & Klees, R. (2012a), ‘Gravimetric monitoring of water influx into a gas reservoir: A numerical study based on the ensemble kalman filter.’, *SPE Journal* **17**(1). SPE-149578-PA.

Glegola, M., Ditmar, P., Vossepoel, F. C., Arts, R., Al-Kindy, F. & Klees, R. (n.d.), ‘Gravimetric monitoring of the first field-wide steam injection in a fractured carbonate field in Oman – a feasibility study.’, *Geophysical Pospecting* . Under review, submitted 11th November, 2012.

Golub, G. H., Heath, M. & Wahba, G. (1979), ‘Generalized cross-validation as a method for choosing a good ridge parameter’, *Technometrics* **21**(2), pp. 215–223.

Gu, Y. & Oliver, D. S. (2005), ‘History matching of the punq-s3 reservoir model using the ensemble kalman filter.’, *SPE Journal* **10**(2), 217–224. SPE-89942-PA.

Habsi, M., Ikwumonu, A., Khabouri, K., Rawnsley, K., Ismaili, I., Yazidi, R. & Putra, P. (2008), The well and reservoir management strategy for the thermally assisted gas-oil gravity drainage project in oman, International Petroleum Technology Conference, Kuala Lumpur, Malaysia.

Hagoort, J. (1980), ‘Oil recovery by gravity drainage’, *SPE Journal* **20**(3), 139–150.

Hamill, T., Whitaker, J. & Snyder, C. (2001), ‘Distance-Dependent Filtering of Background Error Covariance Estimates in an Ensemble Kalman Filter’, *Monthly Weather Review* **129**(11), 2776–2790.

Hansen, P. C. & O’Leary, D. P. (1993), ‘The use of the l-curve in the regularization of discrete ill-posed problems’, *SIAM J. Sci. Comput.* **14**(6), 1487–1503.

Hare, J. L., Ferguson, J. F., Aiken, C. L. V. & Brady, J. L. (1999), ‘The 4-d microgravity method for waterflood surveillance: A model study for the Prudhoe Bay reservoir, Alaska’, *Geophysics* **64**(1), 78–87.

Hare, J. L., Ferguson, J. F. & Brady, J. L. (2008), ‘The 4D microgravity method for waterflood surveillance: Part IV — modeling and interpretation of early epoch 4D gravity surveys at Prudhoe Bay, Alaska’, *Geophysics* **73**(6), WA173–WA180.

Harnisch, G. & Harnisch, M. (2006), ‘Hydrological influences in long gravimetric data series’, *Journal of Geodynamics* **41**(1–3), 276–287. Earth Tides and Geodynamics: Probing the Earth at Sub-Seismic Frequencies.

Hartemink, M., Escovedo, B. M., Hoppe, J. E. & Macaulay, R. (1997), ‘Qarn Alam: the design of a steam-injection pilot project for a fractured reservoir’, *Petroleum Geoscience* **3**(2), 183–192.

Heemink, A. W., Hanea, R. G., Sumihar, J., Roest, M., Velzen, N. & Verlaan, M. (2010), Data assimilation algorithms for numerical models, *in* B. Koren & K. Vuik, eds, ‘Advanced Computational Methods in Science and Engineering’, Vol. 71 of *Lecture Notes in Computational Science and Engineering*, Springer Berlin Heidelberg, pp. 107–142.

Houtekamer, P. L. & Mitchell, H. L. (2001), ‘A Sequential Ensemble Kalman Filter for Atmospheric Data Assimilation’, *Monthly Weather Review* **129**(1), 123–137.

Hu, K., Huang, Y., Li, H., Li, B., Chen, D. & White, R. E. (2005), ‘Spatial variability of shallow groundwater level, electrical conductivity and nitrate concentration, and risk assessment of nitrate contamination in North China Plain’, *Environment International* **31**, 896–903.

IEO (2011), ‘International energy outlook’, Report Number: DOE/EIA-0484(2011).

Isaaks, E. H. & Srivastava, R. M. (1989), *An Introduction to Applied Geostatistics*, Oxford University Press.

Jansen, J., Bosgra, O. & Van den Hof, P. (2008), ‘Model-based control of multiphase flow in subsurface oil reservoirs’, *Journal of Process Control* **18**(9), 846–855.

Jansen, J., Douma, S., Brouwer, D., Van den Hof, P., Bosgra, O. & Heemink, A. (2009), Closed loop reservoir management, SPE Reservoir Simulation Symposium, The Woodlands, Texas, USA.

Jaźwinski, A. H. (1970), *Stochastic Processes and Filtering Theory*, London Academic Press.

Kang, K., Li, H., Peng, P., Hao, H. & Wei, J. (2011), ‘Seasonal variations in hydrological influences on gravity measurements using gphones’, *Terr. Atmos. Ocean. Sci.* **22**(2), 157–168.

Kantha, L. H. & Clayson, C. A. (2000), *Numerical Models of Oceans and Oceanic Processes*, Elsevier.

Koch, K.-R. & Kusche, J. (2002), ‘Regularization of geopotential determination from satellite data by variance components’, *Journal of Geodesy* pp. 259–268.

Kroner, C. & Jentzsch, G. (1999), ‘Comparison of different barometric pressure reductions for gravity data and resulting consequences’, *Physics of the Earth and Planetary Interiors* **115**(3-4), 205–218.

Kwok, Y.-K. (1991), ‘Singularities in gravity computation for vertical cylinders and prisms’, *Geophysical Journal International* **104**(1), 1–10.

LaFehr, T. R. (1980), ‘Gravity method’, *Geophysics* **45**(11), 1634–1639.

Last, B. J. & Kubik, K. (1983), ‘Compact gravity inversion’, *Geophysics* **48**(6), 713–721.

Lea, D. J., Drecourt, J.-P., Haines, K. & Martin, M. J. (2008), ‘Ocean altimeter assimilation with observational- and model-bias correction’, *Quarterly Journal of the Royal Meteorological Society* **134**(636), 1761–1774.

Liu, N. & Oliver, D. S. (2005), ‘Critical evaluation of the ensemble kalman filter on history matching of geologic facies.’, *SPE Reservoir Evaluation & Engineering* **8**(6), 470–477. SPE-92867-PA.

Loague, K. (1992), ‘Soil water content at r-5. part 1. spatial and temporal variability’, *Journal of Hydrology* **139**, 233–251.

Lyard, F., Lefevre, F., Letellier, T. & Francis, O. (2006), ‘Modelling the global ocean tides: modern insights from fes2004’, *Ocean Dynamics* **56**, 394–415.

Lyon, S. W., Seibert, J., Lembo, A. J., Walter, M. & Steenhuis, T. S. (2006), ‘Geostatistical investigation into the temporal evolution of spatial structure in a shallow water table’, *Hydrology and Earth System Sciences* **10**, 113–125.

MacQueen, J. D. & Mann, E. (2007), Borehole gravity meter surveys at the waste treatment plant, Technical report, Microg-LaCoste.

Massey, F. J. (1951), ‘The kolmogorov-smirnov test for goodness of fit’, *Journal of the American Statistical Association* **46**(253), 68–78.

Meisingset, K. (1999), ‘Uncertainties in reservoir fluid description for reservoir modeling.’, *SPE Res Eval & Eng* **2**(5), 431–435. SPE 57886-PA.

Ménard, R. (2010), Bias estimation, *in* W. Lahoz, B. Khattatov & R. Menard, eds, ‘Data Assimilation’, Springer Berlin Heidelberg, pp. 113–135.

Miyoshi, T., Kalnay, E. & Li, H. (2009), Estimation of observation error correlation and the treatment in ensemble kalman filter., Extended abstract of the 5th WMO Symposium on Data Assimilation, Melbourne, Australia.

Morris, D. & Johnson, A. (1967), ‘Summary of hydrologic and physical properties of rock and soil materials as analyzed by the hydrologic laboratory of the u.s. geological survey’, U.S. Geological Survey Water-Supply Paper 1839-D.

Mukai, A., Higashi, T., Takemoto, S., Nakagawa, I. & Naito, I. (1995), ‘Accurate estimation of atmospheric effects on gravity observations made with a superconducting gravity meter at kyoto’, *Physics of The Earth and Planetary Interiors* **91**(1-3), 149–159. Study of the Earth’s Deep Interior.

Nabighian, M. N., Ander, M. E., Grauch, V. J. S., Hansen, R. O., LaFehr, T. R., Li, Y., Pearson, W. C., Peirce, J. W., Phillips, J. D. & Ruder, M. E. (2005), ‘Historical development of the gravity method in exploration’, *Geophysics* **70**(6), 63ND–89ND.

Nævdal, G., Mannseth, T. & Vefring, E. (2002), Near-well reservoir monitoring through ensemble kalman filter., SPE/DOE Improved Oil Recovery Symposium, Tulsa. Paper SPE 75235.

Nagy, D., Papp, G. & Benedek, J. (2000), ‘The gravitational potential and its derivatives for the prism’, *Journal of Geodesy* **74**, 552–560.

Naujoks, M., Kroner, C., Weise, A., Jahr, T., Krause, P. & Eisner, S. (2010), ‘Evaluating local hydrological modelling by temporal gravity observations and a gravimetric three-dimensional model’, *Geophysical Journal International* **182**(1), 233–249.

Neumeyer, J., Hagedoorn, J., Leitloff, J. & Schmidt, T. (2004), ‘Gravity reduction with three-dimensional atmospheric pressure data for precise ground gravity measurements’, *Journal of Geodynamics* **38**(3–5), 437–450. Time Varying Gravimenty, GGP, and Vertical Crustal Motions.

Niebauer, T. M., Sasagawa, G. S., Faller, J. E., Hilt, R. & Klopping, F. (1995), ‘A new generation of absolute gravimeters’, *Metrologia* **32**, 159–180.

Nooner, S., Eiken, O., Hermanrud, C., Sasagawa, G., Stenvold, T. & Zumberge, M. (2007), ‘Constrains on the in situ density of CO2 within the utsira formation from time-lapse seafloor gravity measurements’, *International Journal of Greenhouse Gas Control* pp. 198–214.

Oliver, D. & Chen, Y. (2011), ‘Recent progress on reservoir history matching: a review’, *Computational Geosciences* **15**, 185–221.

Oliver, D., Reynolds, A. & Liu, N. (2008), *Inverse Theory for Petroleum Reservoir Characterization and History Matching*, Cambridge University Press.

Peaceman, D. W. (1977), *Fundamentals of Numerical Reservoir Simulation*, Elsevier, Amsterdam, The Netherlands.

Penney, R., Lawati, S. B. A., Hinai, R., van Ravesteijn, O., Rawnsley, K., Putra, P., Geneau, M., Ikwumonu, A., Habsi, M. & Harrasy, H. (2007), First full field steam injection in a fractured carbonate at Qarn Alam, oman, SPE Middle East Oil and Gas Show and Conference, Kingdom of Bahrain.

Portniaguine, O. & Zhdanov, M. S. (1999), ‘Focusing geophysical inversion images’, *Geophysics* **64**(3), 874–887.

Remy, N., Boucher, A. & Wu, J. (2009), *Applied geostatistics with SGeMS : a user's guide.*, Cambridge University Press.

Rymer, H. (1994), 'Microgravity change as a precursor to volcanic activity', *Journal of Volcanology and Geothermal Research* **61**(3-4), 311–328.

Sasagawa, G., Zumberge, M. & Eiken, O. (2008), 'Long-term seafloor tidal gravity and pressure observations in the north sea: Testing and validation of a theoretical tidal model', *Geophysics* **73**(6), WA143–WA148.

Seiler, A., Aanonsen, S. I., Evensen, G., & Rivenæs, J. C. (2010), 'Structural surface uncertainty modeling and updating using the ensemble kalman filter.', *SPE Journal* **15**(4), 1062–1076. SPE 125352-PA.

Siddique, M. (2011), Application of time lapse gravity in history matching a gas/condensate field, EAGE/SPE Joint Workshop, Istanbul, Turkey.

Skjervheim, J., Evensen, G., Hove, J. & Vabo, J. G. (2011), An ensemble smoother for assisted history matching, SPE Reservoir Simulation Symposium, The Woodlands, USA. Paper SPE 141929-MS.

Speight, J. G. (2009), *Enhanced Recovery Methods for Heavy Oil and Tar Sands*, Gulf Publishing Company, Houston, Texas,USA.

Stenvold, T., Eiken, O. & Landro, M. (2008), 'Gravimetric monitoring of gas-reservoir water influx – a combined flow-and gravity-modeling approach.', *Geophysics* **73**(6), WA123–WA131. doi: 10.1190/1.2991104.

Sun, H., Ducarme, B. & Dehant, V. (1995), 'Effect of the atmospheric pressure on surface displacements', *Journal of Geodesy* **70**, 131–139.

Telford, W. M., Geldart, L. P. & Sheriff, R. E. (1990), *Applied geophysics (second edition)*, Cambridge University Press.

Thulin, K., Li, G., Aanonsen, S. I. & Reynolds, A. C. (2007), Estimation of initial fluid contacts by assimilation of production data with enkf., SPE Annual Technical Conference and Exhibition, Anaheim, California, USA. Paper SPE 109975.

Tikhonov, A. & Arsenin, V. (1977), *Solutions of ill-posed problems*, Scripta series in mathematics, Winston.

Torge, W. (1989), *Gravimetry*, Walter de Gruyter, Berlin, New York.

Turchin, V. F., Kozlov, V. P. & Malkevich, M. S. (1971), 'The use of mathematical-statistics methods in the solution of incorrectly posed problems', *Physics-Uspekhi* **13**(6), 681–703.

Van Camp, M. (2003), 'Efficiency of tidal corrections on absolute gravity measurements at the membach station', *Cahiers du Centre Européen de Géodynamique et de Séismologie* **22**, 99–103.

Van Everdingen, A. & Hurst, W. (1949), ‘The application of the laplace transformation to flow problems in reservoirs’, *Trans. AIME* **186**(305).

van Gelderen, M., Haagmans, R. & Bilker, M. (1999), ‘Gravity changes and natural gas extraction in groningen’, *Geophysical Prospecting* **47**(6), 979–993.

van Leeuwen, P. J. (2009), ‘Particle filtering in geophysical systems’, *Monthly Weather Review* **137**, 4089–4114.

van Leeuwen, P. J. & Evensen, G. (1996), ‘Data assimilation and inverse methods in terms of a probabilistic formulation’, *Monthly Weather Review* **124**, 2898–2913.

Van Popta, J., Heywood, J. M. T., Adams, S. J. & Bostock, D. R. (1990), Use of borehole gravimetry for reservoir characterization and fluid saturation monitoring,, EUROPEC, The Hague, The Netherlands.

Veeken, C. A. M., Chin, H. V., Ross, R. W. & Newell, M. D. (2000), Monitoring and control of water influx in strong aquifer drive gas fields offshore sarawak., SPE Asia Pacific Oil and Gas Conference and Exhibition, Brisbane, Australia. Paper SPE 64402-MS.

Vinnikov, K. Y., Robock, A., Speranskaya, N. A. & Schlosser, C. A. (1996), ‘Bias and data assimilation’, *Journal of Geophysical Research* **101**(D3), 7163–7174.

Vossepoel, F. C. & van Leeuwen, P. J. (2007), ‘Parameter estimation using a particle method: Inferring mixing coefficients from sea level observations.’, *Monthly Weather Review* **135**, 1006–1020.

Walsh, J. B. & Rice, J. R. (1979), ‘Local changes in gravity resulting from deformation’, *Journal of Geophysical Research* **84**(B1), 165–170.

Western, A. W., Zhou, S. L., Grayson, R. B., McMahon, T. A., Blöschl, G. & Wilson, D. J. (2004), ‘Spatial correlation of soil moisture in small catchments and its relationship to dominant spatial hydrological processes’, *Journal of Hydrology* **286**, 113–134.

Xu, J., Sun, H. & Yang, X. (2004), ‘A study of gravity variations caused by polar motion using superconducting gravimeter data from the ggp network’, *Journal of Geodesy* **78**, 437–450.

Yokoyama, I. (1989), ‘Microgravity and height changes caused by volcanic activity: Four’, *Bulletin of Volcanology* **51**, 333–345.

Zhang, L., Koyama, T., Utada, H., Yu, P. & Wang, J. (2012), ‘A regularized three-dimensional magnetotelluric inversion with a minimum gradient support constraint’, *Geophysical Journal International* **189**(1), 296–316.

Zhdanov, M. (2007), New advances in regularized inversion and imaging of gravity, magnetic, and electromagnetic data, EGM International Workshop: Innovation in EM, Grav and Mag Methods:a new Perspective for Exploration, Capri, Italy. Paper SPE 141929-MS.

Zhdanov, M. S. (2002), *Geophysical inverse theory and regularization problems*, Elsevier, Amsterdam - New York - Tokyo.

Zhdanov, M. S. (2009), ‘New advances in regularized inversion of gravity and electromagnetic data’, *Geophysical Prospecting* **57**(4), 463–478.

Zhdanov, M. S., Čuma, M., Wilson, G. A., Velikhov, E. P., Black, N. & Gribenko, A. V. (2011a), ‘Iterative electromagnetic migration for 3d inversion of marine controlled-source electromagnetic data’, *Geophysical Prospecting* **59**(6), 1101–1113.

Zhdanov, M. S., Wan, L., Gribenko, A., Čuma, M., Key, K. & Constable, S. (2011b), ‘Large-scale 3d inversion of marine magnetotelluric data: Case study from the gemini prospect, gulf of mexico’, *Geophysics* **37**(1), F77–F87.

Zhdanov, M. & Tolstaya, E. (2004), ‘Minimum support nonlinear parametrization in the solution of a 3D magnetotelluric inverse problem’, *Inverse Problems* **20**(3), 937–952.

Zhdanov, M., Vignoly, G. & Ueda, T. (2006), ‘Sharp boundary inversion in crosswell traveltime tomography’, *Journal of Geophysics and Engineering* **3**(2), 122–134.

Zumberge, M., vard Alnes, H., Eiken, O., Sasagawa, G. & Stenvold, T. (2008), ‘Precision of seafloor gravity and pressure measurements for reservoir monitoring’, *Geophysics* **73**(6), WA133–WA141.

Summary

Reservoir monitoring is one of the key elements of closed-loop reservoir management, which is recently receiving growing attention in the petroleum industry. Reservoir monitoring data provide information about changes taking place in the reservoir, which are triggered by reservoir management actions. By comparing real observations with the predictions from a numerical model of the reservoir, the uncertain model parameters, e.g., porosity, permeability, can be adjusted such that the real and the simulated observations match. For this purpose data assimilation methods are applied. Typically, reservoir models are updated using production measurements (e.g., well fluid rates, bottomhole pressures) and other data, mostly time-lapse seismic. Information provided by production data, is usually only local and not representative for the whole reservoir. Time-lapse seismics allows field-wide monitoring and makes it possible to determine location-specific production-induced changes in the reservoir. However, seismic data acquisition is usually expensive, may be difficult, and sometimes even prohibitive. Since gravity field variations are directly related to subsurface mass redistribution, time-lapse gravimetry can provide complementary information for reservoir monitoring and characterization. Despite the increasing number of applications of time-lapse gravimetry for the monitoring of hydrocarbon reservoirs, there is little known about the added value of gravimetric observations within a context of closed-loop reservoir management.

In this thesis the added value of gravity observations for hydrocarbon reservoir monitoring and characterization is investigated. Using forward modeling of the gravity signal, reservoir processes and reservoir types most suitable for gravimetric monitoring are identified. Furthermore, a sensitivity analysis is performed to analyze the applicability of various gravity measurement types. It is shown that surface time-lapse gravimetry has a potential to be useful for monitoring reservoir processes with high density contrast, such as gas and water or steam and oil. Also reservoir geometric configuration (size/depth) is relevant. Small and deep reservoirs are difficult to monitor compared to shallow and large fields. Borehole gravity measurements can provide monitoring information on a local scale, typically several tens of meters from the borehole.

In order to better understand the challenges of gravimetric reservoir monitoring, major noise sources affecting time-lapse gravimetry are analyzed. Special attention is

devoted to the analysis of hydrological influences on gravimetric observations, in particular originating from groundwater table variations. A potential contribution of groundwater to the uncertainty budget is evaluated with forward simulations of hypothetical variations of water table change. It is shown that gravity variations caused by water table changes can mask the signal of interest, originating from the reservoir. Therefore, there is a need to acquire groundwater observations to correct the observed gravity. A sensitivity study is performed to investigate under which conditions the hydrological influences on gravimetric reservoir monitoring can be minimized.

The remaining part of the thesis is devoted to the inversion of gravity and reservoir production data. First, the inversion methods used through the thesis are presented. We introduce the focusing inversion method, which belongs to the class of Tikhonov regularization methods, and also the ensemble Kalman filter (EnKF) and the ensemble smoother (ES), which belong to the ensemble-based data assimilation methods. A common framework between the Tikhonov regularization concept and data assimilation is briefly discussed, complemented by illustrative examples of application. Subsequently, an extension of data assimilation to cases when the model and/or the observation errors are not only random but also systematic, is introduced.

The focusing inversion method is applied to a feasibility study on gravimetric monitoring of the Thermally-Assisted Gas-Oil Gravity Drainage (TA-GOGD) process at a carbonate field in the North of Oman. The analysis includes quantification of the predicted changes in the temporal gravity signal resulting from the reservoir mass redistribution induced by the TA-GOGD process. The focusing inversion of the synthetic gravity observations is used to analyze the achievable accuracy of heat-front position estimates. Based on historical groundwater measurements, estimates of the noise in gravity data related to the specific hydrological conditions are also considered. It is shown that hydrological signals can be a very significant source of noise and can affect the gravimetric monitoring of the field. Therefore, it is investigated under which conditions the hydrological influences can be minimized. For this purpose a set of hypothetical scenarios is evaluated, where various densities of the water table observation wells are simulated. We show that already with several groundwater observations the estimation error in the front position can be reduced by a factor of 2-3, compared to the case when no hydrological signal is removed from the data.

To understand the added value of gravity data assimilation for reservoir monitoring and characterization a simplified study is performed based on a 2D gas reservoir model. Synthetic gravity measurements are assimilated with the EnKF to estimate the reservoir permeability. The updated reservoir model is used to predict the water front position. It is shown how the subsurface mass redistribution, induced by water influx, and sensed by time-lapse gravity, can be translated into a better knowledge about the reservoir permeability with the EnKF inversion. The updated permeability can be further used to improve forecasts of the actual mass redistribution and to decrease the uncertainty about the water front configuration. To investigate the impact of gravity measurement noise and the influence of the distance from the gravity observation network to the reservoir formation, a sensitivity analysis is performed. The results show that with increasing gravimetric noise and/or distance, the updated model permeability becomes smoother and its variance higher. Finally, the effect of a combined assimilation of gravity and production data is investigated. In the case when only production data are used, the permeability estimates far from the wells are erroneous, despite a very accurate history match of the data. Consequently, very inaccurate estimates of the water front position are obtained. In the case when production and gravity data are combined within a single data assimilation framework, we obtain a considerably improved estimate of the reservoir permeability and an improved understanding of the subsurface mass flow. These results illustrate the added value of gravimetric observations for monitoring water influx, and they show also that gravimetric and production observations can be a complementary source of information.

After these initial insights into the value of assimilation of gravity data, a more realistic synthetic 3D example, inspired by some of the North Sea gas fields, is considered. The key field uncertainties addressed in this study are not only the permeability field but also the porosity field, reservoir structural parameters and foremost the aquifer support characteristics. We compare scenarios where only gravity, only production and both production and gravity data are assimilated. The added value of gravity data is evaluated in the context of various reservoir engineering aspects, such as reservoir characterization, reservoir state description, forecast reliability and gas reserves estimation. For this purpose the ES method is used. The results show that history-matching a gas field with pressure data only may provide highly non-unique solutions because several parameter combinations can explain the reservoir pressure behavior observed in the wells. Then, it is hardly possible to find at the same time accurate estimates of aquifer support and reservoir structure or permeability. Therefore, additional information is needed which can be provided by time-lapse gravimetry. We demonstrate that a joint assimilation of pressure and gravity data can provide more constrained inverse solutions and result not only in improved gas and water production forecast, but also can give more accurate reservoir reserves evaluation and reservoir state description.

Finally, an example of gravity data assimilation in case of systematic model or observation errors, called bias, is considered. The definitions of the observation and the model bias used in this study relate to some practical aspects of time-lapse gravimetry. The observation bias is defined as a random offset in the observed gravity variations, which can occur in time-lapse gravimetry based on relative measurements. The model bias relates to the undermodeling because, typically, a numerical model is developed for the hydrocarbon reservoir, but such a model is rarely available for the hydrological processes at a site. Consequently, the observed gravity variations, which contain the hydrological signal, cannot be predicted correctly. Thus, the model predictions of the observed data are biased. In this study the model bias is defined as the gravity signal caused by groundwater table variations.

We show that the influence either of the observation bias or the model bias on the assimilation results can be very severe and can lead to a large state/parameter under/overestimation. A bias-aware data assimilation methodology can be used when the model and/or observations are likely to be biased. Information about the presence of a bias can be obtained from the mismatch between the observed and the predicted data, but to distinguish the bias source, which can be the model, the observations or both, additional knowledge, is needed. The constraints on the bias origin and the bias characteristics can be incorporated through prior information. The bias error covariances provide the spatial bias information and the temporal characteristics are included in the bias-evolution models. We showed that by using a bias-aware data assimilation methodology the deteriorating bias influence on the assimilation results can be to a large extent mitigated. However, the presence of a bias implies more uncertain parameter estimates (larger variance) compared to the bias-free scenario.

Samenvatting

Het monitoren van reservoirs is een van de belangrijkste onderdelen van "closed-loop reservoir management", een onderwerp dat de laatste jaren steeds meer aandacht krijgt in de petroleum industrie. Meetgegevens afkomstig van reservoir monitoring geven informatie over veranderingen in het reservoir, die samenhangen met reservoir management acties. Door echte metingen te vergelijken met numerieke modelvoorspellingen van het reservoir, kunnen de met grote onzekerheid bepaalde modelparameters, zoals bijvoorbeeld porositeit en permeabiliteit, dusdanig aangepast worden, dat de echte en gesimuleerde meetgegevens goed overeenkomen. Om dit te bewerkstelligen worden data assimilatie technieken gebruikt. Daarbij worden over het algemeen reservoir modellen aangepast op basis van productiemeetgegevens (zoals vloeistofstroming in de put, drukken onderaan de put (BHP)), maar ook door andere gegevens, zoals in de tijd herhaalde seismische metingen. Informatie verkregen uit productiegegevens is over het algemeen slechts lokaal en niet representatief voor het gehele reservoir. In de tijd herhaalde seismische metingen (ofwel "time-lapse seismiek") daarentegen leveren monitoringgegevens op over het gehele veld en maken het daarmee mogelijk om veranderingen in het reservoir veroorzaakt door productie in specifieke gebieden te identificeren. Daar staat wel tegenover, dat het verkrijgen van seismische gegevens over het algemeen kostbaar is, soms onder lastige condities uitgevoerd moet worden en in enkele gevallen zelfs niet mogelijk is. Aangezien variaties in het zwaartekrachtsveld direct gerelateerd zijn aan de massaherverdeling in de ondergrond , kunnen in de tijd herhaalde zwaartekrachtsmetingen (ofwel "time-lapse zwaartekrachtsmetingen") in principe aanvullende informatie voor reservoir monitoring en karakterisatie geven. Ondanks het groeiende aantal toepassingen van time-lapse zwaartekrachtsmetingen ten behoeve van het monitoren van olie- en gas reservoirs, is er nog steeds weinig bekend omtrent de toegevoegde waarde van zwaartekrachtsmetingen in termen van "closed-loop reservoir management". In dit proefschrift wordt deze toegevoegde waarde van zwaartekrachtsmetingen voor olie- en gas reservoir monitoring en karakterisatie onderzocht. Door gebruik te maken van voorwaartse modellering van het zwaartekrachtsignaal, worden juist die reservoir processen en ook type reservoirs gedentificeerd, die het meest geschikt zijn voor dit type monitoring. Verder wordt er een gevoeligheidsanalyse uitgevoerd om de toepasbaarheid van verschillende type zwaartekrachtsmetingen te analyseren. Hierbij is aangetoond, dat time-lapse zwaartekrachtsmetingen vanaf het oppervlak potentieel nuttig kunnen zijn voor het monitoren van reservoirprocessen, waarbij hoge dichtheidscontrasten aan de orde zijn, zoals het geval is bij gas en water of bij stoom en olie. Tevens speelt hierbij de geometrische configuratie van het reservoir (grootte/diepte) een rol. Smalle en diepliggende reservoirs zijn moeilijk te monitoren vergeleken met ondiepe uitgestrekte velden. Zwaartekrachtsmetingen gedaan vanuit een boorgat leveren meer informatie op een lokale schaal op, in het algemeen tot enkele tientallen meters van het boorgat. Om een beter begrip te krijgen van de uitdagingen, die gepaard gaan met reservoir monitoring middels zwaartekrachtsmetingnen, zijn de belangrijkste bronnen van ruis onderzocht, die het time-lapse signaal benvloeden. Hierbij is speciaal aandacht geschonken aan de analyse van hydrologische invloeden op het zwaartekrachtsignaal, vooral wanneer veroorzaakt door veranderingen in de grondwaterstand. De mogelijke bijdrage van grondwater op de totale onzekerheid is gevalueerd met behulp van voorwaartse simulaties van hypothetische veranderingen in de grondwaterspiegel. Hierbij is aangetoond, dat zwaartekrachtsvariaties veroorzaakt door grondwaterspiegelschommelingen het gewenste meetsignaal van het reservoir kunnen maskeren. Daarom is het dan ook noodzakelijk om grondwaterspiegelwaarnemingen te doen om het geobserveerde zwaartekrachtsignaal te kunnen corrigeren. Een gevoeligheidsanalyse is uitgevoerd om te onderzoeken onder welke omstandigheden de hydrologische invloeden op zwaartekracht reservoir monitoring geminimaliseerd kunnen worden. De rest van dit proefschrift is gewijd aan de inversie van zwaartekracht- en reservoirproductie waarnemingen. Allereerst worden de in dit proefschrift gebruikte inversiemethodes beschreven. We introduceren de "focusing inversiemethode", die tot de klasse van Tikjonov regularisatiemethodes behoort, en tevens het "Ensemble Kalman Filter (EnKF)" en de "Ensemble Smoother (ES)", die tot de ensembe gebaseerde data assimilatiemethodes behoren. De overeenkomsten tussen het Tikhonov regularisatie concept en data assimilatie worden kort bediscussieerd, aangevuld met illustratieve voorbeelden van toepassingen. Vervolgens wordt een uitbreiding van data assimilatie gentroduceerd voor gevallen, waarbij modellen- en/of observatiefouten niet alleen willekeurig zijn, maar ook systematisch. De "focusing inversie methode" is toegepast in een haalbaarheidsstudie naar zwaartekrachtmonitoring van het "Thermally-Assisted Gas-Oil Gravity Drainage (TA-GOGD) proces" in een carbonaatveld in het noorden van Oman. De analyse omvat een kwantificering van de te verwachten veranderingen in het temporele zwaartekrachtsignaal ten gevolge van de massa herverdeling in het reservoir veroorzaakt door het TA-GOGD process. De "focusing inversie" van de synthetische zwaartekrachtsmetingen is gebruikt om de haalbare nauwkeurigheid van de positie van hittefronten te schatten. Gebaseerd op bestaande meetreeksen van grondwaterstanden uit het verleden, zijn schattingen van de ruis in de zwaartekrachtsmetingen, veroorzaakt door de specifieke hydrologische omstandigheden, meegenomen. Hiermee is aangetoond, dat hydrologische signalen een belangrijke bron van ruis vormen, die zwaartekrachtmonitoring van het veld behoorlijk kunnen benvloeden. Vervolgens is bepaald onder welke omstandigheden de hydrologische invloeden tot een minimum beperkt kunnen worden. Daartoe is een set van hypothetische scenario's gevalueerd, waarin verschillende aantallen observatieputten om de waterstanden te meten zijn gesimuleerd. We laten hiermee zien, dat reeds bij een paar grondwaterobservatieputten de geschatte fout in de frontpositie gereduceerd kan worden met een factor 2 tot 3 in vergelijking tot het geval, waarbij geen enkele hydrologische signaalcorrectie wordt toegepast. Om de toegevoegde waarde van data assimilatie met zwaartekrachtsmetingen voor reservoir monitoring en karakterisatie beter te begrijpen, is een studie uitgevoerd gebaseerd op een 2D gas reservoirmodel. Synthetische zwaartekrachtsmetingen zijn geassimileerd met de EnKF om de reservoir permeabiliteit te schatten. Het aangepaste reservoir model is vervolgens gebruikt voor de voorspelling van waterfrontposities. Hierbij wordt aangetoond, hoe de ondergrondse massaherverdeling, veroorzaakt door de waterinstroming en gemeten met de time-lapse zwaartekrachtsmetingen, vertaald kan worden naar een verbeterde kennis van de reservoirpermeabiliteit middels de EnKF inversie. Het aangepaste permeabiliteitsmodel kan verder nog gebruikt worden om voorspellingen van de eigenlijke massaherverdeling te verbeteren en om de onzekerheid omtrent de posities van de waterfronten te reduceren. Om de impact van ruis en van de afstand tussen het meetnetwerk en het reservoir op zwaartekrachtsmetingen te bepalen, is een gevoeligheidsanalyse uitgevoerd. Resultaten tonen aan, dat met een toename van ruis en/of met een toename van de afstand, het aangepaste permeabiliteitsmodel gladder wordt met een hogere variantie. Tenslotte is het effect van een gecombineerde assimilatie van zwaartekrachtsmetingen en productiegegevens onderzocht. In het geval, waarin alleen productiegegevens gebruikt zijn, blijken de permeabiliteitsschattingen ver van de putten foutief, ondanks een zeer goede "history match" van de gegevens. Dit leidt logischerwijze ook tot zeer onnauwkeurige schattingen van waterfrontposities. In het geval, waarin zowel productie- als zwaartekrachtsmeetgegevens zijn gecombineerd in een enkel data assimilatieschema, krijgen we een aanzienlijk verbeterde schatting van de reservoirpermeabiliteit als ook een beter begrip van de ondergrondse massastromen. Deze resultaten laten duidelijk de toegevoegde waarde van zwaartekrachtsmetingen voor het monitoren van water instroming in het reservoir zien. Verder laten ze zien, dat zwaartekrachtsmetingen en productiegegevens complementaire informatie bevatten. Gestimuleerd door deze initile inzichten in de waarde van het assimileren van zwaartekrachtsmetingen, is een realistischer, maar nog steeds synthetisch, 3D voorbeeld gekozen, genspireerd op een set van typische Noordzee gasvelden. De belangrijkste onzekerheden in deze velden, geadresseerd in deze studie, zijn naast het permeabiliteitsveld ook het porositeitsveld, de structurele reservoir parameters en misschien wel het belangrijkste, de karakteristieken van de waterlaag, waaruit water het reservoir instroomt bij productie van gas. We vergelijken wederom scenario's waarin alleen zwaartekrachtsmetingen, alleen productiegegevens en waarin beiden worden geassimileerd. De toegevoegde waarde van zwaartekrachtsmetingen wordt afgemeten aan enkele "reservoir engineering" indicatoren, zoals de kwaliteit van de reservoir karakterisatie, de beschrijving van de staat van het reservoir, de betrouwbaarheid van de voorspellingen en de schatting van de gasreserves. Om dit te bewerkstelligen is de ES methode gebruikt. Resultaten tonen aan, dat "history matching" van een gasveld met drukgegevens alleen, leidt tot niet-unieke oplossingen, waarbij verschillende parametercombinaties tot hetzelfde geobserveerde drukgedrag in de putten kunnen leiden. In zulke gevallen is het bijna onmogelijk om tegelijkertijd betrouwbare schattingen van de karakteristieken van de waterinstroom en van de structurele reservoirvorm of permeabiliteiten te bepalen. Om dit op te lossen is additionele informatie nodig, zoals bijvoorbeeld time-lapse zwaartekrachtsmetingen. We laten zien, dat een gezamenlijke assimilatie van druk- en zwaartekrachtsmetingen veel beter afgebakende inverseoplossingen oplevert, met niet alleen een verbeterde voorspelling van gas- en waterproductie, maar ook een nauwkeuriger reserve evaluatie en beschrijving van de staat van het reservoir. Tenslotte is nog gekeken naar een voorbeeld van assimilatie van zwaartekrachtsmetingen, waarbij systematische model- of observatiefouten, ook wel "bias" genoemd, optreden. De definities van observatiebias en van modelbias, zoals gebruikt in deze studie, zijn gerelateerd aan een aantal praktische aspecten van time-lapse zwaartekrachtsmetingen. De observatiebias is gedefinieerd als een willekeurige verschuiving in de geobserveerde zwaartekrachtsmetingvariaties, die kan optreden bij time-lapse zwaartekrachtsmetingen gebaseerd op relatieve metingen. De modelbias is gerelateerd aan de incompleetheid van een model. Als voorbeeld, een numeriek model wordt over het algemeen alleen gemaakt voor het olie- of gasreservoir, een soortgelijk model is bijna nooit beschikbaar om ook de hydrologische processen boven het veld te modelleren. Dit heeft tot gevolg, dat de geobserveerde variaties in zwaartekrachtsmetingen, waar de hydrologische signaalinvloed in opgesloten zit, niet correct voorspeld kunnen worden. Met andere woorden, de modelvoorspellingen van de meetgegevens bevatten een bias. In deze studie is de modelbias gereduceerd tot het zwaartekrachtssignaal veroorzaakt door grondwaterstandvariaties. We laten zien, dat de invloed van zowel de observatiebias als de modelbias op de assimilatieresultaten aanzienlijk kan zijn en kan leiden tot een behoorlijke onder- of overschatting van de staat van het reservoir en/of van de reservoirparameters. Een zogenaamde bias-bewuste data assimilatiemethode zou een oplossing kunnen bieden, indien men zich er bewust van is, dat het model en/of de observaties inderdaad een bias bevatten. Informatie over de aanwezigheid van een bias kan afgeleid worden uit de mismatch tussen de meetgegevens en de voorspelde gegevens, maar om de bron van de bias te achterhalen (model, waarnemingen of beiden) zijn aanvullende gegevens noodzakelijk. De randvoorwaarden voor de oorzaak van de bias en voor de karakteristieken van de bias kunnen opgelegd worden door a-priori informatie mee te nemen. De bias foutencovarianties bevatten de ruimtelijke biasinformatie, terwijl de karakteristieken in de tijd worden meegenomen in de bias-evolutiemodellen. We hebben aangetoond, dat door een bias-bewuste data assimilatiebenadering, de negatieve invloed van de bias tot een minimum beperkt gehouden kan worden. De aanwezigheid van bias leidt echter wel tot meer onzekere parameterschattingen (grotere variantie) vergeleken met een scenario zonder bias.

Acknowledgements

This research was carried out within the context of the ISAPP Knowledge Centre. ISAPP (Integrated Systems Approach to Petroleum Production) is a joint project of the Netherlands Organization for Applied Scientific Research TNO, Shell International Exploration and Production, and Delft University of Technology.

I thank Petroleum Development Oman for providing data used in this research. The Sultanate of Oman Ministry of Oil and Gas is acknowledged for granting a permission to publish the results in the thesis. Shell International Exploration and Production B.V. is acknowledged for providing financial support to print the thesis.

It was a long journey to arrive to this point when, with a great pleasure, I can write these acknowledgements. Many people have contributed to this research and please forgive me if I forget to acknowledge any of you. In the first place, I would like to thank my supervisors for giving me the opportunity to do this research and for their continuous support. I thank my day-to-day supervisor Pavel Ditmar for many hours of interesting discussions we had together, for his patience, stimulating criticism and many useful comments. I thank Femke Vossepoel for her feedback and for being always very supportive in every big and small matter. I thank my promoters, Roland Klees and Rob Arts, for guidance, openness, and their comments. Rob thank you very much for your effort to translate the propositions and the summary into Dutch. It was a great pleasure to work with you all.

I would like to thank Remus Hanea for his help and enthusiasm which he brought into this research and also for being a good friend. I thank Wiktoria for her friendship and nice coffee breaks we had together. I acknowledge Ola Eiken for many useful suggestions and for sharing his knowledge. Ola it was great to visit you in Norway and to learn from you about time-lapse gravimetry.

I thank all my colleagues at the Department of Geoscience and Remote Sensing at TU Delft for the nice time we spent together. Réne thank you for showing me gravimetry in practice. Cornelis, Hassan thanks for nice chats we always had. Pooja, Anneleen, Sami, it was great to work with you.

Many thanks to my family in Poland for supporting me all the time. Last but not least, special thanks to my wife Monika for her love, encouragement and help, especially in the last days when the thesis was produced. I thank my daughter Natalia for being there and for bringing so much joy into my life.

About the author

Marcin Albert Glegola was born on 3$^{\mathrm{rd}}$ March 1981 in Krosno Odrzanskie, Poland. Between 1996-2000 he attended secondary school at Liceum Ekonomiczne in Zielona Gora, Poland. In 2000 he started his education at Faculty of Management at University of Zielona Gora, Poland, from where in 2005 he obtained M.Sc degree in Marketing and Management. In 2003 he also started M.Sc program at Faculty of Informatics and Computer Science at University of Zielona Gora and he obtained his degree in Computer Science and Econometrics in 2008. From September 2005 he followed M.Sc program in Risk and Environmental Modeling at Delft University of Technology and obtained his M.Sc. degree in Applied Mathematics in 2007.

From February 2008 until August 2012 he was a PhD researcher at Department of Remote Sensing at Delft University of Technology. His PhD research was conducted within ISAPP-1 (Integrated System Approach Petroleum Production) program and it resulted in PhD thesis with title: ”Gravity observations for hydrocarbon reservoir monitoring”.

From September 2012 Marcin is Geophysicist at Shell Global Solutions International B.V.